Targeted Fluorescent Probes for Diagnostic Applications

Weber, Maria

Award date:
2020

Awarding institution:
University of Bath

Targeted Fluorescent Probes for Diagnostic Applications

Maria Weber

A thesis submitted for the degree of Doctor of Philosophy

University of Bath

Department of Chemistry

August 2019

Signature ……. Date ...…..…….

Nothing in life is to be feared, it is only to be understood. Now is the time to understand more, so that we may fear less.

– Marie Curie –

Acknowledgements

First of all, I would like to thank my three supervisors Prof. Tony James, Dr Amanda Mackenzie and Prof. Steven Bull for all the guidance and support during my PhD. Their expertise and enthusiasm have made my PhD experience interesting and very valuable. I mostly enjoyed working at the interface of chemistry and biology.

Working in the James and Bull group has been overall an enjoyable experience. In particular, I would like to thank past members Robert Chapman, William Cunningham, Marc Hutchby and Emma Lampard for being so welcoming at the start of my PhD. Special thanks go to current members Maria Odyniec, Josh Tibbetts, Jordan Gardiner, Ben Emery, and Robin Groleau, for making the office and lab a fun place to work.

As part of my PhD, I had the opportunity to undertake two internships. First, I would like to acknowledge Oliver Price, with whom I did my sustainability placement at Reckitt Benckiser and second, Prof. Kazuya Kikuchi for the opportunity to carry out research at Osaka University. Thanks must also go to Dr. Masafumi Minoshima and Namiko Yamada who helped me significantly during my research stay. Both internships were highly valuable for my PhD and future career development.

This project would not have been possible without the funding from the EPSRC, the Centre for Sustainable & Circular Technologies and the Royal Society of Chemistry. I am grateful for the opportunity to carry out an interdisciplinary project and having had the chance to attend conferences in Thailand, China, and USA.

I would also like to acknowledge John Lowe for NMR training, Shaun Reeksting for MS training, and Anne Gesell for confocal microscopy and plate reader training. Thanks must also go to our collaborators for cellular and animal studies, in particular Prof. Xiao-Peng He and Hai-Hao Han at East China University of Science and Technology, Prof. Jingya Li and Bohan Li at the University of Chinese Academy for Sciences and Prof. Juyoung Yoon and Gyoungmi Kim at Ewha Woman's University.

The PhD would not have been the same without CSCT Cohort 2015. In particular, I wish to thank Miriam Regue, Leyorla Ohene-Yeboah, Isabella Poli, Carlos Lopez-Alled, Felix Abeln, Cei Provis-Evans, and honorary members Oriol Escursell and Jane Provis-Evans for the great times and conversations at lunch, coffee, in the pub and on various trips.

Finally, the PhD would not have been possible without my family. To Mum, Dad, Sophia, and Babu, thank you for the love, encouragement and support during my PhD journey.

Abstract

The work of this thesis is primarily based on the development of novel probes for peroxynitrite ($ONOO^-$) detection and their applications *in vitro*.

Chapter 1 introduces peroxyresorufin-1 (PR1) as an $ONOO^-$ sensitive and selective probe. Confocal imaging in J774.2 macrophages confirmed PR1's ability to detect exogenous and endogenous $ONOO^-$. Subsequent studies using a plate reader focused on validating PR1 as an effective tool to study pathways involved in generating $ONOO^-$. Stimulation with LPS, IFN-γ, PMA and ATP, scavenging effects with $O_2^{\cdot-}$ and NOS inhibitors as well as hypoxic environments were investigated.

Following on from validating PR1 as an effective fluorescent tool in macrophages, Chapter 2 discusses the synthesis and *in vitro* studies of PR1 derivatives. Two classes of PR1 derivatives are explored in this chapter: organelle targeting probes and alkyne and alkane based probes with increasing lipophilicity and *in situ* click chemistry applications. The organelle targeting PR1 derivatives showed poor cell permeability in contrast to the alkyne and alkane derived probes. The latter were shown to detect exogenous and endogenous $ONOO^-$ in RAW264.7 macrophages with one showing good applicability for *in vivo* studies. Subsequently, this led to the development of theranostics probes: detection of $ONOO^-$ and release of a drug *in situ*.

Chapter 3 outlines the development of three $ONOO^-$ coumarin probes that target specific organelles in the cell: mitochondria, lysosome and endoplasmic reticulum. All three ratiometric probes displayed excellent selectivity and sensitivity towards $ONOO^-$ over other ROS. *In vitro* studies with RAW 264.7 macrophages were carried out using exogenous and endogenous $ONOO^-$ generation. The lysosome targeting coumarin probe was the only one found to be cell permeable and able to detect exogenous and endogenous $ONOO^-$.

Chapter 4 introduces a series of $ONOO^-$ probes based on fluorescein, rhodamine, and rhodol fluorophores with benzyl Bpin target groups for $ONOO^-$. Rhodamine and rhodol should allow for targeting the mitochondria and endoplasmic reticulum respectively, whereas fluorescein is of interest since it has been approved by the FDA.

All three probes were selective and sensitive for *in situ* detection of $ONOO^-$ but showed poor properties *in vitro*.

Finally, Chapter 5 describes a rhodamine based probe for the selective and sensitive detection of glutathione (GSH). The unusual reactivity of the azide to preferentially detect GSH over hydrogen sulfide (H_2S) led to comprehensive fluorescence studies to validate the GSH probe *in situ*. Azides are known to be reduced by H_2S into the corresponding amine. To our surprise, the binding of GSH to the azide group is preferred and releases a fluorescence signal.

Output

Publications

- Resorufin derived fluorescent probes for the selective detection of peroxynitrite *in vitro* and *in vivo*; Weber, M.[1], Han, H.-H.[1], Li, B.[1], Jarman, C. E. F., Odyniec, M. L., Sedwick, A. C., Zang, Y., Li, J., Bull, S. D., Mackenzie, A. B., Li, J., He, X.-P., James, T. D., manuscript in preparation.

- Sensing peroxynitrite in different organelles of murine RAW264.7 macrophages with coumarin-based fluorescent probes; Weber, M. Yamada, N., Tian, X., Bull, S. D., Minoshima, M., Kikuchi, K., Mackenzie, A. B., James, T. D., Frontiers in Chemistry, manuscript submitted

- An azulene-derived fluorescent probe for bioimaging: Detection of reactive oxygen species by two-photon microscopy; Murfin, L. C.[1], Weber, M. [1], Park, S. J. [1], Kim, W. T. [1], Lopez-Alled, C. M., McMullin, C. M., Pradaux-Caggiano, F., Lyall, C. L., Kociok-Köhn, G., Wenk, J., Bull, S. D., Yoon J., Kim, H. M., James T. D. & Lewis S. E., JACS, just accepted.

- Protein encapsulation: a new approach for improving the capability of small-molecule fluorogenic probe; Han, H.-H., Sedgwick, A.C., Shang, Y., Li, N., Zang, Y., Brewster, J. T., Odyniec, M. L., Weber, M., Bull, S. D., Li, J., Sessler, J. L., James, T. D., He, X.-P., Tian, H., Chemical Science, just accepted.

- Fluorescence based tool to detect endogenous peroxynitrite in M1-polarized murine J774.2 macrophages; Weber, M., Mackenzie, A. B., Bull, S. D. & James, T. D., Analytical Chemistry, 2018, **90**, 10621–10627.

- ESIPT-based ratiometric fluorescence probe for the intracellular imaging of peroxynitrite; Wu, L., Wang, Y., Weber, M., Liu, L., Sedgwick, A. C., Bull, S. D., Huang, C. & James, T. D., Chemical Communications, 2018, **54**, 9953-9956.

- 'AND'-based fluorescence scaffold for the detection of ROS/RNS and a second analyte; Odyniec, M. L., Sedgwick, A. C., Swan, A. H., Weber, M., Tang, T. M. S., Gardiner, J. E., Zhang, M., Jiang, Y. B., Kociok-Kohn, G., Elmes, R. B. P., Bull, S. D., He, X. P. & James, T. D., Chemical Communications, 2018, **54**, 8466-8469.

[1] Equal contribution

Conferences

Aug 2019: 258th ACS Fall 2019 National Meeting, San Diego, USA – poster presentation

Jun 2019: Bolland Symposium, University of Bath, Bath, UK – oral presentation

Jun 2018: Bolland Symposium, University of Bath, Bath, UK – conference organiser & poster presentation

Jun 2018: Molecular Sensors & Molecular Logic Gates Conference, Dalian, China – oral presentation

Feb 2018: Pure and Applied Chemistry Conference, Hat Yai, Thailand – oral presentation

Feb 2018: Seminar, Walailak University, Nakhon Si Thammarat, Thailand – oral presentation

May 2018: Bolland Symposium, University of Bath, Bath, UK – poster presentation

Apr 2017: Sensors: Diagnostics for Sustainable Healthcare Symposium, Bath, UK – conference organiser & poster presentation

Sep 2016: Sensors Day, Cambridge, UK – poster presentation

Awards & Prizes

Aug 2019:	RSC travel grant – analytical division
Mar 2019:	Japanese research fellowship award from Osaka University
Jun 2018:	Best overall 2nd year PhD poster, Bolland symposium, University of Bath, UK
Jun 2018:	Cancer research network at Bath travel award
Jun 2018:	RSC travel grant – chemistry/biology interface
Feb 2018:	RSC analytical trust fund international travel award
May 2017:	Best healthcare poster sponsored by Atlas Genetics, Bolland symposium, University of Bath, UK
Apr 2017:	RSC scientific meeting grant for Sensors: Diagnostics for Sustainable Healthcare healthcare symposium

Abbreviations

APCI	atmospheric pressure chemical ionisation
aq.	aqueous
Arg-1	arginase-1
ASAP	atmospheric analysis probe
ATP	adenosine triphosphate
Au	gold
Bpin	boron pinacolate
BPO	benzyl peroxidase
br.	broad
C	Celsius
calcd	calculated
CARD	caspase activation and recruitement domain
$CDCl_3$	deuterated chloroform
$(CD_3)_2CO$	deuterated acetone
$(CD_3)_2SO$	deuterated dimethyl sulfoxide
CFU	colonary form units
CO_2	carbon dioxide
d	doublet
DC	dendritic cells
DCM	dichloromethane
DIBAL-H	diisobutylaluminium hydride
DIPEA	diisopropylethylamine
DLC	delocalised lipophilic cations

DMEM	Dulbecco modified eagle medium
DMF	dimethylformamide
dppf	1,1’-bis(diphenylphosphino)ferrocene
EBS	ebselen
e.g.	exempli gratia
EPR	electorn paramagnetic resonance
ESI	electron spray ionization
Et	ethyl
EtOAc	ethyl acetate
FC	flash column chromatography
FDA	food and drug administration
FT	fourier transform
g	gram(s)
GSH	glutathione
h	hour(s)
H_2O_2	hydrogen peroxide
H_2S	hydrogen sulfide
HBSS	Hank’s balanced salt solution
HCl	hydrochloric acid
HEPES	4-(2-hydroxyethyl)-1-piperazineethanesulfonic acid
HIF	hypoxia inducible factor
HR	high resolution
i.e.	id est
IFN	interferon

IL	interleukin
IR	infrared spectroscopy
J	coupling constant (NMR) in Hz
KOAc	potassium acetate
L	liter
LoD	limit of detection
LPS	lipopolysaccharide
m	mili-; medium; multiplet; mitochondrial
M	molar
m.p.	melting point
m/z	mass over charge ratio
MALDI	matrix-assisted laser desortion/ionisation
Me	methyl
MeCN	acetonitrile
MeOH	methanol
min	minute(s)
mol	moles
MRI	magnetic resonance imaging
MS	mass spectrometry
MTS	mitochondrial targeting sequences
N_2	nitrogen
NAC	*N*-acetyl cysteine
NADPH	nicotinamide adenine dinucleotide phosphate
NaH	sodium hydride

$NaHCO_3$	sodium bicarbonate
NK	natural killer
NaOH	sodium hydroxide
$NaNO_2$	sodium nitrite
NBS	*N*-bromosuccinimide
NCD	non-communicable diseases
$NH_4^+Cl^-$	ammonium chloride
NLR	NOD-like receptor
$NO\cdot$	nitric oxide
NOS	nitric oxide synthase
NOX	NADPH oxidase
NMR	nuclear magnetic resonance
NSI	nanospray ionisation
$O_2^{\cdot-}$	superoxide
$ONOO^-$	peroxynitrite
Opti-MEM	reduced serum media
PBS	phosphate buffered saline
PMA	phorbol 12-myristate 13-acetate
ppm	parts per million
PPP	pentose phosphate pathway
PR1	peroxyresorufin-1
PYD	pyrin domain
q	quartet
RCF	relative centrifugal force

RCS	reactive chlorine species
RNS	reactive nitrogen species
ROS	reactive oxygen species
RT	room temperature
s	singlet; strong
s.d.	standard deviation
sat.	saturated
SEM	standard error of mean
SIN-1	3-Morpholino-sydnonimine
SiO_2	silica
SOD	superoxide dismutase
t	triplet
THF	tetrahydrofuran
TLR	toll-like receptor(s)
TOF	time of flight
TPP	triphenylphosphonium
UA	uric acid
UV	ultraviolet
w	weak
wt%	weight percent
δ	chemical shift in ppm relative to TMS
$\tilde{\nu}$	wavenumber(s)
°	degree
µ	micro

Table of Contents

Chapter 1 – Detection of $ONOO^-$ with Peroxyresorufin-1 in a Murine J774.2 Macrophage Cell Line

1. Introduction

Our immune system has developed remarkably when it comes to the combat of extracellular and intracellular harmful pathogens.[1-3] In the event of an extracellular pathogen, the immune system aims to eradicate the pathogen itself and neutralise its products. Intracellular pathogens are either destroyed by lymphocytes, which were previously activated by an antigen or other relevant cells are triggered to combat the pathogen. In fact, during inflammation three major events occur: blood supply to the infected area is increased, capillary permeability is enhanced and leucocytes migrate out of the venules into the surrounding tissues. A classification of different types of cells is illustrated in Figure 1. Immune responses towards harmful stimuli are primarily produced by leucocytes. Mature, circulating leucocytes differentiate from hematopoietic stem cells. There are three main types of leucocytes: phagocytes which are associated with innate immune responses, lymphocytes associated with adaptive immune responses and auxiliary cells such as basophils for example. Among these, different subtypes can be distinguished. Phagocytes can be classified into monocytes, macrophages and polymorphonuclear neutrophils. Essentially, a process called phagocytosis occurs where phagocytes bind to microorganisms, internalise them and subsequently kill the pathogen. This is achieved by a so called phagolysosome which acidic in nature, allows to digests the pathogen. Lymphocytes of which there are two types – B and T lymphocyte – specifically recognise individual pathogens.

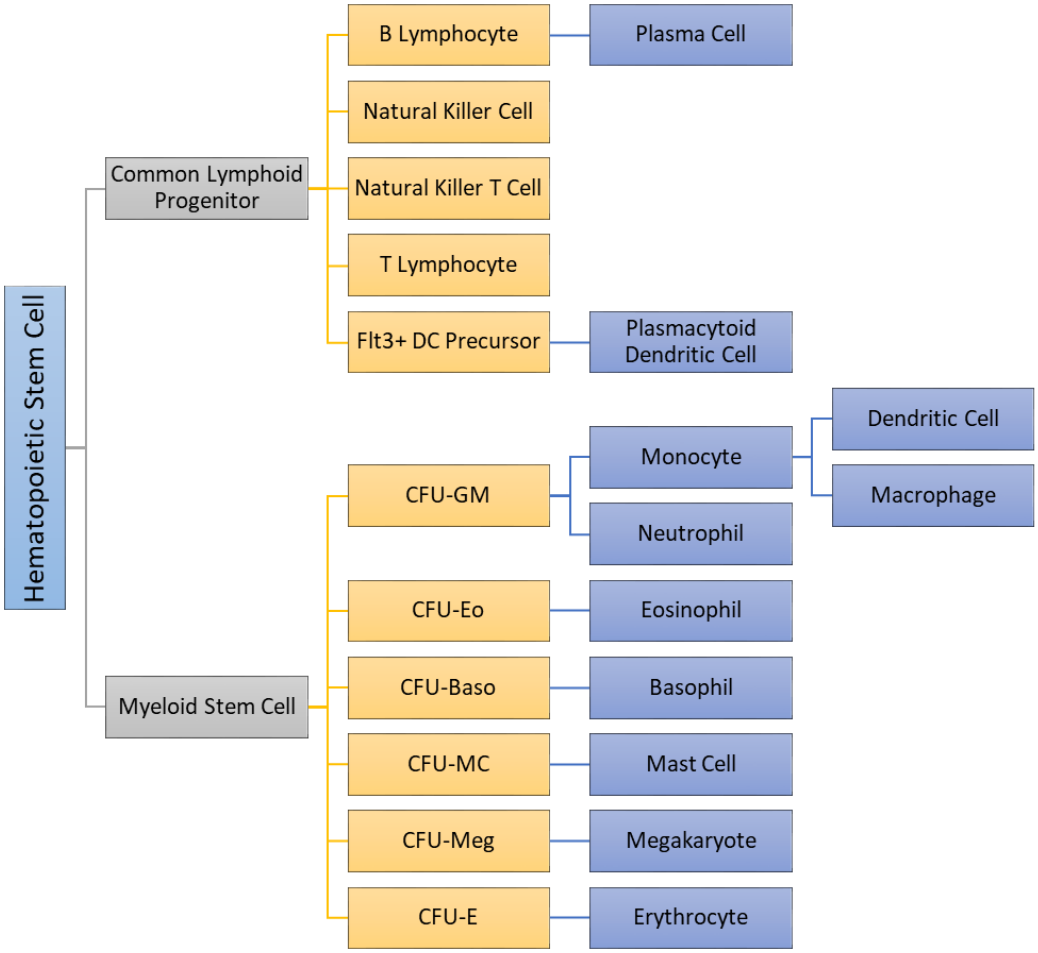

Figure 1: Simplified overview of different types of cells involved in the inflammatory response towards a harmful pathogen. Pluripotent hematopoietic stem cells differentiate in bone marrow into common lymphoid or common myeloid progenitor cells. These two main cell types then give rise to a range of other cell lineages. Lymphoid stem cells can be differentiated into B lymphocytes, natural killer (NK) cells, NK T cells and T lymphocytes whereas myeloid stem cells first give rise to specific colony form units (CFU) which differentiate into granucolyte-macrophages (GM) including monocytes (which then give rise to either macrophages and dendritic cells), and neutrophils, eosinophils, basophils, mast cells, megakaryotes and erythrocytes. Dendritic cells (DC) can also derive from a Flt3 receptor DC precursor which in turn can either come from lymphoid or myeloid stem cells. The diagram has been adapted from Chaplin.[4]

The interaction between lymphocytes and phagocytes is crucial in the effective recognition and combat of harmful internal and external stimuli. The innate immune

system heavily interacts with the adaptive immune system as illustrated in Figure 2. Hereby, one of the crucial signalling molecules between phagocytes and lymphocytes are cytokines of which one of the main classes of cytokines are interferons (IFN). These can limit the spread of certain viral infections. One type of interest is IFN-γ. IFN-γ is released by macrophages, activated CD8 T cells, NK T cells, and Th1 CD4 T cells which in turn activate phagocytes.[5]

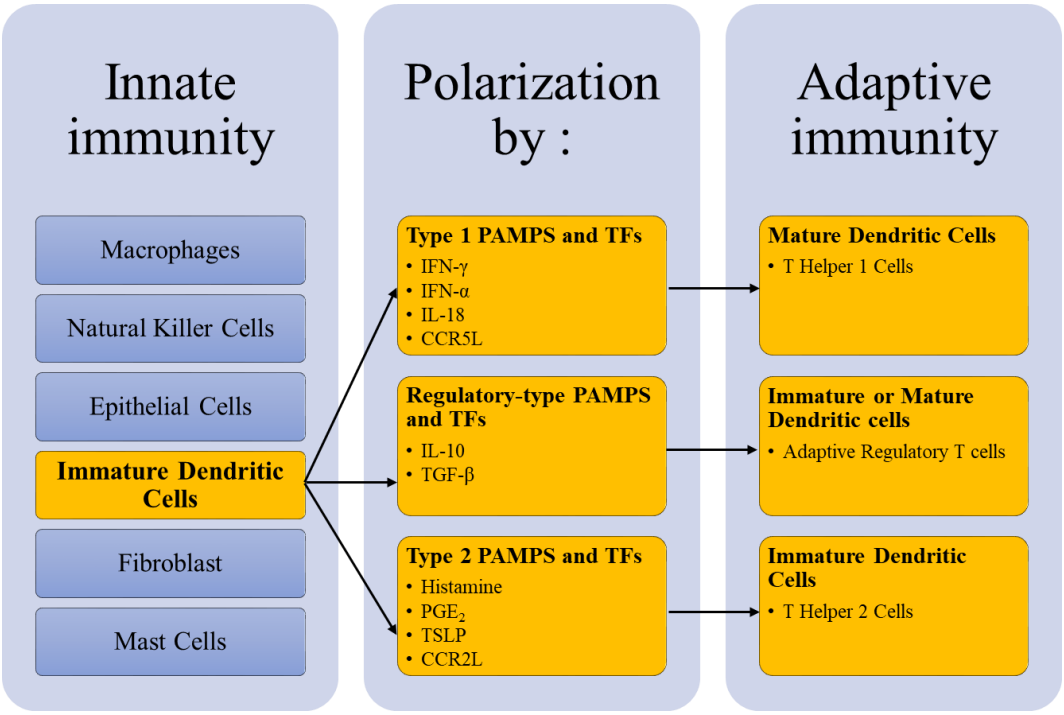

Figure 2: Innate immunity towards a pathogen is mediated by a variety of different cell types: macrophages, NK cells, epithelial cells, immature DC, fibroblasts and mast cells. Immature DC can be polarised by a variety of factors: type 1, 2 and regulatory pathogen-associated molecular patterns (PAMPS) and tissue factors (TFs). This allows then to activate either mature or immature dendritic cells that will differentiate into T Helper 1, 2 or adaptive regulatory cells. If pathogens inhibit dendritic cell expression, other innate immune cells can generate the various polarization factors allowing to proceed towards adaptive immunity. The diagram was adapted from Kapsenberg.[6]

1.1. Macrophage Function and Polarization

In recent years, growing evidence has linked non-communicable diseases (NCDs) such as cancer, autoimmune diseases, and arthritis with inflammation. Changes in mitochondrial function, oxidative stress and inflammation interchangeably determine disease progression of NCDs. It is not clear whether inflammation and oxidative stress are at the origin or constitute consequences of cellular pathology of NCDs. Nevertheless, they significantly contribute to the pathogenesis of NCDs.[7] Detecting signs of infection or damage are mainly mediated by innate immune signalling receptors such as toll-like or NOD-like receptors.[8] These monitor the extracellular and subcellular space and are able to detect changes.[9] As shown in Figure 2, macrophages are part of the innate immune response towards a harmful pathogen. Macrophages respond to micro-environmental stimuli and signals from different tissues by undergoing specific phenotype changes.[10] This process is known as macrophage polarization. Based on the expression of specific cytokines and cell surface markers, two major macrophage sub types can be generated: classically activated or inflammatory (M1) and alternatively activated or anti-inflammatory (M2) macrophages (Figure 3).

M1 macrophages are typically activated by LPS, IFN-γ, or TNF-α. M1 macrophages produce and secrete high levels of pro-inflammatory cytokines IL-1β, IL-6, IL-12, TNF-α and MCP-1. M1 macrophages remove harmful pathogens through activation of the nicotinamide adenine dinucleotide phosphate (NADPH) oxidase system, and subsequent generation of reactive oxygen species (ROS). Hence, M1 macrophages mediate ROS-induced tissue damage, and impair tissue regeneration.[11]

M2 macrophages are mainly polarized by cytokines IL-4 and IL-13 but other cytokines such as IL-10 and TGFβ are also involved. Polarization of M2 macrophages is often associated with the up-regulation of arginase as well as the secretion of IL-10 and TGFβ and low levels of a few other cytokines. M2 macrophages are anti-inflammatory in nature in contrast to M1 macrophages which are pro-inflammatory. Additionally, depending on the stimulus, M2 macrophages can be divided into subsets M2a, M2b, M2c and M2d macrophages.[12]

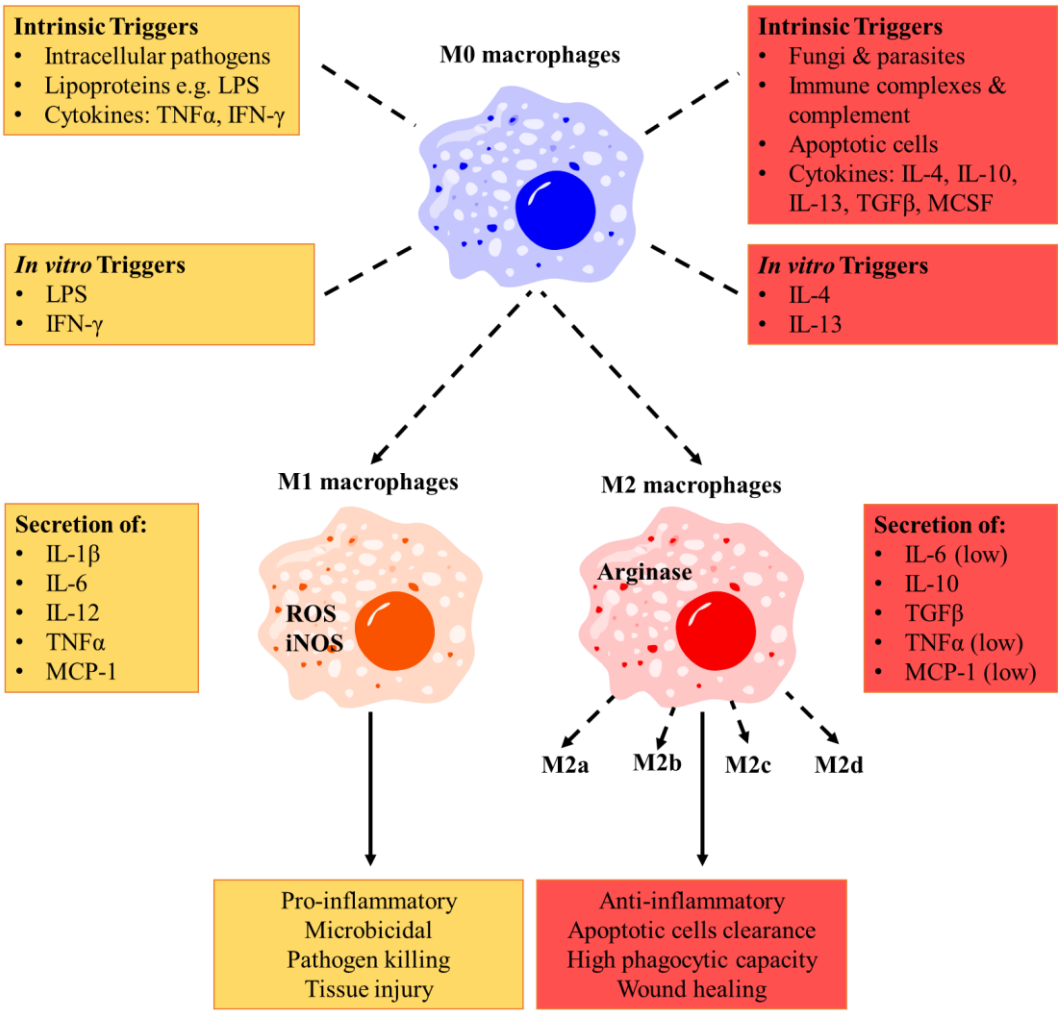

Figure 3: Macrophages can polarise into two main subtypes – M1 and M2 macrophages – with distinct properties. Activation of M1 and M2 macrophages occur by different intrinsic triggers and can also be selectively polarised for *in vitro* studies. Upon polarization into M1 or M2 macrophages, the secretion of different cytokines results. Additionally, M2 macrophages are polarised into different subsets: M2a, M2b, M2c, and M2d macrophages. The diagram was adapted from Laouini *et al.*[13] and Sahebkar *et al.*[11]

Among all these different types of cells involved in the inflammatory response, I am mostly interested in macrophages due to their versatile role. They recycle and clear cells during inflammation, participate in tissue repair and most importantly are involved in the host response towards infectious pathogens through secretion of cytokines, enzymes and ROS. In particular, the secretion of $ONOO^-$, a strong ROS oxidant, allows to directly interact with harmful stimuli and induce their apoptosis.

1.2. Macrophages and Reactive Oxygen Species

Free radical species or most commonly known as ROS are a vital part in many cellular processes (Figure 4). A balanced generation of ROS assures normal cell growth and metabolism. However, lower or higher ROS generation ultimately links to impaired physiological functioning. ROS can originate from three different sources: endogenous sources, antioxidant defences and exogenous sources. In particular, the mitochondria is one of the main intracellular ROS generator and has been linked to many diseases where high levels of ROS are generated.[14]

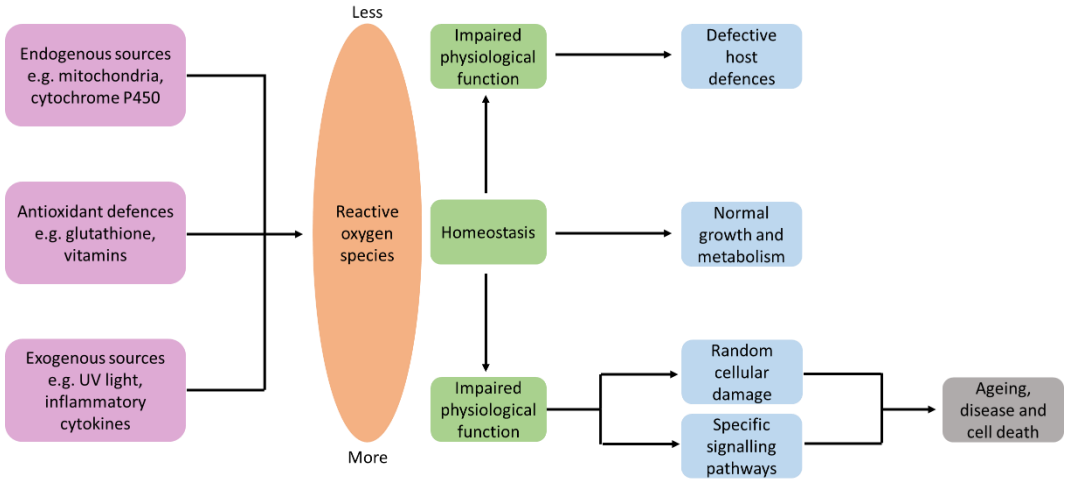

Figure 4: Sources and cellular responses to ROS adapted from Finkel et al.[15]

The term ROS is often used interchangeably with free radical species. However, free radical species can be actually divided into three categories:

- **Reactive oxygen species (ROS):** superoxide anion ($O_2^{\cdot-}$), hydroxyl radical ($HO\cdot$), peroxyl radical ($ROO\cdot$), hydroperoxyl radical ($HO_2\cdot$), hydrogen peroxide (H_2O_2), hypochlorite (ClO^-), ozone (O_3), singlet oxygen ($^1O_2$), peroxynitrite ($ONOO^-$)
- **Reactive nitrogen species (RNS):** nitric oxide ($NO\cdot$), nitrogen dioxide radical ($NO_2\cdot$), nitrous acid (HNO_2), nitrosyl cation (NO^+), nitrosyl anion (NO^-)

- **Reactive chlorine species (RCS):** atomic chlorine (Cl^-), hypochlorous acid (HClO), chlorine (Cl_2), nitronium chloride (NO_2Cl)

Among these three, ROS have gained particular attention in the research community.[15-17] ROS are short-lived species and produced in a variety of physiological processes (Figure 5).

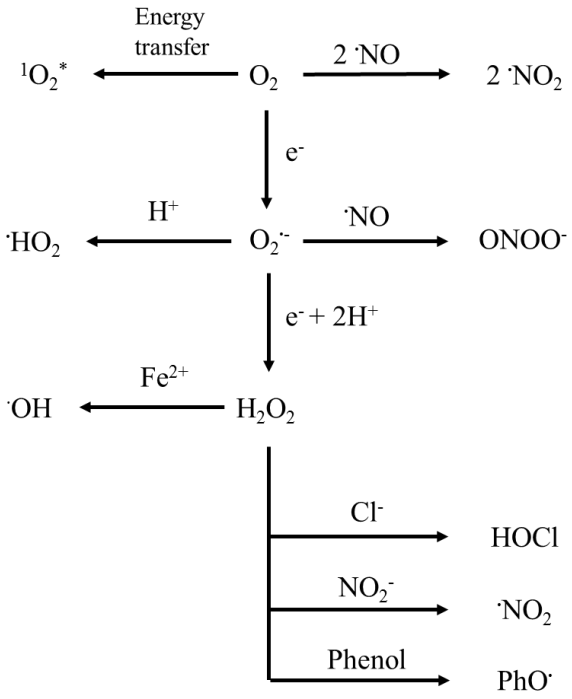

Figure 5: Physiologically relevant ROS – The diagram covers in a simplified way the generation of most ROS species within cells. The diagram has been adapted from Winterbourn and Krumova & Cosa.[18,19]

ROS are involved in the functional and phenotypic regulation of macrophages and promote both M1 and M2 macrophages. M1 macrophages activate lipopolysaccharide (LPS) which triggers the generation of ROS upon contact with a harmful stimuli. ROS are generated from NADPH by NADPH oxidase (NOX), which is produced through the pentose phosphate pathway (PPP).[20] *In vitro* generation of ROS is achieved by LPS stimulation. LPS-induced ROS generation is NOX-dependent and also induces TNFα production. At the same time, ROS can serve as a second messenger by activating NF-κB which is a protein involved in the transcription of DNA, cytokine

production and cell survival. Given that ROS are closely related to the activation of NF-κB, ROS may partially be involved in M1 macrophage polarization. Additionally, the inflammatory response is regulated by stimulation of mitochondrial complexes and adenosine triphosphate (ATP). Activating ATP triggers ROS generation which in turn activates inflammasome formation and, consequently, cytokine production such as IL-1β and IL18 (Figure 6).

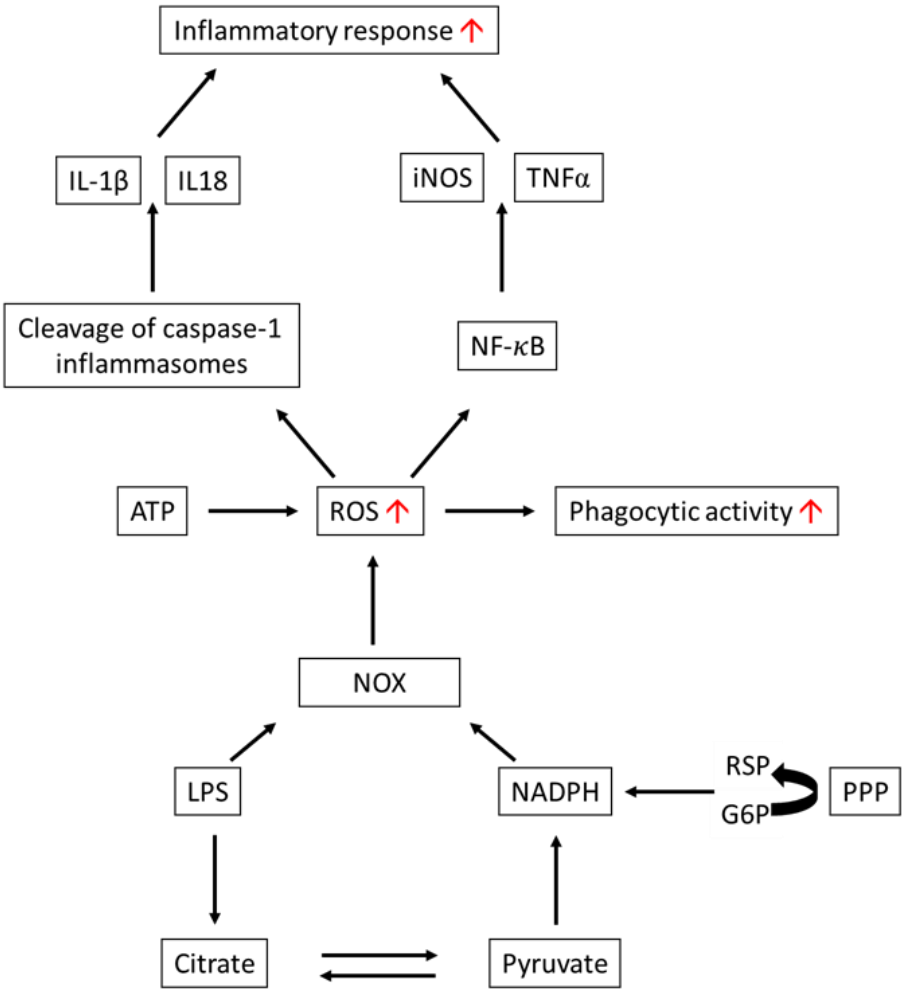

Figure 6: Multiple pathways are involved concerning ROS and their regulatory activity in M1 macrophages phagocytic activity. Generation of NADPH is essential for the NOX to generate ROS. The high levels of ROS mediate enhanced phagocytic activity of M1 macrophages. Additionally, ATP can also enhance increased ROS generation. ROS can also serve as a second messenger through NF-κB and inflammasome activation allowing to induce the inflammatory response of M1 macrophages. The diagram was adapted from *Feng et al*.[21]

M1 macrophages express inflammasome genes. In fact, inflammasomes regulate immune responses. Most inflammasomes contain NOD-like receptor (NLR) sensor molecules such as NLRP1, NLRP3, NLRP6, NLRP7, NLRP12 and NLRC4. Their exact activation mechanism is still under investigation with certain factors emerging as potential therapeutic and diagnostic targets.[22]

As part of the innate immune system, inflammasomes play a major role in the activation of the inflammatory response. Inflammasomes activate one or more caspases which trigger the secretion of pro-inflammatory cytokines. Inflammasomes were first identified by Tschopp *et al*. in 2002.[23] The group went on to identify the role of the NLRP3 inflammasome in 2004.[24] Activation of the NLRP3 inflammasome (Figure 7) contributes to the cellular mechanisms underlying infectious, metabolic, and neurodegenerative diseases.[25-27] NLRP3 inflammasome expression has mostly been observed in macrophages and neutrophils since its expressions is primarily related to myeloid cell types.[27]

An inflammasome is a cytoplasmic multi-protein complex composed of a sensor protein, an adaptor protein and pro-caspase-1:

- Sensor protein: This is the main stimulus for the assembly of the inflammasome and hence its activity. Different stimuli include but are not limited to microbial products, and host-derived danger signals. One of the sensor molecules of interest in elucidating mitochondrial ROS production is the PYD domain containing protein 3 (NLRP3).
- Adaptor protein: It can be defined as an apoptosis-associated speck-like protein. It contains a caspase recruitment domain (ASC).
- Pro-caspase-1: It is a cysteine protease which is initially inactive. The autocatalysis of pro-caspase-1 to active capase-1 is controlled by the caspase-1 inflammasome.[28]

Prior to activation of NLRP3, the sensor protein must be primed. This involves in a first instance LPS binding to TLR4, a toll like receptor, which initiates increased expression of the NLRP3 protein and pro-IL-1β. Moreover, priming induces the deubiquitination of NLRP3, which is essential for further NLRP3 inflammasome assembly. Apart from the priming step, further activation signals are vital for

activation. The current literature suggests a range of factors contributing to the activation[22, 29, 30]:

1. Translocation of NLRP3 to mitochondria
2. Generation of mitochondrial reactive oxygen species (mROS) and release of mitochondrial DNA or cardiolipin
3. Potassium efflux out of the cell
4. Release of cathepsins into cytosol after lysosomal destabilisation

Upon activation of the sensor molecule (NLRP3), the inflammasome assembles through the interaction of the pyrin domain (PYD) and caspase activation and recruitment domain (CARD). The assembly of this complex leads to processing pro-caspase in proximity to caspase-1. Hence, this leads to cleavage of pro-IL-1β, which induces the pro-inflammatory process.

Neurodegenerative diseases[31], type 2 diabetes[32], ageing[33], cancer[34] and other diseases[35] have been associated with the dysregulation of NLRP3 inflammasome activation. Hence, the innate immune system is less capable to sense microbe-derived toxins or host-derived danger signals.[36]

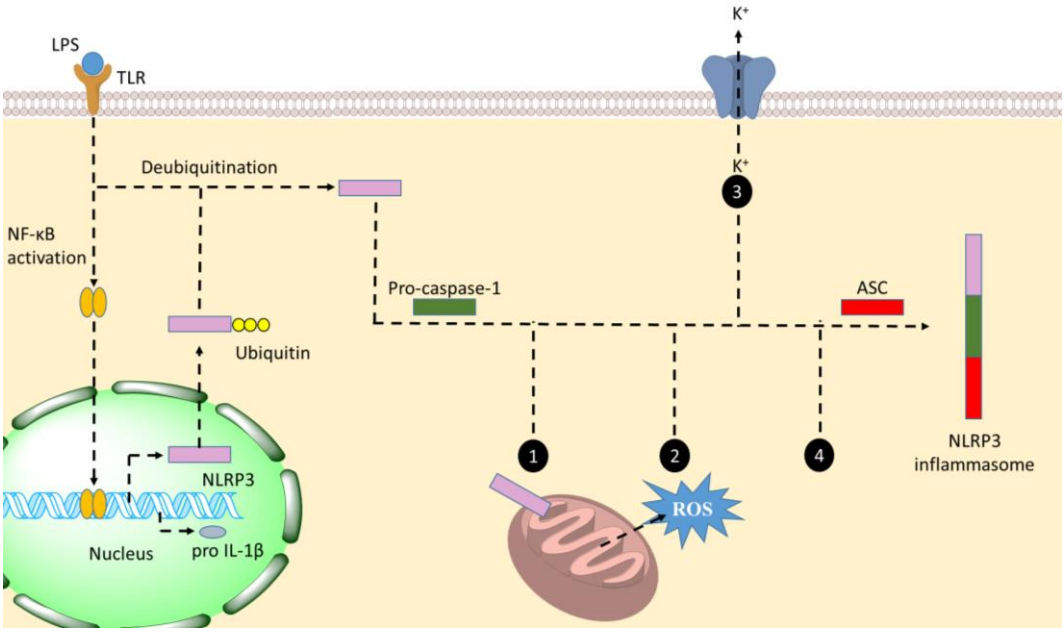

Figure 7: Simplified diagram of the mechanism of NLRP3 inflammasome activation adapted from Ting *et al*.[37] Before activation of NLRP3, two events need to occur that form part of priming: LPS binds to TLR, stimulating NF-κB activation, followed by the expression of pro-IL-1β and the NLRP3 protein. At the same time priming allows to induce the deubiquitination of NLRP3. After priming, a range of activating stimuli are required to activate NLRP3 leading towards NLRP3 inflammasome assembly: 1) translocation of NLRP3 to mitochondria, 2) generation of mROS and release of mitochondrial DNA or cardiolipin, 3) potassium efflux out of the cell, and 4) release of cathepsins into cytosol after lysosomal destabilisation. In addition to the activated NLRP3 protein, activation of pro-caspase 1 and linearly ubiquitinated and phosphorylated adaptor protein ASC are required for assembly.

In contrast to M1 macrophages, activation of M2 macrophages reduces ROS production. M2 macrophages' main function is anti-inflammatory in nature and wound healing. Wound healing properties of M2 macrophages go hand in hand with a reduction of NOX activity and an increase in disulphide protein degradation. The programming of the M2 phenotype is linked to an increase of arginase-1 (Arg-1), YM1 and FIZZ1 which promote anti-inflammatory properties of M2 macrophages. Interestingly, these are regulated by the redox dependant gene STAT6's translocation which is activated by H_2O_2.[38] Moreover, in contrast to M1 macrophages, extracellular

ATP associated with P2X7 receptors blocks IL-1β in M2 macrophages, which impacts ROS generation (Figure 8).

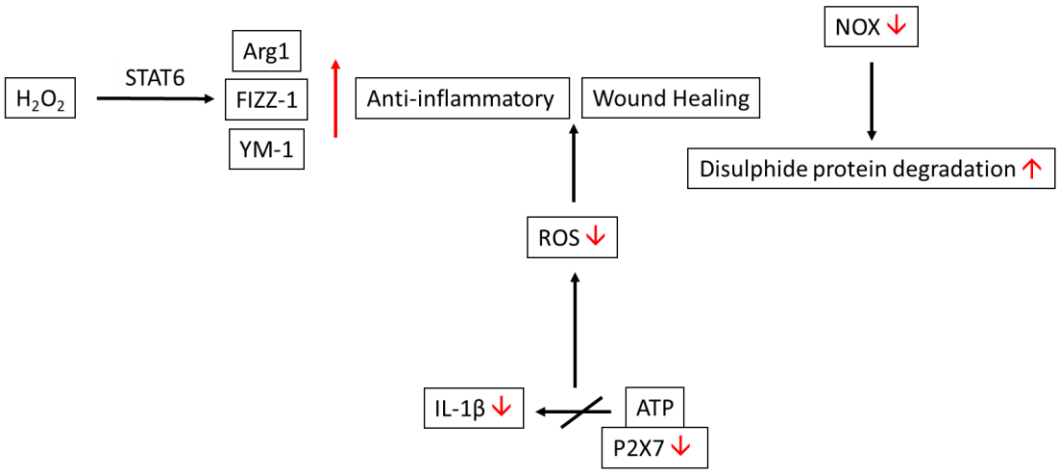

Figure 8: The involvement of ROS in regulating M2 macrophages governs anti-inflammatory and wound healing activities. Multiple pathways are involved in reducing NOX which consequently lowers ROS levels. The low ROS level reduces inflammatory mediators (IL-1β) and increases M2-regulated genes (FIZZ-1, Arg-1, YM-1). The diagram was adapted from Feng *et al.*[21]

ROS are involved in the functional and phenotypic regulation of M1 and M2 macrophages. Hence, ROS are implicated in cell death, proliferation, motility, and the phagocytic ability of macrophages. Essentially, ROS play an important role in maintaining the homeostatic functions of macrophages.

1.3. Detectors of Reactive Oxygen Species

Detection of cellular ROS in physiological and pathological processes requires sophisticated methods. Current analysis of ROS is challenging due to the complexity of the biological environment. Harrison *et al.* and Yuan *et al.* have reviewed recent advancements in methodology development for ROS detection.[39, 40] The main challenges of current methods include specificity issues and lack of subcellular

localisation. Overcoming these deficiencies in the following available techniques remains a great challenge:

- Spin trapping: Spin traps allow to quantify and identify radicals. These form covalent bonds with the radical by addition reaction. Spin traps are used in conjunction with electron paramagnetic resonance (EPR) spectroscopy. Spin traps have been mostly used for $O_2^{\cdot-}$ and $^{\cdot}OH$ identification and quantification with DMPO, DPPO and DEPMPO have been popular choices.[41] However, these spin traps together with $O_2^{\cdot-}$ can easily form adducts in the presence of reducing agents e.g. ascorbate resulting in EPR silent compounds.

- Chemiluminescent probes: These probes are mainly used for the detection of $O_2^{\cdot-}$. Common probes for biological studies include lucigenin, luminol, MCLA, and coelenterazine. Lucigenin has been extensively used but is limited by redox cycling: the lucigenin radical can readily react with oxygen to generate $O_2^{\cdot-}$.[42] Consequently, identification and quantification of cellular produced ROS is biased.

- Fluorescent probes: Most notable examples of fluorescent probes in biological systems include dihydroethidium, mitoSOX, dichlorodihydrofluorescein, dihydrorhodamine and Amplex red.[43] All these fluorescent probes are oxidant sensitive: they only become fluorescent upon reaction with ROS. These have traditionally mostly focused on H_2O_2 detection. Despite new emerging fluorescent probes, specificity for ROS and intracellular vs extracellular detection are challenges to be overcome.

Table 1 summarises the various detection methods currently available to study ROS and shows their main advantages and disadvantages. Some have been briefly discussed above but Table 1 nicely illustrates the vast range of additional methods available. As part of my thesis, I am interested in the identification of new fluorescent probes due to their stability, quantifiable nature and signal intensity. The current drawbacks can be synthetically addressed to assure high specificity and precise localisation.

Table 1: Advantages and disadvantages of different ROS detection methods adapted from Yuan *et al*.[40]

Detection method	Specificity	Advantages	Disadvantages
Spin traps	ROS, RNS	Specific, sensitive	Expensive
Electrochemical biosensors	ROS, RNS	Sensitive, fast	Complex to prepare
Chromatography methods	$^{\cdot}OH$	Sensitive, fast	Complex products
Spectrophotometry methods	$O_2^{\cdot-}$, H_2O_2	Sensitive, fast, single product	Low specificity
Chemiluminescent probes	$O_2^{\cdot-}$, $^{\cdot}OH$	Cell permeable	Low selectivity and sensitivity, intermediates not stable
Fluorescent proteins	H_2O_2, redox status changes	Dynamic, real-time, low toxicity, good permeability	Slow in reaction, restriction in receptor cells, non-sensitive
Fluorescent probes	ROS, RNS, RCS	Cell permeable, signal intensity, quantifiable, stable	Low specificity, interference with other ROS, RNS, RCS, possible toxic by-products

Designing highly specific and sensitive fluorescent probes for ROS is challenging. The choice of fluorophore (Figure 9) is essential to establish a scaffold that can be synthetically easily modified. Fluorophores can be combined with a variety of different sensing motifs which respond to ROS, proteins, metals, or other relevant biological species. In addition to the choice of fluorophore, a good ROS probe requires[44]:

- Good sensitivity
- High selectivity
- Fast and reversible kinetics
- Good signal-to-background and signal-to-noise contrast
- Good intracellular loading and uptake of the probe
- Excitation at visible wavelength
- Non toxic

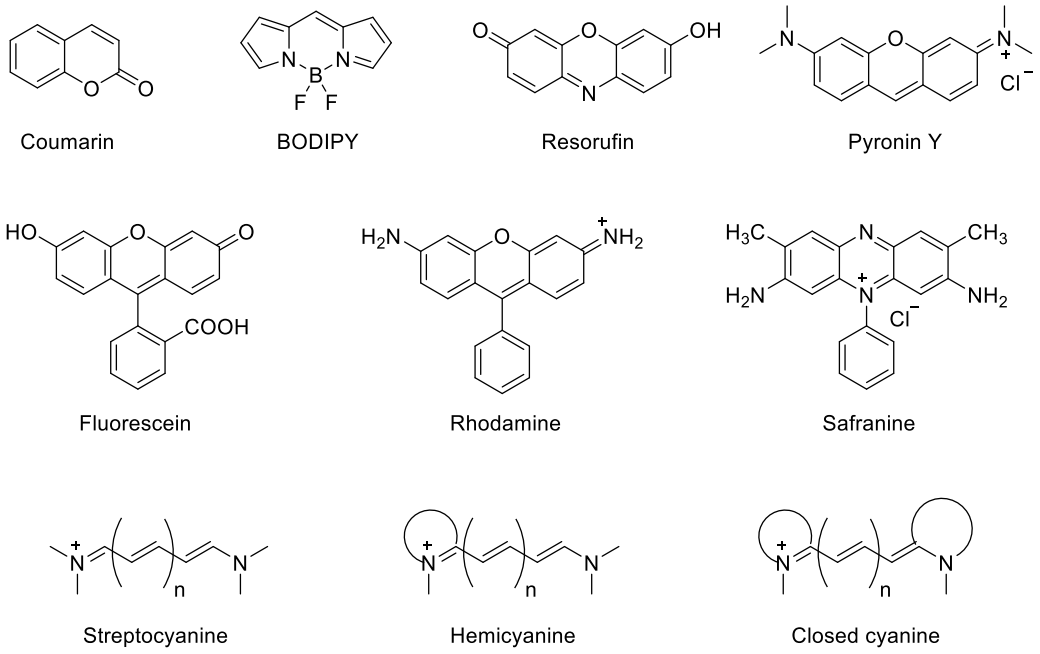

Figure 9: Most commonly used flurophores as scaffolds for sensing applications in the life sciences.

I decided to identify a simple fluorescent probe for $ONOO^-$ detection which upon validation as a biological tool, could be synthetically modified to introduce further functionalities. Due to the short half-life of $ONOO^-$, its detection can be challenging. Therefore, there is a need to find new effective and reliable $ONOO^-$ probes. This led to identifying peroxyresorufin-1 by Chang *et al.*[45] as an ideal candidate for $ONOO^-$ detection and its applicability as a biological tool.

2. Peroxyresorufin-1: Background

In 2005, Chang *et al*. developed the boronate based fluorescent probe peroxyresorufin-1 (**PR1**) for the detection of H_2O_2.[45] **PR1** was achieved in a two-step synthesis (Scheme 1). Bromination of phenoxazine **1.1** gave dibromophenoxazine **1.2** in a poor 10 % yield. Subsequent Miyaura borylation gave target probe **PR1** in 69 % yield.

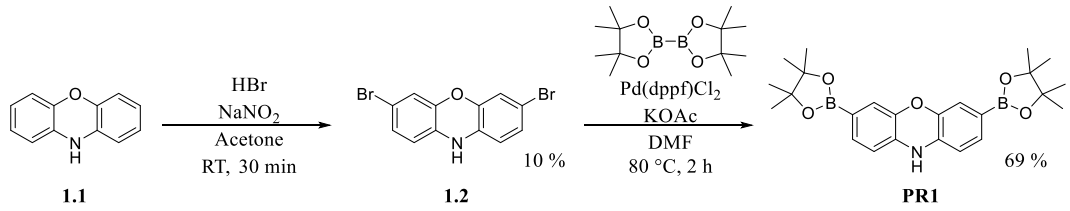

Scheme 1: Synthesis of **PR1** by Chang *et al.*[45]

High selectivity towards H_2O_2 compared to other competing ROS was achieved with **PR1**: recognition of H_2O_2 enhanced the fluorescence > 1000-fold. **PR1** has been of particular interest since it highlights the usage of boronate deprotection as an effective mechanism to probe H_2O_2 in biological systems.[46] Upon reaction with H_2O_2, a well-known fluorescent probe is generated: resorufin. Previous cell studies of **PR1** in the Chang group only focused on the use of HEK 293T cells with exogenous addition of H_2O_2.[45] This system does not truly reflect the ability of **PR1** to detect ROS *in vitro*. Stimulation of macrophages is required for ROS generation to mimic a situation where overexpression of ROS is achieved to simulate an inflammatory environment.

3. Project Aim

The aim of this chapter is to investigate **PR1** as an effective $ONOO^-$ sensing tool. Previously used as an H_2O_2 probe by Chang and co-workers[45], the aim is to show that the boronate groups of **PR1** are more sensitive towards $ONOO^-$. Subsequently, following *in situ* validation, *in vitro* studies will be performed to undermine **PR1**'s potential as an effective $ONOO^-$ evaluating tool. Hereby, J774.2 macrophages have been chosen as the cell line model system. A cell protocol for $ONOO^-$ stimulation in J774.2 macrophages will be developed in order to adequately test **PR1**. Subsequently, this protocol should form the basis for the evaluation of **PR1** analogues with improved functionalities that I have developed in Chapter 2.

4. Peroxyresorufin-1: Synthesis and Fluorescence

I realised that **PR1** could be a useful tool for $ONOO^-$ detection *in vitro*. To validate this, initially the synthesis of **PR1** was revisited and its fluorescence ability upon reaction with $ONOO^-$ was evaluated. The initial synthesis involved a low yielding bromination step with HBr generating a large amount of side products (Scheme 1). The subsequent Miyaura borylation reaction gave **PR1**. The overall yield of the two step process is 7 %. NBS was identified as a brominating agent for phenoxazine **1.1** which affords dibromophenoxazine **1.2** in an 80 % yield, followed by the Miyaura borylation to obtain **PR1**, allowing to increase the overall yield to 56 % (Scheme 2).

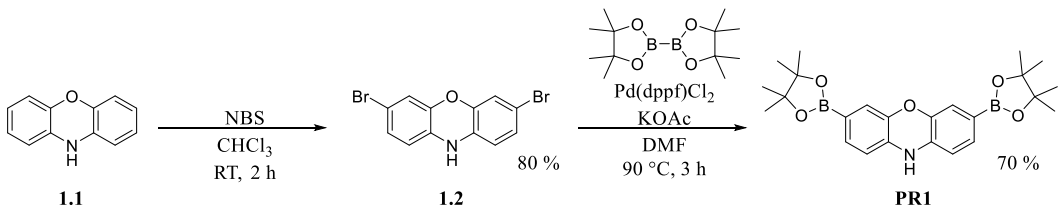

Scheme 2: Synthesis of **PR1** developed in the James group.

Boronic esters are also effective sensing groups for $ONOO^-$. In fact, their reactivity towards $ONOO^-$ is a million times faster than with H_2O_2.[47] The boronate deprotection is the underlying mechanism of **PR1** with $ONOO^-$. $ONOO^-$ attaches to the boronate, generating an intermediate, allowing the boronate group to easily fall off which gives the corresponding alcohol. Then, the other boronate group is cleaved in the same way. The alcohol group then rearranges to the ketone due to keto-enol tautomerism, generating resorufin (Scheme 3).

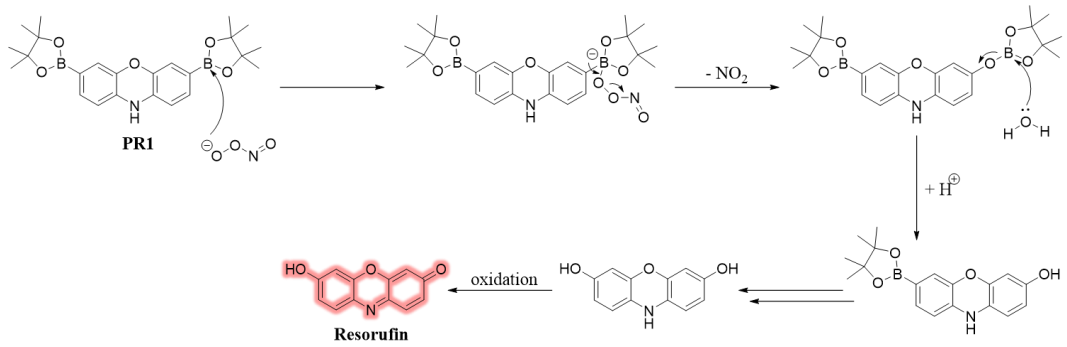

Scheme 3: When reacting with $ONOO^-$, **PR1** undergoes boronate deprotection to give the fluorophore resorufin.

Initial UV studies were carried out to confirm the formation of resorufin: a maximum absorbance close to 573 nm was observed (Figure 10). ROS selectivity studies confirmed **PR1**'s ability to detect $ONOO^-$ whereby an enhanced selectivity over other ROS was achieved (Figure 11). The low activating concentrations and fast reaction time of $ONOO^-$ confirm **PR1**'s superiority over other ROS species. Subsequent screening of different $ONOO^-$ concentrations reveals that **PR1** turns on at concentrations as low as 1 μM and saturates at 50 μM (Figure 13) in contrast to H_2O_2 (Figure 12). Initial studies of Chang *et al.* only tested **PR1** with H_2O_2 at a concentration of 100 μM to show the turn-on response of the probe. The limit of detection (LoD) for **PR1** was determined: 3.4 μM and 32.9 nM for H_2O_2 and $ONOO^-$ respectively.

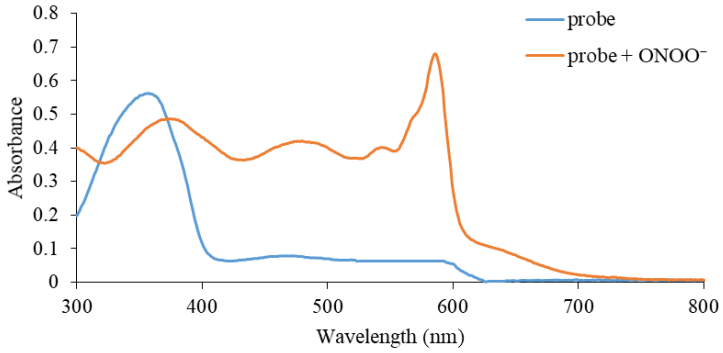

Figure 10: UV spectra of **PR1** without and with $ONOO^-$ (excess) in PBS buffer 52 % MeOH : H_2O, pH = 8.2 at 25 °C measured on a BMG Labtech CLARIOstar® plate reader.

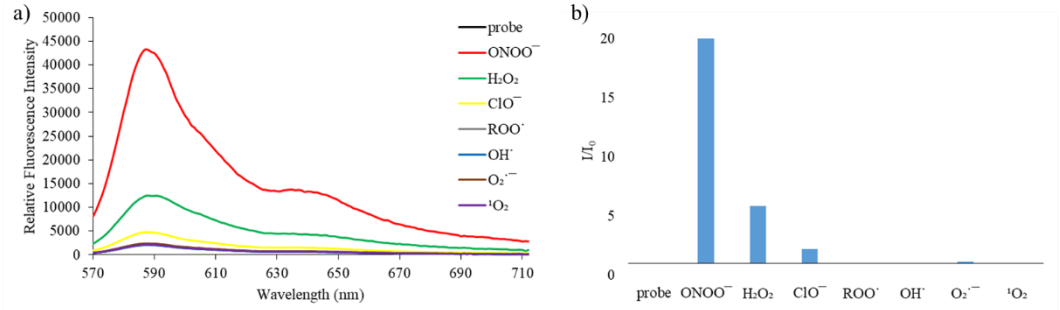

Figure 11: Selectivity data for **PR1** (500 nM): a) emission spectrum and b) relative intensity ratios (I/I_0) in the presence of $ONOO^-$ (50 µM), OH· (500 µM), $O_2^{\cdot-}$ (500 µM), $^1O_2$ (500 µM) after 5 min. H_2O_2 (1 mM), ROO· (500 µM) and ClO^- (500 µM) were measured after 30 min. The data was obtained in PBS buffer 52 % MeOH : H_2O, pH = 8.2 at 25 °C with λ_{ex} = 550 (bandwith: 15) nm and max λ_{em} = 590 nm on a BMG Labtech CLARIOstar® plate reader.

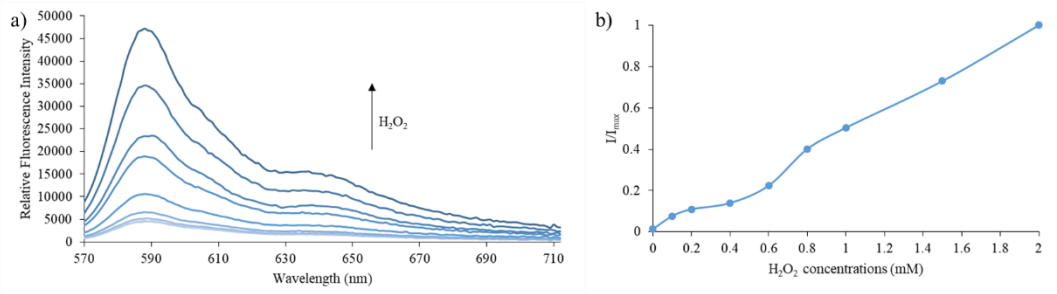

Figure 12: a) Emission spectra and b) dose dependence curve (I/I_{max}) for **PR1** (500 nM) in the presence of H_2O_2 (0.1, 0.2, 0.4, 0.6, 0.8, 1, 1.5, 2 mM) in PBS buffer 52 % MeOH : H_2O, pH = 8.2 at 25 °C. Fluorescence intensities were measured with λ_{ex} = 550 (bandwith: 15) nm and max λ_{em} = 590 nm on a BMG Labtech CLARIOstar® plate reader.

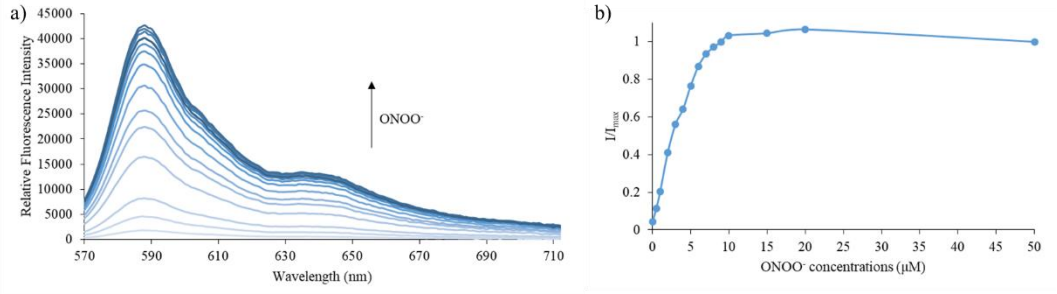

Figure 13: a) Emission spectra and b) dose dependence curve (I/I_{max}) for **PR1** (500 nM) in the presence of $ONOO^-$ (0.5, 1, 2, 3, 4, 5, 6, 7, 8, 9, 10, 20, 50 μM) in PBS buffer 52 % MeOH : H_2O , pH = 8.2 at 25 °C. Fluorescence intensities were measured with λ_{ex} = 550 (bandwith: 15) nm and max λ_{em} = 590 nm on a BMG Labtech CLARIOstar® plate reader.

5. Validating PR1 in J774.2 Macrophages

Having established the selectivity and sensitivity of **PR1** towards $ONOO^-$ *in situ*, the probe was next evaluated *in vitro*. Generation of $ONOO^-$ in J774.2 macrophages under different pro-inflammatory conditions using **PR1** as a detection tool was evaluated.

5.1. Visualising PR1 in J774.2 Macrophages

To my knowledge, **PR1** has not been studied in J774.2 macrophages beforehand, only in HEK 293T cells.[45] Macrophages respond to endogenous and exogenous signals by undergoing a phenotypic change called polarization.[48] They respond to an array of stimuli under conditions of injury and infection that lead to M1 polarization.[48] Factors that trigger M1 polarization include LPS and IFN-γ. A combination of LPS and IFN-γ has previously been used to enhance the production of $ONOO^-$.[46, 49] All recordings were performed in the presence of 1 mM probenecid to reduce the cellular efflux of **PR1**.[50] Further details about how probenicid regulates the efflux is outlined in Section 5.2.4.

First, **PR1**'s sensitivity and sub-cellular localisation in J774.2 macrophages was evaluated (Figure 14). In a subset of experiments, 3-morpholino-sydnonimine (SIN-1) was added as a positive control. **PR1** should display cytosolic localisation without targeting an organelle such as the mitochondria. To probe this hypothesis, **PR1** was co-loaded with a mitochondria fluorescent probe, MitoView Green. **PR1** was permeable in J774.2 macrophages and showed an increase in **PR1** fluorescence upon stimulation with LPS and IFN-γ, as shown by confocal microscopy. As anticipated, **PR1** does not co-localise with MitoView Green. Since **PR1** stains no particular organelle and shows no specificity in localisation, the subsequent chapter looks at approaches to address this, which would allow to monitor mitochondrial and/or lysosomal $ONOO^-$.

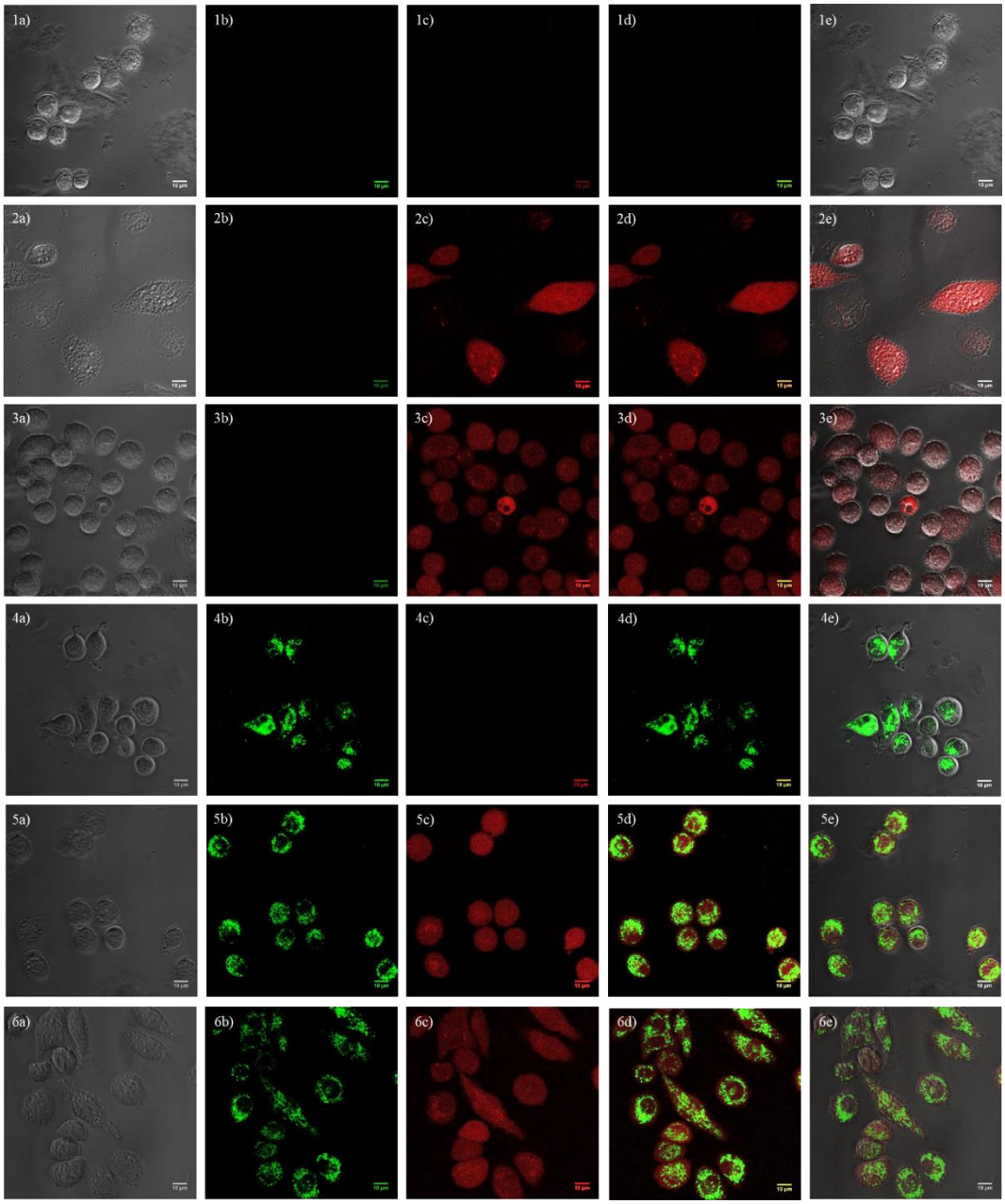

Figure 14: Confocal microscopy images of J774.2 macrophages incubated in probenecid (1 mM): 1a – e: **PR1** (15 µM, 30 min); 2a – e: **PR1** (15 µM, 30 min), LPS (1 µg/ml, 4 h) and IFN-γ (50 ng/ml, 4 h); 3a – e: **PR1** (15 µM, 30 min), LPS (1 µg/ml, 4 h), IFN-γ (50 ng/ml, 4 h) and SIN-1 (15 µM, 5 min); 4a – e: MitoView Green (200 nM, 30 min); 5a – e: MitoView Green (200 nM, 30 min), **PR1** (15 µM, 30 min), LPS (1 µg/ml, 4 h) and IFN-γ (50 ng/ml, 4 h); 6a – e: MitoView Green (200 nM, 30 min), **PR1** (15 µM, 30 min), LPS (1 µg/ml, 4 h), IFN-γ (50 ng/ml, 4 h) and SIN-1 (15 µM, 5 min). Channel (a): brightfield, channel (b): λ_{ex} = 490 nm, λ_{em} = 523 nm, channel (c): λ_{ex} = 572 nm, λ_{em} = 583 nm, channel (d): channel (b) and (c) combined, channel (e): channel (a), (b) and (c) combined. Magnification: x63. Scale bar: 10 µM. N = 3.

5.2. Evaluating PR1 as a Fluorescent Tool for $ONOO^-$ Generating Pathways

The permeability of **PR1** in J774.2 macrophages to detect exogenous and endogenous $ONOO^-$, led me to evaluate **PR1** as a fluorescent tool for the study of $ONOO^-$ generating pathways. **PR1**'s applicability to be used for assays studying $ONOO^-$ linked pathways was evaluated. Hereby, **PR1** fluorescence in M1 polarized macrophages was quantified using a fluorescence plate reader.

5.2.1. Cell Distribution for *in vitro* Studies

Next, I performed plate reader experiments to screen **PR1** responses in J774.2 murine macrophages. First, the cell number/well was evaluated to ensure optimal coverage of the well in a 96-well plate format. This allows to ensure the detection of cell-localised **PR1** fluorescence using a plate reader approach. Using an EVOS microscope, pictures were taken for 10 000, 50 000 and 100 000 cells/well (Figure 15). Poor surface coverage is observed at a cell density of 10 000 cells/well with large areas without adherent cells. On the other hand, 100 000 cells/well lead to densely packed adherent cells at the base of the well. Hence, a cell density of 50 000 cells/well gave the most uniform cell adherence across the base of the well and was selected as the most suitable cell density for further characterisation studies with **PR1**.

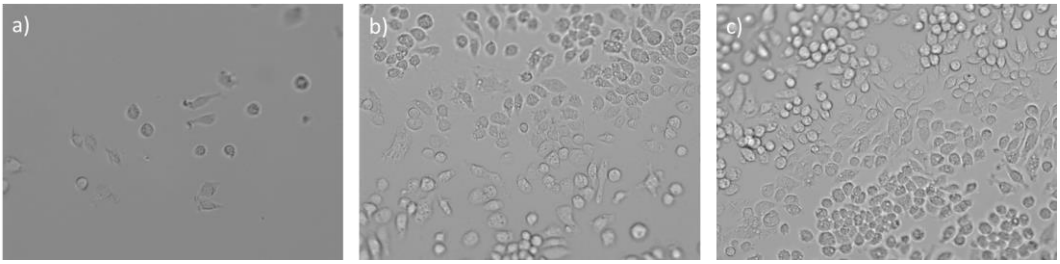

Figure 15: Pictures of different cell densities a) 10 000 cells/well, b) 50 000 cells/well, c) 100 000 cells/well using an EVOS microscope. Pictures were captured from the middle of the well. Magnification: x20. N = 3.

Having shown how densely J774.2 macrophages grow with increasing cell numbers, the aim was to evaluate how cell density affects the fluorescence signal once **PR1** reacts with $ONOO^-$ (generated by SIN-1) in J774.2 macrophages.

SIN-1 is a positive control for $ONOO^-$ and should validate **PR1**'s ability to detect exogenous $ONOO^-$ within J774.2 macrophages. SIN-1 generates $NO\cdot$ and $O_2^{\cdot-}$. These two precursors rapidly react with each other to generate $ONOO^-$. In the first instance, through base catalysis, the sydonimine ring is opened giving **4.1**. SIN-1 reduces O_2 to $O_2^{\cdot-}$ giving a cation radical species **4.2** which decomposes to **4.3** generating $NO\cdot$ as a by-product (Scheme 4).[51]

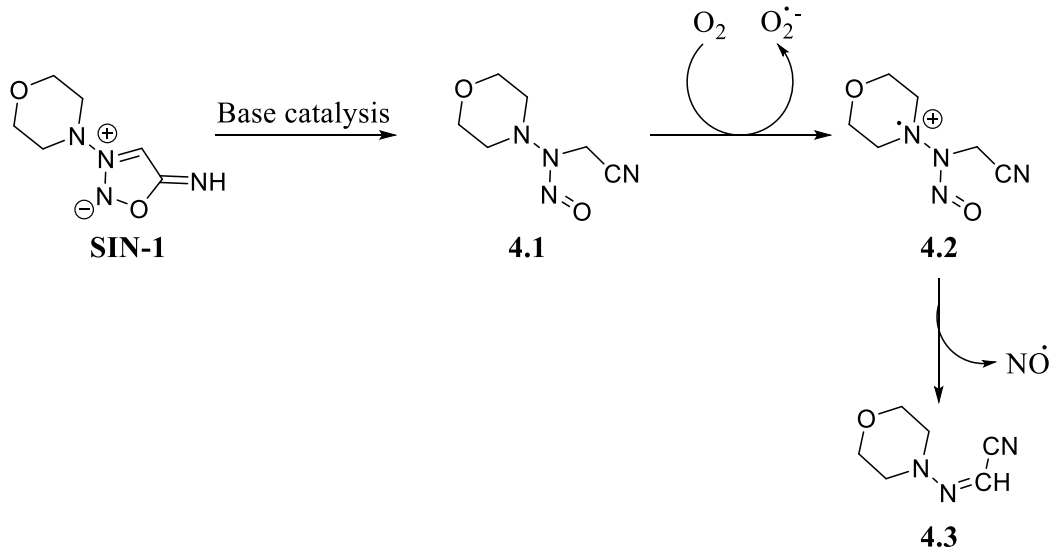

Scheme 4: Generation of $O_2^{\cdot-}$ and $NO\cdot$ through SIN-1, a positive control for $ONOO^-$ detection in J774.2 macrophages. The scheme was adapted from Kalyanaraman *et al.*[51]

Cells were plated at the stated cell number and incubated for 16 h at 37 °C, 5 % CO_2 prior to incubation with **PR1** for 30 min (Figure 16). Subsequent measurements of fluorescence intensities were performed on a BMG Labtech ClarioStar plate reader through which SIN-1 was injected after 5 min (Figure 16 – 17). Figure 16 illustrates the fluorescent response to SIN-1 at different cell numbers. No variation of the fluorescence signal is observed in the negative controls with no **PR1** or SIN-1 as expected. With increasing cell numbers, the rate of fluorescence intensity increases,

though the increase in response is not significantly different. This indicates that despite a constant concentration of **PR1** (15 µM), there is a trend towards an increased **PR1** response with an increase in cell number. I concluded from this data that a higher cell number resulted in improved $ONOO^-$ detection. Figure 17 shows an example response when 50 000 cells/well are evaluated. As can be seen at this cell number, reaction of **PR1** and SIN-1 is instantaneous and a significant increase in fluorescence intensity of **PR1** can be observed. **PR1** shows a small fluorescent response when untreated with SIN-1. This is due to the inherent ability of macrophages to produce low levels of ROS including $ONOO^-$.

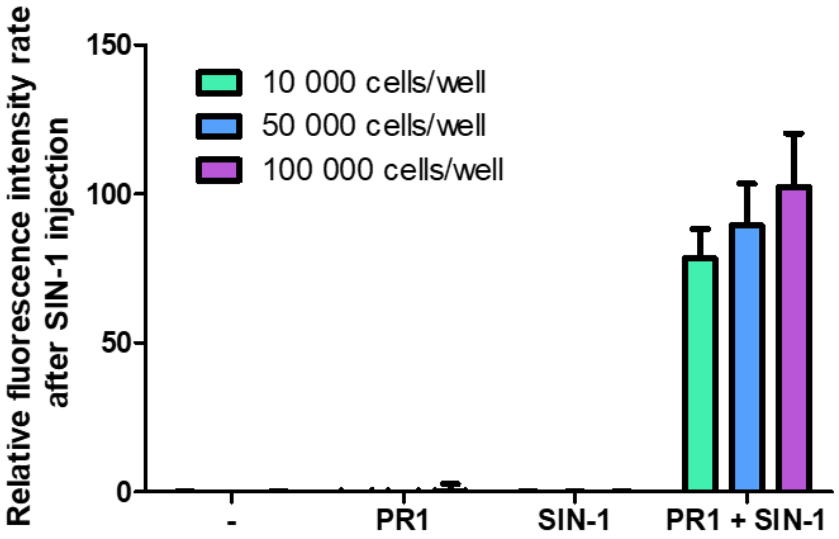

Figure 16: A **PR1** fluorescence rate increase with increasing J774.2 macrophages cell number. After SIN-1 injection, the fluorescence intensity rate of **PR1** increases at all cell distributions. Increasing cell numbers show increased rates of fluorescence intensity signal of **PR1** detecting $ONOO^-$. The control conditions show no change in rate of fluorescence intensity. Data show mean values (n = 3) ± SEM, no statistical significance. Fluorescence intensities were measured with λ_{ex} = 550 (bandwith: 15) nm and max λ_{em} = 590 nm on a BMG Labtech CLARIOstar® plate reader.

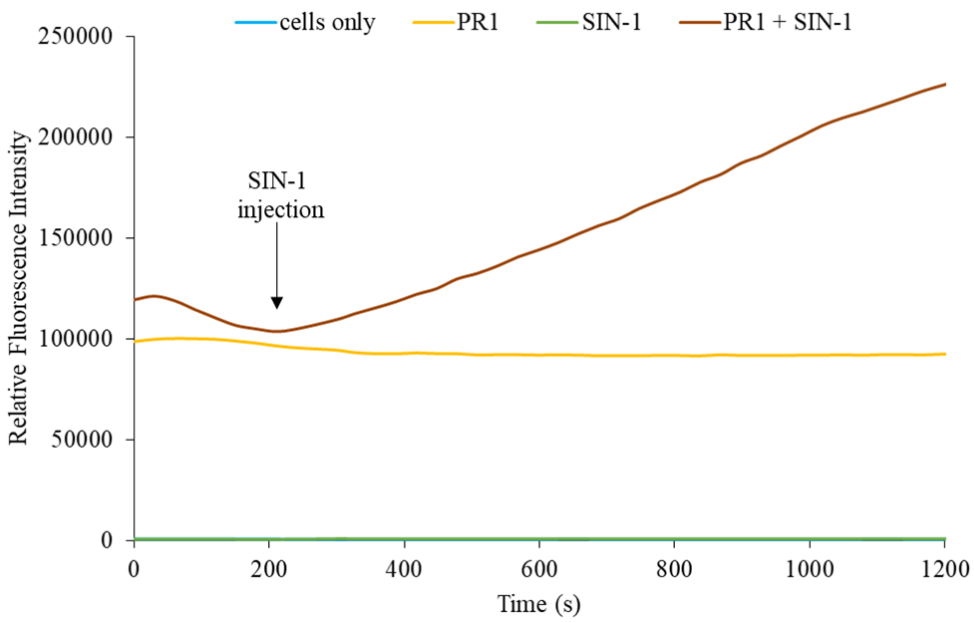

Figure 17: An increase in fluorescence intensity of **PR1** upon reaction with SIN-1 at a cell density of 50 000 cells/well. Upon injection of SIN-1, an increase of fluorescence intensity of **PR1** is observed, validating its ability to detect exogenous $ONOO^-$. Fluorescence intensities were measured with λ_{ex} = 550 (bandwith: 15) nm and max λ_{em} = 590 nm on a BMG Labtech CLARIOstar® plate reader.

5.2.2. SIN-1, a Positive Control for $ONOO^-$ Detection

Different SIN-1 concentrations were investigated with **PR1** to probe the sensitivity of $ONOO^-$ detection in J774.2 macrophages (Figure 18). The initial results with different cell numbers showed that **PR1** detects $ONOO^-$ *in vitro*. Hence, the study of different SIN-1 concentrations should allow for optimised concentrations for the validation of **PR1**.

Increasing concentrations of SIN-1 respectively produce higher concentrations of $ONOO^-$. As reported by Feelisch & Kelm in 1991, 1 mM of SIN-1 generates 10 µM of $ONOO^-$/min.[52] This can be extrapolated to the investigated SIN-1 concentrations: 2 µM of SIN-1 generate 20 nM $ONOO^-$/min and 40 µM of SIN-1 generate 400 nM of $ONOO^-$/min. Considering that **PR1**'s LoD is 32 nM, sufficient amounts of $ONOO^-$

should be present to release resorufin. After SIN-1 injection, the fluorescence signal of **PR1** was recorded for a further 15 min. Within this time frame, I was able to look at two extremes of $ONOO^-$ production: 300 nM and 6 µM of $ONOO^-$ respectively. The results validate a) sensitivity of the probe (loaded at 15 µM) at low concentrations of $ONOO^-$ produced in the nanomolar range and b) the ability of the probe to detect $ONOO^-$ intracellularly in J774.2 macrophages. 15 µM of SIN-1 was selected as the optimal concentration for further studies where using SIN-1 as a positive control for $ONOO^-$ (Figure 18). This allows sufficient production of $ONOO^-$ and avoids overproduction of $ONOO^-$ which could lead to apoptosis of J774.2 macrophages.

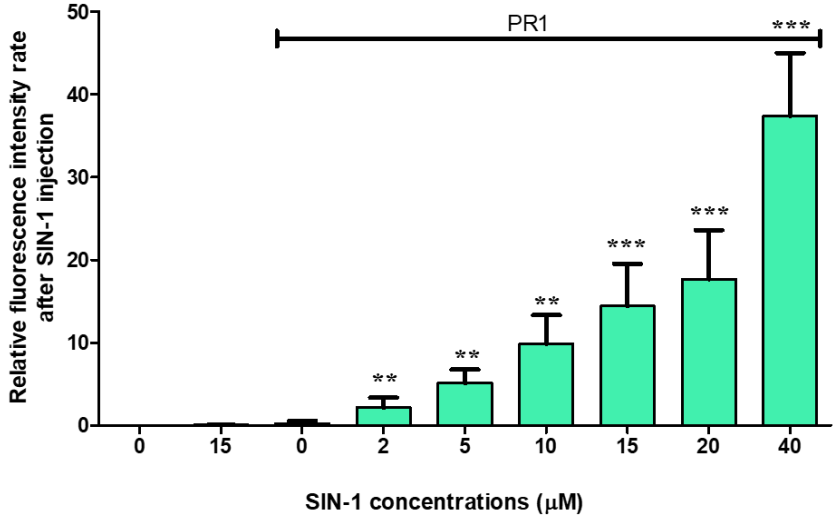

Figure 18: <u>A SIN-1 concentration dependent increase in **PR1** fluorescence in J774.2 macrophages.</u> Fluorescence intensity was measured after SIN-1 injection. The control conditions show no change in rate of fluorescence intensity. In the presence of **PR1**, increasing SIN-1 concentrations show increasing rates of fluorescence intensity of **PR1**. Data show mean values (n = 3) ± SEM, ***p ≤ 0.001, **p ≤ 0.01with respect to the **PR1** only treated group. Fluorescence intensities were measured with λ_{ex} = 550 (bandwith: 15) nm and max λ_{em} = 590 nm on a BMG Labtech CLARIOstar® plate reader.

5.2.3. LPS Stimulation to Induce Endogenous $ONOO^-$ Production

LPS (Figure 19) is an agonist that binds to toll-like receptors and consequently, induces enhanced production of $NO\cdot$[53], which upon reaction with $O_2^{\cdot-}$ generates $ONOO^-$. LPS also primes NOX, which is linked to increasing $O_2^{\cdot-}$ production. Inducing enhanced expression of $ONOO^-$ allows to simulate a biological environment where the inflammatory system is exposed to a harmful stimuli. Herein, enhanced ROS and consequently $ONOO^-$ production is observed.

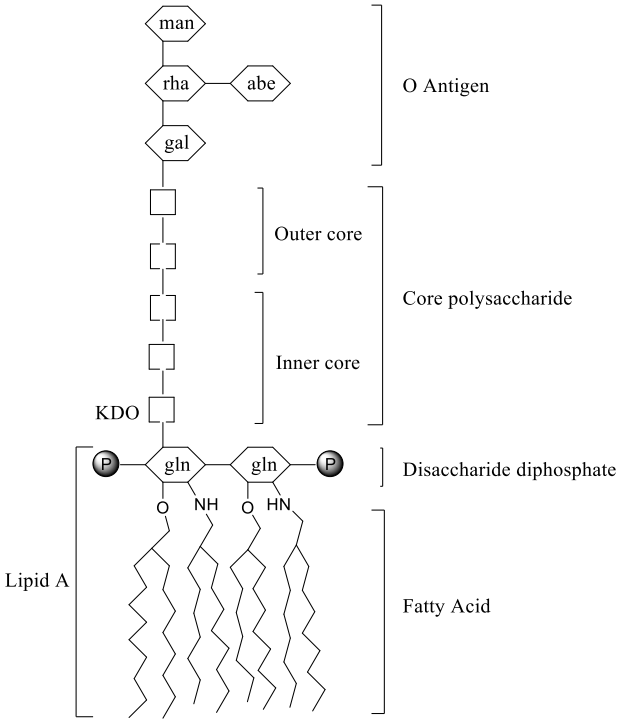

Figure 19: Schematic representation of the general structure of LPS.

Examples in the literature have used LPS to stimulate RAW264.7 macrophages.[54] Hereby, LPS was incubated for 4 h at a concentration of 1 µg/ml. Taking these conditions as an initial starting point, different concentrations of LPS (0.1, 1, 100, and 1000 ng/ml) and times of LPS incubation (4 and 24 h) were investigated. This should allow to a) induce endogenous $ONOO^-$ production within J774.2 macrophages and b) establish favourable detection conditions. Achieving a fine balance of sufficient $ONOO^-$ production is challenging as apoptosis can be easily induced by high

concentrations of LPS stimulation. $ONOO^-$ was successfully detected by **PR1** at all investigated concentrations and incubation times (Figure 20). As seen previously, **PR1** exhibits initial fluorescence in J774.2 macrophages which can be attributed to low levels of $ONOO^-$ present within normal cell metabolism.[55] In comparison to this baseline fluorescence signal, increasing LPS concentration at both 4 h and 24 h incubation times respectively increased the fluorescence signal of **PR1**. However, comparing 4 h and 24 h incubation of LPS in J774.2 macrophages, slight differences between the two can be observed. The fluorescence signal of **PR1** at 4 h LPS incubation does not change substantially between the different LPS concentrations. In contrast, for 24 h of LPS incubation, a substantial increase in **PR1** fluorescence is observed when using LPS concentration from 0.1 ng/ml to 100 ng/ml. This validates the role of LPS as an $O_2^{\cdot-}$ inducer where high levels of $O_2^{\cdot-}$ can react more readily with $NO\cdot$ to form $ONOO^-$.

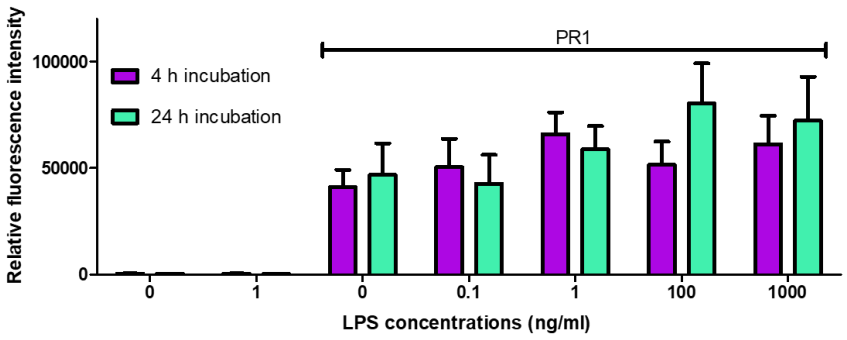

Figure 20: LPS concentration and incubation time dependant increase in **PR1** fluorescence in J774.2 macrophages. Different LPS concentration (0.1, 1, 100, and 1000 ng/ml) and incubation times (4 and 24 h) were evaluated at 1 min of fluorescence signal recording. The histogram indicates that **PR1** successfully detects $ONOO^-$ induced via LPS stimulation in J774.2 macrophages. Increasing times of LPS incubation do not alter fluorescence intensity significantly. Data show mean values (n = 3) ± SEM, no statistical significance. Fluorescence intensities were measured with λ_{ex} = 550 (bandwith: 15) nm and max λ_{em} = 590 nm on a BMG Labtech CLARIOstar® plate reader.

5.2.4. Stimulation of $ONOO^-$ Production with PMA

Phorbol 12-myristate 13-acetate (PMA, Figure 21) stimulates the production of $O_2^{\cdot-}$. $O_2^{\cdot-}$ was identified as the major ROS species induced by PMA.[56] PMA activates protein kinase C which stimulates NOX. NOX are a family of enzyme complexes that generate $O_2^{\cdot-}$ from molecular oxygen at the expense of NADPH.[57] Hence, PMA can induce enhanced $O_2^{\cdot-}$ production via this pathway. In conjunction with LPS, high levels of $ONOO^-$ should be favoured.

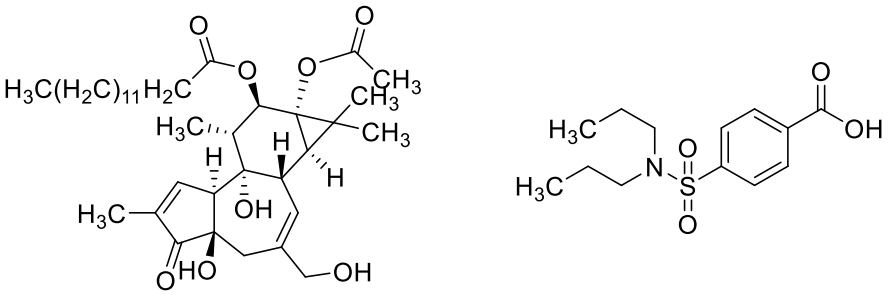

Figure 21: General structure of phorbol 12-myristate 13-acetate (PMA) and probenecid.

J774.2 macrophages have the ability to transport probes out of the cell via organic anion transporters.[58] This can impact ROS signalling studies since the probe is only partially or not present in J774.2 macrophages. Probenecid (Figure 21) inhibits organic anion transporters, enhancing hereby the retention of probes within macrophages.[59] To test whether this impacts the loading of macrophages with probe **PR1**, probenecid was incubated in one set of experiments together with **PR1**. This should indicate a) whether **PR1** is being removed by J774.2 macrophages through transporters, b) how probenecid prevents **PR1** from being pumped out by J774.2 macrophages and c) investigate the ability of PMA to induce $O_2^{\cdot-}$. However, using probenicid could also have a direct inhibitory effect on the P2X7 receptors.[60]

The fluorescence intensity after PMA injection increases with increasing PMA concentrations when compared to **PR1** (15 µM, 30 min) and LPS incubation (100 ng/ml, 4 h) in J774.2 macrophages (Figure 22). This is true with and without probenecid incubation. However, the rate of increase is minimal and variation within certain PMA concentrations is prominent. No significant difference with and without probenecid incubation can be observed in terms of fluorescence signal of **PR1**.

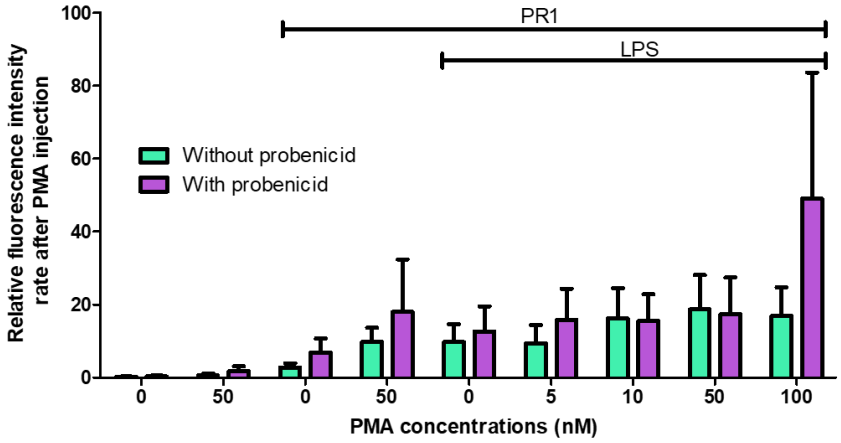

Figure 22: PMA stimulation of J774.2 macrophages shows no significant increase of $ONOO^-$ production. Different PMA concentrations (5, 10, 50, and 100 nM) and incubation with and without probenecid were investigated. The histogram indicates that **PR1** successfully detects $ONOO^-$ induced via PMA and LPS stimulation in J774.2 macrophages. The usage of probenecid does not alter the fluorescence response of **PR1** and hence, its ability of $ONOO^-$ detection. Data show mean values (n = 3) ± SEM, no statistical significance. Fluorescence intensities were measured with λ_{ex} = 550 (bandwith: 15) nm and max λ_{em} = 590 nm on a BMG Labtech CLARIOstar® plate reader.

5.2.5. IFN-γ: Activation of Nitric Oxide Synthase

IFN-γ is a cytokine that is involved in innate and adaptive immunity. One of its key roles is the activation of inducible nitric oxide synthase (NOS), therefore, increasing the concentration of NO· produced. In addition to LPS, priming of macrophages with IFN-γ enhances $ONOO^-$ production.[61] Recent literature reveals that a combination of LPS and IFN-γ can be used for $ONOO^-$ production for evaluating newly developed probes.[46]

Most commonly, IFN-γ is used at a concentration of 50 ng/ml and incubated for 4 h.[62] Using these conditions, 50 ng/ml IFN-γ was added with 100 ng/ml LPS and incubated together for 4 h to enhance $ONOO^-$ production (Figure 23). A combination of IFN-γ and LPS triggered an increase in **PR1** fluorescence compared to untreated macrophages (***$p \leq 0.001$, $n = 3$). Over a time period of 20 min, an increase in the macrophages' availability to produce enhanced levels of $ONOO^-$ was observed. Lower fluorescent responses were observed with LPS or IFN-γ alone compared to using both factors. Also, a basal response was observed in the absence of LPS and IFN-γ which could reflect a low level of endogenous ROS production converting **PR1** into fluorescent resorufin during the loading period. Hence, enhanced $O_2^{\cdot-}$ production through LPS and NO· production through IFN-γ allowed for larger amounts of $ONOO^-$ to be detected by **PR1** in J774.2 macrophages.

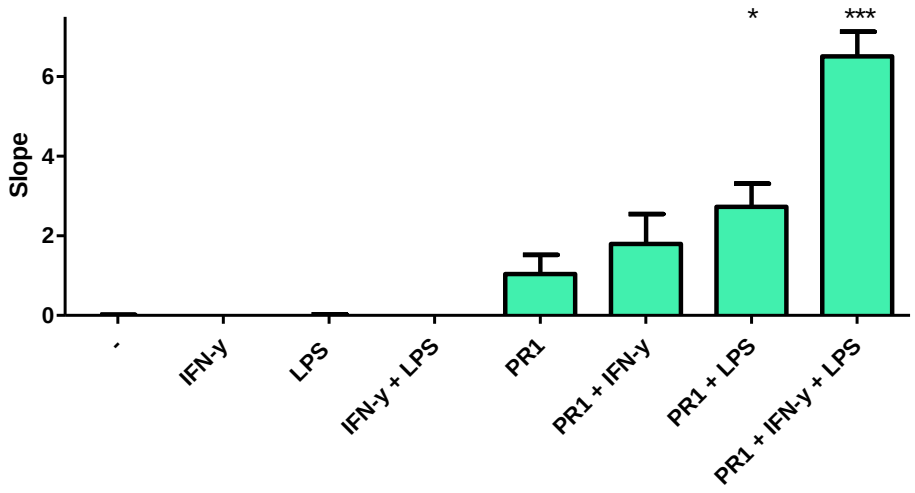

Figure 23: A rate increase in **PR1** fluorescence in J774.2 macrophages when using both LPS and IFN-γ. Fluorescence intensity measured over a time period of 20 min whereby the slope of fluorescence intensity increase is evaluated. The control conditions show no change in rate of fluorescence intensity. LPS and IFN-γ alone induce increased rates of $ONOO^-$. When used together, the rate of $ONOO^-$ produced increases more substantially. Data show mean values (n = 3) ± SEM, ***p ≤ 0.001, *p ≤ 0.05 with respect to **PR1**. Fluorescence intensities were measured with λ_{ex} = 550 (bandwith: 15) nm and max λ_{em} = 590 nm on a BMG Labtech CLARIOstar® plate reader.

5.2.6. Scavenging $ONOO^-$ Production

As mentioned earlier, $ONOO^-$ is generated by the reaction of $O_2^{\cdot-}$ and $NO\cdot$. Therefore, by inhibiting the production of one of the precursors, $ONOO^-$ concentrations should decrease. The ability of **PR1** to detect changes in $ONOO^-$ generation was studied. First, only LPS stimulation and scavenger effects were evaluated. Then, IFN- γ stimulation is introduced to revaluate scavenging effects.

The generation of $O_2^{\cdot-}$ within biological processes is a particularly fundamental one. The reaction of oxygen with NADPH rapidly generates $O_2^{\cdot-}$ and $NADP^+$ (Equation 1). This process is mediated by the NOX. As part of the NOX enzyme family, there are seven enzymatic isoforms which are classified according to their domain, and

structure. All these enzymes are able to transfer electrons from NADPH from oxygen to generate $O_2^{\cdot-}$.[63] Together with mitochondrial respiration, they are at the origin of ROS generation.

$$2O_2 + \mathrm{NADPH} \xrightarrow{(\mathrm{oxidase})} 2O_2^{\cdot-} + \mathrm{NADP^+} + \mathrm{H^+} \qquad \text{(Equation 1)}$$

Subsequently $O_2^{\cdot-}$ reacts with a variety of other ROS such as NO· for example to generate $ONOO^-$. Hence by inhibiting the production of $O_2^{\cdot-}$, this should allow for a decrease in $ONOO^-$ production. It is anticipated that **PR1** should be able to detect the change in $ONOO^-$ production in J774.2 macrophages.

First, three $O_2^{\cdot-}$ scavengers and one $ONOO^-$ scavenger were investigated (Figure 24). The rational for their usage and involvement in scavenging is given below:

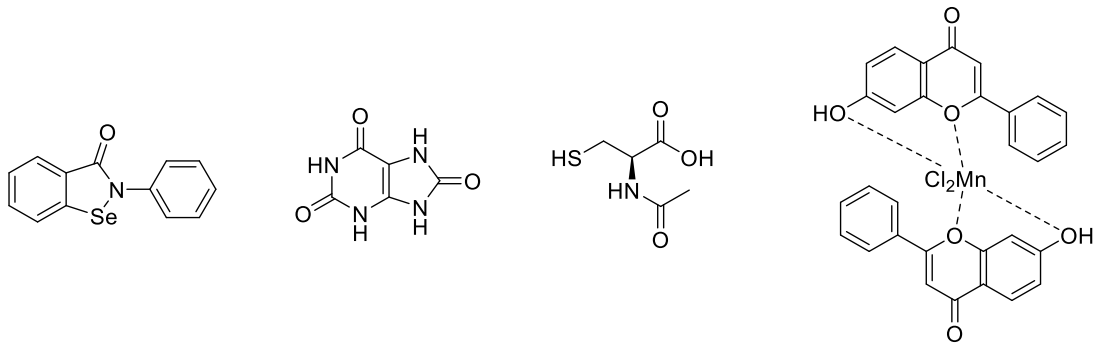

ebselen uric acid *N*-acetyl-L-cysteine Mn-cpx3

Figure 24: Investigation of different scavengers: ebselen, uric acid, *N*-acetyl-L-cysteine and Mn-cpx3.

- Ebselen

2-phenyl-1,2-benzisoselenazol-3(2*H*)-one most commonly known as ebselen (EBS) is a GSH peroxidase mimic. Therefore, EBS-Se is readily oxidised by ROS to EBS-SeOH at the active Se site. It is then reduced by GSH to the intermediate EBS-SeSG followed by a further reduction to its original form (Figure 25). It is a well-known $O_2^{\cdot-}$ scavenger illustrated by numerous examples in the literature.[64-66]

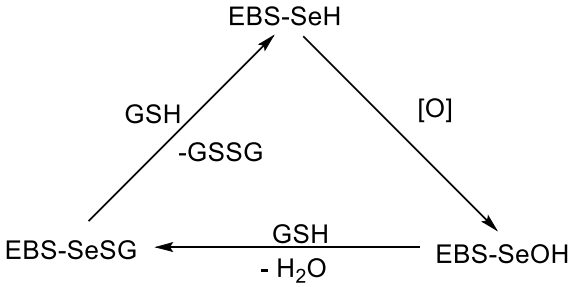

Figure 25: Simplified catalytic mechanism of action of ebselen (EBS) adapted from Azad and Tomar.[67]

- Uric acid

Uric acid is an $ONOO^-$ scavenger. It requires ascorbic acid and thiols for its full scavenging activity. It also scavenges secondary radicals produced from $ONOO^-$ such as $CO_3^{\cdot-}$ and $^{\cdot}NO_2$.[68]

- *N*-acetyl-*L*-cysteine

N-acetyl-*L*-cysteine (NAC) is an antioxidant that can increase intracellular reduced GSH. This in turn allows to minimise oxidative stress.

- Mn-cpx3

This manganese complex containing 7-hydroxflavonones (flavones act as antioxidants) acts as a superoxide dismutase (SOD) mimetic. SODs are the major antioxidant defence systems against $O_2^{\cdot-}$.[69] Additionally, SODs are able to inactivate $NO\cdot$ production and are involved in the regulation of mitochondrial $O_2^{\cdot-}$ production.

J774.2 macrophages were treated with LPS (100 ng/ml) for 4 h, followed by incubation with scavengers (1 mM) for 1 h and incubation with **PR1** (15 µM) for 30 min. The fluorescence response of **PR1** was studied over a 20 min timeframe. Figure 26 displays **PR1**'s fluorescence intensity at a time point of 10 min. All scavengers display a significant decrease in **PR1**'s fluorescence compared to control conditions: LPS stimulation without probe incubation (Figure 26). Each scavenger seems to operate along the suggested mechanism of action of either directly inhibiting $O_2^{\cdot-}$ formation, $ONOO^-$ formation or enzymatic pathways that are linked to oxidative stress. The results are statistically significant with respect to the control conditions (**p ≤ 0.01) in the case of ebselen, uric acid and *N*-acetyl-L-cysteine. The fluorescence intensity of **PR1** does not decrease significantly in the case of Mn-cpx3. This could be due to light sensitivity, leading to the decomposition of Mn-cpx3 over time.

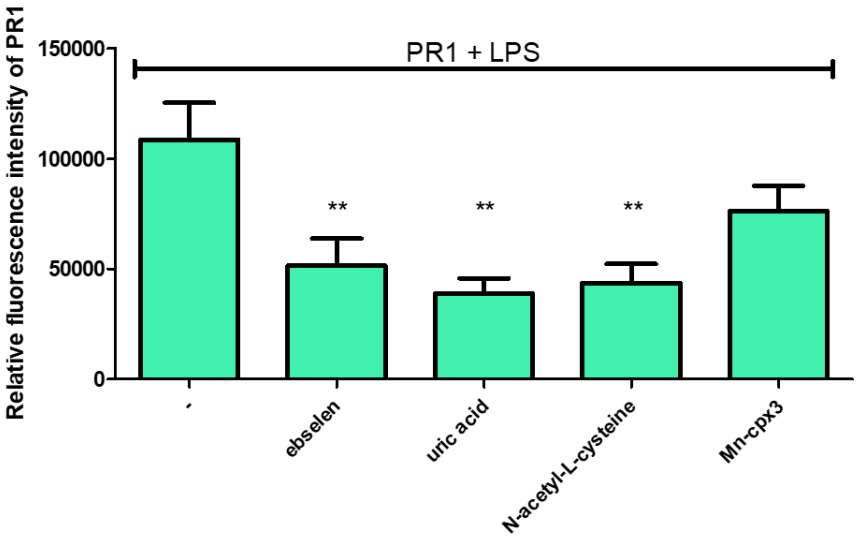

Figure 26: Effectiveness of scavengers in J774.2 macrophages. Different scavengers (ebselen, uric acid, *N*-acetyl cysteine, and Mn-cpx3 – final concentration: 1 mM) were investigated. The histogram shows the fluorescence response of **PR1** at the time point of 10 min of recording. The ability of **PR1** to detect changes in $ONOO^-$ generation was validated with each scavenger, whereby uric acid showed the most significant decrease. Data show mean values (n = 3) ± SEM, **p ≤ 0.01 with respect to control conditions. Fluorescence intensities were measured with λ_{ex} = 550 (bandwith: 15) nm and max λ_{em} = 590 nm on a BMG Labtech CLARIOstar® plate reader.

The initial screening of scavengers was to determine a saturated inhibition response and maintain cell viability. Ebselen was chosen to be evaluated at different concentrations since **PR1**'s ability to indirectly detect the inhibition of $O_2^{\cdot-}$ was of main interest. Different concentrations of ebselen were incubated for 1 h: 0.1, 0.25, 0.5, 0.75, 1 mM (Figure 27). From 0.25 mM upwards, a decrease in **PR1** fluorescence can be observed which is statistically significant from 0.5 mM upwards when compared to the control group. Interestingly, when comparing the fluorescence intensity of **PR1** when J774.2 macrophages are exposed to ebselen (0.5 mM) and to LPS and ebselen (100 ng/ml and 0.5 mM respectively), the same level is achieved. The stimulation of J774.2 macrophages with LPS is cancelled out by the introduction of ebselen at 0.5 mM. Hence, ebselen allows to validate the inhibition of $O_2^{\cdot-}$ production. Also, background **PR1** fluorescence in untreated J774.2 macrophages was also partially reduced by 0.5 mM ebselen indicating detection of basal $ONOO^-$ formation by **PR1**. In the presence or absence of LPS, 0.5 mM ebselen reduces **PR1** fluorescence to a comparable baseline level. Consequently, this impacts $ONOO^-$ production, whereby **PR1**'s fluorescence signal decreases.

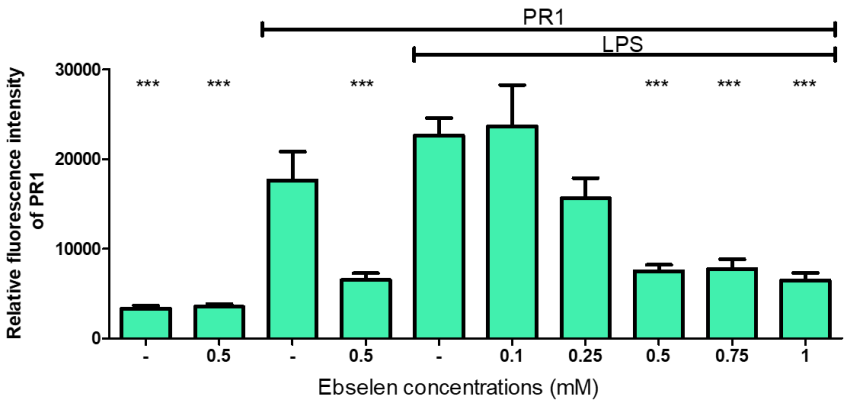

Figure 27: Effect of ebselen concentration on the scavenging of $O_2^{\cdot-}$ consequently, limiting the ability of $ONOO^-$ production. Different ebselen concentrations (0.1, 0.25, 0.5, 0.75, 1 mM) were investigated. Increasing concentrations of ebselen impact the production of $O_2^{\cdot-}$: less $O_2^{\cdot-}$ is readily available, as a consequence less $ONOO^-$ is produced. Hence, the ability of **PR1** to detect $ONOO^-$ diminishes in fluorescence signal due to less $ONOO^-$ being produced in J774.2 macrophages. Data show mean values (n = 3) ± SEM, ***p ≤ 0.001 with respect to the **PR1** and LPS treated group. Fluorescence intensities were measured with λ_{ex} = 550 (bandwith: 15) nm and max λ_{em} = 590 nm on a BMG Labtech CLARIOstar® plate reader.

Having shown that $O_2^{\cdot-}$ production in J774.2 macrophages can be impacted and hence, limit $ONOO^-$ formation, this should allow evaluation of NO· production. As NO· is the other key component for $ONOO^-$ formation, inhibiting NOS, a family of enzymes (NOS 1-3) that produces NO· from L-arginine, should also limit $ONOO^-$ formation. In the same manner as $O_2^{\cdot-}$, if less NO· is readily available, less $ONOO^-$ can be produced when J774.2 macrophages are subjected to stress conditions. This led to the introduction of two NOS inhibitors (Figure 28).

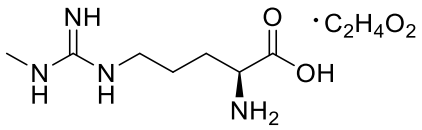

N^G-Methyl-L-arginine acetate

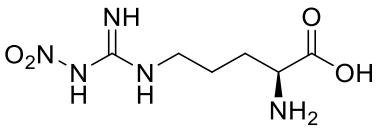

N_w-Nitro-L-arginine

Figure 28: NOS inhibitors: non-competitive N^G-methyl-L-arginine-acetate and competitive N_w-nitro-L-arginine inhibitors.

- N^G-methyl-L-arginine-acetate: Initially reported as an inhibitor of macrophage nitrite generation, it is also a competitive inhibitor for NOS established through studies in RAW264.7 macrophages.[70, 71]
- N_w-nitro-L-arginine: It mostly acts as a competitive inhibitor for NO· formation. Numerous examples in the literature have shown that N_w-nitro-L-arginine is effective in a variety of biological systems as a NOS inhibitor.[72-74]

A range of different concentration of N^G-methyl-L-arginine-acetate and N_w-nitro-L-arginine were incubated for 1 h: 0.1, 0.25, 0.5, 0.75, 1 and 2 mM. Comparing the inhibitor and LPS treated groups towards the control group of **PR1** and LPS only, in both cases a decrease of fluorescent intensity of **PR1** was observed. Similarly, a decrease in **PR1** fluorescence is observed for both competitive inhibitors. Comparing the inhibitor only with the inhibitor and LPS treated group, the fluorescence intensity of **PR1** achieves the same level as the inhibitor only with concentrations of LPS > 0.5 mM onwards. Since LPS also induces NOS activity next to enhanced production of $O_2^{\cdot-}$, this suggests that both inhibitors are successful in diminishing NO· levels. Overall, the inhibition of NOS is not as significant as $O_2^{\cdot-}$ inhibition (Figure 29).

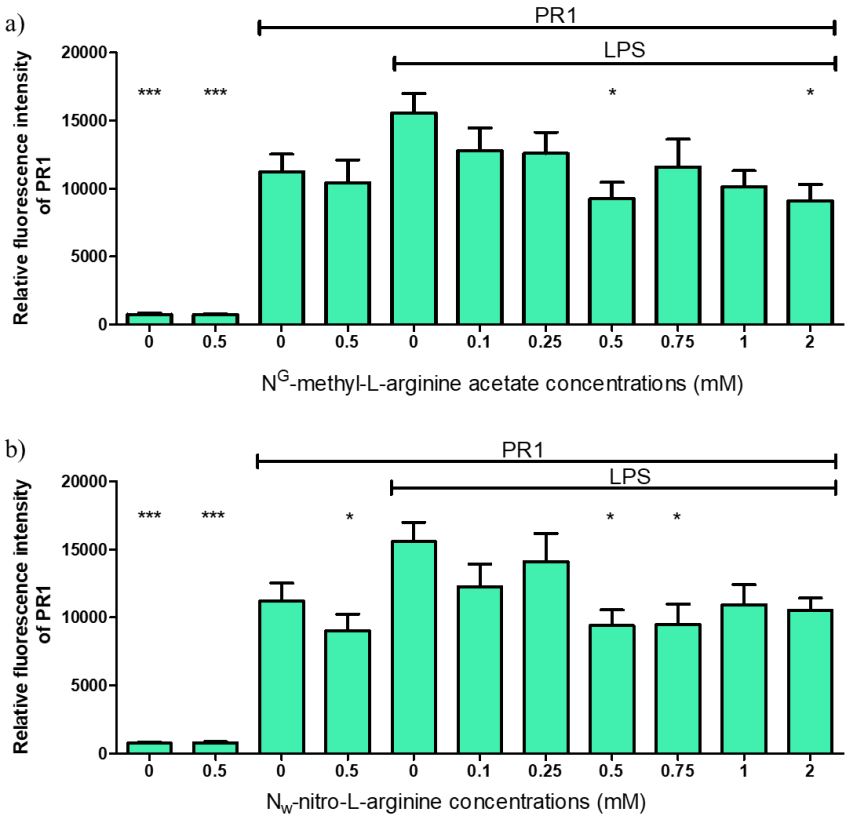

Figure 29: Effect of a) N^G-methyl-L-arginine-acetate and b) N_w-nitro-L-arginine, competitive inhibitors of NOS, on the inhibition of the catalytic production of NO· from L-arginine in J774.2 macrophages. Different N^G-methyl-L-arginine-acetate and N_w-nitro-L-arginine concentrations (0.1, 0.25, 0.5, 0.75, 1, 2 mM) were investigated. Increasing concentrations of both NOS inhibitors impact towards a greater extent the catalytic production of NO·. Less NO· is readily available to react with $O_2^{\cdot-}$ to form $ONOO^-$. Consequently, **PR1** detects less $ONOO^-$ due to the diminishing fluorescence signal. Data show mean values (n = 3) ± SEM, ***p ≤ 0.001, * p ≤ 0.05 with respect to the **PR1** and LPS treated group. Fluorescence intensities were measured with λ_{ex} = 550 (bandwith: 15) nm and max λ_{em} = 590 nm on a BMG Labtech CLARIOstar® plate reader.

With the introduction of IFN-γ, a screen of NOS inhibitors, $O_2^{\cdot-}$ scavenger, and $ONOO^-$ scavenger was repeated to see how these results compare to the previous ones where only LPS was used to induce NO· and $O_2^{\cdot-}$ production.

J774.2 macrophages were stimulated with LPS (100 ng/ml) and IFN-y (50 ng/ml) for 4 h. NOS inhibitors (500 µM, 1 h) - N^G-methyl-L-arginine-acetate (NO1) and N_w-nitro-L-arginine (NO2) – ebselen (500 µM, 1 h) and uric acid (500 µM, 1 h) were incubated after LPS and IFN-γ treatment. After **PR1** (15 µM, 30 min) incubation, the fluorescence intensity was recorded. At a time point of 4 min of recording, the ability of **PR1** to detect $ONOO^-$ was evaluated (Figure 30). Upon treatment with LPS and IFN-γ, a high fluorescence response of **PR1** was observed as expected through the induced $ONOO^-$ stimulation, compared to the control conditions. By introducing NOS inhibitors, $O_2^{\cdot-}$ and $ONOO^-$ scavengers, the fluorescence signal of **PR1** diminishes as expected.

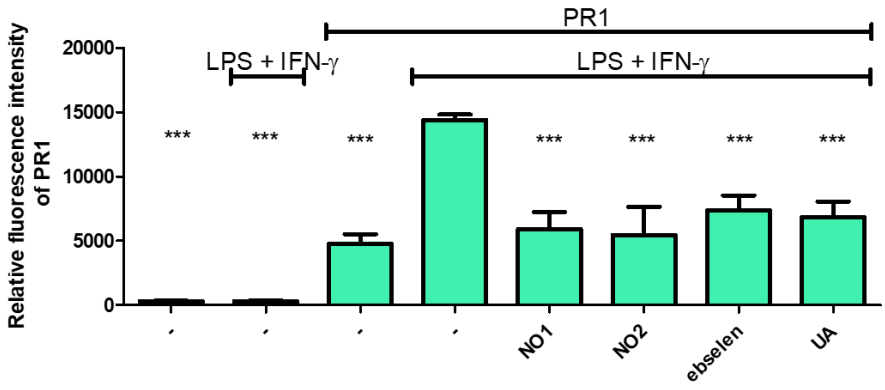

Figure 30: <u>LPS and IFN-γ induced $ONOO^-$ production quenched by inhibitors and scavengers.</u> The fluorescence signal of **PR1** is quenched with the introduction of NOS inhibitors (N^G-methyl-L-arginine-acetate (NO1) and N_w-nitro-L-arginine (NO2)) and scavengers (ebselen and uric acid (UA)), which impact $O_2^{\cdot-}$ and NO production. Data show mean values (n = 3) ± SEM, ***p ≤ 0.001 with respect to the **PR1**, LPS and IFN-γ treated group. Fluorescence intensities were measured with λ_{ex} = 550 (bandwith: 15) nm and max λ_{em} = 590 nm on a BMG Labtech CLARIOstar® plate reader.

5.2.7. Activation and Inhibition of P2X7 Receptors

By definition, ATP (Figure 31) transports (bio)chemical energy within cells for metabolism. However, extracellular ATP also plays a pivotal role in inflammation. In the late 1980s, evidence emerged that ATP generates $O_2^{\cdot-}$.[75, 76]

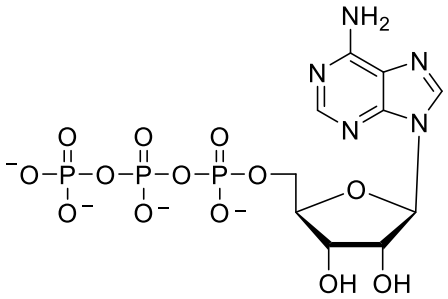

Figure 31: Adenosine-5'-triphosphate (ATP) is involved in inflammation.

Under inflammatory conditions, cells are able to release ATP that is being recognised by purinergic receptors.[77] In fact, ATP, its metabolites (adenosine diphosphate , AMP and adenosine), uridine triphosphate and uridine diphosphate, all stimulate the activation of purinergic receptors. There are two types of purinergic receptors: P1 adenosine receptors and P2 receptors which are subdivided into P2Y GPCRs and P2X ligand gated ion channels whereby I will focus on the latter one. P2X receptors mediate many of the extracellular actions of ATP.[78] There are seven different subtypes: P2X1, P2X2, P2X3, P2X4, P2X5, P2X6 and P2X7 (Table 2). ATP acts as an agonist for all subtypes, however different types of antagonists are able to block these receptors. Each subtype is associated with a variety of diseases and constitute essential therapeutic targets for thrombosis (P2X1), chronic neuropathic and inflammatory pain (P2X3, P2X2/3, P2X4, P2X7), dysfunctional urinary bladder (P2X1, P2X2, P2X3), rheumatoid arthritis and osteoarthritis (P2X7), and depression (P2X7).

Table 2: A summary of the role of the different subtypes of P2X receptors and selective antagonists of P2X receptors is presented. The table was summarized using data from Kennedy *et al*.[78]

P2X receptor	Role	Antagonists
any	various	Suramin, PPADS
P2X1	expression in smooth muscle, mediation of neurotransmitter actions of ATP	PPNDS, MRS2159, TNP-ATP, NF110
P2X2	expression in central and peripheral neurones, mediation of neuro-transmission and sensory transduction	PSB-1011
P2X3	expression in sensory neurones, also in combination with P2X2	A317491, RO-329, AF-353
P2X4	expression in central and peripheral neurones, and glandular tissues	5-BDBD
P2X5	expression in central neurones, eye, cardiac muscle, skin, and skeletal muscle	Suramin, PPADS
P2X6	Expression in central nervous system	Suramin, PPADS
P2X7	Expressed in glial cells of the CNS, peripheral nervous system, and in cells of the immune system, including macrophages, monocytes, lymphocytes, dendritic cells, and mast cells	AZ11645373, A740003, A438079, A804598, GSK314181A

I am mainly interested in the sub-type P2X7 since it has been associated with inflammasome assembly and is believed to play a major role in NLRP3 inflammasome activation, thus, initiating the release of IL-1β. Hence, I decided to look at their activation with ATP and consequently whether inhibition with one of the

commercially available antagonists would go in line with changes in $ONOO^-$ stimulation.

No or minimal increase of $ONOO^-$ generation was detected by **PR1** during ATP stimulation with concentrations up to 1 mM of ATP (Figure 32). This could indicate that the P2X7 receptors were not activated at this concentration and hence, no enhanced $ONOO^-$ production is induced. However, upon injection of ATP at a concentration of 5 mM, the rate of fluorescence intensity of **PR1** increased above control conditions (no ATP added following LPS priming). The change in rate was not statistically significant. This is true for and without the use of probenecid. Though, the usage of probenecid (1 mM) reduced variation of the samples within each ATP concentration used. 5 mM of ATP with probenecid incubation hints at the activation of P2X7 receptors and their involvement in inflammasome assembly. Subsequent investigation of a P2X7 antagonist could validate my hypothesis.

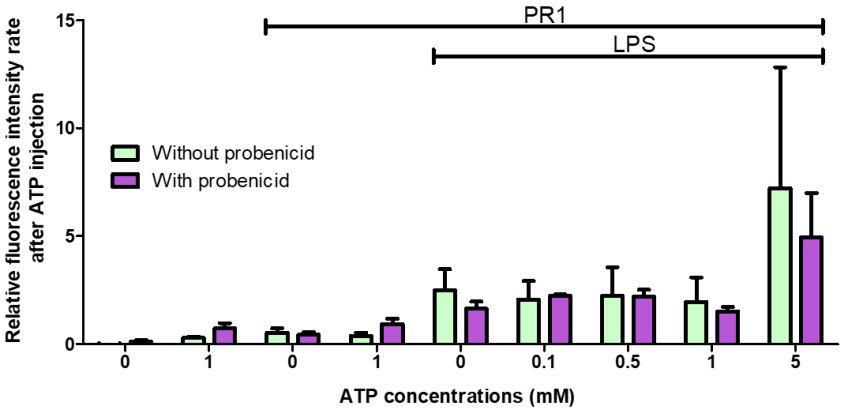

Figure 32: <u>Concentration dependant ATP stimulation of J774.2 macrophages shows an increase in **PR1** fluorescence.</u> Different ATP concentrations (0.1, 0.5, 1, 5 mM) and incubation with and without probenicid (1 mM) were investigated. The histogram indicates that **PR1** successfully detects $ONOO^-$ induced via ATP and LPS stimulation in J774.2 macrophages. Using probenecid allows for less variation for ATP stimulation. This allows for reproducibility of $ONOO^-$ detection via **PR1**. Data show mean values (n = 3) ± SEM, no statistical significance of the results was observed. Fluorescence intensities were measured with λ_{ex} = 550 (bandwith: 15) nm and max λ_{em} = 590 nm on a BMG Labtech CLARIOstar® plate reader.

The same conditions were then used to evaluate how ATP could overcome scavenging $ONOO^-$ behaviour. After injection of ATP (5 mM), the rate of $ONOO^-$ production was monitored by the change of fluorescence signal of **PR1**. Comparing the **PR1**, LPS and IFN-γ group with the **PR1**, LPS, IFN-γ and ATP, a decrease in the fluorescence signal can be observed. As such, the response to 5 mM ATP is changed with the co-addition of IFN-γ with LPS in the priming stage. It seems that when in addition to LPS, IFN- γ is present, it takes a more dominant role: NOS expression is increased and ATP has an inhibitory effect (Figure 33).[79] In contrast, when LPS is used alone (Figure 32), the signal increases after ATP injection suggesting that the activation of P2X7 could be the prominent response. Evaluating the rate of $ONOO^-$ production through **PR1** in the case of the NOS inhibitors and ROS scavengers when ATP is introduced, shows in all cases an increase in $ONOO^-$ production compared to when no ATP is present. It seems interesting that there could be an ATP-dependant increase in the presence of inhibitors and scavengers (Figure 33).

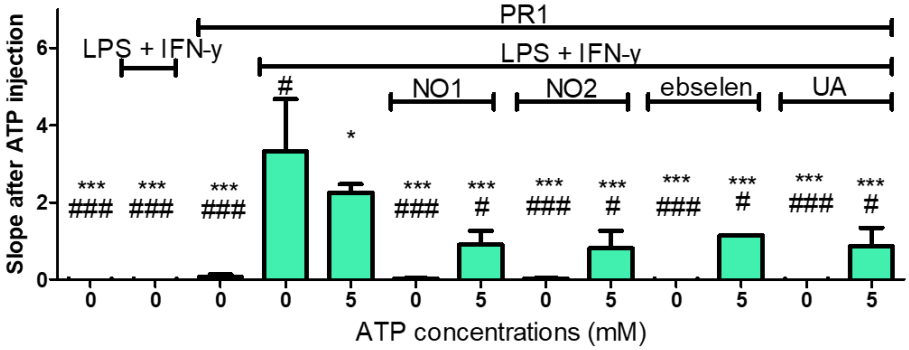

Figure 33: ATP induces $O_2^{\cdot-}$ production, overcoming inhibitor and scavenger effects. The rate of $ONOO^-$ production is quenched by NOS inhibitors (N^G-methyl-L-arginine-acetate (NO1) and N_w-nitro-L-arginine (NO2)) and scavengers (ebselen and uric acid (UA)). Introduction of ATP (5 mM) allows to overcome this effect. Increased $O_2^{\cdot-}$ production is stimulated via ATP, suggesting also the activation of purinergic receptors. Data show mean values (n = 3) ± SEM, ***p ≤ 0.001, * p ≤0.05 with respect to the **PR1**, LPS and IFN-γ treated group and ###p ≤ 0.001, # p ≤ 0.05 with respect to the **PR1**, LPS, IFN-γ and ATP treated group. Fluorescence intensities were measured with λ_{ex} = 550 (bandwith: 15) nm and max λ_{em} = 590 nm on a BMG Labtech CLARIOstar® plate reader.

When stimulating J774.2 macrophages with high levels of ATP, P2X7 receptors should be activated. This leads to subsequent cell signalling events including the formation of ROS.[80] Oxidative stress increases adenosine release (partly through ATP degradation into adenosine) by activating adenosine receptors which can also play a key part in the immune response. In this study, I looked at two specific receptor antagonists: A-438079 and CGS 15943 (Figure 34). A-438079 is a competitive P2X7 antagonist, which inhibits small cation flux (such as calcium and potassium) and IL-1β release.[81] On the other hand, CGS 15943 is a competitive, non-selective adenosine receptor antagonist.[82] Under oxidative stress, increased amounts of adenosine are released, activating adenosine receptors (a class of purinergic G protein-coupled receptors) which through a cascade of other signalling events activate NF-κB. NF-κB plays a key role in the regulation of the immune response towards an infection.

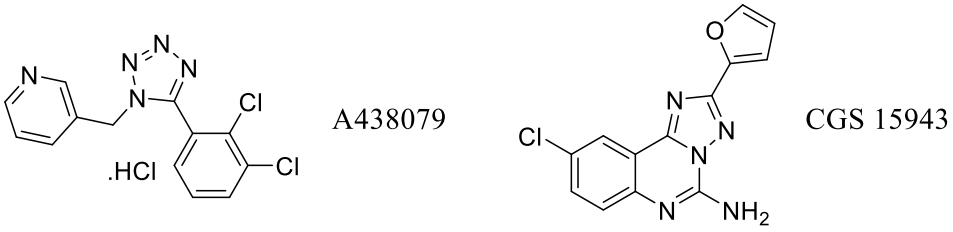

Figure 34: P2X7 receptor inhibitor: 3-[[5-(2,3-Dichlorophenyl)-1*H*-tetrazol-1-yl]methyl]pyridine hydrochloride (A438079) and adenosine receptor inhibitor: 9-Chloro-2-(2-furanyl)-[1,2,4]triazolo[1,5-c]quinazolin-5-amine (CGS 15943).

Different concentrations of ATP were investigated while keeping the concentration of the respective antagonist constant at 100 μM (Figure 35). Control conditions with no antagonist present were also evaluated in order to correctly attribute inhibition to the relevant receptors. The rate of $ONOO^-$ formation after ATP injection detectable by **PR1** was evaluated. In the case of the P2X7 inhibitor A-438079, no clear trend was established other than an ATP-dependant increase in **PR1** fluorescence was not observed at 5 mM ATP in the presence of antagonists. At 1 mM ATP when LPS is present, it seems to stimulate higher ROS generation. However, the antagonist should show a decline in ROS generation detectable for **PR1**. No clear conclusion can be drawn in terms of the ability to inhibit the P2X7 receptor. As for the adenosine receptor

inhibitor CGS 15943, the same conditions were employed as with A-438079. The anticipated effect of adenosine receptor inhibition was not fulfilled: significant reduction of ROS. On the contrary, it seems that high concentrations of ATP seem to overcome CGS 15943 inhibitory effects. Nevertheless, it seems that ATP increases $ONOO^-$ formation with no limiting effect by CGS 15943.

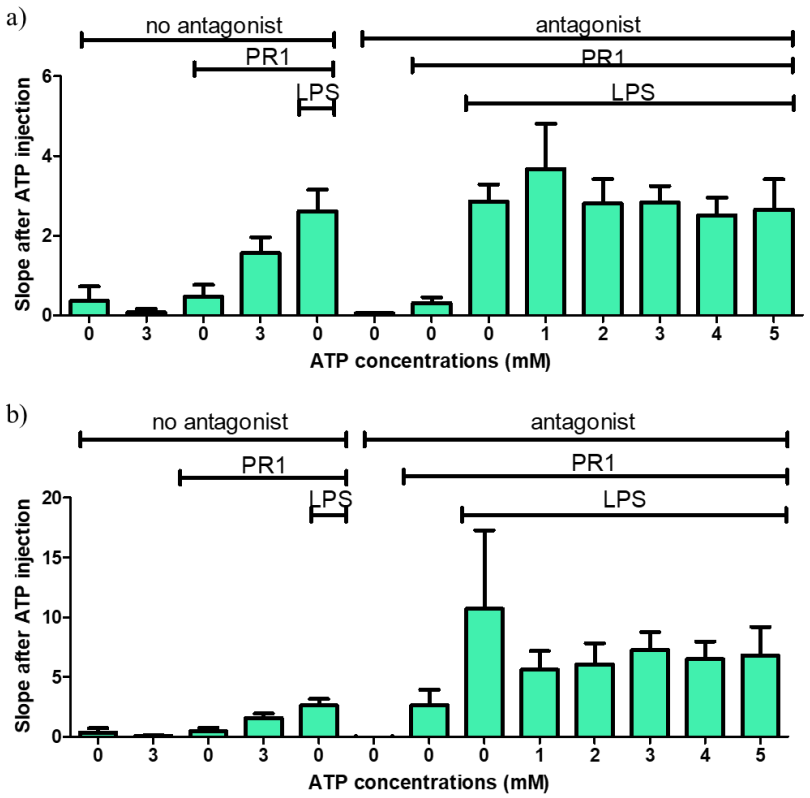

Figure 35: Effect of using a) A-438079, a P2X7 inhibitor, and b) CGS 15943, an adenosine receptor inhibitor and how this alters ATP's ability to open the receptors. Different ATP concentrations (1, 2, 3, 4, 5 mM) were investigated when exposed to a receptor inhibitor and compared to control conditions when no antagonist was present. No clear effect was observed on the usage of the antagonist when exposed to different ATP concentrations, suggesting in comparison to the no antagonist data that it has no effect on this receptor due to the continuous increase in rate of **PR1**'s ability to detect $ONOO^-$. Data show mean values (n = 3) ± SEM, no statistical significance of the results was observed. Fluorescence intensities were measured with λ_{ex} = 550 (bandwith: 15) nm and max λ_{em} = 590 nm on a BMG Labtech CLARIOstar® plate reader.

5.2.8. Comparing Hypoxic and Normoxic Environments

A common feature of tumours such as cancer cells for example, is a low availability of oxygen. This state is called hypoxia where oxygenation of the tumour tissue is poor and usually at levels of 1 – 2 % O_2. In contrast, normoxia is the healthy state of tissues where oxygenation is assured. Depending on the tissue, these oxygen levels can vary (Table 3).[83]

Table 3: Comparison of oxygen levels in healthy and diseased tissues adapted from Azab *et al*.[83]

Tissue	Normoxia (% O_2)	Hypoxia (% O_2)
Breast	8.5	1.5
Liver	4.0 – 7.3	0.8
Cervix	5.5	1.2
Kidney	9.5	1.3

The tumour microenvironement is composed of blood vessels, lymphatic vessels, fibroblasts, immune cells and chemico-physical components. During tumour development and progression, access to oxygen is restricted. This low oxygen state is mainly linked to hypoxida-inducible factors (HIFs) which contain an oxygen-sensitive HIF-α subunit.[84] Under hypoxic conditions, increased levels of ROS are generated, particularly in the mitochondria. This is mainly due to the effects of ROS on the mitochondria electron transport chain whereby the exact mechanisms are still not clear.[85] In order to stimulate J774.2 macrophages towards a hypoxic environment, a limited supply of O_2 was induced using a hypoxic chamber. J774.2 macrophages were cultured at 1 % O_2. These were then compared to normoxic J774.2 macrophages. Hypoxia influences key macrophage functions, such as energy metabolism and different immune responses.[86] The fluorescence intensity of **PR1** varies significantly when comparing normoxic to hypoxic conditions (Figure 36). **PR1** will detect basal levels of $ONOO^-$, which are naturally produced by J774.2 macrophages as well as by LPS stimulation. Under hypoxic conditions, I hypothesize that less $O_2^{\cdot-}$ is produced by

J774.2 macrophages, limiting the availability of $ONOO^-$ produced as shown by **PR1**'s ability to detect those decreased levels. One would expect increased amounts of $ONOO^-$ under hypoxic conditions in J774.2 macrophages.

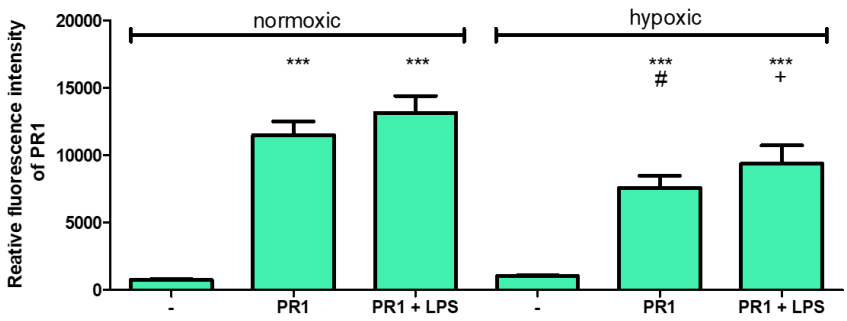

Figure 36: Comparing the ability of **PR1** to detect $ONOO^-$ under normoxic and hypoxic conditions. J774.2 macrophages were stimulated with LPS under normoxic and hypoxic conditions. The fluorescence intensity of **PR1** was measured allowing to evaluate the ability of **PR1** to detect $ONOO^-$. A clear decrease of $ONOO^-$ production can be observed under hypoxic conditions in comparison to normoxic conditions. Data show mean values (n = 3) ± SEM, ***p ≤ 0.001 with respect to the relevant normoxic/hypoxic control conditions, #p ≤ 0.05 with respect to the **PR1** treated group under normoxic conditions, and +p ≤ 0.05 with respect to the **PR1** and LPS treated group under normoxic conditions. Fluorescence intensities were measured with λ_{ex} = 550 (bandwith: 15) nm and max λ_{em} = 590 nm on a BMG Labtech CLARIOstar® plate reader.

6. Conclusions

I have successfully identified a new fluorescent tool to study $ONOO^-$ mediated pathways. I have taken a known H_2O_2 probe, **PR1**, and evaluated it as an $ONOO^-$ selective and sensitive probe. **PR1** showed excellent permeability in J774.2 macrophages and was able to detect endogenous $ONOO^-$ as confirmed by confocal imaging. Subsequently, by using a plate reader, **PR1** was evaluated as a fluorescent tool for assays. Using SIN-1, exogenous $ONOO^-$ was evaluated followed by an

investigation of LPS, IFN-γ, PMA and ATP as endogenous stimulants to increase $O_2^{\cdot-}$ and NO· generation, both essential precursors to form $ONOO^-$. At the same time $O_2^{\cdot-}$, NOS and $ONOO^-$ scavengers were introduced to evaluate the impact on inhibition of $ONOO^-$ precursors as well as $ONOO^-$ itself. Additionally, the inhibition of P2X7 and adenosine receptors was evaluated, which are essential receptors in the activation of ROS related mechanisms. Finally, I also looked at comparing the hypoxic and normoxic environment and **PR1**'s ability to detect changes in $ONOO^-$ generation. The established protocol allowed to evaluate some of the **PR1** derived probes (Chapter 2). Evaluating all these factors, allows us to draw a picture about some of the cellular processes and how **PR1** is able to detect these (Figure 37).

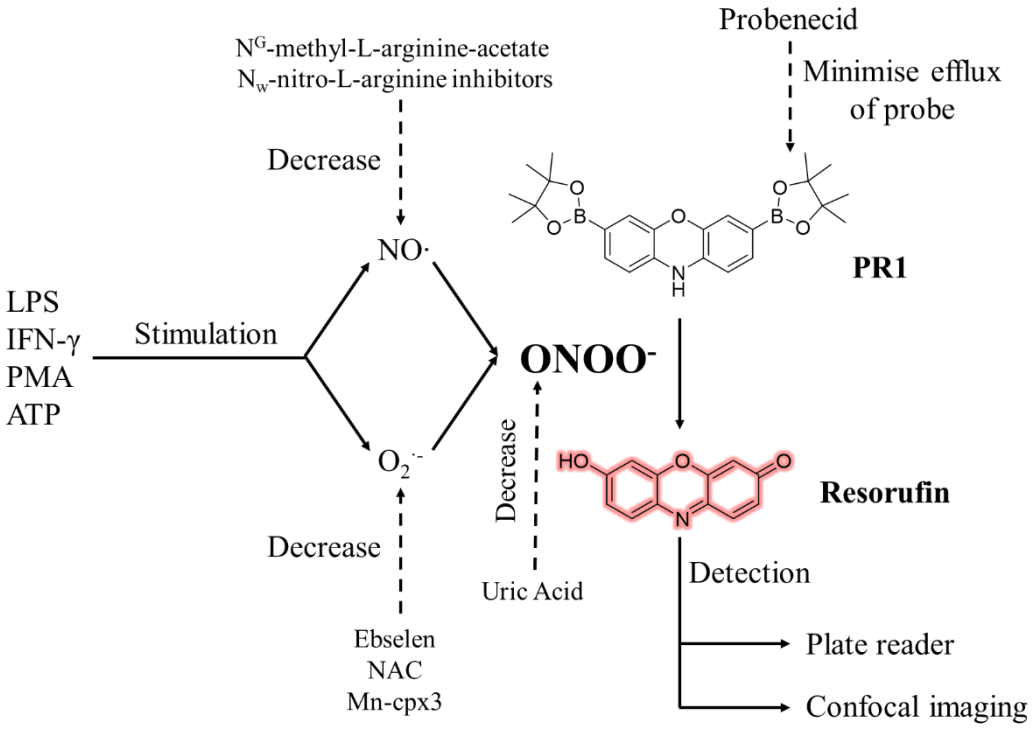

Figure 37: A range of factors have been successful in stimulating and inhibiting $ONOO^-$ generation. These changes were detected by **PR1** which upon reaction with $ONOO^-$ generates resorufin. The fluorescence output of resorufin was closely monitored by a plate reader and confocal microscopy.

7. Future Work

Until this point, **PR1** has only been used as a fluorescent tool for the detection of $ONOO^-$ in M1 polarized macrophages. ROS are also implicated in M2 polarization as outlined in Section 1.2. Whereby in M1 macrophages an increase in ROS is observed, for M2 polarized macrophages, the generation of ROS should decline. To validate M2 polarization, stimulation with cytokines IL-4 and IL-13 should activate this phagocytic change.

Additionally, the introduction of chemotherapy agents would be interesting to evaluate in macrophages. Chemotherapeutics drive an increase in ROS generation, including $ONOO^-$ and also alter redox homeostasis. For example, doxorubicin and daunorubicin are common anti-cancer drugs used in combination with other chemotherapy agents (Figure 38). Both drugs are made biosynthetically whereby daunorubicin is a precursor for doxorubicin. A previous study demonstrated that both doxorubicin and daunorubicin stimulate an increase in IL-1β production and other inflammatory cytokines in conjunction with LPS in murine bone marrow derived macrophages.[87] IL-1β is generated from pro IL-1β and caspase-1 whereby the latter is activated by the NLRP3 inflammasome.[88] However, it is important to note that both doxorubicin and daunorubicin are inherently fluorescent and this needs to be accounted for when using **PR1** to evaluate $ONOO^-$ levels.

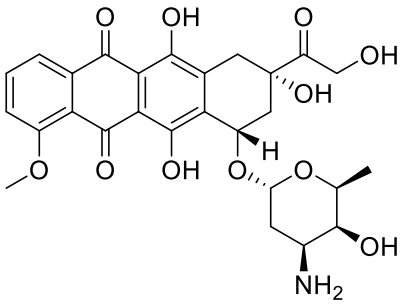

Doxorubicin

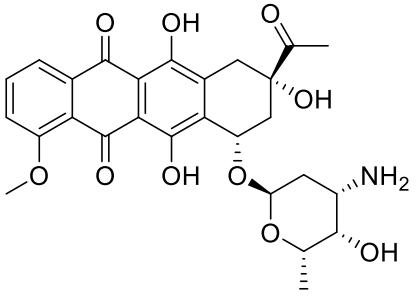

Daunorubicin

Figure 38: Anti-cancer drugs doxorubicin and daunorubicin stimulate an increase in ROS production.

Chapter 2 – Resorufin Analogues for the Selective Detection of $ONOO^-$

1. Introduction

As outlined in Chapter 1, **PR1** is based on resorufin. Resorufin is an attractive fluorophore since it is water soluble and emits red light. The most prominent example of using resorufin in immunoassays is Amplex Red **1.1**. The commercial probe **1.1** is mainly utilised for the quantitative study of H_2O_2 (Scheme 1).[89] The amine of resorufin is masked which upon reaction with H_2O_2 releases resorufin.

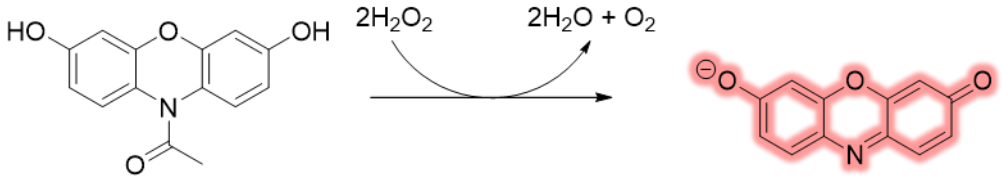

1.1

Scheme 1: Amplex Red **1.1**, a commercially available probe for the quantitative study of H_2O_2.

Resorufin is a fairly underexploited fluorophore in contrast to fluorescein or coumarin where many ROS probes exist. I have reviewed the literature and was able to mainly identify probes for the detection of sulphur and nitrogen species, with few examples of ROS species. A small overview of the current literature is herein provided.

Resorufin based probes **2.1** and **2.2** for reactive sulphur species were developed by Chang *et al.*[90] and Tian *et al.*[91] (Scheme 2). Resorufin was masked with relevant sensing groups for thiols. Upon reaction of the probe with the thiol, resorufin is released. Tian and co-workers even went a step further and designed a dual analyte probe **2.2** for simultaneous thiol and redox sensing. Using macrophages, the probe was successfully validated to detect both analytes.

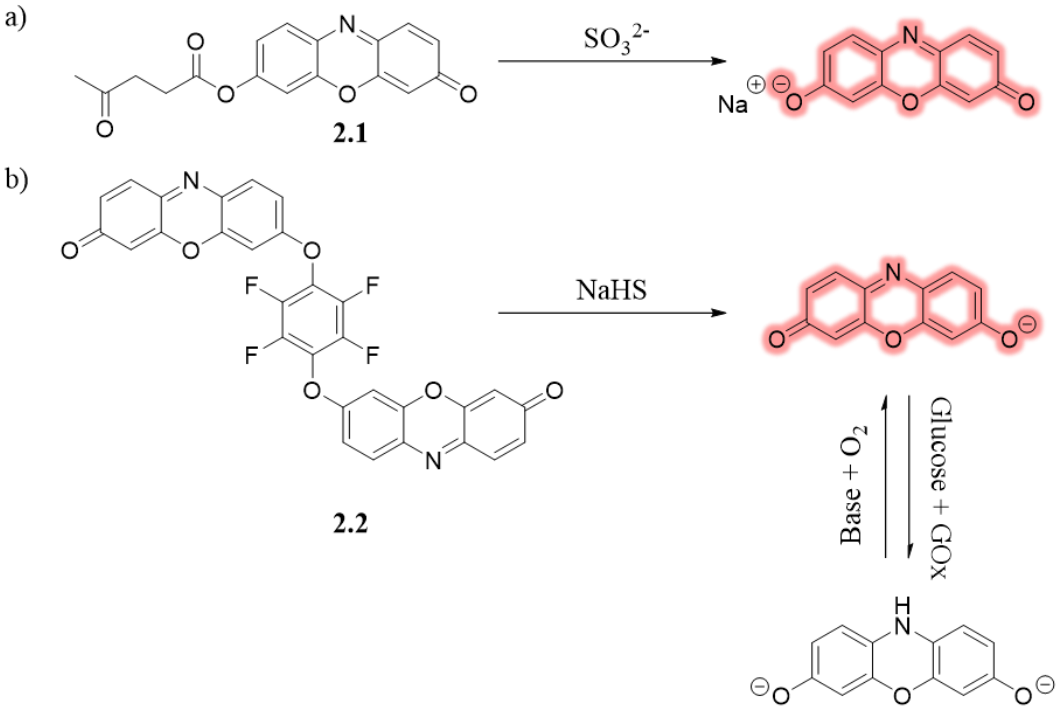

Scheme 2: Resorufin-based probes **2.1** and **2.2** for RSS sensing: a) sulphite sensor and b) dual analyte sensor for thiol and redox homeostasis.

Chemical probes based on a resorufin core for hydrazine and nitroxyl have been developed by *Zhu et al.*[92] and Bhuniya *et al.*[93] (Scheme 3). Exposure to increased levels of hydrazine can damage the liver, lungs, kidneys and nervous system either through inhalation or oral absorption.[94] The resorufin probe **3.1** is activated by the deprotection of the bromo-butyric ester. Selectivity studies were carried out with a range of metal ions and halides. However, the probe could also potentially be cleaved by $ONOO^-$ since this strong nucleophile can easily attack the ester group and generate free resorufin. The reaction based probe **3.2** by Bhuniya and co-workers uses a phosphine unit that selectively reacts with nitroxyl. The selectivity study looked at a variety of ROS and RNS. $ONOO^-$ was not included but could lead to cleavage of the ester group, impacting the claims of nitroxyl sensitivity and selectivity. Only exogenous nitroxyl was evaluated in Chinese hamster ovary cells. Endogenous nitroxyl generation could potentially give a false positive if the probe selectively reacts with $ONOO^-$ over nitroxyl in an oxidative stress related environment.

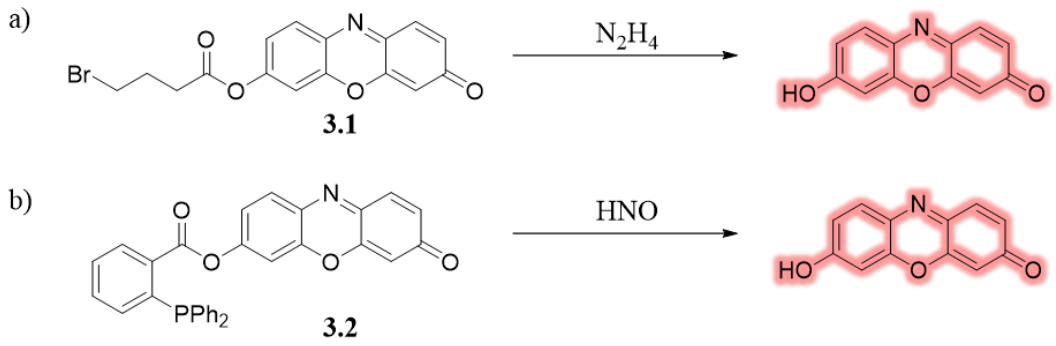

Scheme 3: Resorufin-based molecular probes **3.1** and **3.2** for the detection of a) hydrazine and b) nitroxyl.

Zhang *et al.* developed a resorufin based probe **4.1** with a benzyl Bpin group attached for tyrosinase detection.[95] The authors also evaluated H_2O_2 as part of their study, acknowledging that it could interfere and compete with tyrosine. It would have been interesting to see what effect $ONOO^-$ has on the probe **4.1** since similar to H_2O_2 it can easily oxidise the boronic ester. A similar probe **4.2** was developed by Ma and co-workers[96] whereby the boronic ester was placed at the ortho position instead of the meta one (Scheme 4). Their probe has been developed for benzoyl peroxide (BPO) detection with a selectivity study plainly looking at inorganic salts and amino acids. Ma *et al*. realised that probe **4.2** shows good turn on responses with H_2O_2. For the purpose of their application, the probe seems suitable for selective BPO detection. Nevertheless, probe **4.2** could be also a ROS probe for $ONOO^-$ and H_2O_2 *in vitro*.

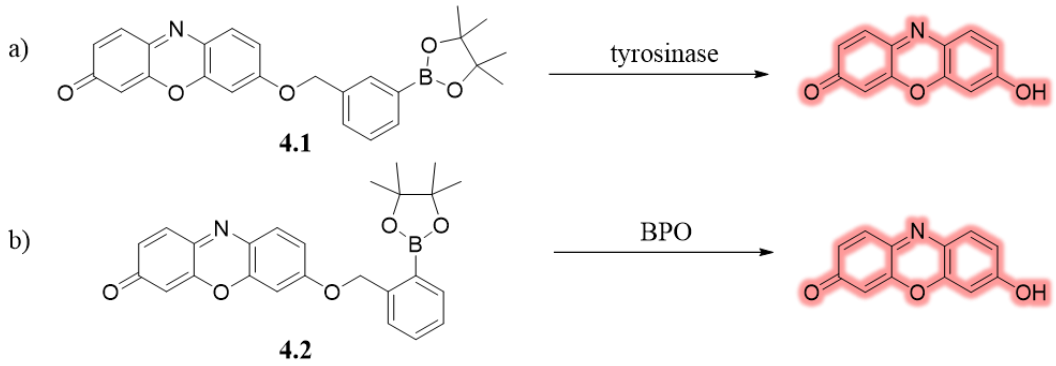

Scheme 4: Resorufin-based probes **4.1** and **4.2** with a benzyl Bpin motif for the detection of a) tyrosinase and b) benzoyl peroxidase (BPO) respectively.

The functionalisation of resorufin has mainly focused on the masking of the alcohol group of resorufin with relevant sensing groups for a variety of analytes. I wanted to explore the functionalisation at the amine position in the hope to access a new class of reaction based fluorophores for the sensitive and selective detection of $ONOO^-$ by ideally incorporating an organelle targeting aspect i.e. direct selective sensing.

1.1. Project Aim

As seen in Chapter 1, **PR1** shows good selectivity and sensitivity for $ONOO^-$ and is a useful tool in understanding $ONOO^-$ mediated pathways in J774.2 macrophages. Functionalisation at the amine position of **PR1** should allow the development of (organelle) targeted $ONOO^-$ molecular sensors. Previous work in the group led to the development of **5.8**, a useful intermediate for further functionalisation at the alcohol position (Scheme 5). The incorporation of the 4-hydroxyphenyl moiety at the amine position has been previously shown by Guo *et al.* to increase sensitivity towards $ONOO^-$ in addition to the boronic esters.[49] **5.8** was afforded in a six step synthesis with an overall yield of 13.7 %. First, selective protection of the alcohol in the 1 position of 4-hydroxybenzyl alcohol **5.1** was achieved using pivaloyl chloride. Subsequent bromination of the alcohol in the 4-position of **5.2** afforded **5.3** in 76 %. Alkylation of phenoxazine **5.4** with **5.3** gave **5.5** followed by a NBS bromination to yield **5.6**. Following the deprotection of the pivalate group of **5.6** with DIBAL-H, Miyaura borylation of **5.7** gave **5.8** in 53 %.

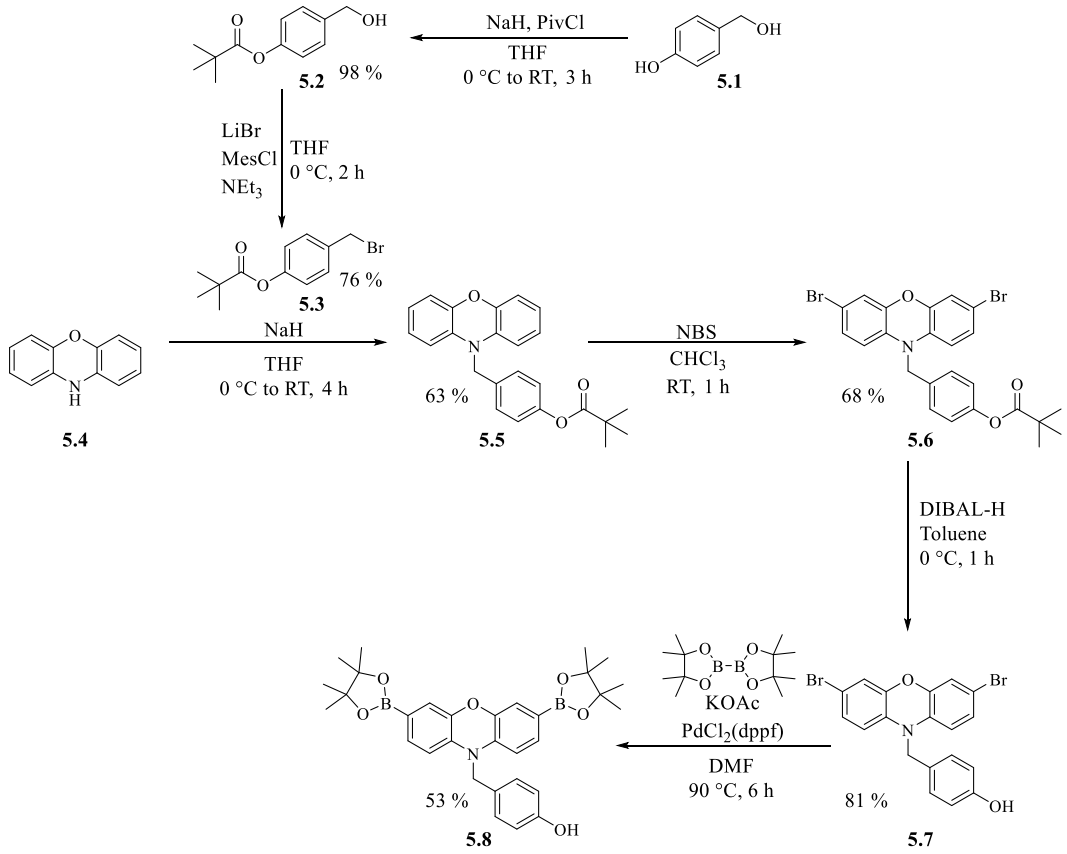

Scheme 5: Synthesis of resorufin-based intermediate **5.8**.

Fluorescence studies confirmed **5.8**'s ability to be an affective $ONOO^-$ probe. Titration studies of **5.8** with $ONOO^-$ showed that towards 10 μM, the fluorescence response is starting to saturate (Figure 1). A subsequent ROS selectivity study showed that **5.8** preferentially detects $ONOO^-$ over other ROS species (Figure 2). The fluorescence response of **5.8** with H_2O_2 is expected due to the ability of boronic esters to also act as targeting group for H_2O_2. However, the reactivity with $ONOO^-$ is instantaneous and requires lower concentrations for a turn-on response in comparison to H_2O_2.

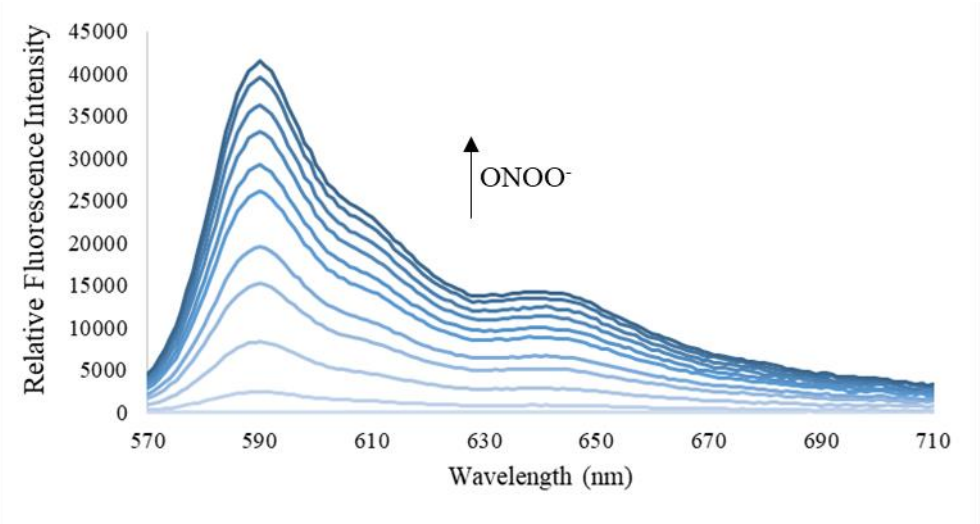

Figure 1: Emission spectra for probe **5.8** (500 nM) in the presence of $ONOO^-$ (1, 2, 3, 4, 5, 6, 7, 8, 9, 10 µM) in PBS buffer 52 % MeOH : H_2O, pH = 8.2 at 25 °C. Fluorescence intensities were measured with λ_{ex} = 550 (bandwith 15) nm on a BMG Labtech CLARIOstar® plate reader.

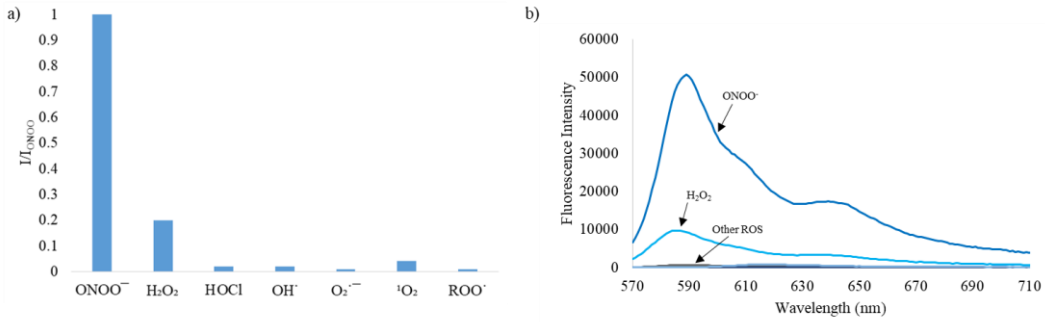

Figure 2: Selectivity data for **5.8** (500 nM) in the presence of $ONOO^-$ (50 µM), OH·(500 µM), $O_2^{\cdot-}$ (500 µM), $^1O_2$ (500 µM) after 5 min. H_2O_2 (1 mM), ROO· (500 µM) and ClO^- (500 µM) were measured after 30 min. (a) Bar chart of relative fluorescence intensities. (b) Emission spectra. The data was obtained in PBS buffer 52 % MeOH : H_2O, pH = 8.2 at 25 °C at λ_{ex} = 550 (bandwith 15) nm and max λ_{em} = 590 nm on a BMG Labtech CLARIOstar® plate reader.

Given this useful intermediate, it was decided to explore the scope further by developing a series of analogues (Appendix). For the purpose of this thesis, only a selection of these **PR1** derivatives will be discussed.

2. Organelle Targeting Fluorescent Probes

2.1. Synthesis of Organelle Targeting $ONOO^-$ Resorufin Based Probes

The development of probes that preferentially localise in a certain type of organelle are highly preferable to understand cellular pathways in more depth as outlined in Chapter 1. The mitochondria is one of the main sources of ROS. To this end, two mitochondrial targeting probes and one endoplasmic reticulum targeting probe were developed. The two mitochondrial targeting probes use the core structure of **5.8** and include a lipophilic cation such as triphenylphosphonium (TPP) and quaternised pyridine. These cations allow for easier passage through the mitochondrial membrane.[97, 98] Targeted delivery of molecular sensors towards the endoplasmic reticulum can be achieved for example through the attachment of a short alkane chain with a Cl atom at the end.[99, 100] Hence, three structures were proposed that should be synthetically easily accessible (Scheme 6).

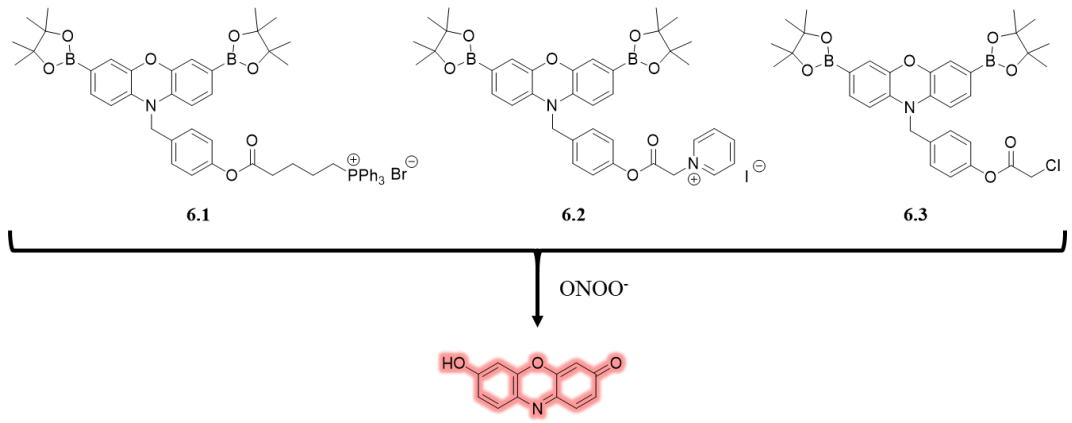

Scheme 6: Organelle targeting $ONOO^-$ probes based on a resorufin scaffold.

To achieve final target probe **6.1**, intermediate **5.8** was reacted with acyl chloride **7.2**, which was previously synthesised from carboxylic acid **7.1**. The addition elimination reaction allowed **6.1** to be obtained in a 40 % yield (Scheme 7).

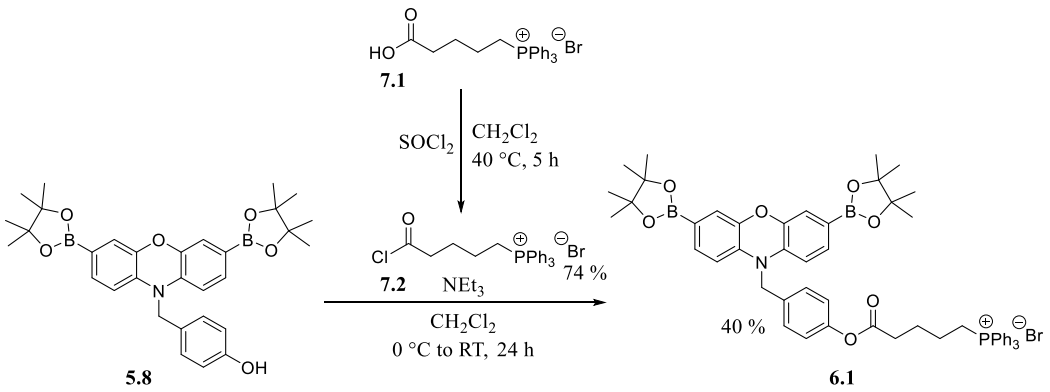

Scheme 7: Synthetic route towards a mitochondrial targeting probe **6.1**.

Following the successful synthesis of **6.1**, a peptide coupling approach was investigated for the conversion of the alcohol into the ester (Scheme 8). Peptide coupling reagents such as HATU for example are also used for alcohol acylation reactions with carboxylic acids whereby the corresponding ester is generated. Using HATU as a coupling reagent, **6.1** was obtained in 38 % yield, similar to the previous synthetic strategy. The peptide coupling reaction allowed the overall synthesis of **6.1** to be shortened by one step.

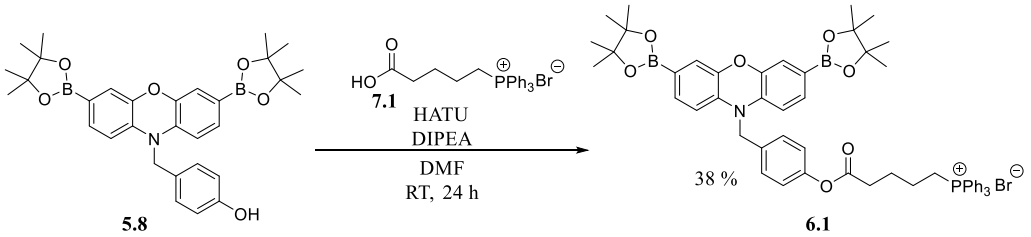

Scheme 8: Alternative route towards a mitochondrial targeting probe **6.1**.

The postulated mechanism for the conversion of **6.1** into resorufin, a well-known fluorescent probe, is illustrated in Scheme 9. Essentially, $ONOO^-$ allows for the cleavage of the boronic esters as well as the attached phenyl moiety at the amine position giving free resorufin.

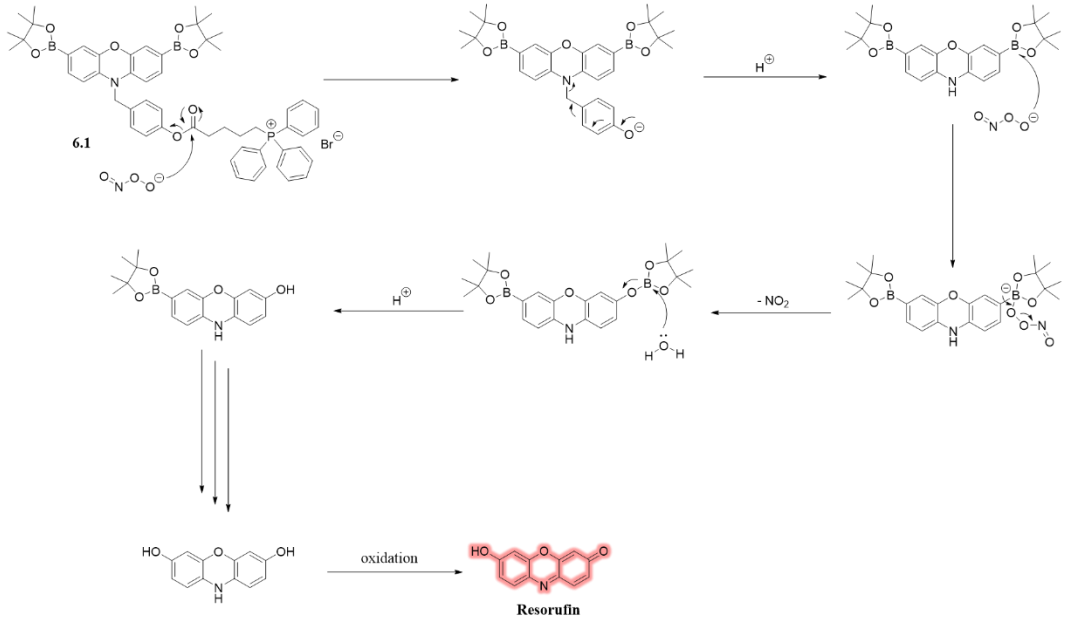

Scheme 9: Postulated mechanism for the conversion of **6.1** into resorufin.

A second mitochondrial targeting probe was developed whereby pyridinium was incorporated as the mitochondrial targeting group (Scheme 10). Reaction of **5.8** with 2-chloroacetyl chloride **11.1** gave **6.3** in a very low yield of 12 %. Further functionalisation with pyridine then gave the mitochondrial target probe **6.2** in 90 %.[101] Coincidentally, it was realised that the intermediate leading towards **6.2** could be used as an endoplasmic reticulum targeted probe **6.3**. The short alkane chain with a Cl atom at the end has previously been shown to be an effective group to localise probes within the endoplasmic reticulum.[99, 100]

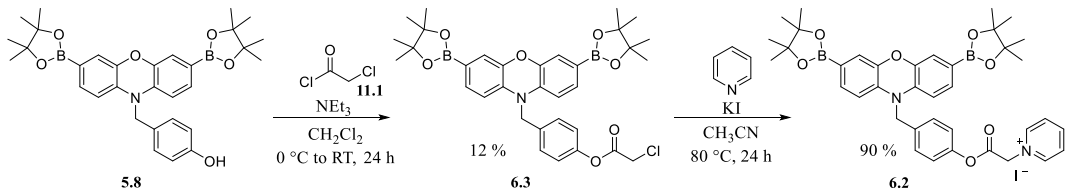

Scheme 10: Synthesis of mitochondrial targeting probe **6.2** and endoplasmic reticulum targeting probe **6.3**.

2.2. Fluorescence Studies

Due to the inherent nature of boronic esters to act as sensing groups for $ONOO^-$ and H_2O_2, fluorescence titration studies were carried out for both ROS in order to validate the faster reaction time and sensitivity with $ONOO^-$. ROS selectivity studies were carried out to confirm this hypothesis.

In a first instance, UV spectra were collected for **6.1**, **6.2**, and **6.3** in order to validate the change in absorbance in the presence of $ONOO^-$. The formation of a new species was observed upon addition of $ONOO^-$ (Figure 3). The new absorption peak matches with resorufin, validating the release of the fluorophore after reaction with $ONOO^-$.

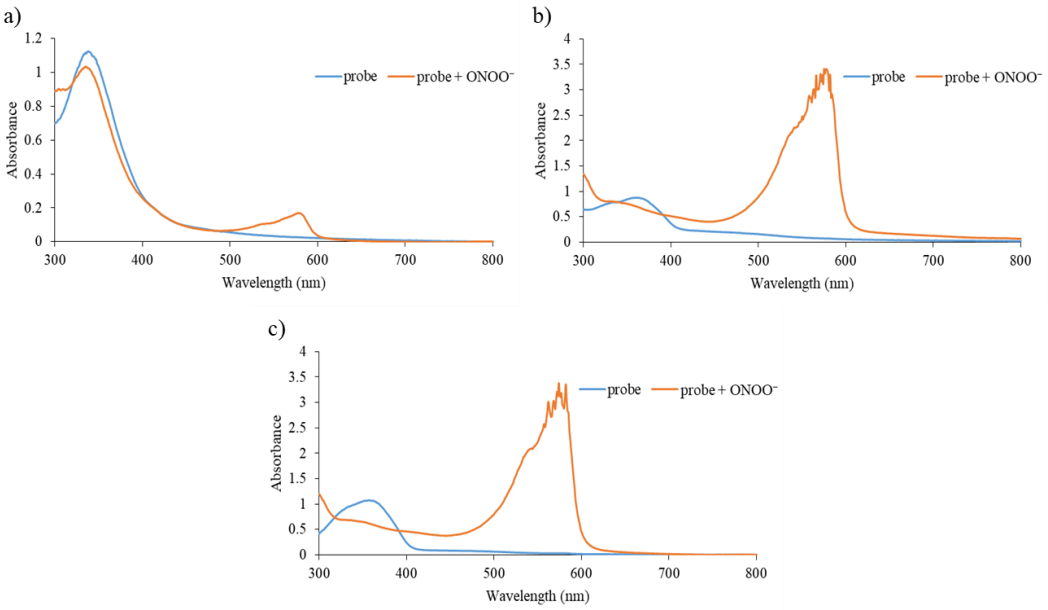

Figure 3: UV spectra of a) **6.1** (50 µM), b) **6.2** (50 µM), and c) **6.3** (50 µM), with and without $ONOO^-$ (excess) in PBS buffer 52 % MeOH : H_2O, pH = 8.2 at 25 °C measured on a BMG Labtech CLARIOstar® plate reader.

ROS selectivity studies were carried out for **6.1**, **6.2**, and **6.3** to assure selectivity towards $ONOO^-$ over other ROS (Figure 4). As expected preferential detection for $ONOO^-$ was seen for all probes. At the same time, H_2O_2 was also detected.

Nevertheless, in a biological environment, boronic esters would be more quickly and easily oxidised by $ONOO^-$ rather than H_2O_2.

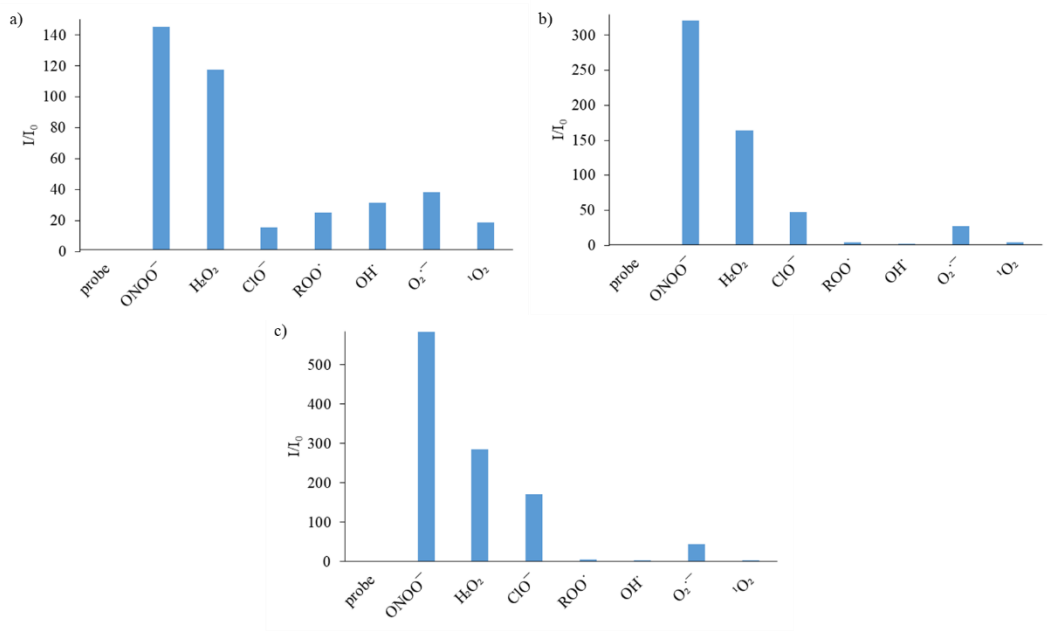

Figure 4: Selectivity data for a) probe **6.1** (500 nM), b) probe **6.2** (500 nM), and c) probe **6.3** (500 nM) in the presence of $ONOO^-$ (50 µM), OH· (500 µM), $O_2^{\cdot-}$ (500 µM), $^1O_2$ (500 µM) after 5 min. H_2O_2 (1 mM), ROO· (500 µM) and ClO^- (500 µM) were measured after 30 min. The data was obtained in PBS buffer 52 % MeOH : H_2O, pH = 8.2 at 25 °C with λ_{ex} = 550 (bandwith: 15) nm and max λ_{em} = 590 nm on a BMG Labtech CLARIOstar® plate reader.

Following these selectivity results, H_2O_2 was investigated with concentrations ranging from 100 µM – 2 mM over 1 h. For a significant fluorescence signal, H_2O_2 needs to be incubated for at least 30 min to react. No fluorescence is initially observed with H_2O_2 alone. Upon addition of the probe, the fluorescence signal increases relative to H_2O_2 concentrations validating its reactivity towards H_2O_2 (Figure 5).

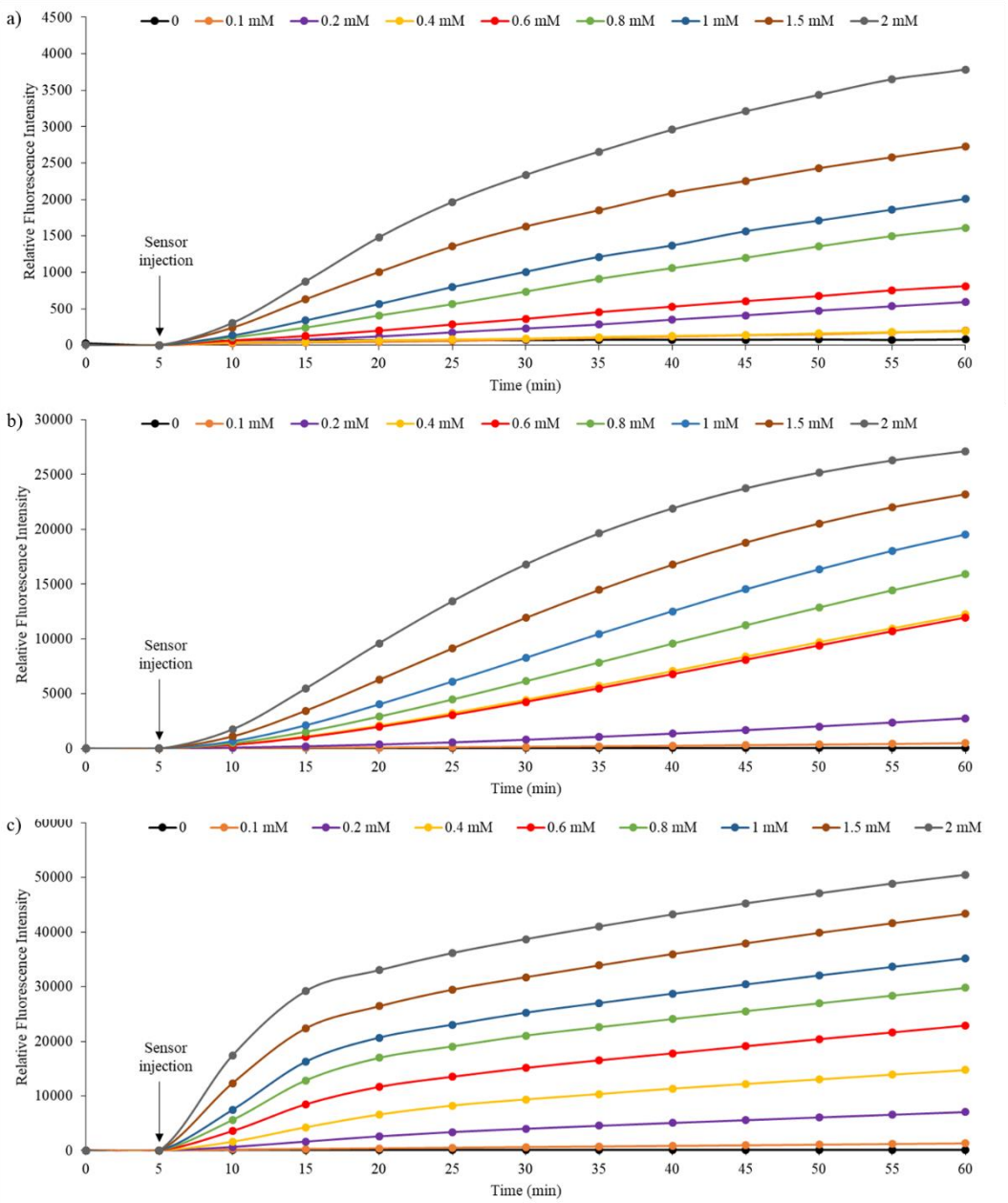

Figure 5: Fluorescence intensity changes over time of a) probe **6.1** (500 nM), b) probe **6.2** (500 nM) and c) probe **6.3** (500 nM) in the presence of H_2O_2 (0.1, 0.2, 0.4, 0.6, 0.8, 1, 1.5, 2 mM) in PBS buffer 52 % MeOH : H_2O, pH = 8.2 at 25 °C. Fluorescence intensities were measured with λ_{ex} = 550 (bandwith: 15) nm and max λ_{em} = 590 nm on a BMG Labtech CLARIOstar® plate reader.

H_2O_2 titrations (100 µM – 2 mM) of **6.1**, **6.2**, and **6.3**, all show no saturation of the fluorescence signal (Figure 6). Higher H_2O_2 concentrations are not biologically relevant and were therefore, not investigated. Lower H_2O_2 concentrations than 100 µM

did not activate **6.1**, **6.2**, and **6.3** limiting the detection of H_2O_2 at small biologically relevant levels. LoDs for **6.1**, **6.2**, and **6.3** were established as 83.3 µM, 60 µM and 35 µM respectively.

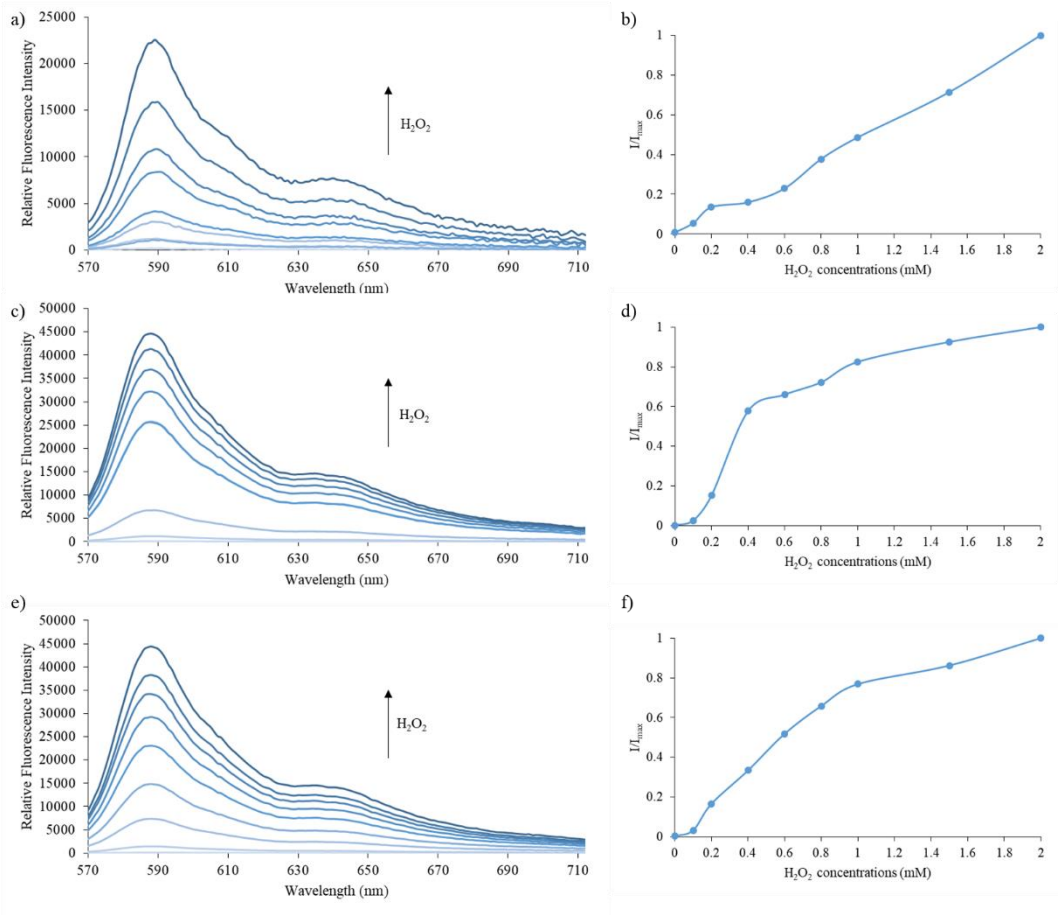

Figure 6: Emission spectra and dose dependence curve (I/I_{max}) for a) & b) probe **6.1** (500 nM), c) & d) probe **6.2** (500 nM) and e) & f) probe **6.3** (500 nM) in the presence of H_2O_2 (0.1, 0.2, 0.4, 0.6, 0.8, 1, 1.5, 2 mM) after 1 h in PBS buffer 52 % MeOH : H_2O, pH = 8.2 at 25 °C. Fluorescence intensities were measured with λ_{ex} = 550 (bandwith: 15) nm and max λ_{em} = 590 nm on a BMG Labtech CLARIOstar® plate reader.

Subsequent evaluation of **6.1**, **6.2**, and **6.3** with $ONOO^-$ gave insights into sensitivity towards a different ROS. The time frame of reacting probes with H_2O_2 and $ONOO^-$ differs significantly with $ONOO^-$ being a stronger oxidant and hence, a faster reacting species. Titration of **6.1**, **6.2**, and **6.3** with $ONOO^-$ (1 – 50 µM) confirmed that much

lower concentrations of $ONOO^-$ are required for a turn-on response compared to H_2O_2 (Figure 7). All react almost instantaneously with $ONOO^-$, indicating their potential for $ONOO^-$ detection. LoDs for **6.1**, **6.2**, and **6.3** are 3 µM, 0.8 µM and 0.2 µM respectively. Therefore, all three probes are highly applicable for low concentration detection of $ONOO^-$ in biological systems.

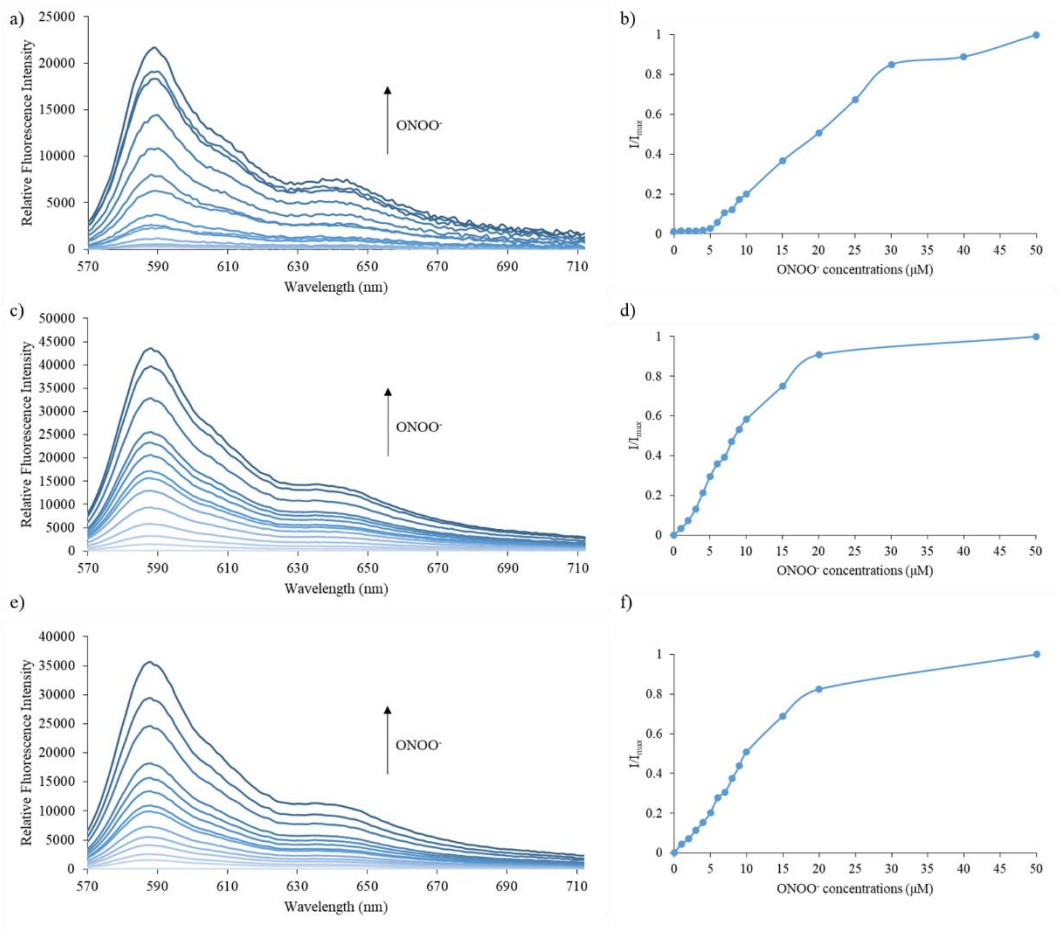

Figure 7: Emission spectra and dose dependence curve (I/I_{max}) for a) & b) probe **6.1** (500 nM), c) & d) probe **6.2** (500 nM) and e) & f) probe **6.3** (500 nM) in the presence of $ONOO^-$ (1, 2, 3, 4, 5, 6, 7, 8, 9, 10, 15, 20, 30, 40, 50 µM) after 5 min in PBS buffer 52 % MeOH : H_2O, pH = 8.2 at 25 °C. Fluorescence intensities were measured with λ_{ex} = 550 (bandwith: 15) nm and max λ_{em} = 590 nm on a BMG Labtech CLARIOstar® plate reader.

2.3. Cell Studies

The cell protocol established in Chapter 1 was used to assess the ability of probes **6.1**, **6.2** and **6.3** to detect endogenously produced $ONOO^-$. J774.2 macrophages were stimulated with LPS and IFN-γ. At the same time, ebselen and N_ω-nitro-*L*-arginine were used to assess the ability to suppress $ONOO^-$ production and if this could be detected by **6.1**, **6.2** and **6.3**. **PR1** was used as a positive control. Unfortunately, all three organelle targeting probes **6.1**, **6.2**, and **6.3** showed negligible activity in detecting endogenous $ONOO^-$ and subsequent suppression of its production by inhibitors (Figure 8). Strangely enough, for **6.3**, a higher fluorescence signal was observed upon usage of $ONOO^-$ inhibitors then stimulation with LPS and IFN- γ alone. Hence, the organelle targeting $ONOO^-$ probes seem to have cell permeability issues.

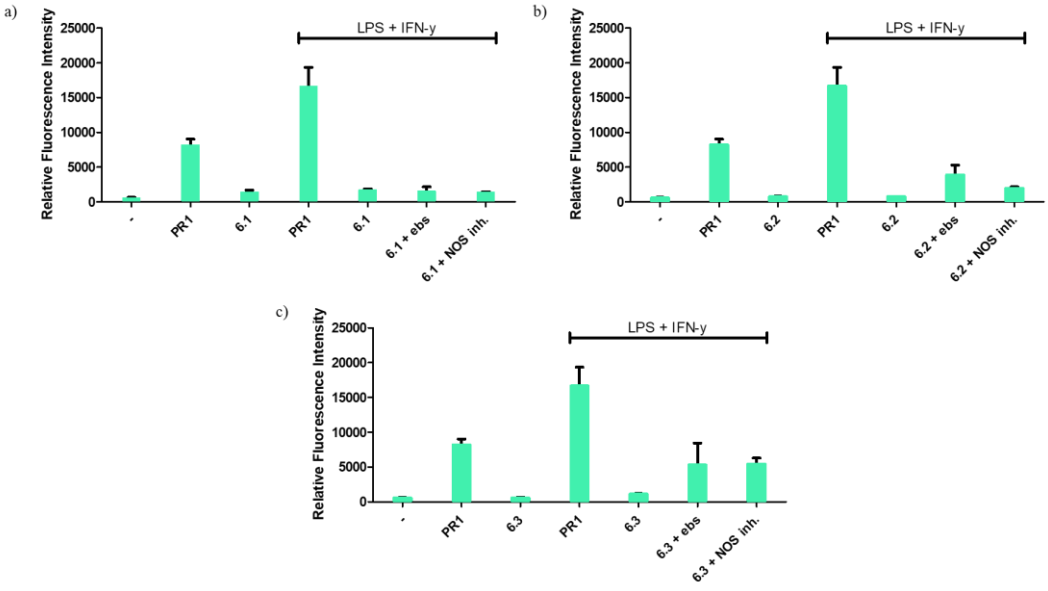

Figure 8: LPS and IFN-γ induced $ONOO^-$ production quenched by ebselen (ebs) and N_ω-nitro-L-arginine (NOS inh.) with respective incubation of a) probe **6.1**, b) probe **6.2**, and c) probe **6.3**. Fluorescence intensities were measured with λ_{ex} = 550 (bandwith: 15) nm and max λ_{em} = 590 nm on a BMG Labtech CLARIOstar® plate reader. Data show mean values (n = 3) ± SEM. No statistical significance.

Despite these results, **6.1** was evaluated using confocal microscopy. It was anticipated that **6.1** would be able to penetrate the mitochondria and detect $ONOO^-$ inside the organelle. To be able to rationalise whether localisation occurs in the mitochondria, MitoView Green was used as a complimentary commercially available mitochondrial stain. Unfortunately, poor penetration of the mitochondrial targeting probe **6.1** was observed (Figure 9). It also seems that it is competing to a certain extent with MitoView Green, which seems to weaken the signal in the presence of **6.1** compared to when used alone. This suggest that the use of **6.1** for mitochondria targeting is unsuccessful due to solubility issues.

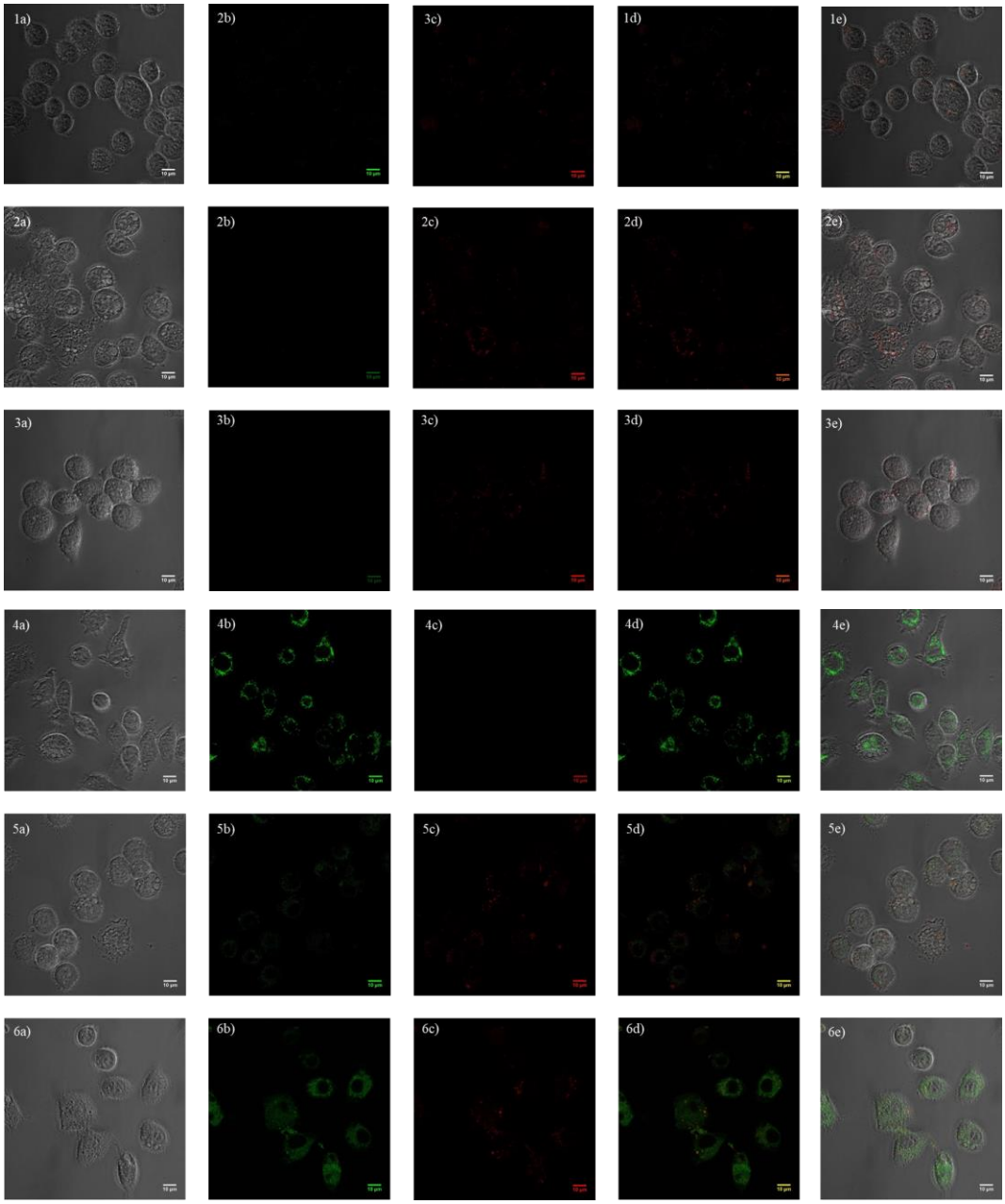

Figure 9: Confocal microscopy images of J774.2 macrophages incubated in probenecid (1 mM): 1a – e: **6.1** (15 µM, 30 min); 2a – e: LPS (1 µg/ml, 4 h), IFN-γ (50 ng/ml, 4 h) and **6.1** (15 µM, 30 min); 3a – e: LPS (1 µg/ml, 4 h), IFN-γ (50 ng/ml, 4 h), **6.1** (15 µM, 30 min) and SIN-1 (15 µM, 5 min); 4a – e: MitoView Green (200 nM, 30 min); 5a – e: LPS (1 µg/ml, 4 h), IFN-γ (50 ng/ml, 4 h), MitoView Green (200 nM, 30 min), and **6.1** (15 µM, 30 min); 6a – e: LPS (1 µg/ml, 4 h), IFN-γ (50 ng/ml, 4 h), MitoView Green (200 nM, 30 min), **6.1** (15 µM, 30 min), and SIN-1 (15 µM, 5 min). Channel (a): brightfield, channel (b): λ_{ex} = 490 nm, λ_{em} = 523 nm, channel (c): λ_{ex} = 572 nm, λ_{em} = 583 nm, channel (d): channel (b) and (c) combined, channel (e): channel (a), (b) and (c) combined. Magnification: x63. Scale bar: 10 µM. N = 3.

Since the organelle targeting $ONOO^-$ probe **6.1** showed poor cell permeability, the focus was shifted towards more soluble and cell permeable **PR1** derivatives.

3. Alkyne and Alkane Chain Functionalised Resorufin Probes

3.1. Synthesis of Alkyne and Alkane Chain Functionalised $ONOO^-$ Fluorescent Probes

A series of $ONOO^-$ probes were developed containing ester or ether groups connected to either an alkyne chain or alkane chain (Figure 10). It was postulated that these functionalities would on the one hand improve cell permeability (alkane chain to improve lipophilicity) or allow for the development of future theranostic systems (alkyne group allows for *in situ* click chemistry).

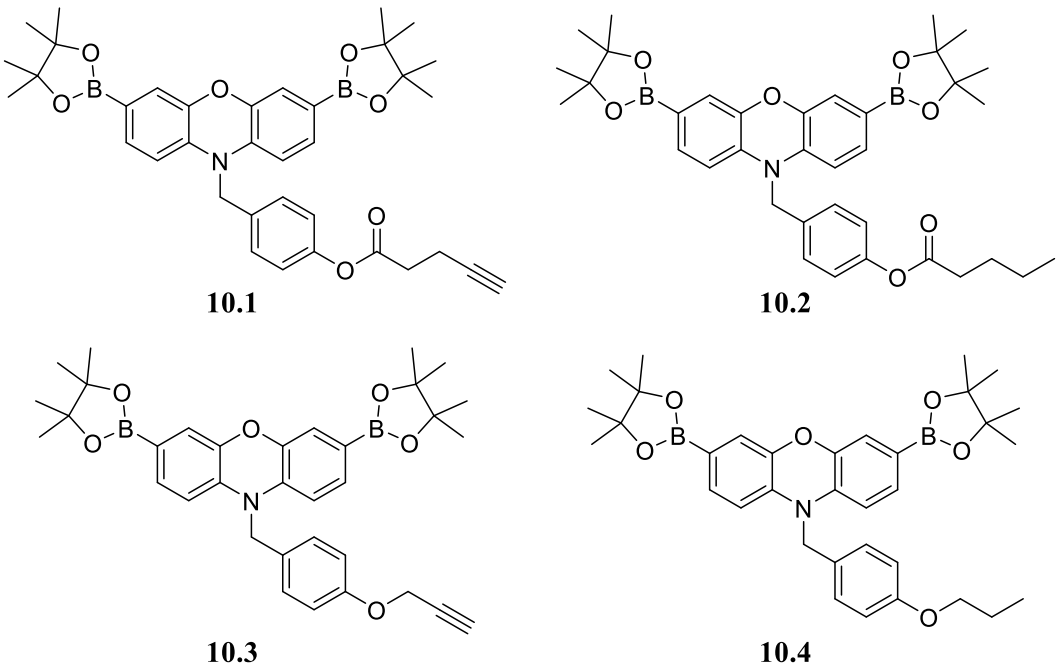

Figure 10: A series of $ONOO^-$ probes incorporating alkyne and alkane chain functionalities: **10.1**, **10.2**, **10.3** and **10.4**.

10.1 and **10.2** were easily accessible from **5.8**. Coupling the relevant acyl chlorides **11.2** (previously accessed from **11.1**) and **11.3** to **5.8**, yielded final target compounds **10.1** and **10.2** in 47 % and 51% yield respectively (Scheme 11).

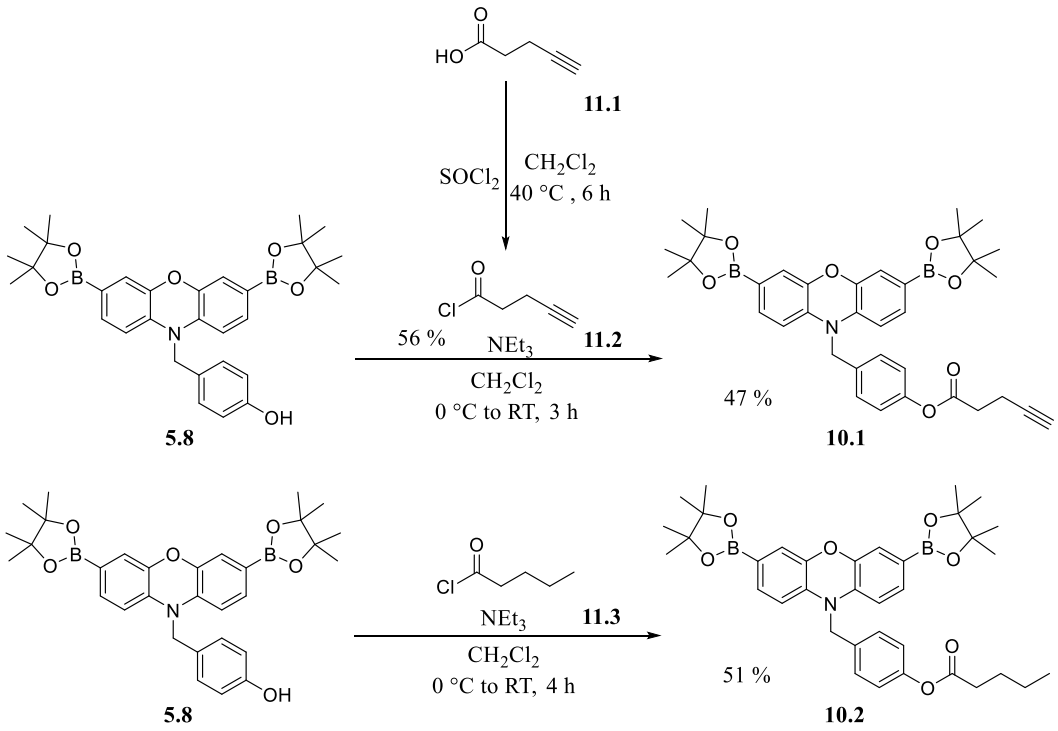

Scheme 11: Synthesis of $ONOO^-$ probes **10.1** and **10.2**.

Ether functionalised probes were also easily accessible in a one-step synthesis from **5.8**. Nucleophilic substitution between bromide **12.1** and **12.2** respectively and alcohol **5.8** allowed for the ether version of **10.1** and **10.2**. **10.3** and **10.4** were obtained in moderate yields: 48 % and 50 % respectively (Scheme 12).

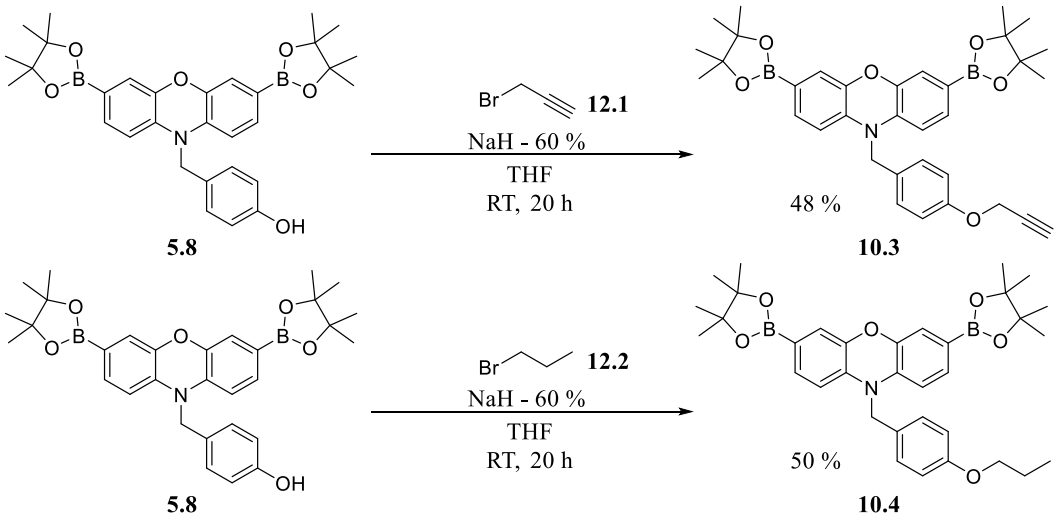

Scheme 12: Synthesis of target probes **10.3** and **10.4**.

We were interested to evaluate how the structural variation of ester and ether groups with corresponding alkyne and alkane groups would impact the fluorescence ability of the resorufin derived probes as well as their cell permeation ability.

3.2. Fluorescence Studies

UV spectra confirmed the formation of resorufin as expected when probes **10.1**, **10.2**, **10.3** and **10.4** were reacted with $ONOO^-$ (Figure 11).

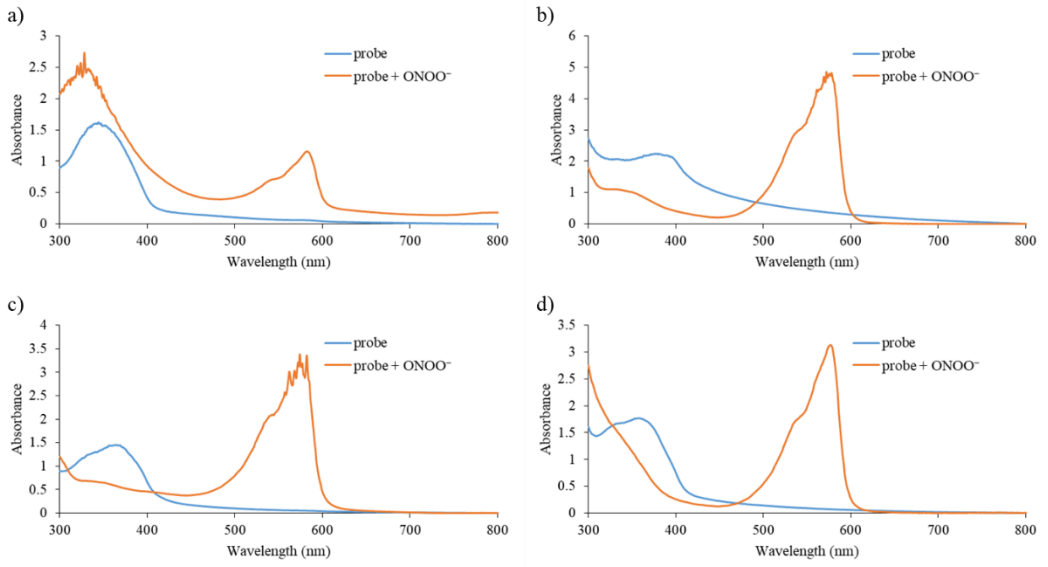

Figure 11: UV spectra of a) probe **10.1**, b) probe **10.2**, c) probe **10.3** and d) probe **10.4** with and without $ONOO^-$ (excess) in PBS buffer 52 % MeOH : H_2O, pH = 8.2 at 25 °C measured on a BMG Labtech CLARIOstar® plate reader.

ROS selectivity studies allowed to confirm selectivity and sensitivity towards $ONOO^-$ for probes **10.1**, **10.2**, **10.3** and **10.4** (Figure 12).

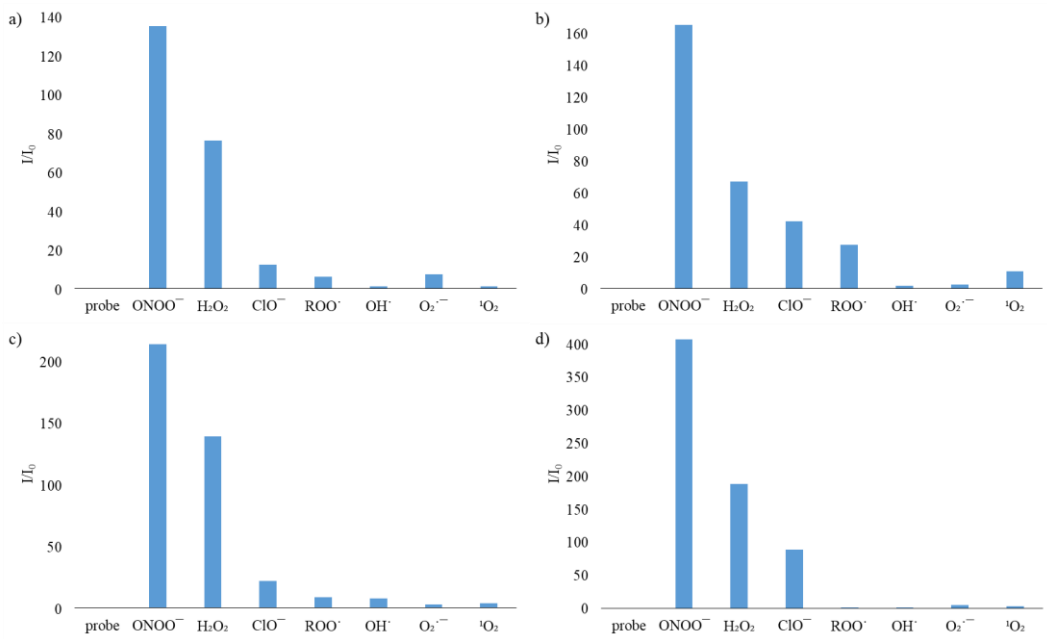

Figure 12: Selectivity data for a) probe **10.1** (500 nM), b) probe **10.2** (500 nM), c) probe **10.3** (500 nM) and d) probe **10.4** in the presence of $ONOO^-$ (50 µM), OH· (500 µM), $O_2^{\cdot-}$ (500 µM), $^1O_2$ (500 µM) after 5 min. H_2O_2 (1 mM), ROO· (500 µM) and ClO^- (500 µM) were measured after 30 min. The data was obtained in PBS buffer 52 % MeOH : H_2O, pH = 8.2 at 25 °C at λ_{ex} = 550 (bandwith: 15) nm and max λ_{em} = 590 nm on a BMG Labtech CLARIOstar® plate reader.

In the same manner as in Section 2.2, fluorescence of the probes was evaluated over time with different concentrations of H_2O_2, followed by titration studies with H_2O_2. These were carried out for probes **10.1**, **10.2**, **10.3** and **10.4** (Figure 13 and Figure 14). Good turn-on responses were observed with H_2O_2. LoDs were determined as 24 µM, 17 µM, 26 µM, and 19 µM respectively for **10.1**, **10.2**, **10.3** and **10.4** from Figure 15.

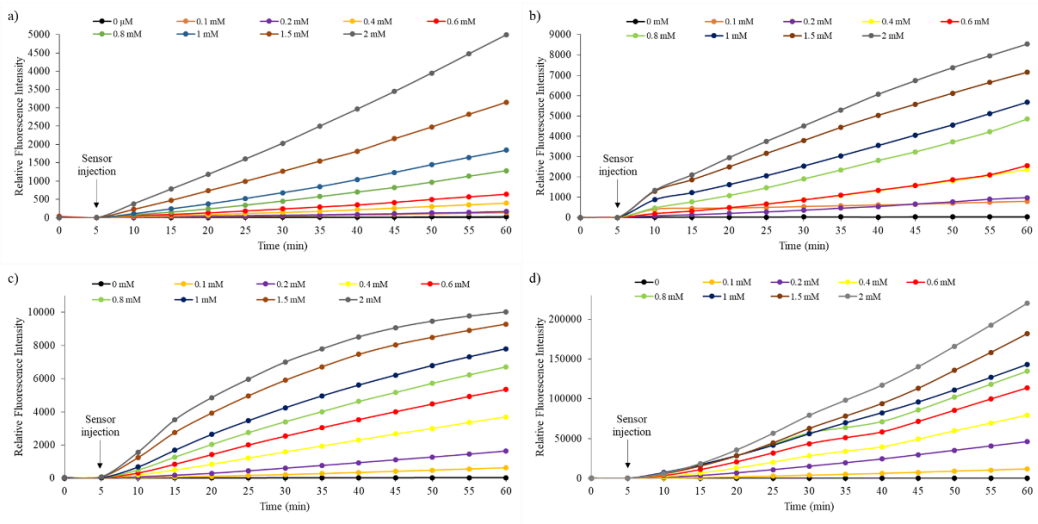

Figure 13: Fluorescence intensity changes over time for probes a) **10.1** (500 nM), b) **10.2** (500 nM), c) **10.3** (500 nM) and d) **10.4** (500 nM) in the presence of H_2O_2 (0.1, 0.2, 0.4, 0.6, 0.8, 1, 1.5, 2 mM) in PBS buffer 52 % MeOH : H_2O, pH = 8.2 at 25 °C. Fluorescence intensities were measured with λ_{ex} = 550 (bandwith: 15) nm and max λ_{em} = 590 nm on a BMG Labtech CLARIOstar® plate reader.

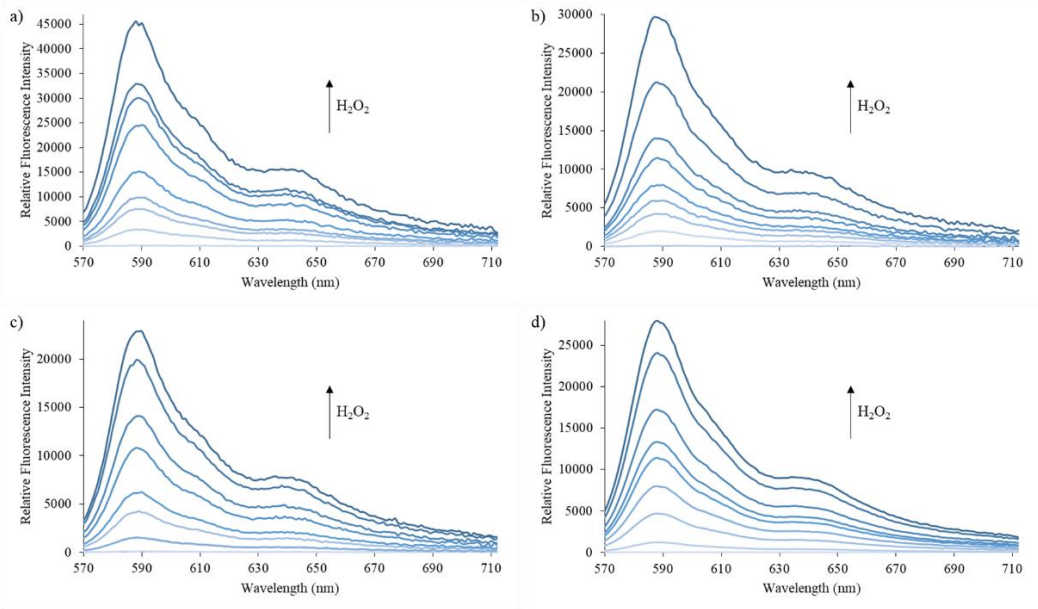

Figure 14: Emission spectra for probes a) **10.1** (500 nM), b) **10.2** (500 nM), c) **10.3** (500 nM) and d) **10.4** (500 nM) in the presence of H_2O_2 (0.1, 0.2, 0.4, 0.6, 0.8, 1, 1.5, 2 mM) after 1 h in PBS buffer 52 % MeOH : H_2O, pH = 8.2 at 25 °C. Fluorescence intensities were measured with λ_{ex} = 550 (bandwith: 15) nm on a BMG Labtech CLARIOstar® plate reader.

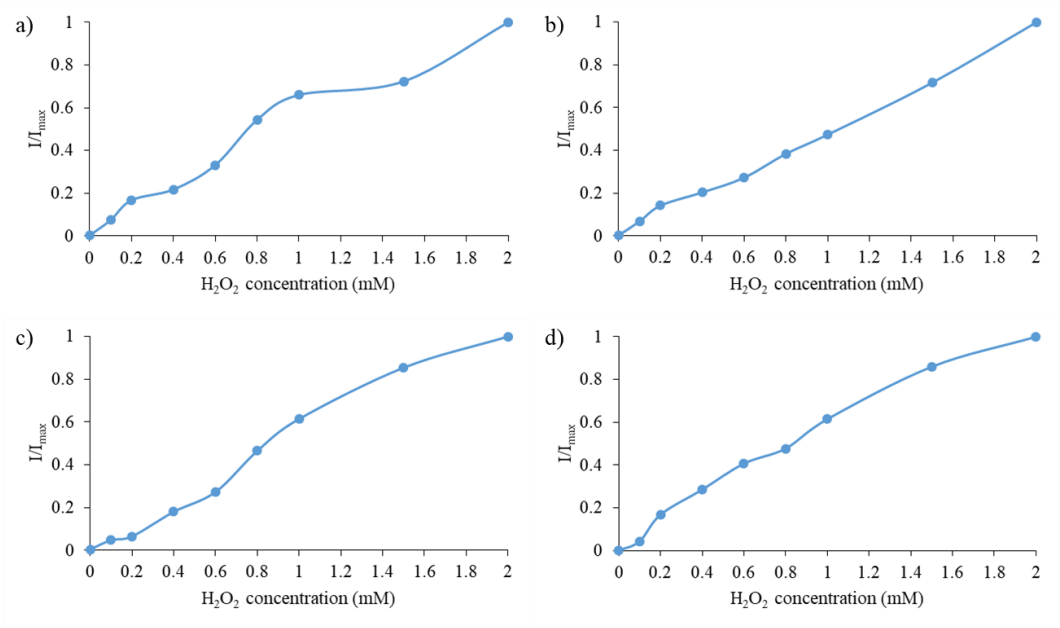

Figure 15: Dose dependence curve (I/I_{max}) for probes a) **10.1** (500 nM), b) **10.2** (500 nM), c) **10.3** (500 nM) and d) **10.4** (500 nM) in the presence of H_2O_2 (0.1, 0.2, 0.4, 0.6, 0.8, 1, 1.5, 2 mM) in PBS buffer 52 % MeOH : H_2O, pH = 8.2 at 25 °C. Fluorescence intensities were measured with λ_{ex} = 550 (bandwith: 15) nm and max λ_{em} = 590 nm on a BMG Labtech CLARIOstar® plate reader.

Following H_2O_2 studies, **10.1**, **10.2**, **10.3** and **10.4**'s ability to detect $ONOO^-$ was evaluated. As expected, the probes show much higher sensitivity towards $ONOO^-$ requiring concentrations in the low micromalor range for turn-on effects. Titration studies (Figure 16) allowed to establish dose dependence curves (Figure 17) giving LoDs of 0.39, 0.19 µM, 0.46 µM and 0.13 µM for **10.1**, **10.2**, **10.3** and **10.4** respectively.

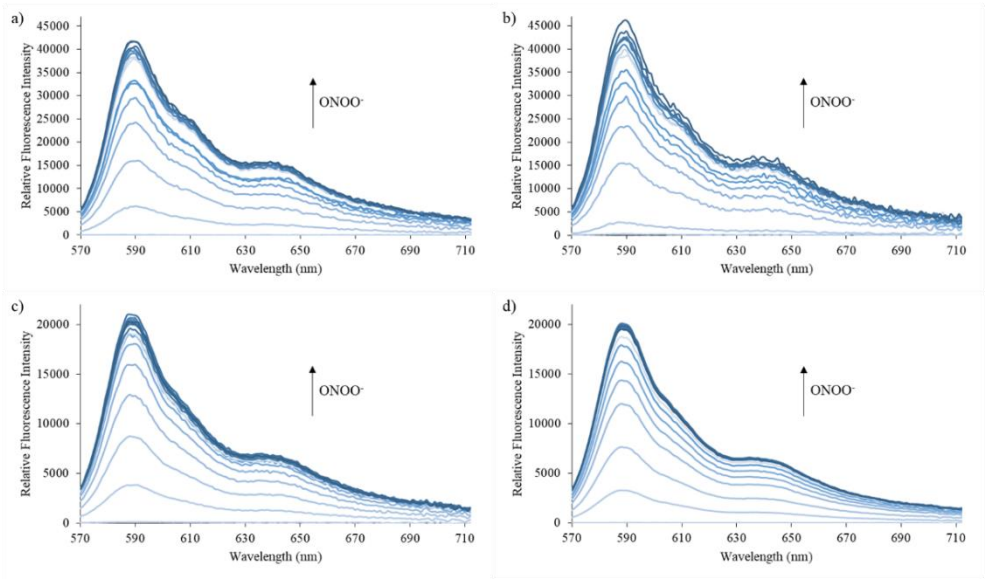

Figure 16: Emission spectra for probes a) **10.1** (500 nM), b) **10.2** (500 nM), c) **10.3** (500 nM) and d) **10.4** (500 nM) in the presence of $ONOO^-$ (1, 2, 3, 4, 5, 6, 7, 8, 9, 10, 20, 30, 40, 50 µM) in PBS buffer 52 % MeOH : H_2O, pH = 8.2 at 25 °C. Fluorescence intensities were measured with λ_{ex} = 550 (bandwith: 15) nm and max λ_{em} = 590 nm on a BMG Labtech CLARIOstar® plate reader.

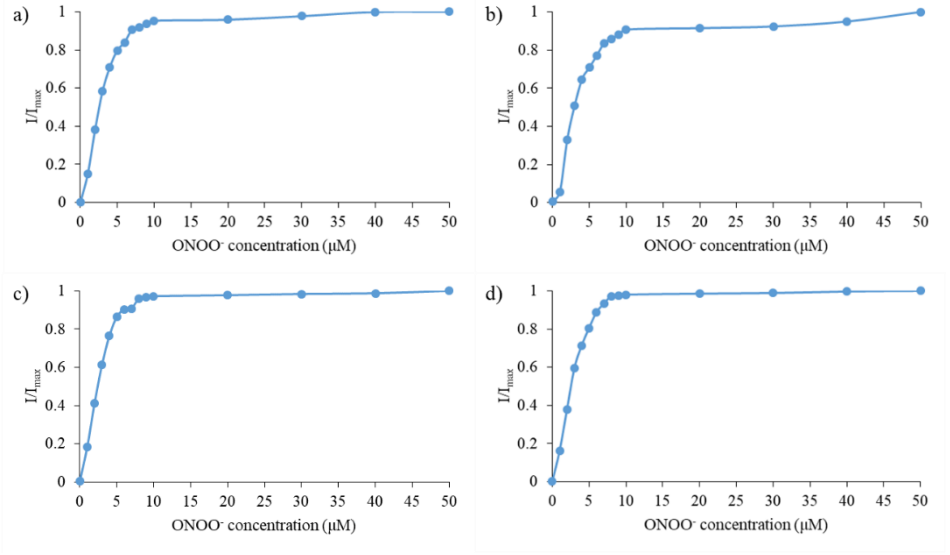

Figure 17: Dose dependence curve (I/I_{max}) for probes a) **10.1** (500 nM), b) **10.2** (500 nM), c) **10.3** (500 nM) and d) **10.4** (500 nM) in the presence of $ONOO^-$ (1, 2, 3, 4, 5, 6, 7, 8, 9, 10, 20, 30, 40,50 µM) in PBS buffer 52 % MeOH : H_2O, pH = 8.2 at 25 °C. Fluorescence intensities were measured with λ_{ex} = 550 (bandwith: 15) nm and max λ_{em} = 590 nm on a BMG Labtech CLARIOstar® plate reader.

3.3. Cell Studies

In collaboration with Xiao-Peng He from ECUST, probes **10.1**, **10.2**, **10.3** and **10.4** were assessed in HeLa and RAW264.7 macrophages.

All four probes were evaluated in terms of their toxicity in murine RAW264.7 macrophages. Using a MTS proliferation assay, probes **10.1**, **10.2**, **10.3** and **10.4** were incubated at different concentrations ranging from 5 to 40 µM for 24 h (Figure 18). Probes **10.1**, **10.3** and **10.4** were shown to be non-toxic. Probe **10.2** decreases the viability of RAW264.7 macrophages by 40 % at a concentration of 40 µM. This limits the usage of probe **10.2** since high concentrations might be required for *in vivo* studies.

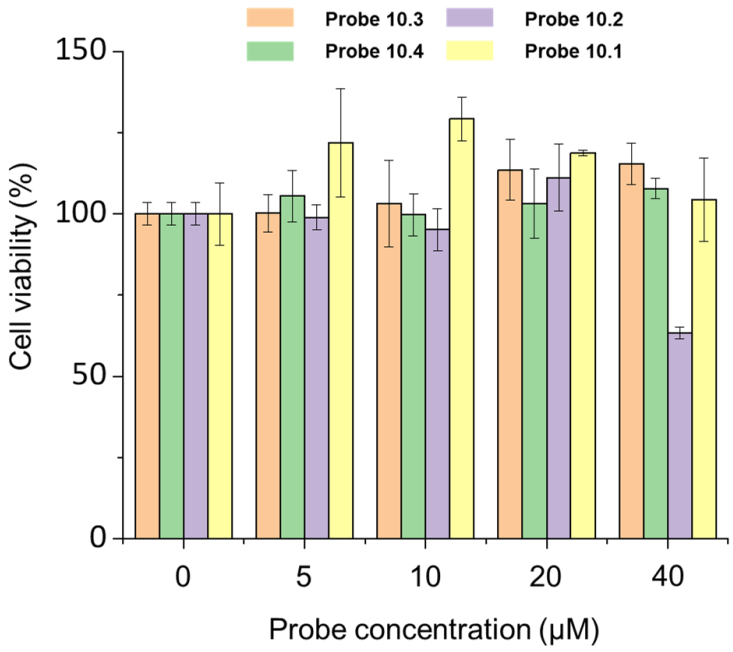

Figure 18: Viability of RAW264.7 macrophages upon incubation of probes **10.1**, **10.2**, **10.3** and **10.4** at different probe concentrations (0, 5, 10, 20, and 40 µM) determined by a MTS proliferation assay. Error bars represent s. d. (n = 3).

Given the slight toxic nature of probe **10.2**, a simple evaluation in RAW264.7 macrophages allowed to show that the probe is cell permeable and can detect

exogenous $ONOO^-$ generated from SIN-1 (Figure 19). At this point, probe **10.2** was not taken for further cell studies but was shown to be cell-permeable.

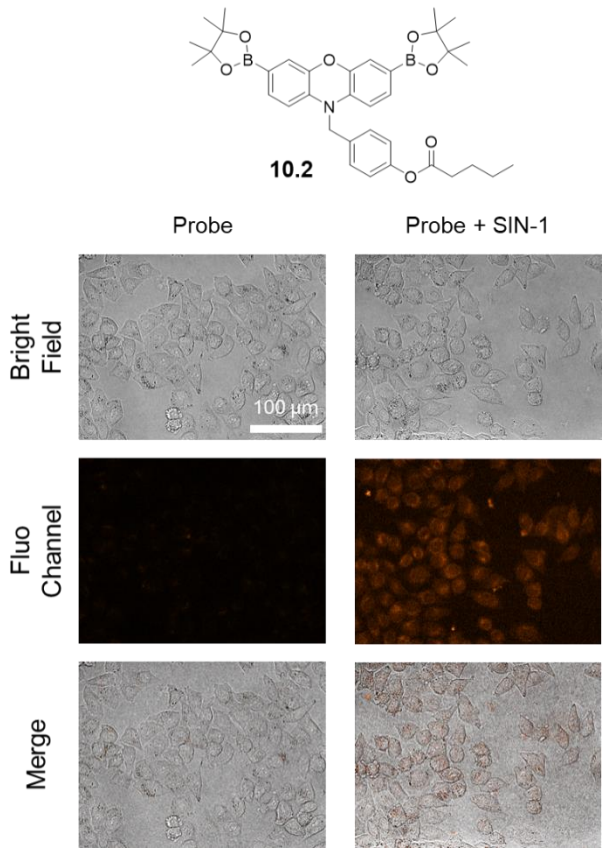

Figure 19: Fluorescence imaging of RAW264.7 macrophages with probe **10.2** (20 µM, 30 min) without or with addition of SIN-1 (500 µM, 30 min) with probe fluorescence collected at λ_{ex} = 520 – 550 nm and λ_{em} = 580 – 650 nm. Scale bar = 100 µm. N = 3. Cell experiments were kindly carried out by Xiao-Peng He's research group.

Since probes **10.1**, **10.3** and **10.4** were shown to be non-toxic in RAW264.7 macrophages, these were evaluated with exogenous $ONOO^-$ (Figure 20). All three probes were cell permeable and increased in fluorescence with the addition of SIN-1. Using uric acid as a scavenger for $O_2^{\cdot-}$ generation, the fluorescent signal detected by all probes was sensitive to uric acid loading demonstrating a requirement of $O_2^{\cdot-}$ anion in the signal detected. Simultaneously, a Hoechst33342 dye was used, which stains the nuclei of the cell and confirms the presence of cells in each experiment. Furthermore, as expected, the fluorescent probes do not localise in the nuclei and

hence, are good tools to detect $ONOO^-$ produced by various organelles located in the cytoplasm.

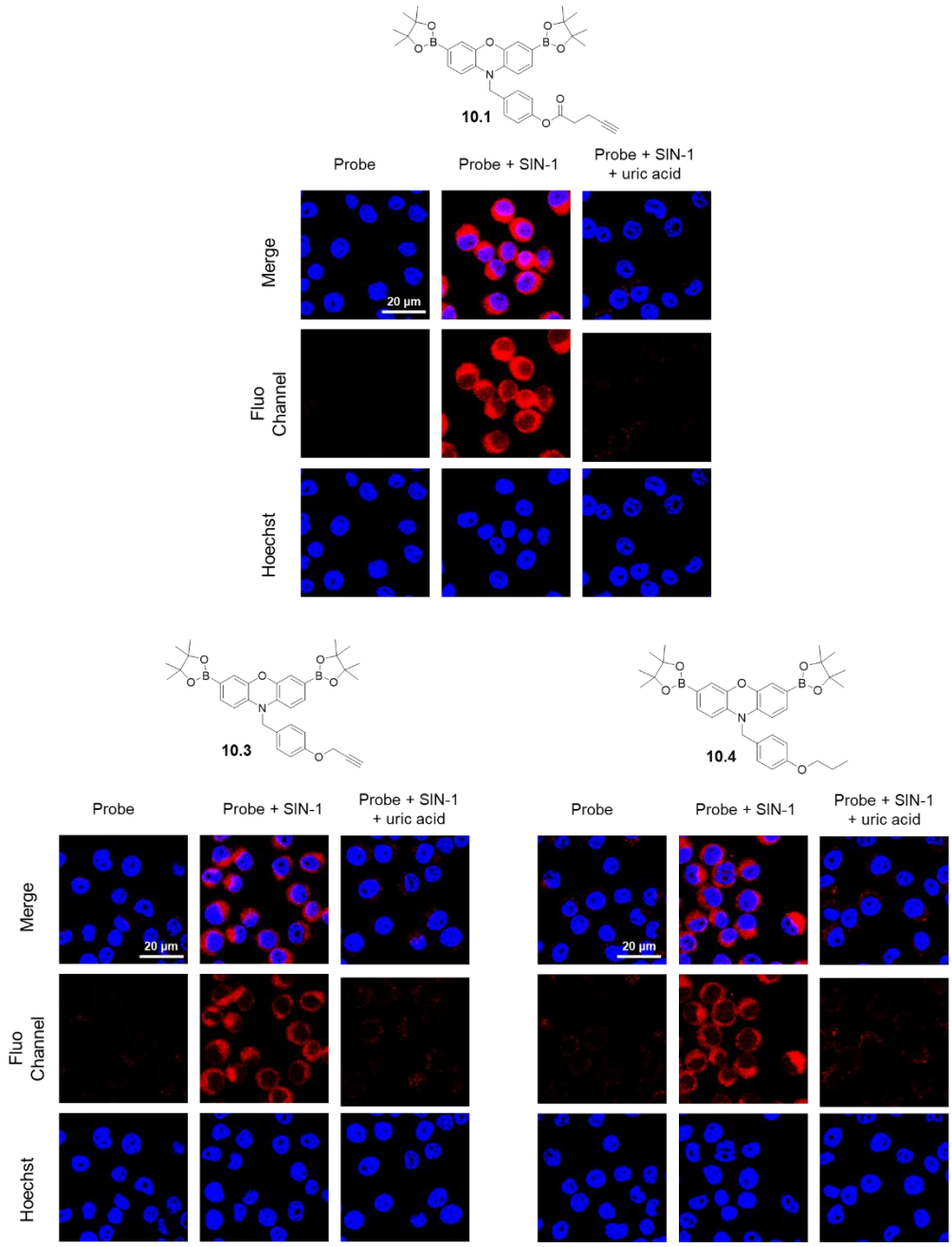

Figure 20: Confocal imaging of RAW264.7 macrophages were loaded with probes **10.1** (20 µM, 30 min), **10.3** (20 µM, 30 min) or **10.4** (20 µM, 30 min) and treated with SIN-1 (500 µM, 30 min) or uric acid (100 µM, 2 h) and SIN-1 (500 µM, 30 min), as indicated. Probe fluorescence was collected at λ_{ex} = 559 nm and λ_{em} = 580 – 650 nm, respectively. The cell nuclei was stained by Hoechst 33342 and fluorescence collected at λ_{ex} = 405 nm and λ_{em} = 470 – 520 nm. Scale bar = 20 µm. N = 3. Cell experiments were kindly carried out by Xiao-Peng He's research group.

Probes **10.1**, **10.3** and **10.4** were also evaluated in HeLa cells with exogenous $ONOO^-$ generation (Figure 21). The cervical cancer cell line is a useful model system to evaluate fluorescent probes as it allows to simulate a scenario of high amounts of ROS present to kill a harmful pathogen. This means that the immune system will be under oxidative stress and generating vast amounts of ROS in order to fight and kill the cancer cells.[102] Hence, exogenous ROS generation allows to simulate this scenario with the fluorescent probes. All three probes showed good fluorescent responses upon stimulation with SIN-1 of HeLa cells. Uric acid attenuated the SIN-1 mediated fluorescent signal of probes **10.1**, **10.3**, and **10.4** confirming the detection of $ONOO^-$ in HeLa cells. The probes showed a very low level of localisation in the nuclei as confirmed by the usage of the Hoechst staining probe.

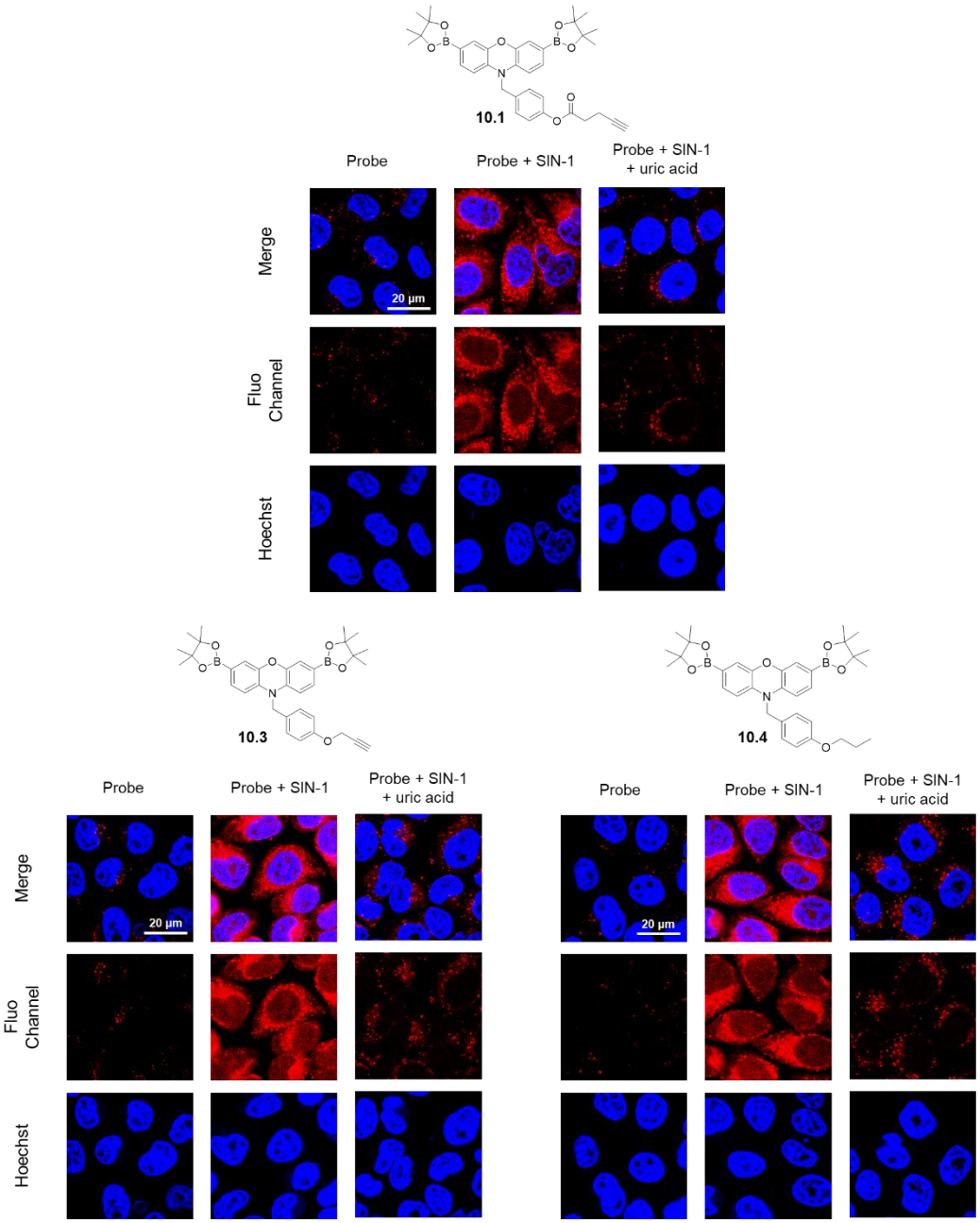

Figure 21: Confocal imaging of HeLa cells loaded with probes **10.1** (20 μM, 30 min), **10.3** (20 μM, 30 min) or **10.4** (20 μM, 30 min) then treated with SIN-1 (500 μM, 30 min) or uric acid (100 μM, 2 h) and SIN-1 (500 μM, 30 min), as indicated. Probe fluorescence was collected at λ_{ex} = 559 nm and λ_{em} = 580 – 650 nm, respectively. The cell nuclei was stained by Hoechst33342 and fluorescence collected at λ_{ex} = 405 nm and λ_{em} = 470 – 520 nm. Scale bar = 20 μm. N = 3. Cell experiments were kindly carried out by Xiao-Peng He's research group.

Having confirmed the ability of probes **10.1**, **10.3**, and **10.4** to detect exogenous $ONOO^-$, these were evaluated in RAW264.7 macrophages for endogenous $ONOO^-$ generation. Endogenous $ONOO^-$ production allows to simulate in a more accurate way how the immune system would behave towards a pathogen. Exogenous $ONOO^-$ can give insights into permeability and how the probe will eventually behave in a real system. Exposing the cells under oxidative stress to increase their $ONOO^-$ production gives more accurate insights into the ability of the probes to detect physiological and pathophysiological responses. Probes **10.1**, **10.3**, and **10.4** successfully detected endogenously produced $ONOO^-$ in RAW264.7 macrophages (Figure 22). The cells were stimulated with LPS for 24 h which enhances indirectly $O_2^{\cdot -}$ production, a key precursor of $ONOO^-$. The localisation of the probes showed little penetration into the nuclei as confirmed by using a Hoechst staining probe. ROS species can be generated by the mitochondria but also other organelles such as lysosomes. Future cell studies would need to focus on determining the specific localisation of the probes. This can be easily achieved by using relevant commercial organelle specific staining probes e.g. MitoTracker for the mitochondria, LysoTracker for the lysosome, and EndoTracker for the endoplasmic reticulum.

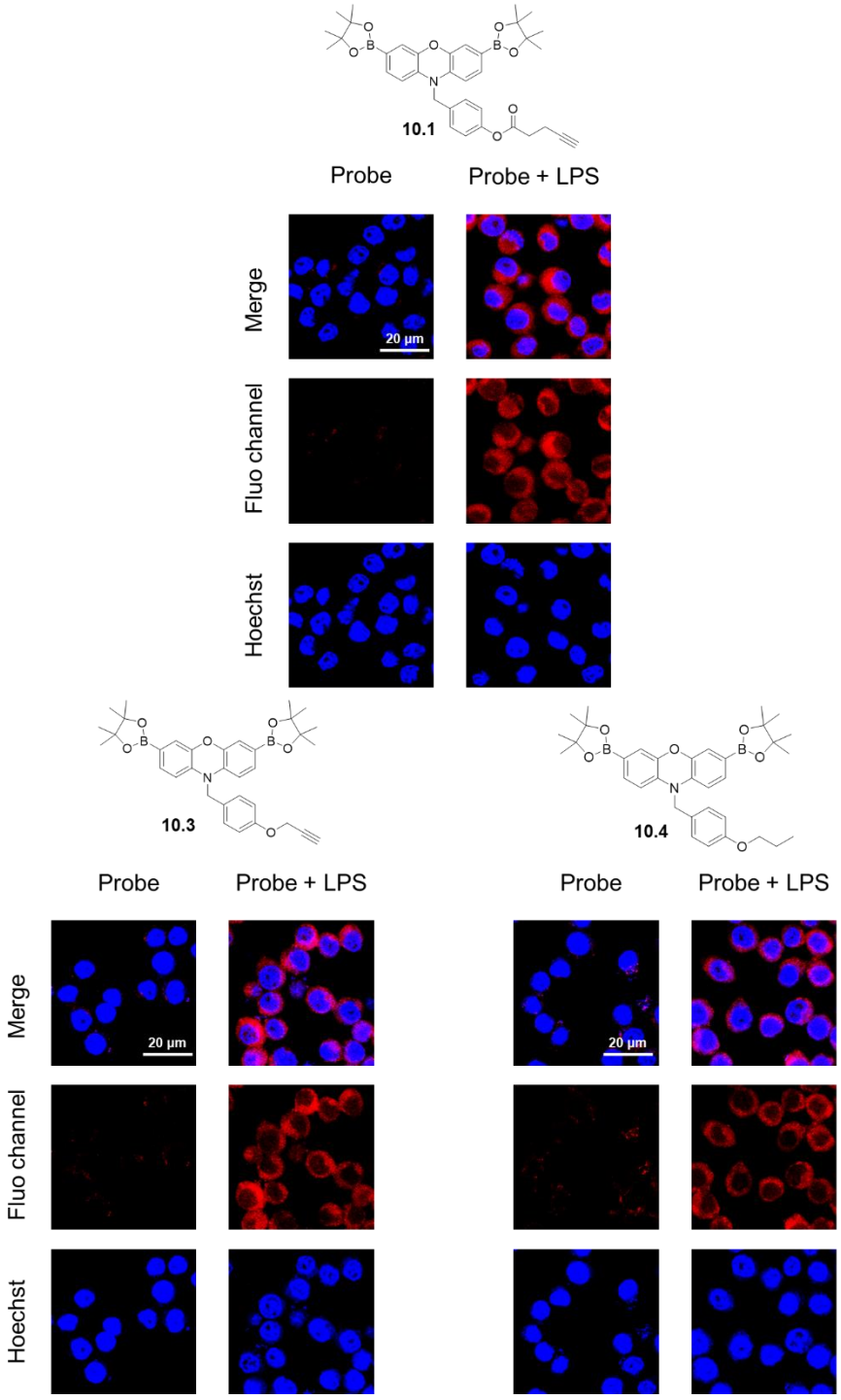

Figure 22: Confocal imaging of RAW264.7 macrophages primed with LPS (1 µg/ml, 24 h) and then loaded with probe **10.1** (20 µM, 30 min), **10.3** (20 µM, 30 min) or **10.4** (20 µM, 30 min) as indicated. Probe fluorescence was collected at λ_{ex} = 559 nm and λ_{em} = 580 – 650 nm, respectively. The cell nuclei was stained by Hoechst33342 and fluorescence collected at λ_{ex} = 405 nm and λ_{em} = 470 – 520 nm. Scale bar = 20 µm. N = 3. Cell experiments were kindly carried out by Xiao-Peng He's research group.

Additionally, probe **10.1** was evaluated in A549 cells, a cancerous lung tissue cell line (Figure 23). The probe was able to detect exogenous $ONOO^-$. Using various cell lines while simulating oxidative stress scenarios allows to validate the versatility of the probes. In the future, it would be also useful to assess the other probes of this series to validate them as useful $ONOO^-$ tools in a variety of cell lines.

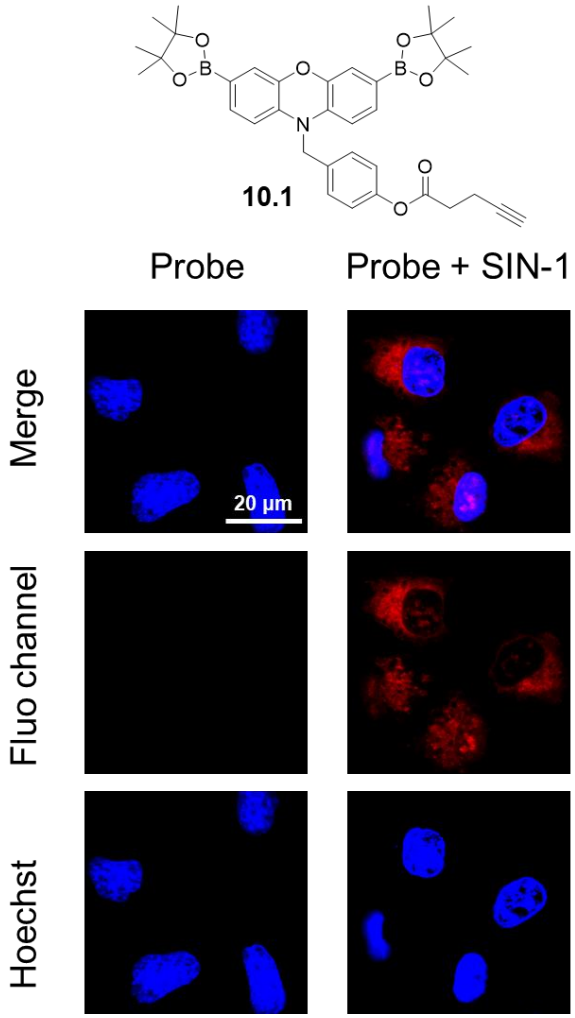

Figure 23: Confocal imaging of A549 cells were loaded with probe **10.1** (20 µM, 30 min) without and with SIN-1 (500 µM, 30 min) as indicated. Probe fluorescence was collected at λ_{ex} = 559 nm and λ_{em} = 580 – 650 nm, respectively. The cell nuclei was stained by Hoechst33342 and fluorescence collected at λ_{ex} = 405 nm and λ_{em} = 470 – 520 nm. Scale bar = 20 µm. N = 3. Cell experiments were kindly carried out by Xiao-Peng He's research group.

Overall, all four probes **10.1**, **10.2**, **10.3** and **10.4** were validated as cell permeable $ONOO^-$ detection tools. Some showed more promise than others in terms of their toxicity profile but overall all had the same applicability to detect exogenous and endogenous $ONOO^-$ in a range of cell lines.

3.4. *In vivo* Studies

Since probes **10.1**, **10.2**, **10.3** and **10.4** showed good cell permeability and were able to detect exogenous and endogenous $ONOO^-$, probe **10.1** was evaluated *in vivo* in collaboration with Jingya Li from the Chinese Academy of Sciences, China. A LPS-induced acute inflammation mouse model C57BL/6J[103] was used to evaluate **10.1**'s ability to detect endogenous $ONOO^-$ (Figure 24). As expected, the probe by itself shows no fluorescence even after subcutaneous injection with saline as a control group. Control experiments with saline and LPS alone were conducted to rule out any autofluorescence. Upon treatement of the mice with LPS, the probe was activated in the abdomindal region of the mice. A peak emission of 2.8×10^7 p s^{-1} cm^{-2} sr^{-1} was observed compared to negligible peak emission in saline treated mice (n = 3) (Figure 24). These observations were quantified in Figure 25. The quantified fluorescence intensity in the probe (+) / LPS (+) group was significantly larger than that in the probe (+) / LPS (-) group, suggesting the potential of the probe to be used in monitoring $ONOO^-$ *in situ* during acute inflammation.

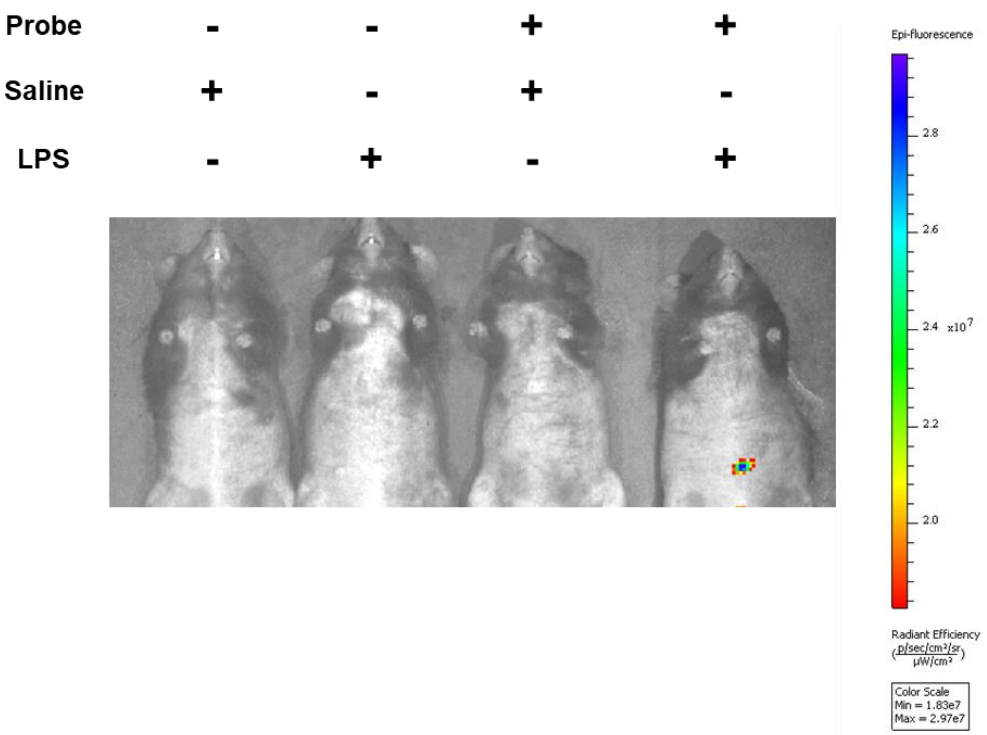

Figure 24: Intraperitoneal injection of male C57BL/6J mice with probe **10.1** (200 μM) or saline in the absence and presence of LPS (2 mg/ml in saline) with λ_{ex} = 535 nm and λ_{em} = 600 nm. N = 3. Mice experiments were kindly carried out by Jingya Li's research group.

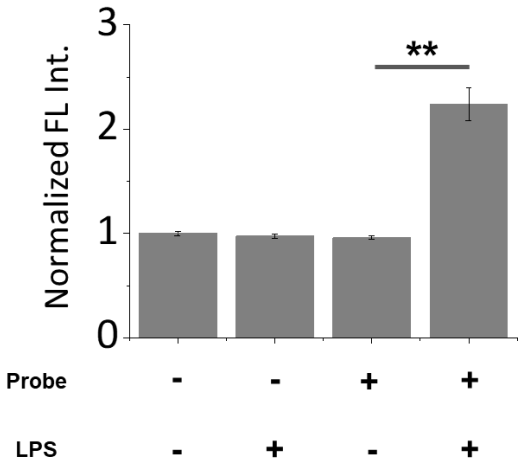

Figure 25: Quantification of Figure 24 – C57BL/6J male mice treated with probe **10.1** (200 μM) or saline in the absence and presence of LPS (2 mg/ml in saline) with λ_{ex} = 535 nm and λ_{em} = 600 nm. Error bars represent s. d. with **p ≤ 0.01. N = 3.

4. Moving towards Theranostic Systems

With these encouraging *in vitro* and *in vivo* results outlined in Section 3.3 and 3.4, I decided to explore the possibility of designing theranostic systems. A theranostics combines the terms therapy and diagnosis and aims to incorporate these two units into one system. One of the pioneers in this field is Jong Seung Kim who has published numerous examples in the literature of which two of his theranostic systems will be birefly reviewed. This should guide the design of my theranostic resorufin probes.

Kim and co-workers designed a H_2O_2 coumarin specific probe **13.1** incorporating the anticancer drug SN-38 (Scheme 13).[104] The coumarin unit was masked with a boronic ester as the sensing unit for H_2O_2, which would then allow to access the drug via cleavage at the carbonate group. The theranostic probe **13.1** was evaluated in HeLa cells with exogenous H_2O_2 and co-localisation studies showed that the probe mainly localises in lysosomes. The release of the drug was also studied in HeLa cells and showed similar activity to the drug alone. *In vivo* studies with mice induced with lung metastasis confirmed the applicability of probe **13.1** in a living system.

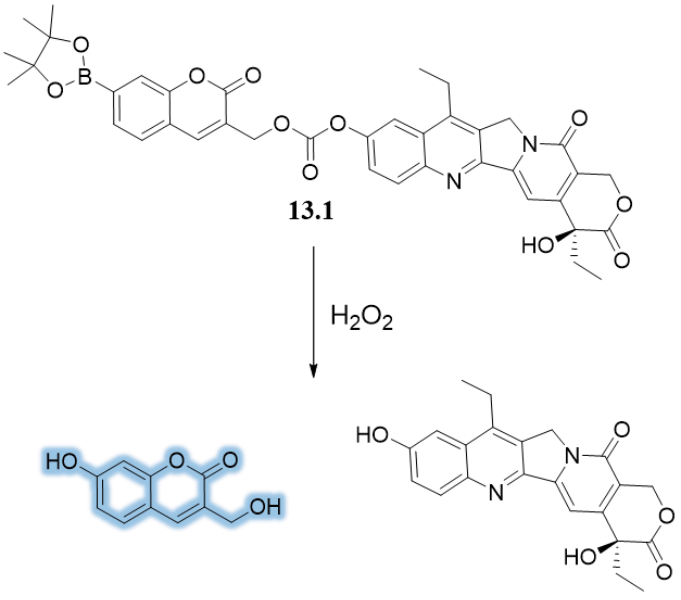

Scheme 13: Theranostic probe **13.1** gives upon reaction with H_2O_2 fluorescent coumarin and anticancer drug SN-38.

Following the development of this system, a closely releated theranostic probe **14.1** was prepared using rhodol as a fluorophore, the anticancer drug SN-38 and biotin as a targeting unit to direct the theranostic towards cancer cells (Scheme 14).[105] *In vitro* studies with HeLa, A549, and NIH3T3 cells were carried out in conjunction with the drug release profile. *In vivo* studies with HeLa tumour-bearing mice were carried out including comparison of tumours when untreated and treated with the theranostic. The drug is released *in vivo* and results in an observed reduction in size of the tumour.

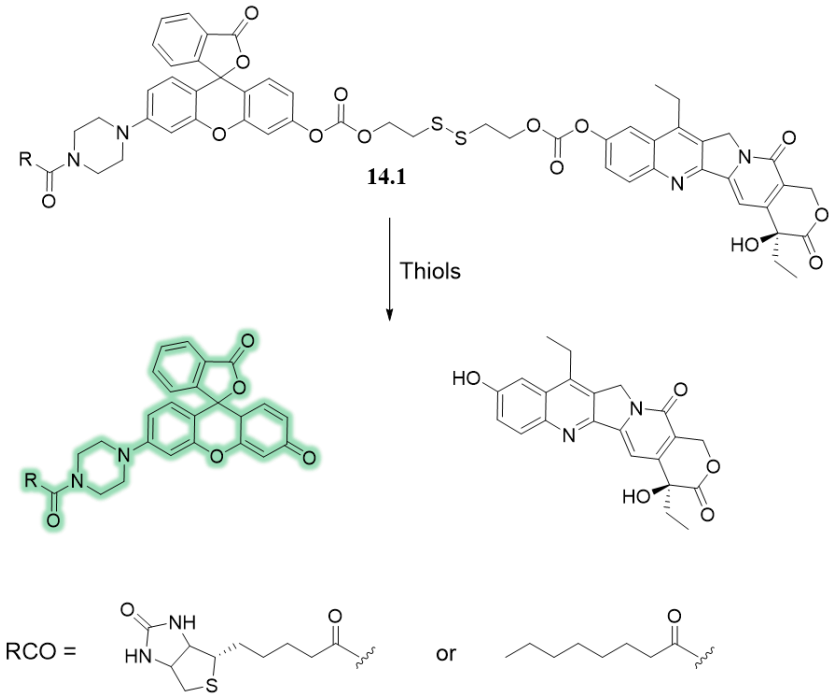

Scheme 14: Theranostic probe **14.1** relasing the active fluorophore, and anticancer drug SN-38 upon reaction with thiols.

These two examples using two different fluorophore systems incorporating anticancer drug SN-38 allowed us to rationalise the development of resorufin based theranostic systems.

4.1. Synthesis of Theranostic Resorufin Based Systems

Our aim was to synthesise two theranostic probes incorporating different drug motifs: chlorambucil and indomethacin (Figure 26). Chlorambucil is mainly used for chronic lympothatic leukemia and indomethacin as a non-steroidal anti-inflammatory drug. Both conditions, the drugs are respectively used for, are largely associated with oxidative stress and hence, an increased release of ROS species.

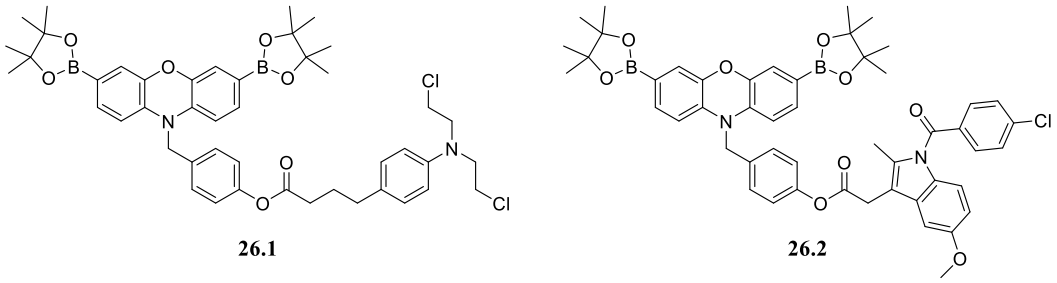

Figure 26: Theranostic probes **26.1** and **26.2**.

Both **26.1** and **26.2** were easily accessible from **5.8** through coupling of the alcohol with the carboxylic acid **16.1**/**16.2** to create the corresponding ester (Scheme 15). **26.1** and **26.2** were achieved in low yields – 20 % and 28 % respectively.

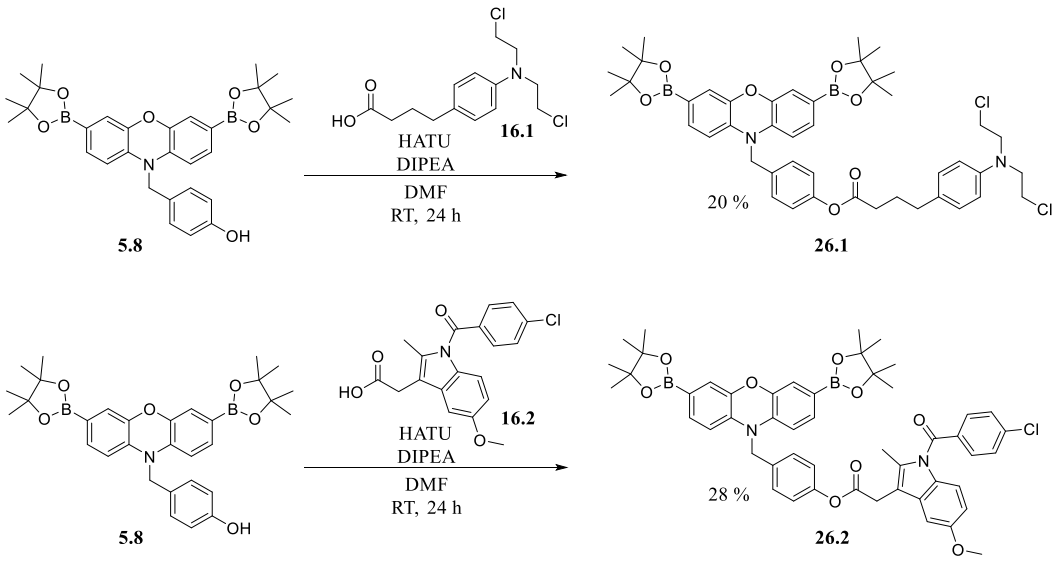

Scheme 15: Synthesis of theranostic probes **26.1** and **26.2**.

26.1 and **26.2** were evaluated with mass spectrometry (MS) to assure the release of resorufin and more importantly the drug fragment (chlorambucil and indomethacin respectively) upon reaction of the probes with $ONOO^-$. As expected, both **26.1** and **26.2** were able to release the fluorophore and the drug, hence, validating the theranostic ability of **26.1** and **26.2** (Figure 27 – 28).

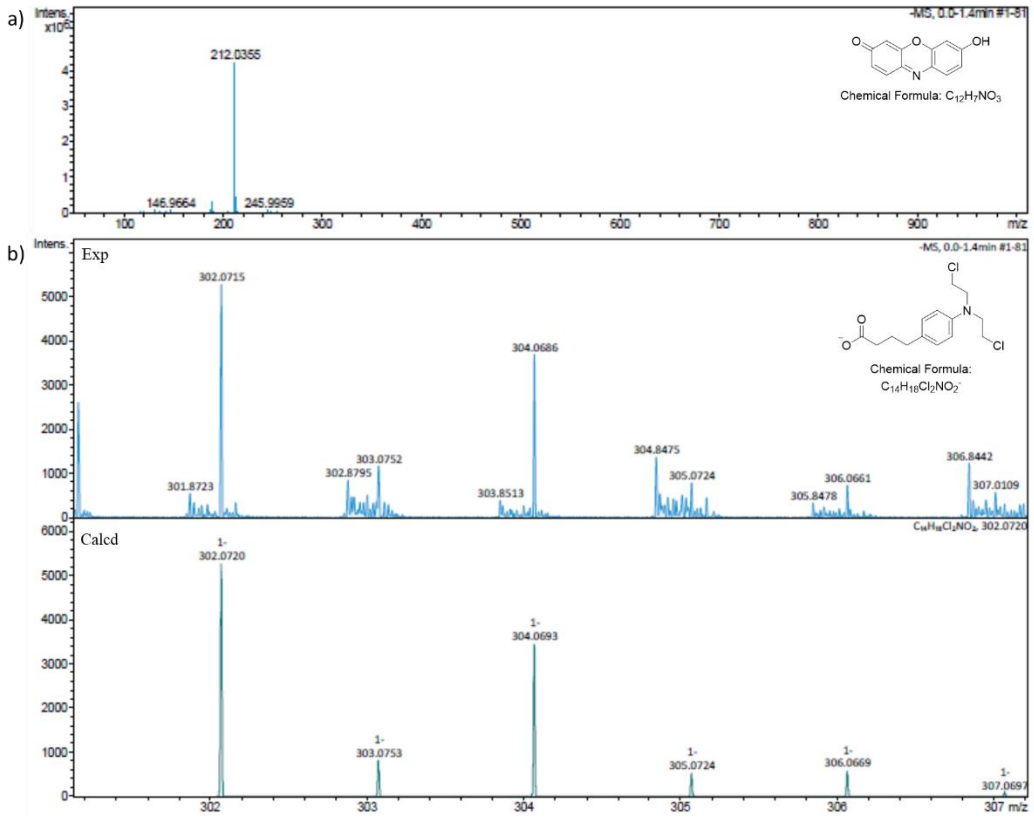

Figure 27: MS data revealed that probe **26.1** upon reaction with $ONOO^-$ releases (a) resorufin and (b) chlorambucil.

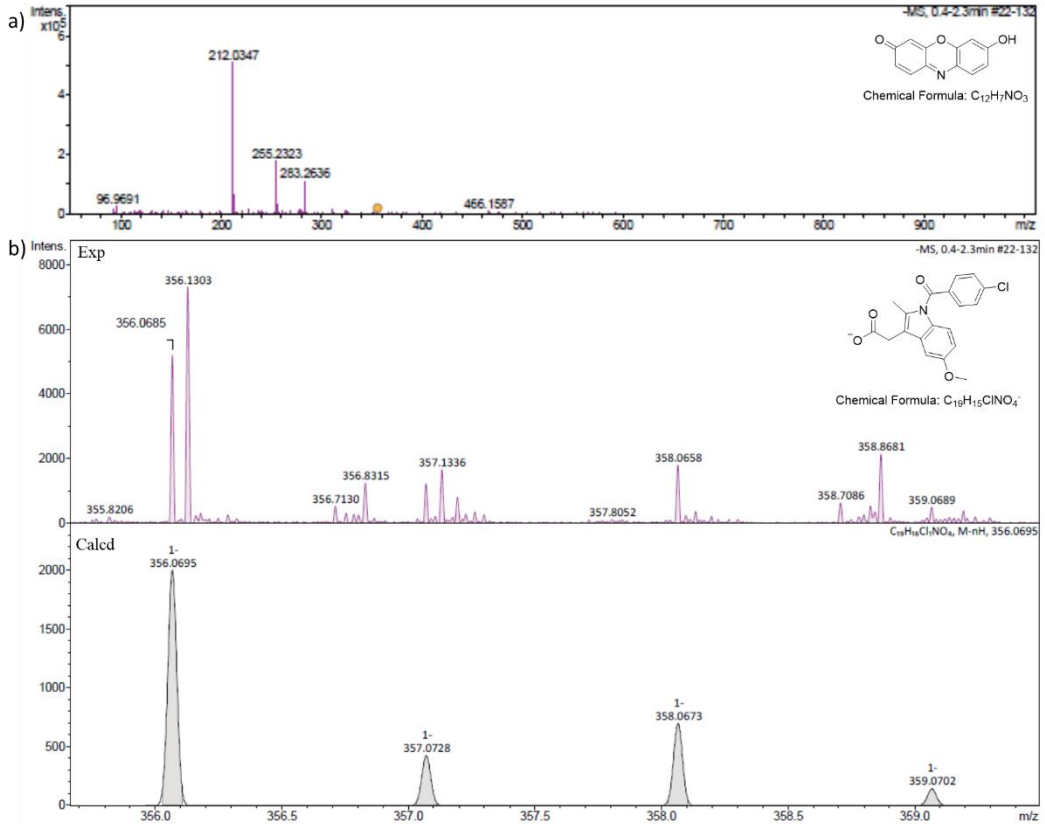

Figure 28: MS data revealed that probe **26.2** upon reaction with $ONOO^-$ releases (a) resorufin and (b) indomethacin.

4.2. Fluorescence Studies

Theranostic probes **26.1** and **26.2** were initially evaluated with UV to confirm the formation of resorufin (Figure 29). Upon reaction with $ONOO^-$, both **26.1** and **26.2** show a maximum absorption close to 573 nm which is consistent with the release of resorufin.

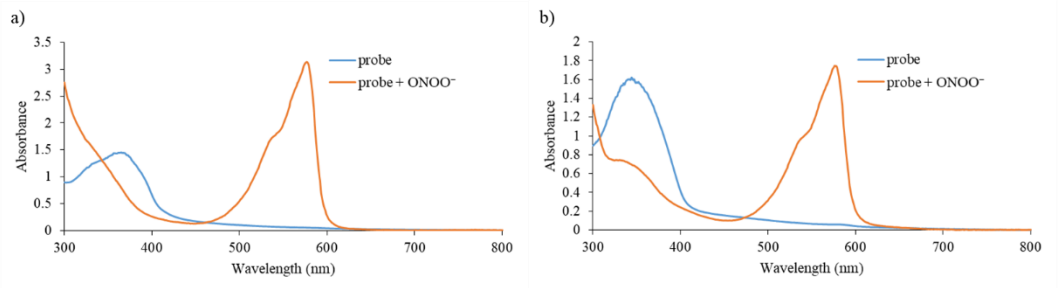

Figure 29: UV spectra of a) probe **26.1** and b) probe **26.2** with and without $ONOO^-$ (excess) in PBS buffer 52 % MeOH : H_2O, pH = 8.2 at 25 °C measured on a BMG Labtech CLARIOstar® plate reader.

The standard fluorescence studies were carried out including ROS selectivity studies (Figure 30), H_2O_2 fluorescence intensity changes over time and titration studies (Figure 31 – 32) and $ONOO^-$ titration studies (Figure 33). This allowed on the one hand to establish LoDs – for H_2O_2: 17 µM for probe **26.1** and 6 µM for probe **26.2**; for $ONOO^-$: 5 nM for both probes **26.1** and **26.2** – and on the other hand confirm sensitivity and selectivity towards $ONOO^-$.

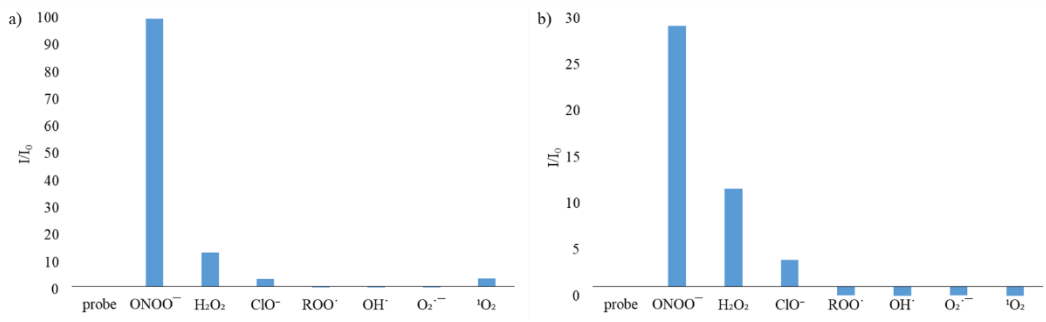

Figure 30: Selectivity data for a) probe **26.1** (500 nM) and b) probe **26.2** (500 nM) in the presence of $ONOO^-$ (50 µM), $OH\cdot$ (500 µM), $O_2^{\cdot-}$ (500 µM), $^1O_2$ (500 µM) after 5 min. H_2O_2 (1 mM), $ROO\cdot$ (500 µM) and ClO^- (500 µM) were measured after 30 min. The data was obtained in PBS buffer 52 % MeOH : H_2O, pH = 8.2 at 25 °C at λ_{ex} = 550 (bandwith: 15) nm and max λ_{em} = 590 nm on a BMG Labtech CLARIOstar® plate reader.

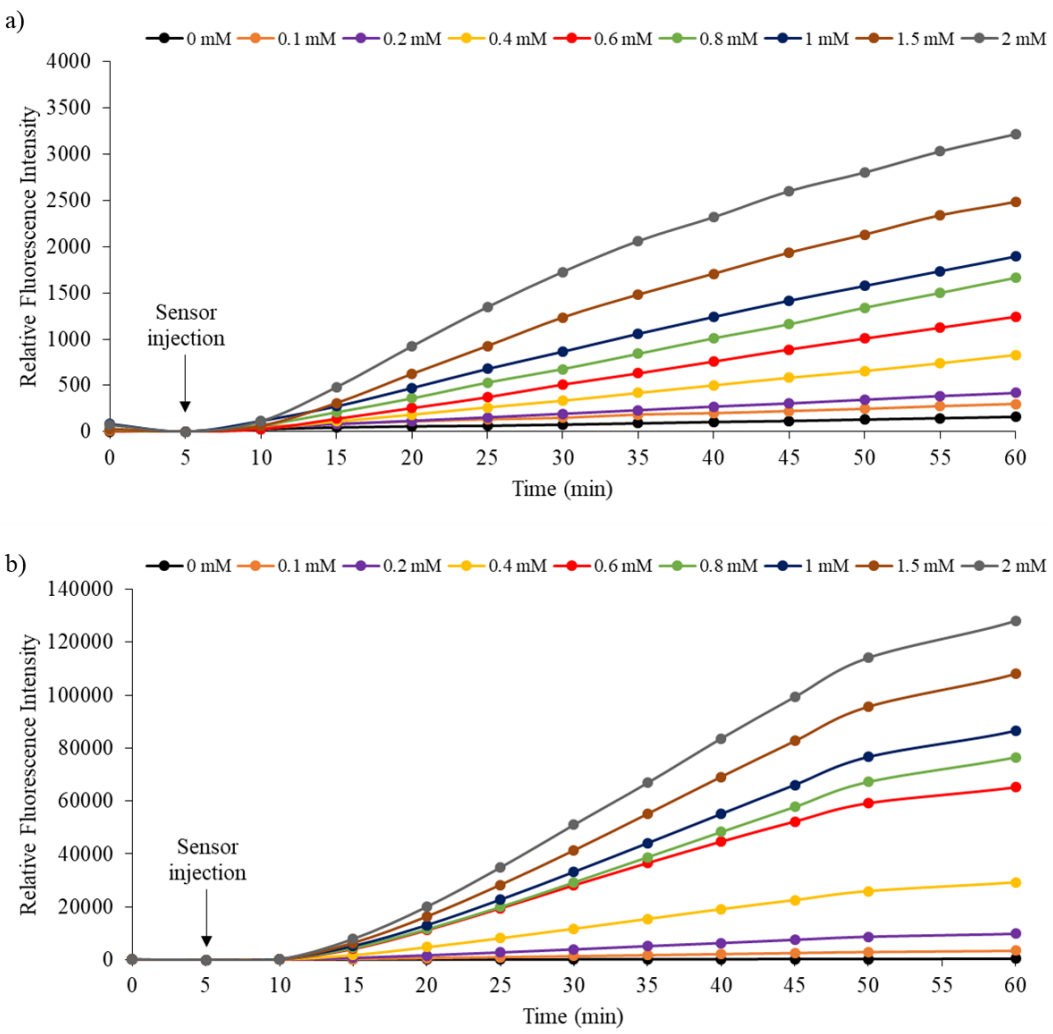

Figure 31: Fluorescence intensity changes over time for a) probe **26.1** (500 nM) and b) probe **26.2** (500 nM) in the presence of H_2O_2 (0.1, 0.2, 0.4, 0.6, 0.8, 1, 1.5, 2 mM) in PBS buffer 52 % MeOH : H_2O, pH = 8.2 at 25 °C. Fluorescence intensities were measured with λ_{ex} = 550 (bandwith: 15) nm and max λ_{em} = 590 nm on a BMG Labtech CLARIOstar® plate reader.

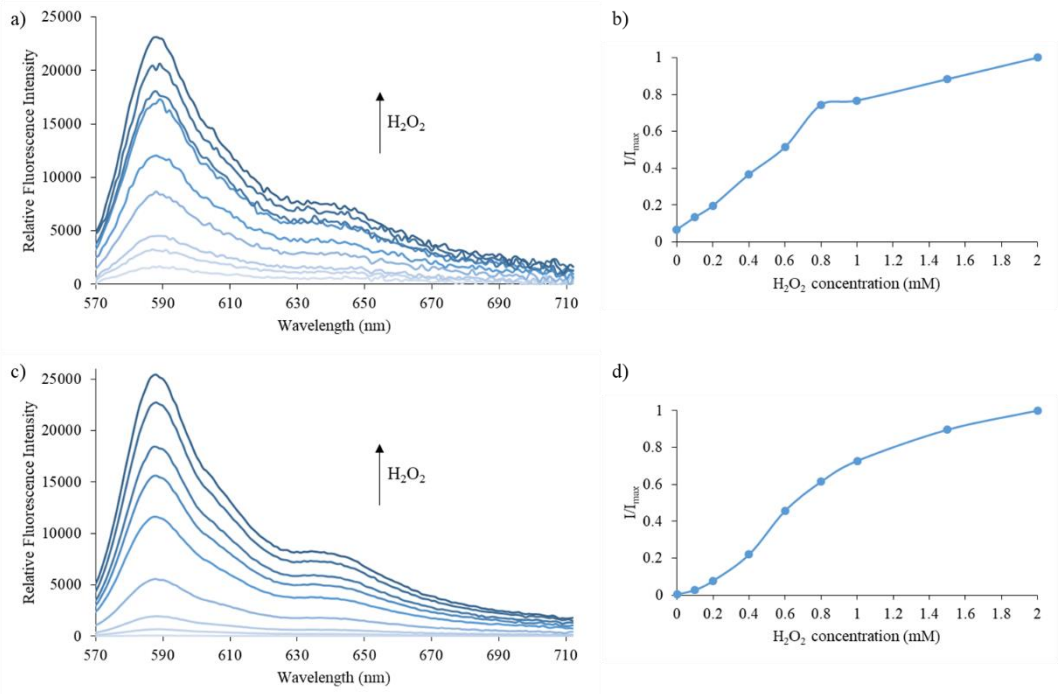

Figure 32: Emission spectra and dose dependence curve (I/I_{max}) for a) & b) probe **26.1** (500 nM) and c) & d) probe **26.2** (500 nM) in the presence of H_2O_2 (0.1, 0.2, 0.4, 0.6, 0.8, 1, 1.5, 2 mM) after 1 h in PBS buffer 52 % MeOH : H_2O, pH = 8.2 at 25 °C. Fluorescence intensities were measured with λ_{ex} = 550 (bandwith: 15) nm and max λ_{em} = 590 nm on a BMG Labtech CLARIOstar® plate reader.

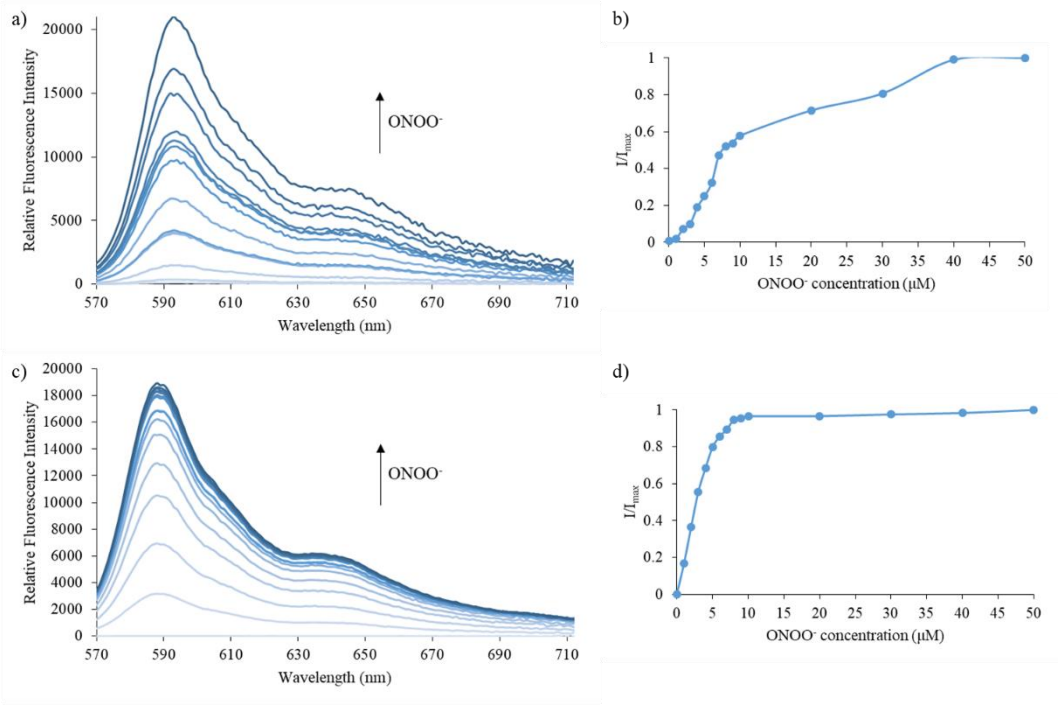

Figure 33: Emission spectra and dose dependence curve (I/I_{max}) for a) & b) probe **26.1** (500 nM) and c) & d) probe **26.2** (500 nM) in the presence of $ONOO^-$ (1, 2, 3, 4, 5, 6, 7, 8, 9, 10, 20, 30, 40, 50 μM) in PBS buffer 52 % MeOH : H_2O, pH = 8.2 at 25 °C. Fluorescence intensities were measured with λ_{ex} = 550 (bandwith: 15) nm and max λ_{em} = 590 nm on a BMG Labtech CLARIOstar® plate reader.

4.3. Cell Studies

Cell studies are currently being carried out by our collaborator Xiao-Peng He at ECUST in Shanghai, China.

5. Conclusions

I have successfully expanded the scope of **PR1** based probes. In particular, the introduction of alkyne and alkane groups allowed us to overcome the initial cell permeability issues. All probes evaluated displayed excellent selectivity and sensitivity for $ONOO^-$ in solution. This was confirmed *in vitro* with the detection of

exogenous and endogenous $ONOO^-$ in RAW264.7 macrophages. Probe **10.1** was also evaluated *in vivo* confirming the applicability of the probe to detect the induced inflammatory state of the mouse. Following these positive results, two theranostic probes that would be able to detect $ONOO^-$ and release an inflammatory related disease drug were developed. The resorufin analogue series developed as part of this PhD constitutes a new class of resorufin functionalised probes for $ONOO^-$ detection. The unique tunability of the scaffold has opened up new red fluorescent probes, which are underexploited as demonstrated in the introduction of this chapter.

6. Future Work

The alkyne functionalised probes **10.1** and **10.3** allow for the exploration of *in situ* click chemistry. Test reactions have been carried out confirming the feasibility of click chemistry for these probes: a mitochondrial targeting group to achieve **34.1** and **34.2** was introduced (Figure 34). This can be expanded with the introduction of other organelle targeting groups (for lysosome or endoplasmic reticulum) or drug molecules (e.g. chlorambucil) for the treatment of oxidative stress related diseases such as cancer.

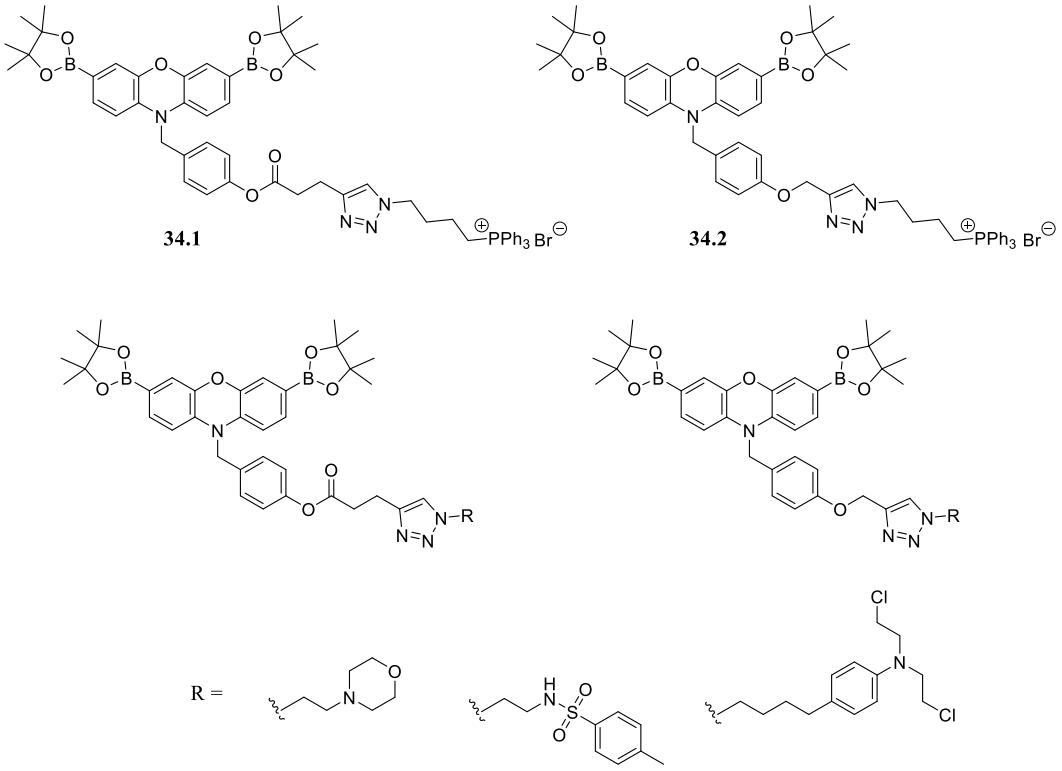

Figure 34: Proposed $ONOO^-$ probes for diagnostic and/or therapeutic applications.

Additionally, the evaluation of all developed probes *in vivo* would help determine which structural motifs are the most biocompatible. Consequently, this raises the question whether the C57BL/6J mouse model is the most applicable one. A large number of commonly used mouse models for inflammation and arthritis has been reviewed by Webb outlining advantages and disadvantages of each.[106] This could be taken into consideration for probe evaluation if a particular animal model is more suited than the C57BL/6J mouse model. The intraperitoneal injection of LPS into C57BL/6J mice does not necessarily accurately simulate endogenous $ONOO^-$ production. The next step would be to initiate the translation of the *in vivo* studies to clinical studies to enhance current efforts in fluorescence guided surgery. In a first instance, it would be beneficial to evaluate the probes in human macrophages which should allow for comparison to the murine equivalent cell line. Additionally, further mice experiments could focus on tumour containing mice where the inherent immune system should produce large amounts of $ONOO^-$, detectable by the probes. A continuous evaluation of the fluorescent response over a longer time period would be beneficial in understanding the kinetics of the probes *in vivo*.

Chapter 3 – Targeting Different Organelles Using Coumarin-Based Fluorescent Probes

1. Introduction

Coumarins are widely employed in a variety of applications, notably as fluorescent tools for the detection of biologically relevant analytes, with coumarin scaffolds having been used as fluorescent tools for the selective and sensitive detection of ROS.[107] Coumarin fluorophores exhibit good photostability, large Stokes shift and high quantum yields, and so, a brief review of coumarin fluorescent probes that have been developed for ROS detection are now described.

Lo and Chu developed a selective and sensitive H_2O_2 probe in 2003 that combined a coumarin unit and a benzyl Bpin based sensing group (Scheme 1).[108] The coumarin unit reacts with H_2O_2 to afford fluorescent 7-amino-4-methylcoumarin. This probe works through H_2O_2 mediated oxidative cleavage of its arylboronate group to afford an unstable phenol that decomposes via elimination of a quinomethane unit and CO_2 (from the carbamate group) to afford the 7-amino-4-methylcoumarin fluorophore. This probe is quite a simplistic example since no ROS selectivity test was carried out to determine the selectivity of the probe towards H_2O_2 and it is likely that the boronic ester would show greater reactivity towards $ONOO^-$. Nevertheless, this probe illustrates effectively the tunability of boronic acid containing coumarins to act as efficient fluorescent reporters for the detection of ROS.

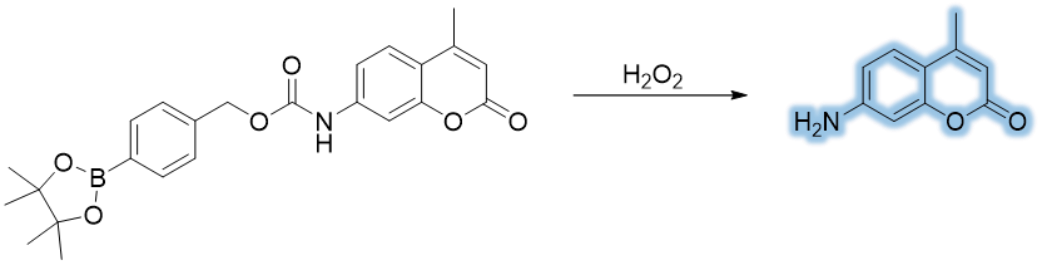

Scheme 1: H_2O_2 selective probe containing a 7-amino-4-methylcoumarin fluorophore.

Kim *et al.* then reported a boronic ester reaction based probe containing an iminocoumarin unit (Scheme 2),[109] which undergoes oxidative cleavage of its arylboronate group when exposed to $ONOO^-$. This results in formation of an unstable phenol intermediate that eliminates a quinomethane unit to generate a new phenolate unit that undergoes rapid cyclisation to generate a fluorescent aminocoumarin. The probe was able to detect endogenously produced $ONOO^-$ in J774A.1 macrophages as well as detect changes in $ONOO^-$ production when ROS scavengers were introduced, although no *in vivo* studies were carried out.

Yu *et al.* and Yang *et al* developed ROS selective fluorescent probes containing an iminocoumarin scaffold for $ONOO^-$ and ClO^- detection respectively (Scheme 2),[46, 110] which exhibited better fluorescent properties because iminocoumarins emit at longer wavelengths when compared to simple coumarin scaffolds. Yu's probe incorporated a pyridinium moiety to increase water solubility which could potentially also function as a targeting unit for the mitochondria (not demonstrated).

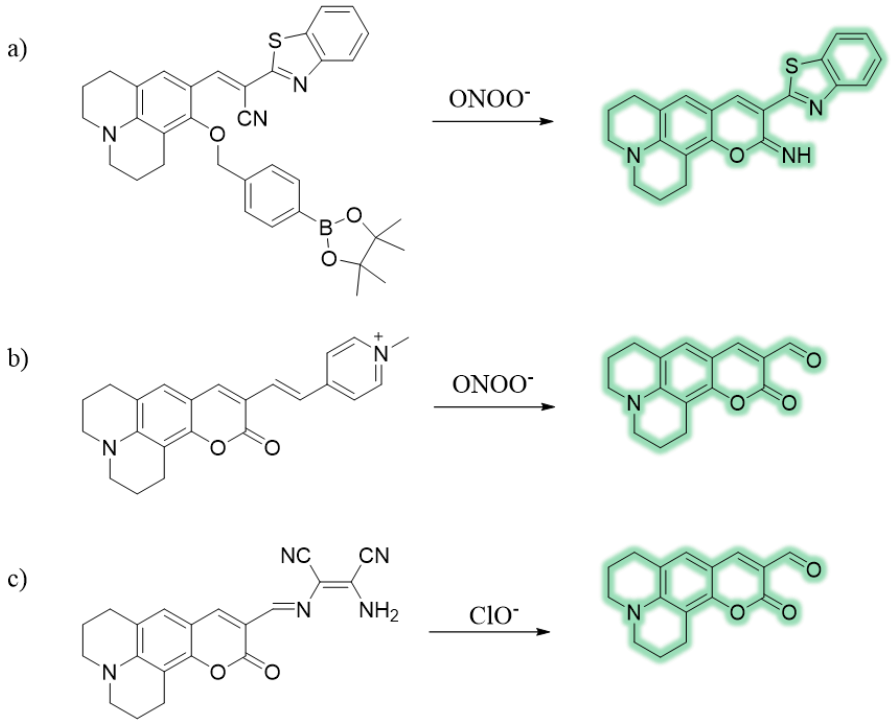

Scheme 2: Iminocoumarin scaffolds containing reactive targeting groups for ROS based on: a) $ONOO^-$ mediated cleavage of a benzyl Bpin group (Kim *et al.*); b) $ONOO^-$ mediated cleavage of the conjugated alkene of a pyridinium unit (Yu *et al.*); c) ClO^- mediated cleavage of a diaminomaleonitrile group (ICT probe by Yang *et al.*).

Imato and co-workers were interested in designing probes to detect ROS in specific parts of the cell and so designed a coumarin probe which could effectively detect hydroxyl radicals in lipid membranes.[111] The design of this probe is based on an off-on strategy. The probe reacts with hydroxyl radicals to produce a highly fluorescent 7-hydroxy-coumarin unit (Scheme 3). Incorporation of a phospholipid moiety assured preferential localisation in the lipid membrane when the probe was evaluated in RAW264.7 macrophages.

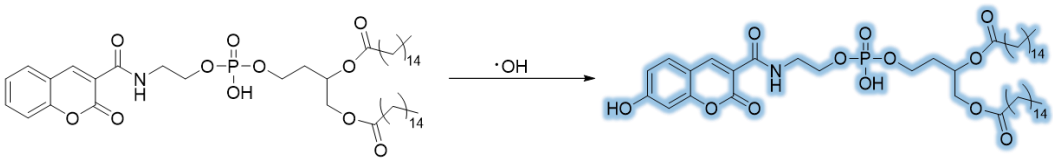

Scheme 3: A coumarin based probe for hydroxyl radicals that is preferentially localised in lipid membranes in cells.

Coumarins have increasingly been used for the development of ratiometric probes, which have the potential to closely monitor intracellular ROS concentrations as a function of time (Scheme 4).[112, 113] Yoon and co-workers developed a coumarin-hemicyanine system to detect $ONOO^-$,[112] that exhibits a red emission in the absence of any analyte due to the presence of its extended conjugation system that results in an intramolecular charge transfer process. Oxidation of the probe by $ONOO^-$ results in cleavage of the alkene bond which in turn results in the formation of a coumarin unit that exhibits green emission. Stimulation of RAW264.7 macrophages with $ONOO^-$ resulted in this coumarin probe undergoing a shift from red to green emission *in vivo*.

A slightly different strategy was employed by Zhou *et al.*[112] who developed a ratiometric dual emission probe containing conjoined rhodamine and coumarin fragments that exhibits a green emission in its unreacted form (Scheme 4). Reaction with ClO^- results in hydrolysis of the hydrazinyl fragment to afford separated rhodamine and coumarin units with the release of N_2 gas. This results in rhodamine which gives a red emission profile and coumarin which affords a blue emission profile (coumarin's emission profile has slightly shifted) enabling ratiometric determination of ClO^- concentrations in biological environments.

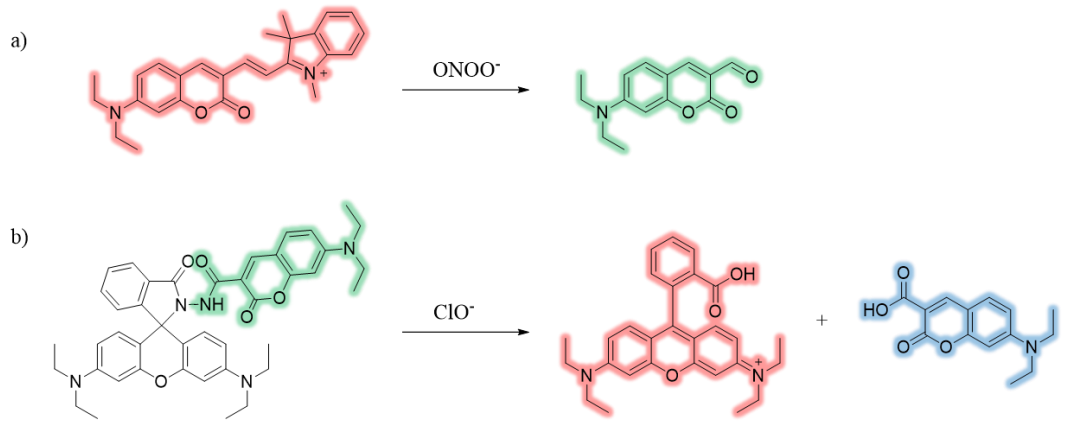

Scheme 4: Ratiometric fluorescent probes for the detection of ROS: a) a coumarin-hemicyanine scaffold for the detection of $ONOO^-$, and b) a coumarin-rhodamine scaffold to detect ClO^-.[112, 113]

1.1. Project Aim

The aim of this chapter was to synthesise a series of coumarin-based $ONOO^-$ molecular probes which would target different organelles, such as the mitochondria, the lysosome and the endoplasmic reticulum. I was particularly interested in gaining an understanding of $ONOO^-$ formation in different organelles, since this could provide information on the prevalence and importance of $ONOO^-$ in different biological processes. This required the attachment of organelle-specific targeting groups to the coumarin probe, with a variety of commonly used targeting groups outlined in Figure 1.

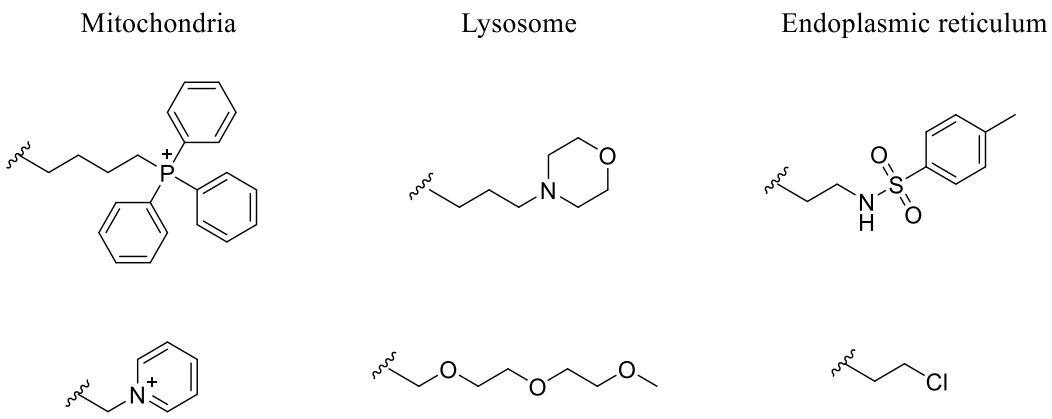

Figure 1: Targeting groups that have been used to localise probes in the mitochondria, lysosome and endoplasmic reticulum of cells.[114]

I choose to develop coumarin probes containing an oxidatively cleavable benzyl Bpin group to allow for the selective and sensitive sensing of $ONOO^-$, which contained specific targeting group for each organelle. This would include probes containing a triphenylphosphonium unit for targeting the mitochondria; a morpholine unit for targeting the lysosome; and a sulphanilamide unit for targeting the endoplasmic reticulum. (Figure 2).

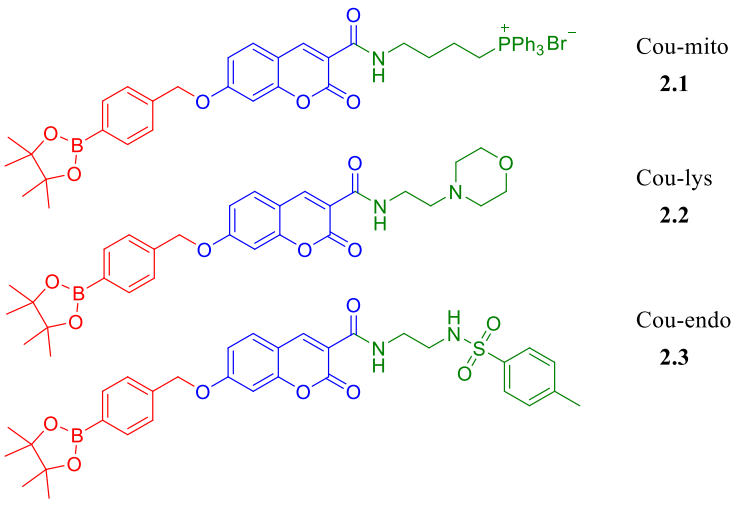

Figure 2: A series of coumarin based fluorescent probes for $ONOO^-$ detection that target different organelles. Key: red – $ONOO^-$ targeting group, blue – coumarin fluorophore, green - organelle targeting unit.

2. Results & Discussion

2.1. Synthesis of Coumarin Organelle Targeting Fluorescent Probes for $ONOO^-$

The synthesis of Cou-Bpin **5.5** has previously been reported by Zhang[115], Borbas[116] and Zhu[117] (Scheme 5), and an adaptation of these protocols was used for its synthesis. The alcohol at position 2 of 2,4-dihydrobenzaldehyde **5.1** was selectively substituted using 4-(bromomethyl) benzeneboronic acid pinacol ester **5.2** to afford intermediate **5.3** containing the desired benzyl Bpin sensing group in 49 % yield. This was followed by addition of Meldrum's acid **5.4**, piperidine and acetic acid in ethanol to afford Cou-Bpin **5.5** in 55 % yield. Amide bond forming reactions were then used to functionalise the free carboxylic acid unit of Cou-Bpin **5.5** with different targeting units to afford the three organelle targeting probes **2.1**, **2.2** and **2.3**.

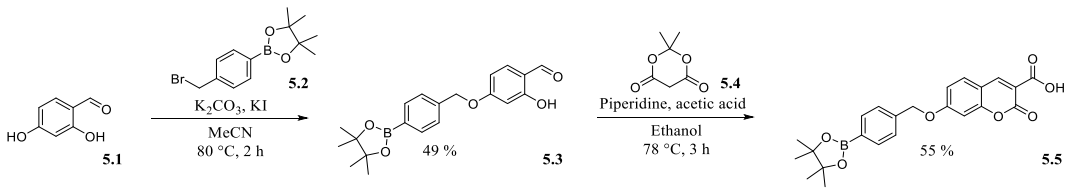

Scheme 5: Synthetic route for the synthesis of the key intermediate Cou-Bpin **5.5**.

In the first instance, (4-bromobutyl) triphenylphosphonium bromide **6.1** was converted into its corresponding amine **6.2** via treatment with ammonia (7M solution in methanol), giving an excellent 76 % yield after a long reaction time of 72 h. Amine **6.2** was subsequently used in a peptide coupling with coumarin acid **6.5** to afford Cou-mito **2.1** in an unoptimised low yield of 18 % (Scheme 6).

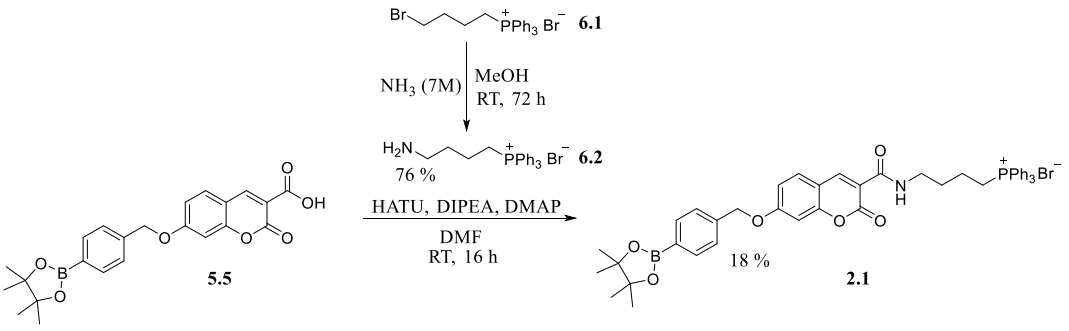

Scheme 6: Synthesis of mitochondrial targeting $ONOO^-$ probe Cou-mito **2.1**.

The same coupling conditions were then used to couple the commercially available morpholine amine **7.1** with coumarin acid **5.5** to form the lysosome targeting probe Cou-lys **2.2** in an unoptimized 28 % yield (Scheme 7).

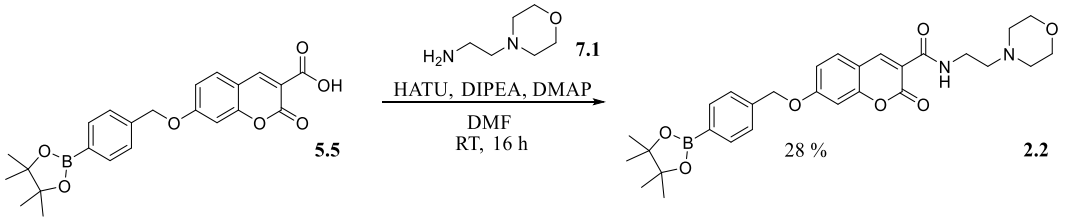

Scheme 7: Synthesis of lysosomal targeting $ONOO^-$ probe Cou-lys **2.2**.

The mono-tosyl-diamine **8.3** coupling partner required to prepare Cou-endo **2.3** was synthesised in 63 % yield through treatment of ethylenediamine **8.1** with one equivalent of *p*-toluenesulfonyl chloride **8.2**, and Et_3N in DCM. Finally, the endoplasmic reticulum based probe for $ONOO^-$ was prepared (Scheme 8). Mono-tosyl-diamine was then coupled with coumarin acid **5.5** using HATU as a coupling agent to afford Cou-endo **2.3** in 24 % yield.

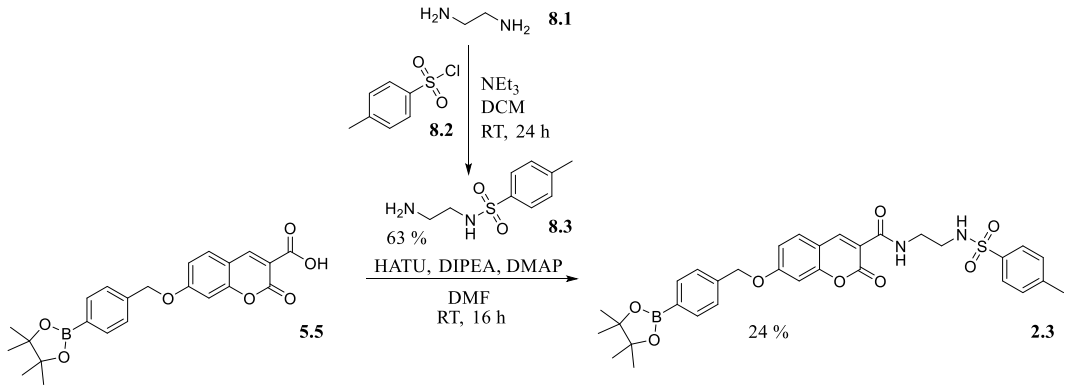

Scheme 8: Synthesis of endoplasmic targeting $ONOO^-$ probe Cou-endo **2.3**.

2.2. Fluorescence Studies

Initial UV studies allowed the excitation wavelengths of Cou-mito **2.1**, Cou-lys **2.2** and Cou-endo **2.3** to be determined. 7-hydroxycoumarin-3-carboxylic acid (referred to as Cou-acid **9.1**) is a widely commercially used fluorophore with an excitation wavelength of λ_{ex} = 342 nm (Figure 3a). Cou-mito **2.1** and Cou-endo **2.3** both showed maximum absorbances at 350 nm, whilst Cou-lys **2.2** had a maximum absorption at 375 nm. Cou-Bpin **5.5** was used as a reference compound and exhibited the same UV behaviour as Cou-acid **9.1**, with a maximal λ_{ex} = 342 nm. Figure 3b – d illustrate the UV spectra of Cou-mito **2.1**, Cou-lys **2.2** and Cou-endo **2.3** in the absence and presence of $ONOO^-$, with a clear shift in the absorbance maxima observed in all three cases upon addition of $ONOO^-$. Interestingly, relative to Cou-acid **9.1**, a red shift was observed for the absorbance profiles of Cou-mito **2.1** and Cou-endo **2.3** whereas a small blue shift was observed for Cou-lys **2.2**.

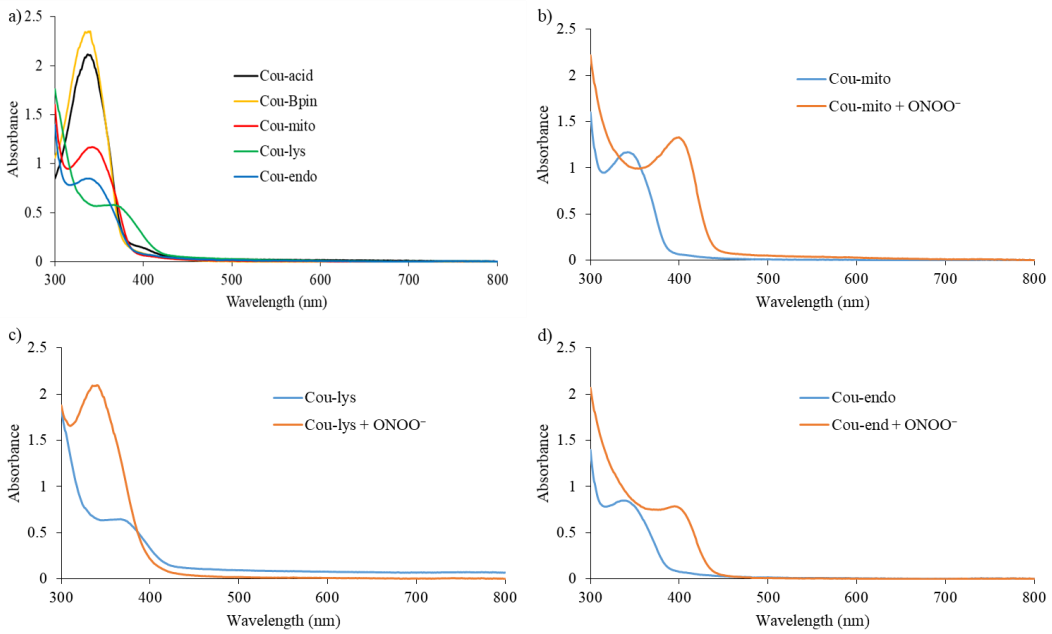

Figure 3: UV spectra of: a) Cou-acid **9.1**, Cou-Bpin **5.5**, Cou-mito **2.1**, Cou-lys **2.2** and Cou-endo **2.3**, b) Cou-mito **2.1** without and with $ONOO^-$ (excess), c) Cou-lys **2.2** without and with $ONOO^-$ (excess), and d) Cou-endo **2.3** without and with $ONOO^-$ (excess) in PBS buffer 52 % MeOH : H_2O, pH = 7.4 at 25 °C measured on a BMG Labtech CLARIOstar® plate reader.

Figure 4a shows the emission spectrum of Cou-mito **2.1**, Cou-lys **2.2** and Cou-endo **2.3** without $ONOO^-$, which gave maximum fluorescent emission values at λ_{max} = 400 nm, λ_{max} = 395 nm and λ_{max} = 405 nm, respectively (*cf* λ_{max} = 447 nm for Cou-acid **9.1** and λ_{max} = 395 nm for Cou-Bpin **2.5**). Addition of $ONOO^-$ to probes **2.1**, **2.2** and **2.3** resulted in a change in their emission spectra, which resembled the emission spectra observed for Cou-acid **9.1** (Figure 4b). This suggests that the generated species must be structurally linked to Cou-acid **9.1**, whose presence was confirmed by MS analysis. Therefore, it was postulated that addition of $ONOO^-$ to the probes results in oxidative cleavage of their benzyl Bpin groups to afford a phenolic intermediate whose amidic organelle targeting groups are then hydrolysed to give Cou-acid **9.1** (Scheme 9).

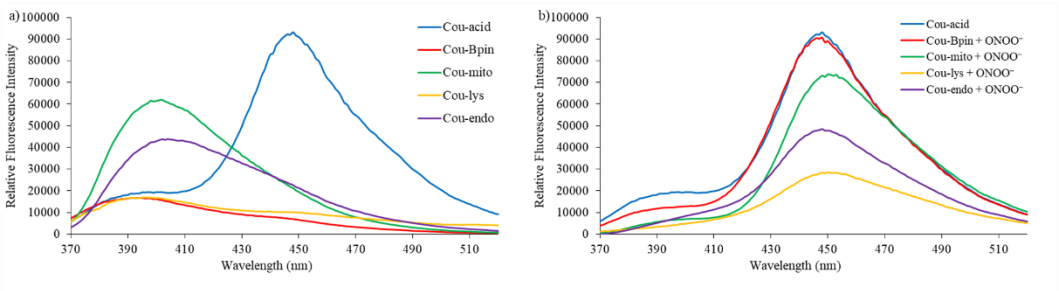

Figure 4: a) Emission spectra for Cou-acid **9.1** (5 µM), Cou-Bpin **5.5** (5 µM), Cou-mito **2.1** (5 µM), Cou-lys **2.2** (5 µM), Cou-endo **2.3** (5 µM) and b) Emission spectra for Cou-acid **9.1** (5 µM), Cou-Bpin **5.5** (5 µM), Cou-mito **2.1** (5 µM), Cou-lys **2.2** (5 µM), Cou-endo **2.3** (5 µM) in the presence of $ONOO^-$ (50 µM) in PBS buffer 52 % MeOH : H_2O, pH = 7.4 at 25 °C. Fluorescence intensities were measured with λ_{ex} = 340 (bandwith: 20) nm on a BMG Labtech CLARIOstar® plate reader.

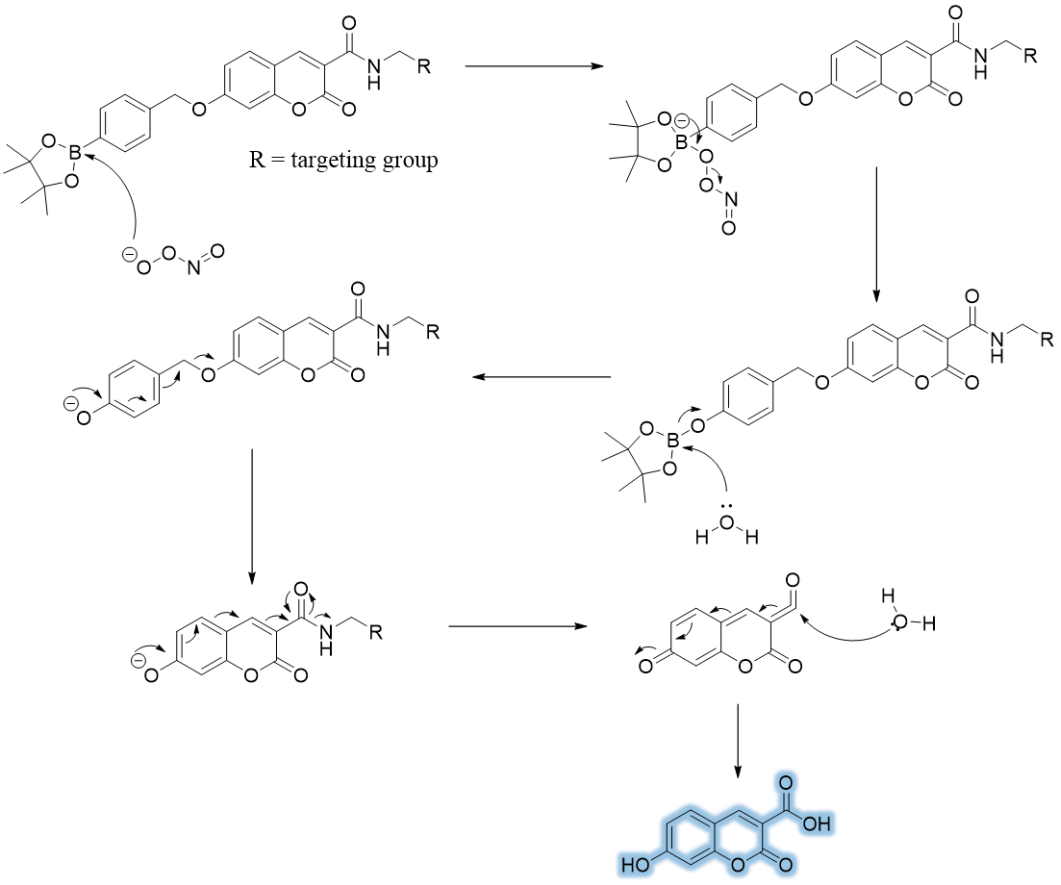

Scheme 9: Postulated mechanism upon reaction of Cou-mito **2.1**, Cou-lys **2.2**, Cou-endo **2.3** with $ONOO^-$ to give Cou-acid **9.1**.

Having established these initial findings, ROS selectivity and titration studies were carried out, with the aim of confirming preferential selectivity and sensitivity of Cou-mito **2.1**, Cou-lys **2.2** and Cou-endo **2.3** for $ONOO^-$ over H_2O_2. ROS selectivity studies were carried out for Cou-mito **2.1**, Cou-lys **2.2** and Cou-endo **2.3** as illustrated in Figure 5 – 7. All three probes exhibited the same behaviour, only showing a significant change in their emission spectrum when exposed to the stronger oxidant $ONOO^-$, with essentially no changes in the presence of H_2O_2, and other ROS.

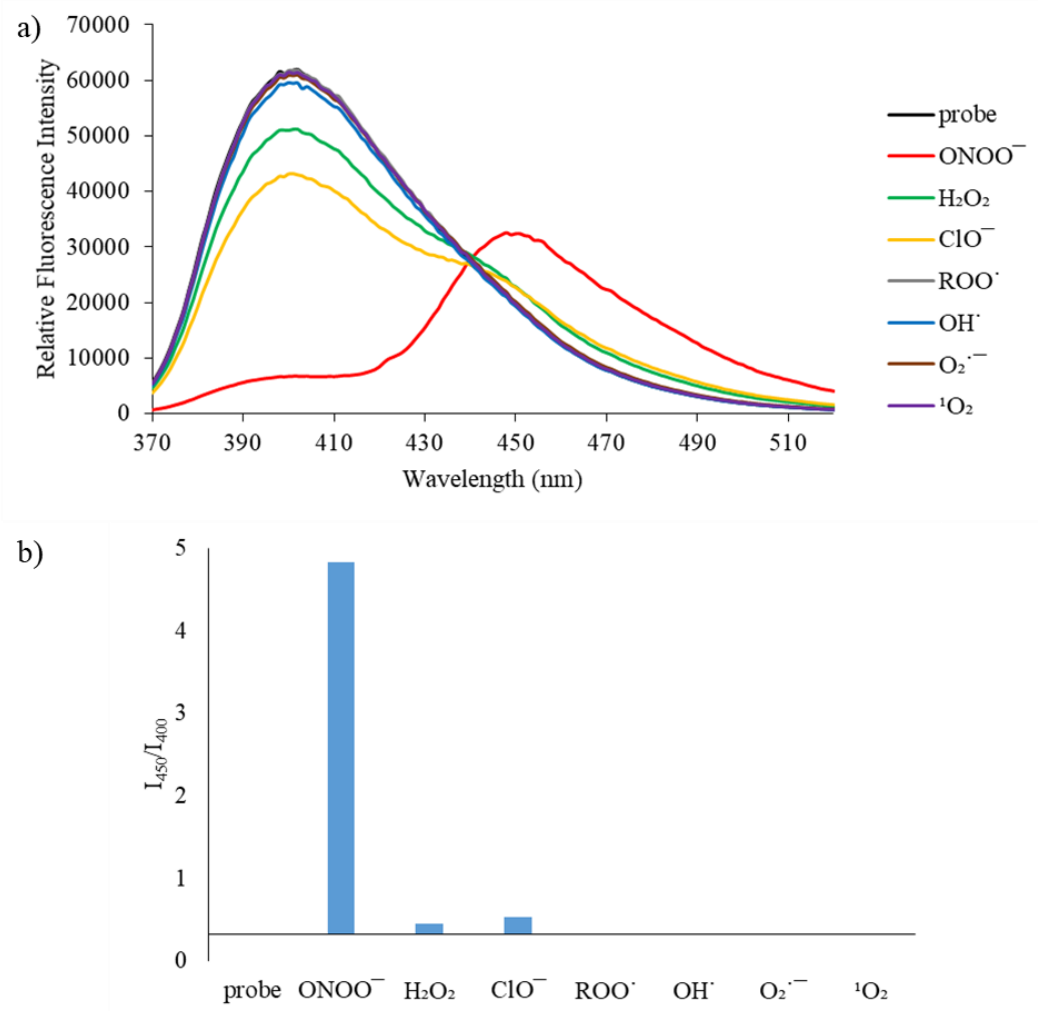

Figure 5: Selectivity data for Cou-mito **2.1** (5 µM): a) emission spectrum and b) relative intensity ratios (I_{450}/I_{400}) in the presence of $ONOO^-$ (50 µM), OH· (500 µM), $O_2^{\cdot-}$ (500 µM), $^1O_2$ (500 µM) after 5 min. H_2O_2 (1 mM), ROO· (500 µM) and ClO^- (500 µM) were measured after 30 min. The data was obtained in PBS buffer 52 % MeOH : H_2O, pH = 7.4 at 25 °C at λ_{ex} = 340 (bandwith: 20) nm on a BMG Labtech CLARIOstar® plate reader.

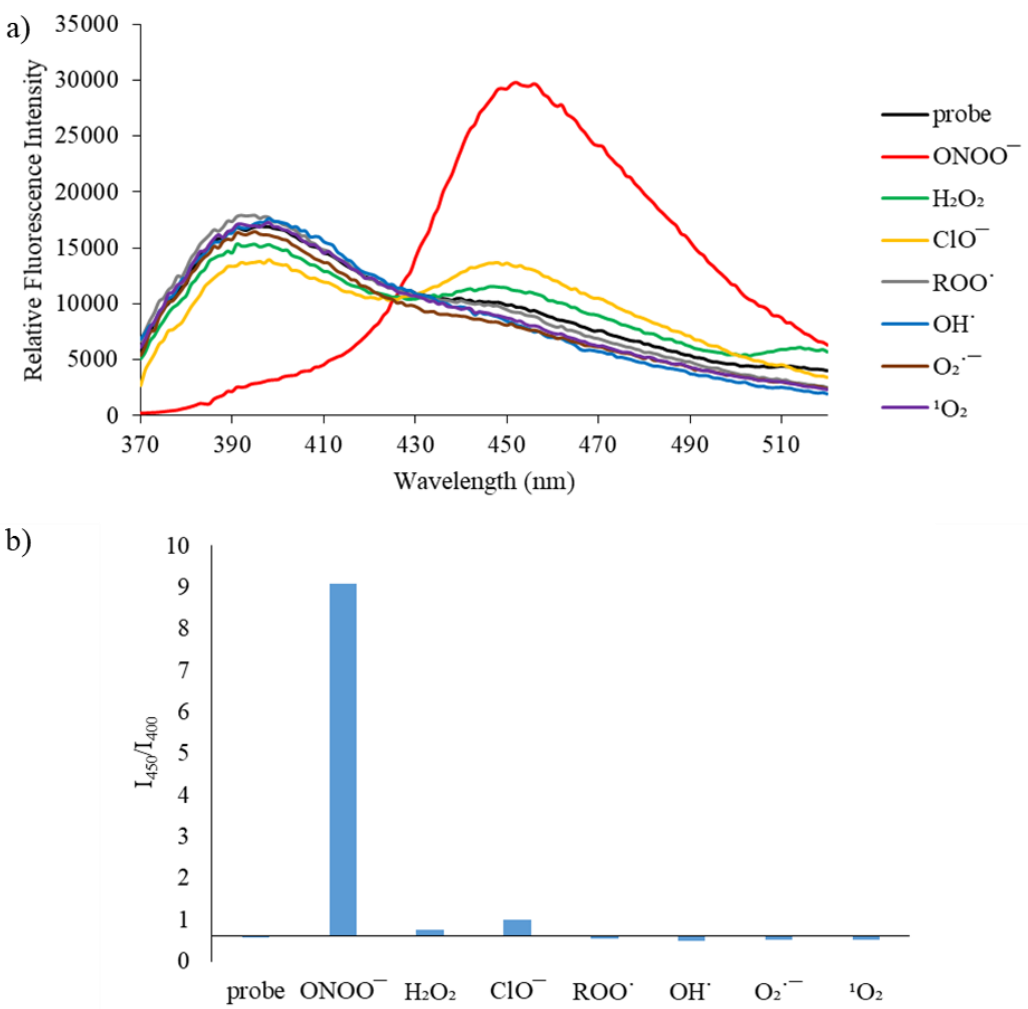

Figure 6: Selectivity data for Cou-lys **2.2** (5 µM): a) emission spectrum and b) relative intensity ratio (I_{450}/I_{400}) in the presence of $ONOO^-$ (50 µM), OH· (500 µM), $O_2^{\cdot-}$ (500 µM), $^1O_2$ (500 µM) after 5 min. H_2O_2 (1 mM), ROO· (500 µM) and ClO^- (500 µM) were measured after 30 min. The data was obtained in PBS buffer 52 % MeOH : H_2O, pH = 7.4 at 25 °C at λ_{ex} = 340 (bandwith: 20) nm on a BMG Labtech CLARIOstar® plate reader.

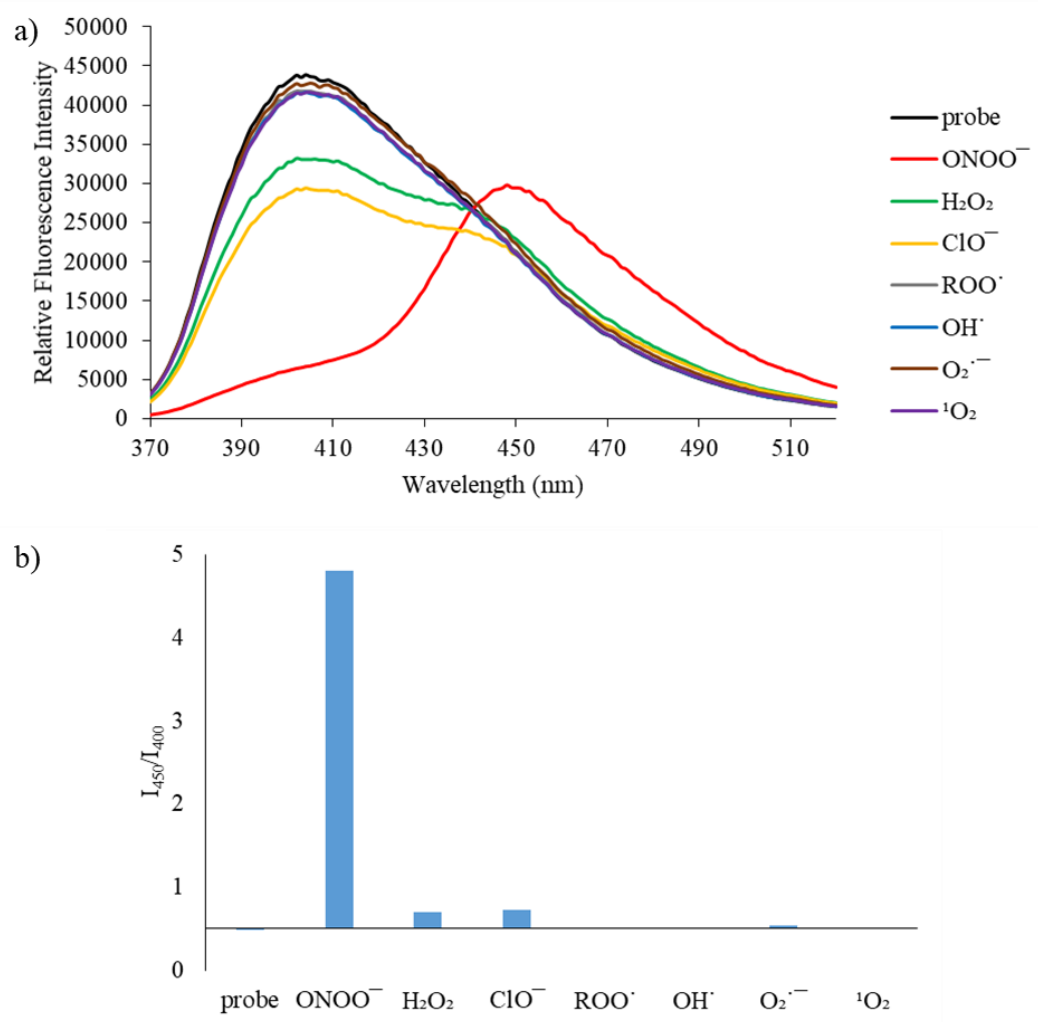

Figure 7: Selectivity data for Cou-endo **2.3** (5 µM): a) emission spectrum and b) relative intensity ratio (I_{450}/I_{400}) in the presence of $ONOO^-$ (50 µM), OH· (500 µM), $O_2^{\cdot-}$ (500 µM), $^1O_2$ (500 µM) after 5 min. H_2O_2 (1 mM), ROO· (500 µM) and ClO^- (500 µM) were measured after 30 min. The data was obtained in PBS buffer 52 % MeOH : H_2O, pH = 7.4 at 25 °C at λ_{ex} = 340 (bandwith: 20) nm on a BMG Labtech CLARIOstar® plate reader.

Titration studies for Cou-mito **2.1**, Cou-lys **2.2** and Cou-endo **2.3** with $ONOO^-$ showed similar reaction profiles (Figure 8 – 10). These three probes **2.1**, **2.2** and **2.3** (in the absence of $ONOO^-$) exhibit emission profiles at λ_{max} ≈ 400 nm, which decrease with increasing $ONOO^-$ concentrations with the appearance of new strong emission profiles at λ_{max} ≈ 450 nm. Consequently, it was concluded that Cou-mito **2.1**, Cou-lys **2.2**, and

Cou-endo **2.3** could be used to sense $ONOO^-$ in a ratiometric manner. LoDs were determined to be 0.28 µM, 0.26 µM and 0.36 µM for **2.1**, **2.2** and **2.3** respectively.

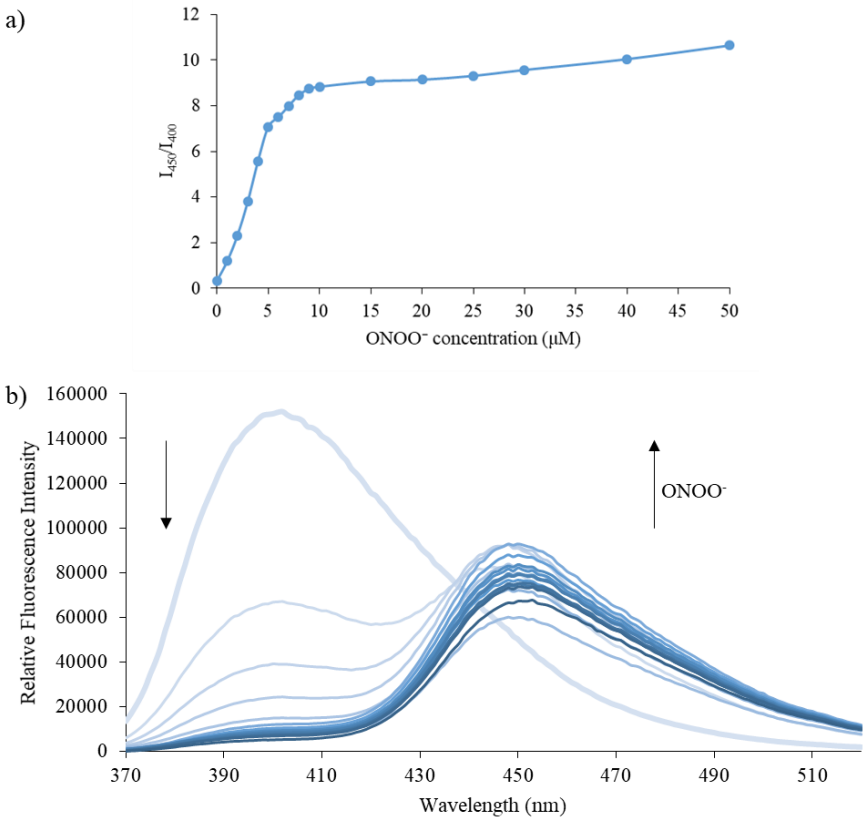

Figure 8: a) Dose dependence curve (I_{450}/I_{400}) and b) Emission spectra for Cou-mito **2.1** (5 µM) in the presence of $ONOO^-$ (1, 2, 3, 4, 5, 6, 7, 8, 9, 10, 15, 20, 25, 30, 40, 50 µM) in PBS buffer 52 % MeOH : H_2O, pH = 7.4 at 25 °C. Fluorescence intensities were measured with λ_{ex} = 340 (bandwith: 20) nm on a BMG Labtech CLARIOstar® plate reader.

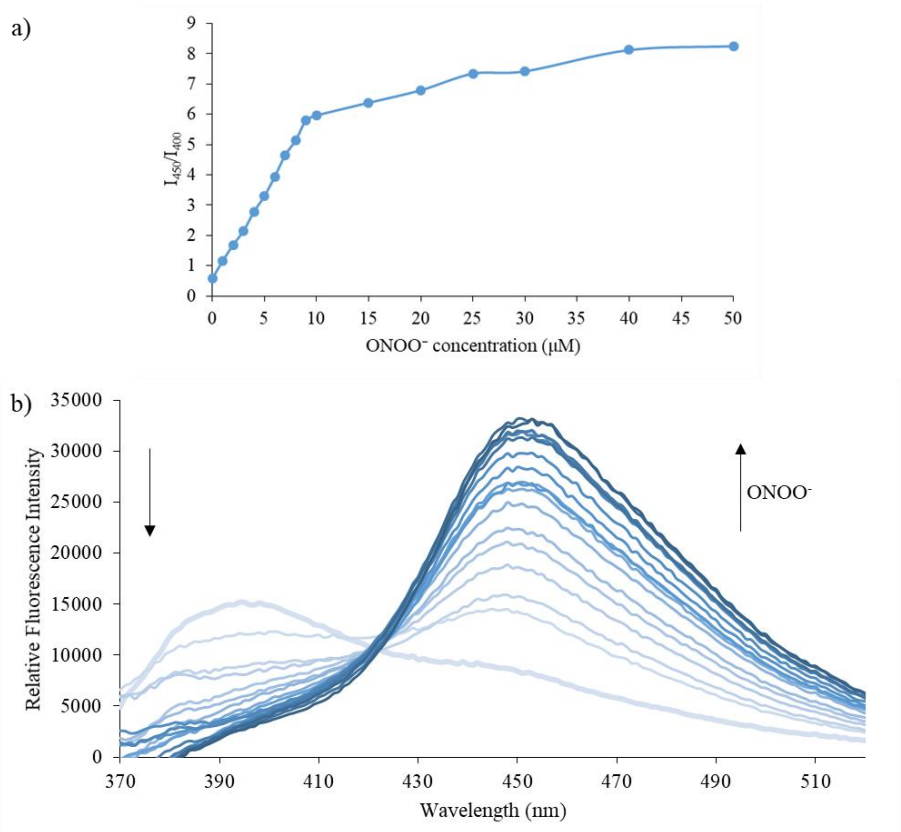

Figure 9: a) Dose dependence curve (I_{450}/I_{400}) and b) Emission spectra for Cou-lys **2.2** (5 µM) in the presence of $ONOO^-$ (1, 2, 3, 4, 5, 6, 7, 8, 9, 10, 15, 20, 25, 30, 40, 50 µM) in PBS buffer 52 % MeOH : H_2O, pH = 7.4 at 25 °C. Fluorescence intensities were measured with λ_{ex} = 340 (bandwith: 20) nm on a BMG Labtech CLARIOstar® plate reader.

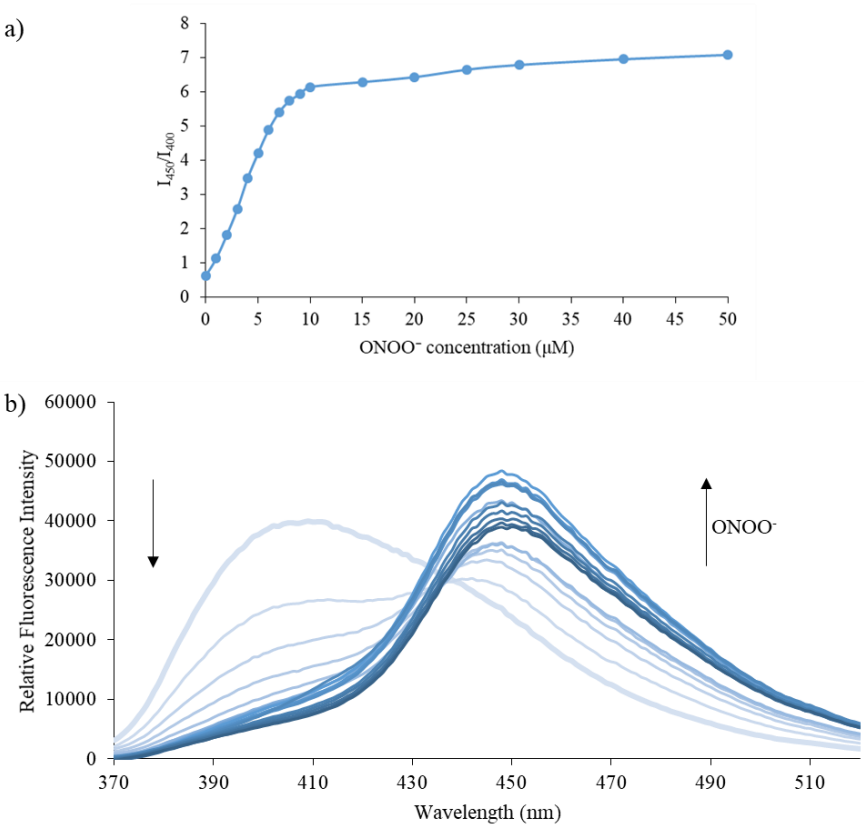

Figure 10: a) Dose dependence curve (I_{450}/I_{400}) and b) Emission spectra for Cou-endo **2.3** (5 μM) in the presence of $ONOO^-$ (1, 2, 3, 4, 5, 6, 7, 8, 9, 10, 15, 20, 25, 30, 40, 50 μM) in PBS buffer 52 % MeOH : H_2O, pH = 7.4 at 25 °C. Fluorescence intensities were measured with λ_{ex} = 340 (bandwith: 20) nm on a BMG Labtech CLARIOstar® plate reader.

As the ROS selectivity studies revealed, all three probes show little sensitivity towards H_2O_2, which was confirmed through a series of H_2O_2 titrations (Figure 11a – c), which revealed that their emission at λ_{max} = 400 nm only diminished slightly, with no new emission peaks appearing at λ_{max} = 450 nm, even when very high concentrations of H_2O_2 (2 mM) were used. Therefore, it can be concluded that the oxidising strength of H_2O_2 is insufficient to oxidatively cleave the boronate ester and organelle targeting fragments of the probes to generate Cou-acid **9.1**, thus, accounting for its selectivity for $ONOO^-$, which is a stronger oxidant.

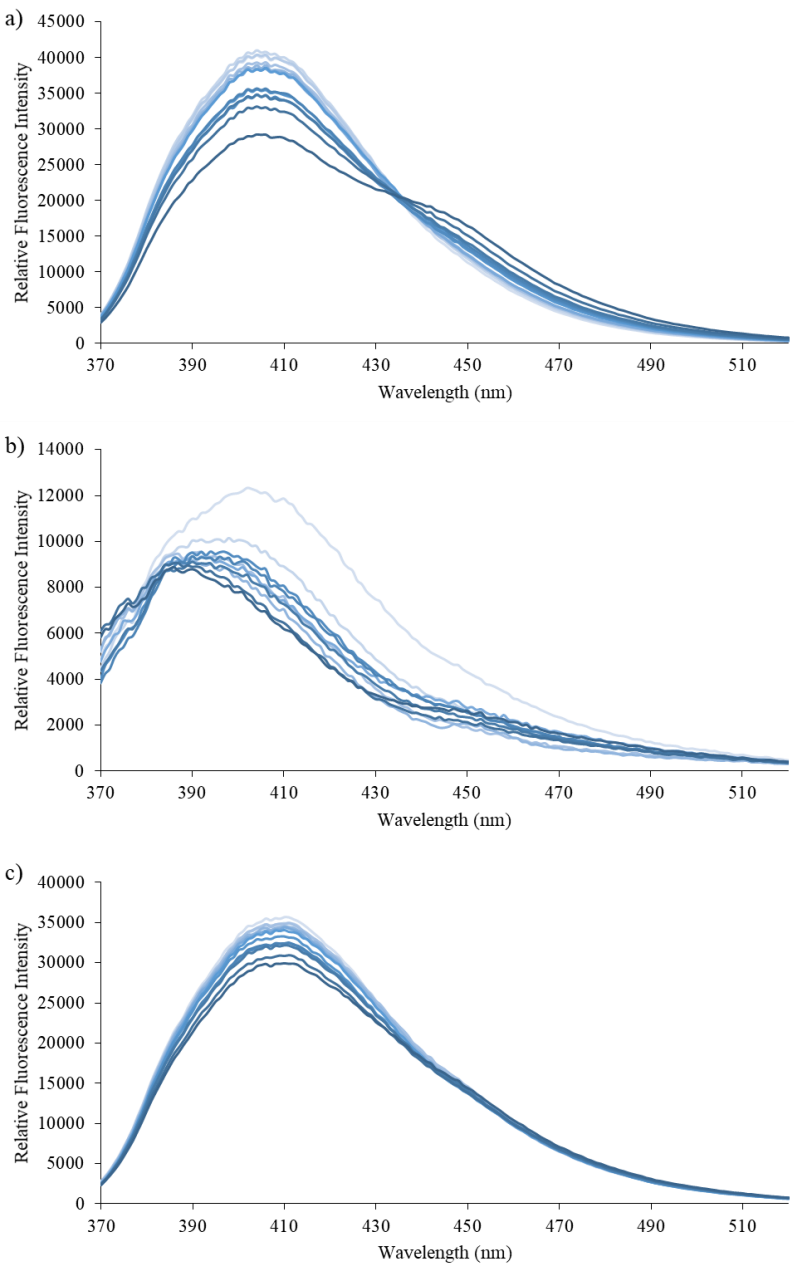

Figure 11: Emission spectra for a) Cou-mito **2.1** (5 µM), b) Cou-lys **2.2** (5 µM), c) Cou-endo **2.3** (5 µM) in the presence of H_2O_2 (0.1, 0.2, 0.3, 0.4, 0.5, 0.6, 0.7, 0.8, 0.9, 1, 1.5, 2 mM) in PBS buffer 52 % MeOH : H_2O, pH = 7.4 at 25 °C. Fluorescence intensities were measured with λ_{ex} = 340 (bandwith: 20) nm on a BMG Labtech CLARIOstar® plate reader.

2.3. Cell Studies

Since Cou-mito **2.1**, Cou-lys **2.2** and Cou-endo **2.3** showed great promise for selectively detecting $ONOO^-$ *in situ* over other ROS species, it was decided to study these organelle targeting $ONOO^-$ probes *in vitro*. Consequently, the three coumarin $ONOO^-$ sensitive probes **2.1**, **2.2**, and **2.3** were evaluated in RAW264.7 macrophages during a research stay in the group of Professor Kazuya Kikuchi at Osaka University.

First, exogenous generation of $ONOO^-$ was used to validate whether the probes were cell permeable. SIN-1 was used to generate and deliver $ONOO^-$ to the cells. Cells were first incubated with a 100 μM solution of SIN-1 for 1 h, followed by addition of the relevant probes Cou-mito **2.1**, Cou-lys **2.2** and Cou-endo **2.2** for 30 min at a concentration of 20 μM (Figure 12). Lack of fluorescent response revealed that Cou-mito **2.1** and Cou-endo **2.3** were unable to permeate inside RAW264.7 macrophages. However, Cou-lys **2.2** showed decent solubility and cell permeability levels and so, was taken forward for further cell studies.

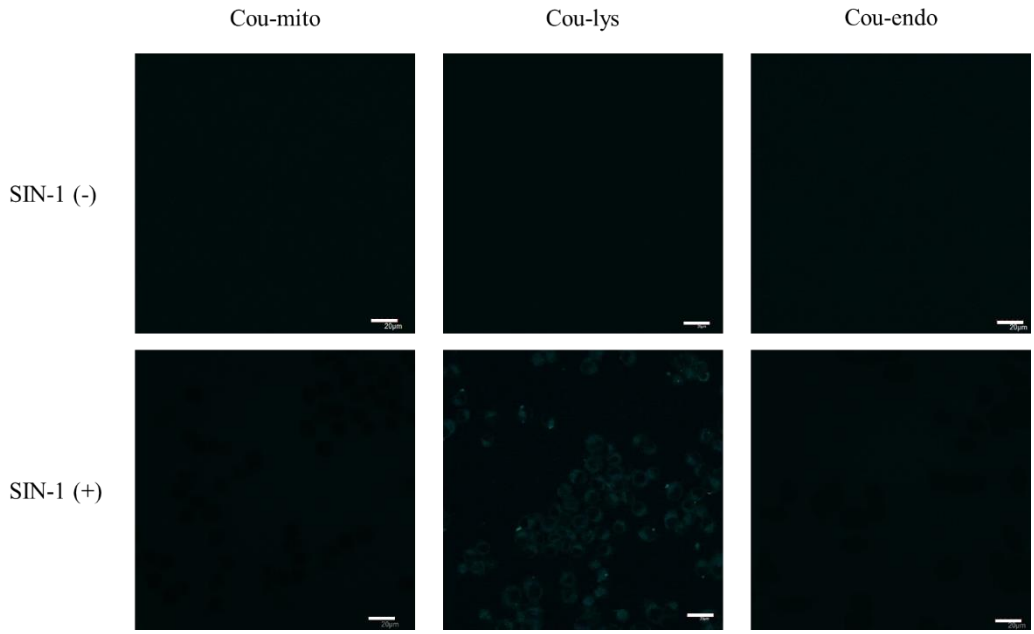

Figure 12: RAW264.7 macrophages were stimulated for 1 h with SIN-1 (100 μM, 1 h). Cou-mito **2.1** (20 μM), Cou-lys **2.2** (20 μM) and Cou-endo **2.3** (20 μM) were then incubated for 30 min, respectively. Blue channel: λ_{ex} = 405 nm, λ_{em} = 420 – 460 nm. Scale bar: 20 μm. Magnification x60. N = 3.

Next, we investigated whether Cou-lys **2.2** could be used to detect endogenous generation of $ONOO^-$ in RAW264.7 macrophages (Figure 13), which was produced by stimulating the cells with LPS (1 μg/ml) and IFN-γ (50 ng/ml) for 4 h. The cells were then incubated with Cou-lys **2.2** (20 μM) for 30 min, with ebselen added as a $O_2^{\cdot-}$ scavenger to ensure that the Cou-lys **2.2** probe can selectively detect changes in $ONOO^-$ production. Cou-lys **2.2** was shown to exhibit the ability to act as a probe for detecting endogenously produced $ONOO^-$, with a decrease in its fluorescence observed when the scavenging agent was present. However, the relatively low intensity of the fluorescence signal suggested that Cou-lys **2.2** has some cell permeability issues.

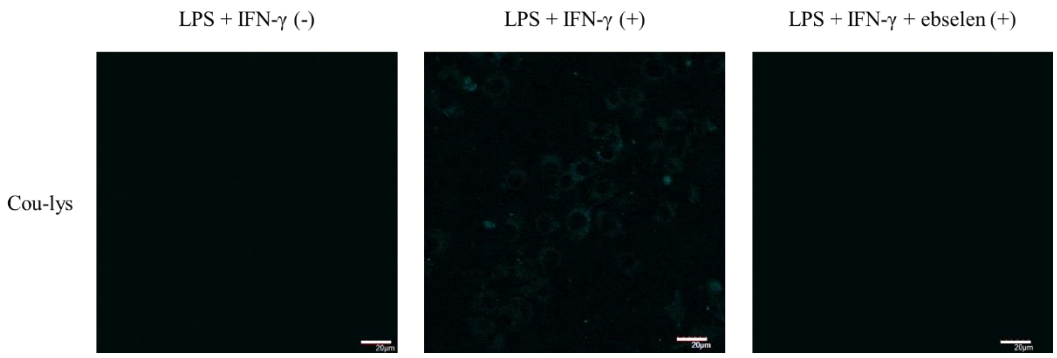

Figure 13: RAW264.7 macrophages were stimulated with LPS (1 μg/ml, 4 h) and IFN-γ (50 ng/ml, 4 h) and where indicated treated with ebselen (50 μM, 1 h). Cou-lys **2.2** (20 μM), was incubated for 30 min. Blue channel: λ_{ex} = 405 nm, λ_{em} = 420 – 460 nm. Scale bar: 20 μm. Magnification x60. N = 3.

Lastly, I decided to evaluate the performance of Cou-lys **2.2** in RAW264.7 macrophages upon stimulation with PMA, which induces high levels of $O_2^{\cdot-}$ (Figure 14) and hence, activates intracellular $ONOO^-$ production in a different way to LPS and IFN-γ. As before with LPS and IFN-γ stimulation, the induced fluorescence signal of the Cou-lys probe **2.2** was relatively weak, thus confirming that the probe was not fully permeating into the cells. Unfortunately, the weak signal produced by Cou-lys **2.2** generated under the various $ONOO^-$ cell stimulation conditions, meant that co-localisation studies with LysoTracker were inconclusive.

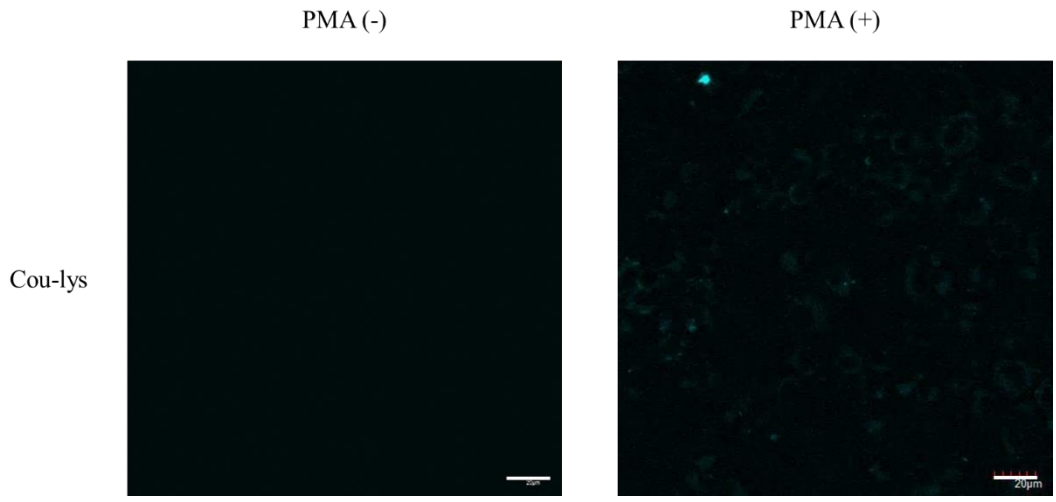

Figure 14: RAW264.7 macrophages were stimulated with PMA (1 µg/ml) for 1 h. Cou-lys **2.2** (20 µM), was incubated for 30 min. Blue channel: λ_{ex} = 405 nm, λ_{em} = 420 – 460 nm. Scale bar: 20 µm. Magnification x60. N = 3.

3. Preliminary Work on a FRET Dual Analyte Probe

The Cou-Bpin **5.5** unit offers great potential for functionalising its acid fragment, as demonstrated by previous coumarin and naphthalimide based FRET systems that have been used for ratiometric sensing of analytes.[118-120] Ratiometric sensing allows an isobestic point to be identified helping to quantify analyte concentrations. It would be useful to construct a probe that could detect two analytes, hence, the synthesis of a proof of concept compound **10.6** was explored (Scheme 10). One of the amines of ethylenediamine **10.1** was *N*-Boc-protected to afford mono-protected diamine **10.2** in 89 % yield. Subsequently, **10.2** was reacted with 4-bromo-1,8-naphthalic anhydride **10.3** to give *N*-Boc-naphthalimide **10.4** in 85 % yield that was then deprotected via treatment with TFA to afford amino-naphthalimide **10.5** in 96 % yield. This amine **10.5** was then coupled with Cou-Bpin **5.5** to achieve the core structure of the FRET probe **10.6** in 26 % yield. This precursor is designed to allow the detection of $ONOO^-$ (through the boronic ester unit) with its aryl bromide unit being functionalised with other sensing groups allowing for the simultaneous detection of a range of other analytes.

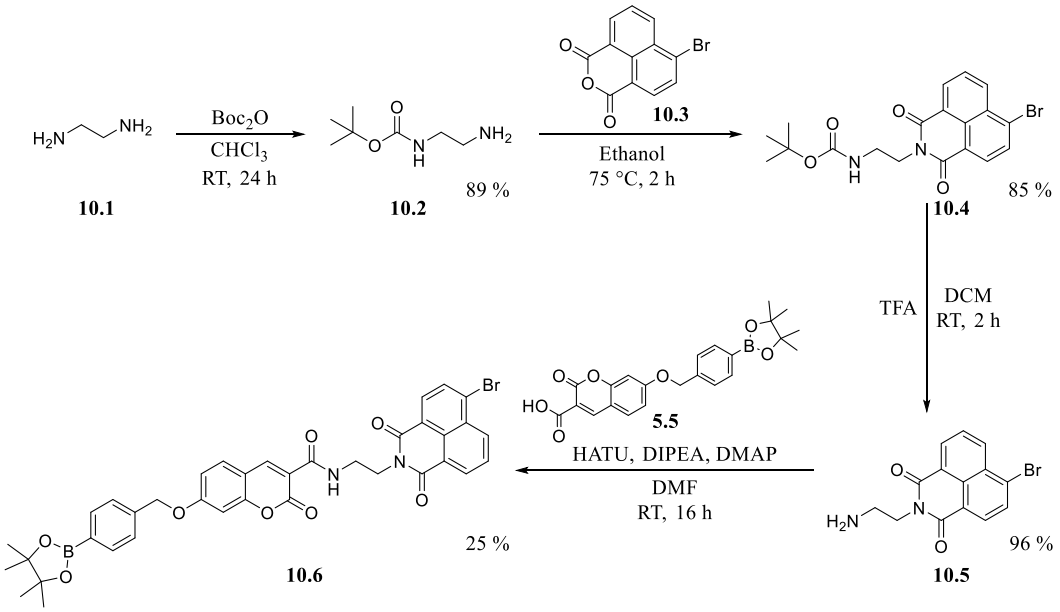

Scheme 10: Synthesis of an advanced FRET sensing precursor **10.6**.

Some preliminary analytical data was collected for the sensing precursor **10.6**, whose UV spectrum and $ONOO^-$ titration data are reported in Figure 15 and Figure 16, respectively. As expected, the coumarin fragment of the probe was found to be fluorescent (λ_{em} = 400 nm) which shifted its emission profile to λ_{em} = 450 nm upon addition of $ONOO^-$, as expected for formation of the 7-hydroxycoumarin-3-carboxylic acid cleavage product. As anticipated, no FRET response (around $\lambda_{max} \approx 550$ nm) was observed because the naphthalimide unit is not activated for this type of emission process at this stage.

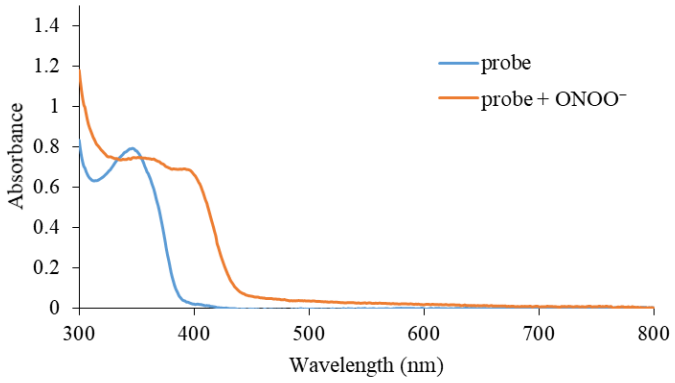

Figure 15: UV spectrum of probe **10.6** without and with $ONOO^-$ (excess) in PBS buffer 52 % MeOH : H_2O, pH = 7.4 at 25 °C measured on a BMG Labtech CLARIOstar® plate reader.

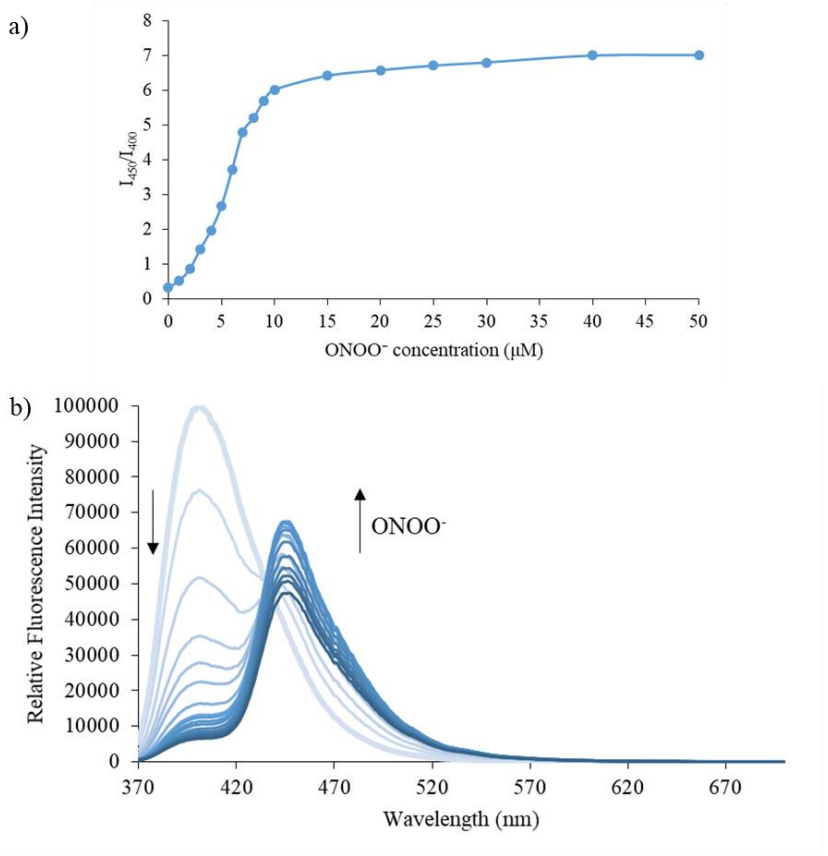

Figure 16: a) Dose dependence curve (I_{450}/I_{400}) and b) emission spectrum of **10.6** (5 µM) in the presence of $ONOO^-$ (1, 2, 3, 4, 5, 6, 7, 8, 9, 10, 15, 20, 25, 30, 40, 50 µM) in PBS buffer 52 % MeOH : H_2O, pH = 7.4 at 25 °C. Fluorescence intensities were measured with λ_{ex} = 340 (bandwith: 20) nm on a BMG Labtech CLARIOstar® plate reader.

4. Conclusions

To conclude, a series of organelle targeting $ONOO^-$ probes has been successfully synthesized, with each probe designed to target a different organelle (mitochondria, lysosome, and endoplasmic reticulum) to allow for the selective and sensitive detection of $ONOO^-$ in cellular systems. The ratiometric fluorescent response of all three probes made them interesting candidates for *in vitro* studies. Cell studies with RAW264.7 macrophages revealed poor cell permeability of Cou-mito **2.1** and Cou-endo **2.3**. However, Cou-lys **2.2** was able to detect exogenously and endogenously produced $ONOO^-$ in RAW264.7 macrophages. The strength of the fluorescence signal of Cou-lys **2.2** was relatively weak, which indicated that further synthetic modifications are required to the scaffold to increase its permeability to allow for co-localisation studies. Still, the development of **2.1**, **2.2** and **2.3** allowed to introduce a new series of ratiometric probes with potential for organelle targeting. These initial findings led to the preliminary work on a FRET probe **10.6** which has potential for the development of dual analyte FRET probes and orgnalle targeting motifs.

5. Future Work

Future work will now focus on converting the bromine of the naphthalimide unit of the FRET probe with relevant sensing groups to demonstrate the potential of the FRET design strategy for sensing different types of bioanalytes (Figure 17). FRET probe **11.1** allows the targeting of $ONOO^-$ and β-glucosidase (β-glc). The introduced glucose unit at the naphthalimide would be enzymatically cleaved by β-glc, giving the free phenol. Probe **11.2** allows for the simultaneous detection of $ONOO^-$ and H_2S. Azides are excellent sensing groups for H_2S since they are reduced to amines by H_2S, consequently, activating the naphthalimide unit. Studying the interplay between $ONOO^-$ and H_2S should allow for a more in depth understanding of redox homeostasis in cells. Finally, probe **11.3** could be used as a dual analyte FRET theranostics probe. **11.3** is activated by $ONOO^-$ and thiols in which the latter cleaves the disulfide bond allowing for the release of chlorambucil and activation of the FRET probe.

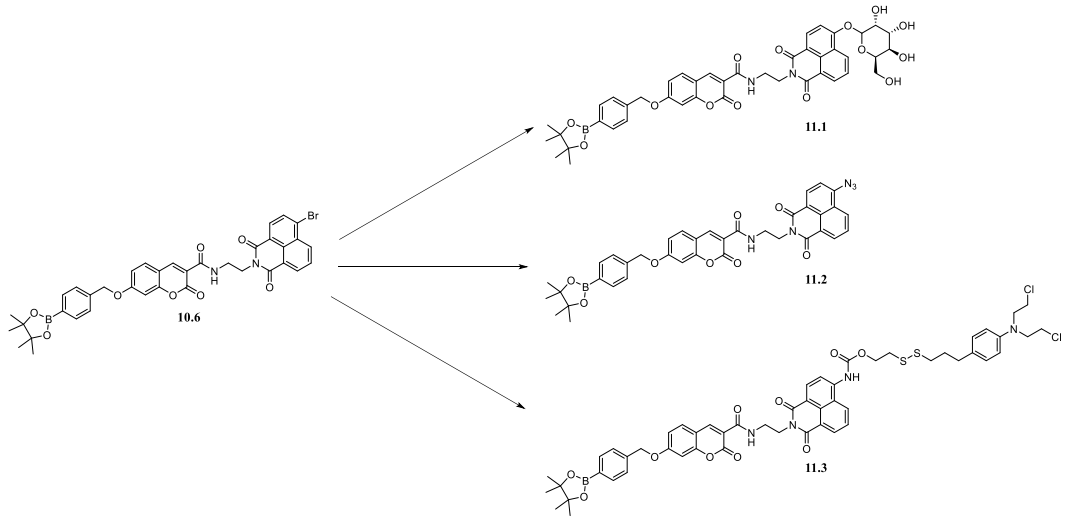

Figure 17: Probe **10.6** can be easily functionalised at the Br of naphthalimide allowing for the development of dual analyte FRET probes sensing $ONOO^-$ and β-glc (**11.1**), $ONOO^-$ and H_2S (**11.2**) and $ONOO^-$ and thiols (**11.3**) with the release of a drug upon activation.

Chapter 4 – Targeting Organelles with Specific Fluorophores: Fluorescein, Rhodamine and Rhodol

1. Introduction

Fluorescein, rhodamine 110 and rhodol are structurally highly similar fluorophores with the same tetracyclic core structure, only differing by the attachment of alcohol and amine groups (Figure 1). Functionalisation of these commonly used fluorophores is possible: at the alcohol or amine positions respectively as well as the phthalic anhydride moiety. This has led to the development of commercially available probes based on these fluorophores which are essential tools in biological research. Prominent examples include FITC (fluorescein isothiocyanate) or TRITC (tetramethylrhodamine), which can also be easily conjugated to antibodies and proteins, particularly useful for highly specific imaging applications.

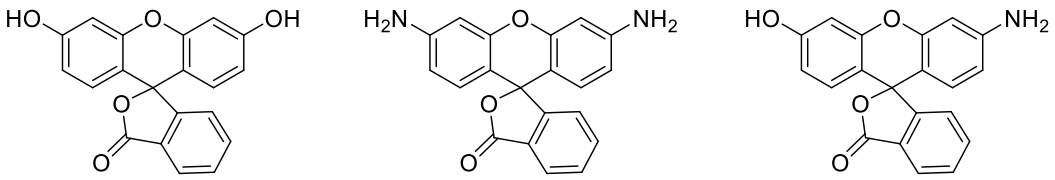

Fluorescein **Rhodamine 110** **Rhodol**

Figure 1: Core structures of fluorescein, rhodamine 110 and rhodol.

Each fluorophore offers different advantages in terms of potential clinical usage as well as targeting of different organelles. In the following, examples from the literature of $ONOO^-$ or other ROS species specific fluorescent probes will be discussed.

Fluorescein in contrast to rhodamine and rhodol is one of the few U.S. Food and Drug Administration (FDA) approved fluorophores, making it particularly attractive for clinical applications. Chang and co-workers have developed a range of boronate probes using fluorescein (and rhodol) scaffolds (Figure 2).[45, 121-124] All boronate based

probes were developed for the detection of H_2O_2 whereas these could also show great promise for $ONOO^-$ sensing due to their inherent reactivity with boronic esters.

In 2004, a water soluble turn-on optical probe **2.1** was developed, which was able to detect changes of intracellular H_2O_2 within living mammalian cells.[122] Fluorescent probe **2.4** was able to detect endogenous intracellular H_2O_2 generated by EGF/Nox activation as well as detecting H_2O_2 in live hippocampal neurons.[123] Following this, **2.8** was developed for imaging mitochondrial H_2O_2 in HeLa cells.[124] Elevated levels of H_2O_2 were detected, originating from an oxidative stress system associated with Parkinson's disease. These examples and many more from the Chang group illustrate the effectiveness of detection and monitoring of H_2O_2 in different oxidative stress conditions associated with cancer and other diseases.[121] Synthetic modification of these scaffolds allows for selectivity and specific reactivity.

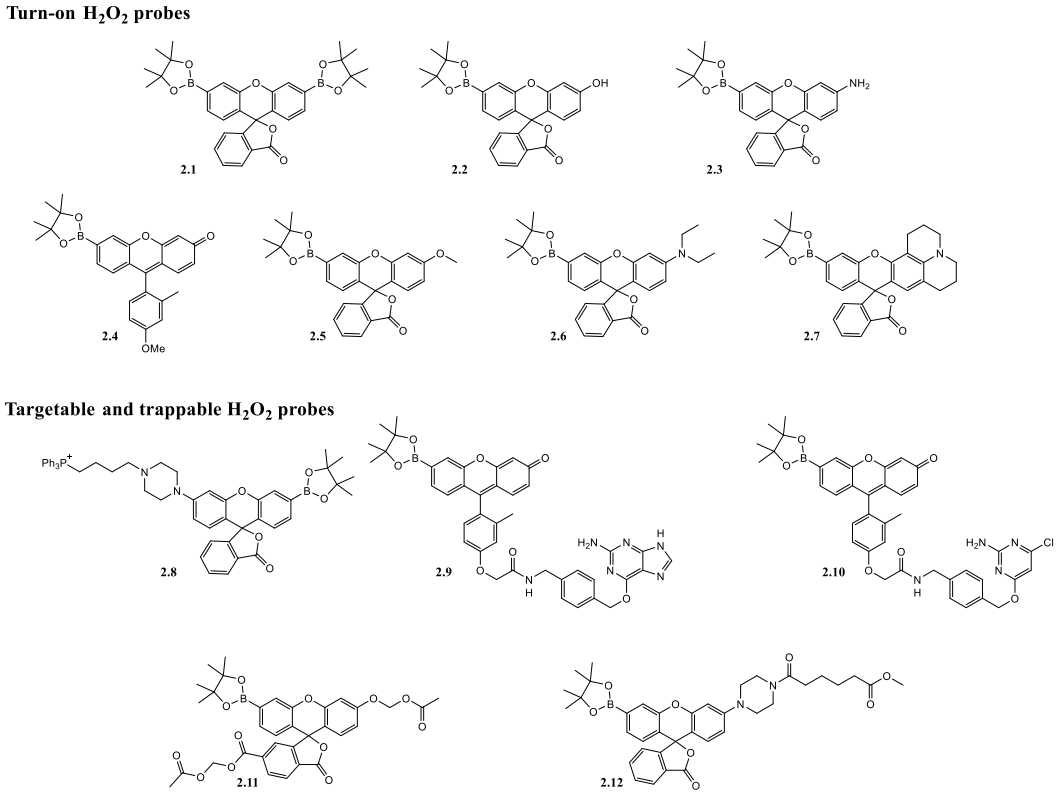

Figure 2: Boronate based probes with fluorescein or rhodol scaffolds for the detection of H_2O_2.

Another interesting series of $ONOO^-$ probes based on fluorescein, rhodamine or rhodol scaffolds was developed by Yang and co-workers: HKGreen fluorescent probes (Figure 3). The initial focus centred upon the development of green fluorescent probes which later on moved towards yellow fluorescent probes. The first probe HKGreen-1 **3.1** based on a fluorescein scaffold incorporated an anisol derived ketone unit.[125] The group previously showed that $ONOO^-$ reacts with activated ketones to form dioxiranes.[126] This motif enhances preferential detection of $ONOO^-$ as demonstrated by fluorescence studies. Nevertheless, considerable amounts of other ROS were also detected, which could pose selectivity issues for *in vivo* studies. *In vitro* studies with primary cultured neuronal cells confirmed the initial concerns: HKGreen-1 detects $ONOO^-$ but the reaction between the two is fairly poor.

The next generation of HKGreen replaced the fluorescein with a BODIPY scaffold and employed a PET mechanism.[62] High sensitivity and selectivity towards $ONOO^-$ over other ROS was more substantial with HKGreen-2 **3.2** compared to HKGreen-1 **3.1**. *In vitro* studies with J774.2 macrophages showed enhanced localisation of the probe in the mitochondria. $ONOO^-$ generation in cells was achieved via stimulation with LPS, IFN-y and PMA.

HKGreen-3 incorporated a different fluorescent scaffold compared to the last two generations: rhodol. Upon reaction of the trifluoromethyl ketone with $ONOO^-$, subsequent N-dearylation generates the fluorescent moiety.[127] Fluorescence studies indicated preferential sensing of $ONOO^-$. However, as in HKGreen-1 **3.1**, significant amounts of other ROS such as $OH^\cdot$ and ClO^- were also detected. HKGreen-3 **3.3** was changed to **3.4** in order to improve cell membrane permeability. *In vitro* studies with RAW264.7 and J774.2 macrophages confirmed intracellular $ONOO^-$ detection with **3.4**. No apparent cytotoxicity of **3.4** was displayed in the MTT assay, enhancing the probe's suitability for *in vivo* studies.

The rhodol scaffold was used for the development of the fourth generation of probes by the Yang group. The five synthesised probes **3.5** – **3.9** include phenol and aniline moieties. These were designed with the strong oxidising ability of $ONOO^-$ in mind to generate, via oxidative N-dearylation, the fluorescent N-methylrhodol. Yang *et al.* also suggested that the nitrogen atom linking towards the phenyl ring increases electron density of the phenyl and hence, facilitates increased reactivity towards $ONOO^-$.[128]

Fluorescence studies of **3.5** – **3.9** showed that **3.6** is highly selective towards $ONOO^-$ whereas the other scaffolds show preferential detection of ClO^-. High selectivity towards $ONOO^-$ over ClO^- is required since the analytes could easily interfere in cellular processes and consequently, produce false results. The acetate derivative of **3.6** was taken forward for RAW264.7 macropgaes studies since the acetate favours cell membrane permeability. **3.6** in conjunction with MitoTrackerRed confirmed the probe's ability to detect mitochondrial produced $ONOO^-$. *In vivo* studies with live tissues from a mouse model of atherosclerosis provided significant evidence for linking high $ONOO^-$ production with the atherosclerotic condition. The apolipoprotein E knockout mouse model readily develops atherosclerosis. The mice were fed on a normal diet for 20 weeks prior to investigation of the probe on the mouse's heart. In comparison to the wild type mice, a two-fold increase in fluorescent intensity of the probe was observed at the smooth muscle of the aortic root of the apolipoprotein E knockout mouse.

Following the investigation of multiple green fluorescent probes, the focus was shifted towards yellow and red fluorescent probes.[129] These are more desirable for biological applications since probes in the yellow and red region show low intracellular auto-fluorescence, deeper tissue penetration, low photo-induced damage and are more compatible for multicolour imaging.[130] HKYellow **3.10** incorporated previous developed synthetic strategies: acetate moiety for cell membrane permeability and a phenol scaffold for targeted $ONOO^-$ sensing. The yellow fluorescent dye based on a rhodamine scaffold detected exogenously and endogenously produced $ONOO^-$ in SH-SY5Y human neuroblastoma cells. *In vivo* studies on mouse livers with endogenous $ONOO^-$ stimulation showed that HKYellow **3.10** is a promising molecular imaging probe with high selectivity and sensitivity, low cytotoxicity and significant applicability.

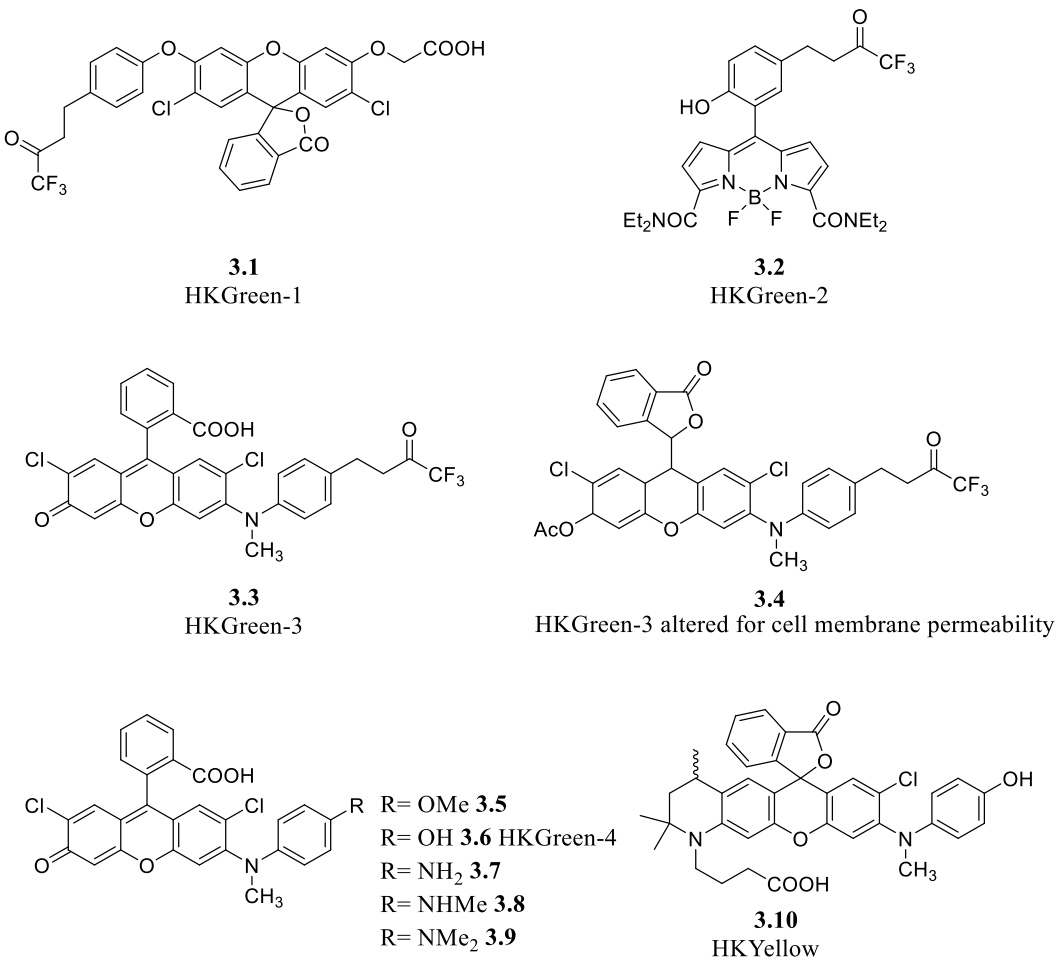

Figure 3: Different generations of $ONOO^-$ probes: HKGreen 1 – 4 and HKYellow.

Yu and co-workers have developed various mitochondrial targeting probes for ClO^- based on a rhodamine scaffold. In a first instance, rhodamine based probes **4.1** and **4.2** with two different mitochondrial targeting units (TPP and pyridinium units) were successfully synthesised (Figure 4).[101] The mitochondrial targeting units as well as the rhodamine scaffold enhance the lipophilicity of the probe which facilitates passage into the mitochondria. **4.1** and **4.2** are selective and sensitive towards ClO^-: fluorescence intensity of both remained constant once the probes reacted with ClO^-. *In vivo* studies with a nude mouse model successfully detected the exogenous ClO^-, which was added in the form of NaOCl. The nude mouse model is particularly applicable since the mouse has been genetically modified in a way that fewer T cells are produced resulting in an inhibited immune system.

Based on this initial scaffold, **4.1** and **4.2** were extended by a coumarin unit that would allow for ratiometric detection of ClO^-. **4.3** and **4.4** were successfully used for exo- and endogenous ClO^- detection in RAW264.7 macrophages and HEK293 cells. Interestingly, **4.3** showed better cell membrane penetration since the TPP unit increased lipophilicity more substantially compared to the pyridinium one.[131]

Due to the lipophilic nature of **4.3**, the probe was taken forward for additional tumour specific targeting through a biotin unit. Probe **4.5** showed excellent cell membrane and mitochondria permeability. Cell studies with RAW264.7 macrophages, HEK293, and HeLa cells validated endogenous and exogenous ClO^- detection as well as its tumour specificity due to the choice of cell lines investigated.[132] Yu *et al*. claim to have synthesised the first mitochondrial targeted and tumour specific probe. Further *in vitro* and *in vivo* studies are required to fully validate the initial results.

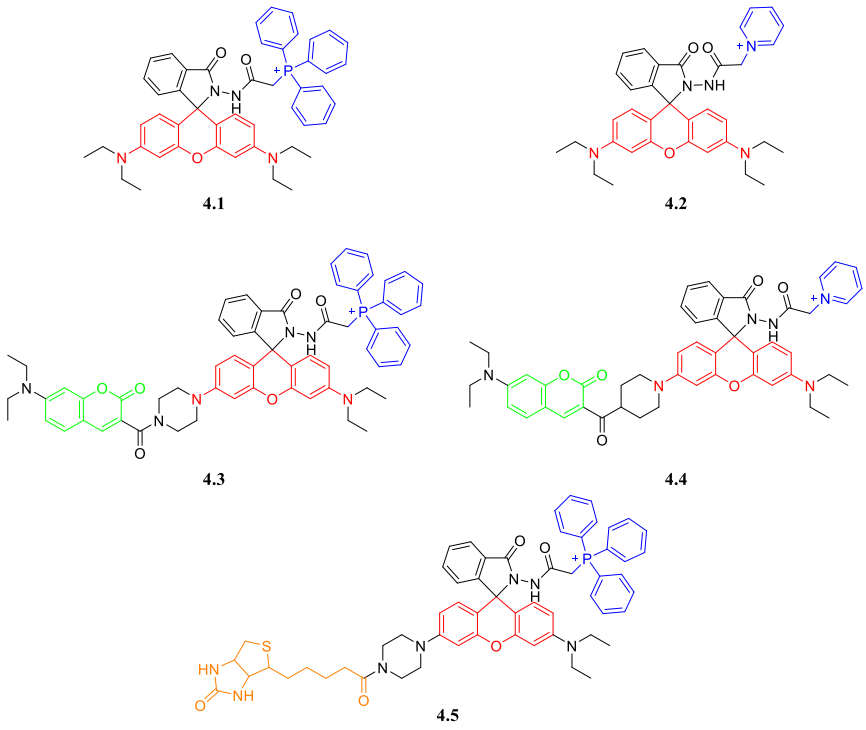

Figure 4: Yu *et al.* developed three generations of ClO^- probes. In a first instance, a rhodamine (red) based scaffold with mitochondrial targeting units 1) TPP (blue) **4.1** and 2) pyridinium (blue) **4.2** was prepared. Following on from the promising animal studies, the scaffold was extended by a coumarin unit (green) to give ratiometric ClO^- probes **4.3** and **4.4**. The highly lipophilic TPP probe **4.3** was further extended towards tumor targeting with the introduction of a biotin unit (orange) to give probe **4.5**.

In addition to the introduction of organelle specific targeting groups, rhodamine and rhodol scaffolds are also used solely for targeting the mitochondria[133] and endoplasmic reticulum[134] respectively.

Guo and co-workers introduced a methyl(4-hydroxyphenyl)amino group into the rhodamine scaffold, allowing them to specifically target $ONOO^-$ in the mitochondria through the combination of these two structural motifs (Scheme 1).[49] *In vitro* studies with RAW264.7 macrophages allowed validation of the probe's ability to detect exogenous and endogenous $ONOO^-$. To confirm the localisation of the rhodamine probe in the mitochondria in BIU-87 cells, MitoTracker Red was used to compare its overlap with the probe. Pearson's coefficient was 0.86 confirming an excellent overlap of both probes. Additionally, LysoTracker and ERTracker were used to examine lysosome and endoplasmic reticulum localisation. As expected, the probe solely localised in the mitochondria.

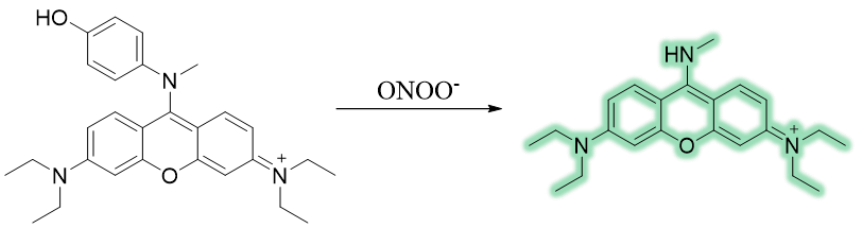

Scheme 1: A mitochondria targeted rhodamine probe for $ONOO^-$.

Yoon *et al*. developed a $ONOO^-$ selective near-infrared (NIR) probe (Scheme 2).[135] They decided to extend rhodamine's tricyclic core structure to create a semi-naphthalene rhodamine core and incorporate hydrazine as an $ONOO^-$ sensing group in order to achieve a mitochondrial NIR probe for the detection of $ONOO^-$. Selective and sensitive detection of $ONOO^-$ was achieved *in situ*, *in vitro* and ex vivo. Initially, exogenous $ONOO^-$ was evaluated in HeLa cells, followed by endogenous $ONOO^-$ in RAW264.7 macrophages and mouse bone marrow-derived neutrophils from a PAO1 infested mouse model. They also compared the mice with a NOX2 deficient mouse model to ensure that $ONOO^-$ production is caused by the primary neutrophils in the wild type mice and that the probe is able to detect these changes under biological conditions. Additional *in vitro* studies could have centered on the specific localisation

of the probe in organelles. One would assume for the probe to localise in the mitochondria due to the rhodamine related core structure.

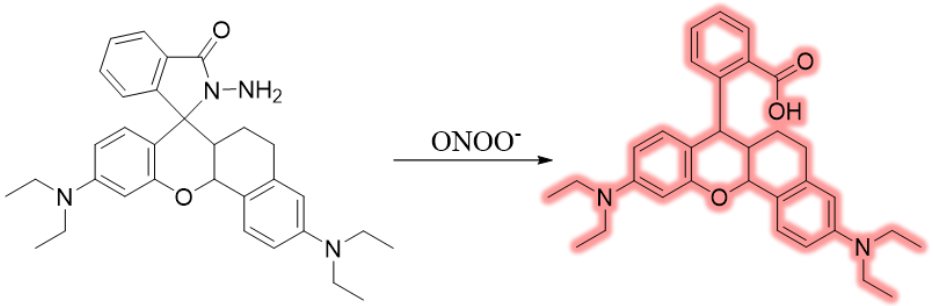

Scheme 2: A NIR probe to detect endogenous $ONOO^-$.

Similarly, Zhu and co-workers developed a highly similar probe to Yoon *et al.* but with the ability to localise in the mitochondria (Scheme 3).[136] The development of NIR probes allows for the minimisation of photo-damage to biological samples and achieves deeper tissue penetration. *In vitro* studies with MitoTracker allowed to confirm the localisation of the NIR probe in the mitochondria. Despite these positive results, the authors failed to evaluate endogenous $ONOO^-$. HeLa cells are used with SIN-1 accounting only for the evaluation of exogenous $ONOO^-$.

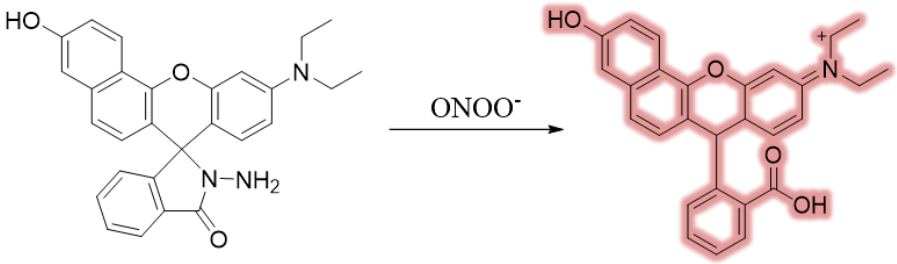

Scheme 3: A NIR probe for $ONOO^-$ localising in the mitochondria.

Peterson *et al.* used rhodol's inherent ability to localise in the endoplasmic reticulum to develop a series of probes for selective and sensitive $ONOO^-$ detection.[137] Their most promising candidate (Scheme 4) was taken forward for *in vitro* studies with

RAW264.7 macrophages. Interestingly, the group employed a different approach to stimulate RAW264.7 macrophages to produce endogenous $ONOO^-$ compared to standard procedures where LPS and IFN-γ are used. DNP-modified amino tentagel beads bound to anti-DNP IgG were used to stimulate phagocytosis resulting in the production of $ONOO^-$. Essentially the bead bound antibodies are recognised by Fc receptors which then are engulfed by receptor mediated phagocytosis triggering the production of cellular $ONOO^-$. The rhodol probe was able to detect endogenous $ONOO^-$ in the endoplasmic reticulum, confirmed through the usage of an ERTracker probe.

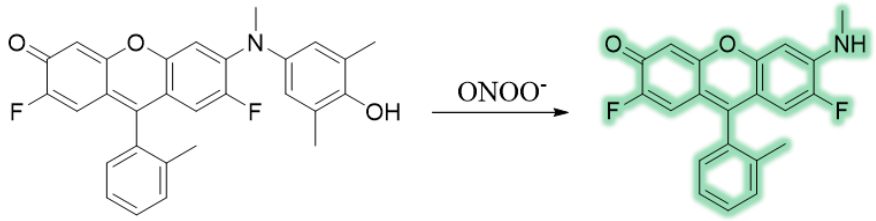

Scheme 4: An $ONOO^-$ sensitive and selective rhodol based fluorescent probe localising in the endoplasmic reticulum.

In summary, fluorescein, rhodamine and rhodol fluorophores have all been used in the development of ROS probes. Using rhodamine or rhodol as the core structure allows for targeted localisation of the probe in the mitochondria or the endoplasmic reticulum respectively. Studying ROS production in organelles allows for more accurate studies of ROS diffusion and its implications in physiological processes. While organelle targeted probes might be more useful for imaging applications, they can still be valuable tools for clinical studies.

1.1. Project Aim

The aim of this chapter was to synthesise a small series of $ONOO^-$ probes incorporating a benzyl boronate unit as a sensing unit. Hereby, this unit was introduced

into fluorescein, rhodamine and rhodol with the aim to develop targeted organelle probes. Upon reaction of **5.1**, **5.2** and **5.3** with $ONOO^-$, the benzyl Bpin unit is cleaved giving the respective fluorescent fluorophores (Scheme 5).

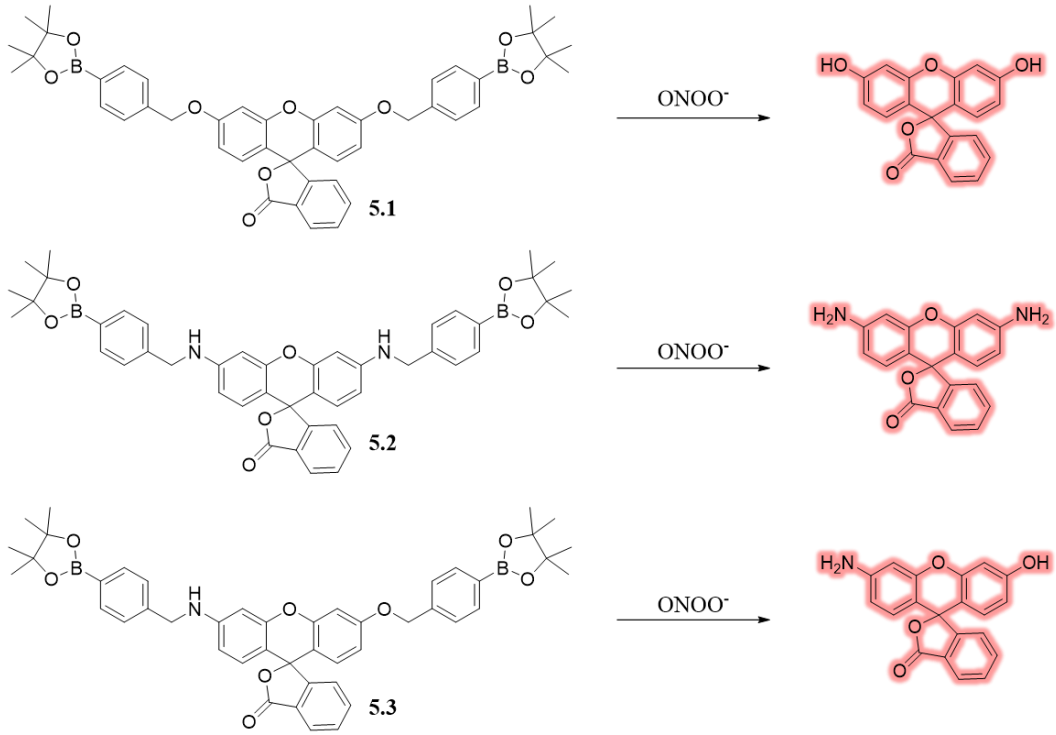

Scheme 5: A series of $ONOO^-$ probes based on fluorescein, rhodamine and rhodol.

2. Results & Discussion

2.1. Synthesis of a Series of $ONOO^-$ Fluorescent Probes

Fluorescein based probe **5.1** has previously been synthesised by Cohen *et al.* validating it as a H_2O_2 probe.[138] However, due to the inherent nature of boronic esters, it seemed to be an excellent opportunity to study its ability to detect $ONOO^-$. The bis(benzyl boronic ester) moiety has previously been used in the literature as a scaffold to mask fluorophores. Additionally, a further literature search revealed that Strongin *et al.* designed a highly similar probe to **5.2** for saccharide sensing (Figure 5).[139, 140] Hence, targets **5.1**, **5.2** and **5.3** should be synthetically achievable.

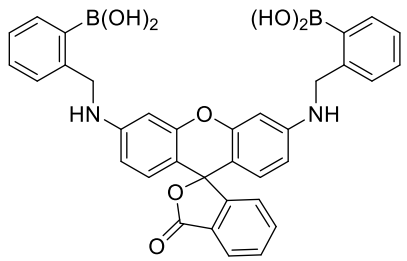

Figure 5: A rhodamine based probe for saccharide sensing.

Target probe **5.1** was synthetically easily accessible as previously reported.[138] Briefly, fluorescein **6.1** was substituted with 4-bromomethylphenylboronic acid pinacol ester **6.2** to give **5.1** in 30 % yield (Scheme 6).

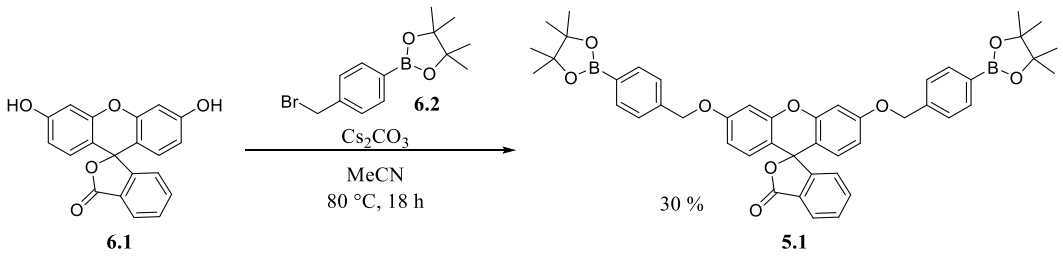

Scheme 6: Synthesis of fluorescein based probe **5.1**.

Next, the synthesis of rhodamine based probe **5.2** was accessed (Scheme 7). Rhodamine 110 is commercially available but 1g of rhodamine 110 costs £263 on Sigma Aldrich. Hence, in contrast to fluorescein, the core structure of the fluorophore had to be developed. Rhodamine 110 **7.3** was achieved in 35 % yield by refluxing 3-aminophenol **7.1** and phthalic anhydride **7.2** in methanesulfonic acid. This was followed by a reductive amination with **7.5** which was previously synthesised from 4-bromobenzaldehyde **7.4** via a Miyaura borylation. This gave **5.2** in 27 % yield.

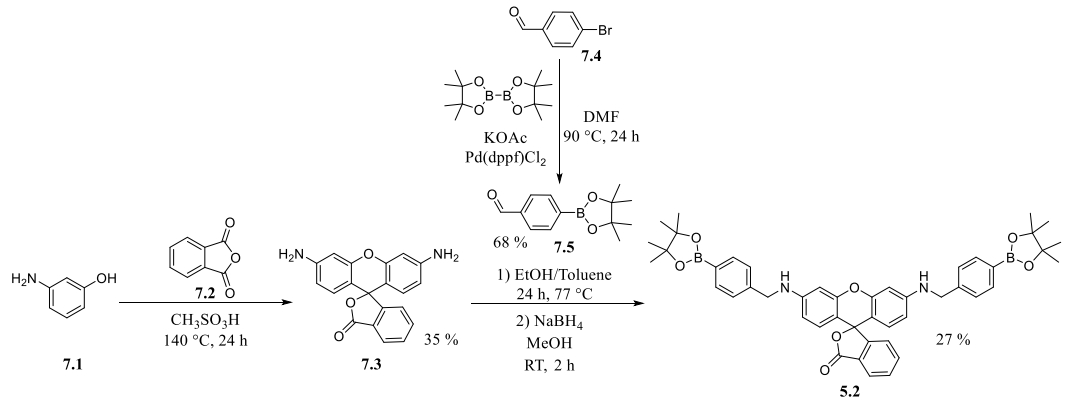

Scheme 7: Synthesis of rhodamine based probe **5.2**.

Similarly, rhodol based probe **5.3** was accessed. 3-aminophenol **7.1**, resorcinol **8.1** and phthalic anhydride **7.2** were refluxed in methanesulfonic acid. This gave rhodol **8.2** in 33 % yield. Target probe **5.3** was successfully achieved in 33 % from rhodol **8.2** and 4-bromomethylphenylboronic acid pinacol ester **6.2** (Scheme 8).

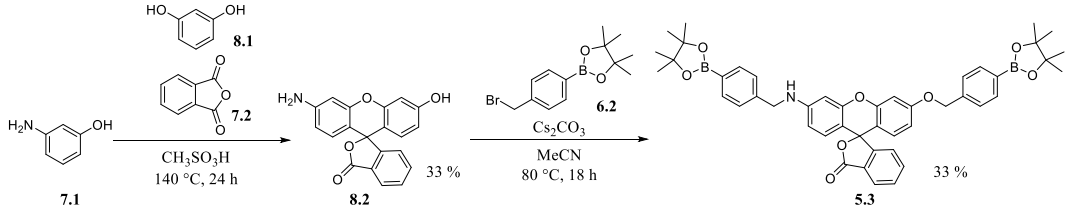

Scheme 8: Synthesis of rhodol based probe **5.3**.

It was postulated that all three probe **5.1**, **5.2**, **5.3** upon reaction with $ONOO^-$ will be activated in the same fashion as outlined in Scheme 9. The benzyl Bpin moieties are essentially cleaved giving free fluorescein, rhodamine and rhodol respectively.

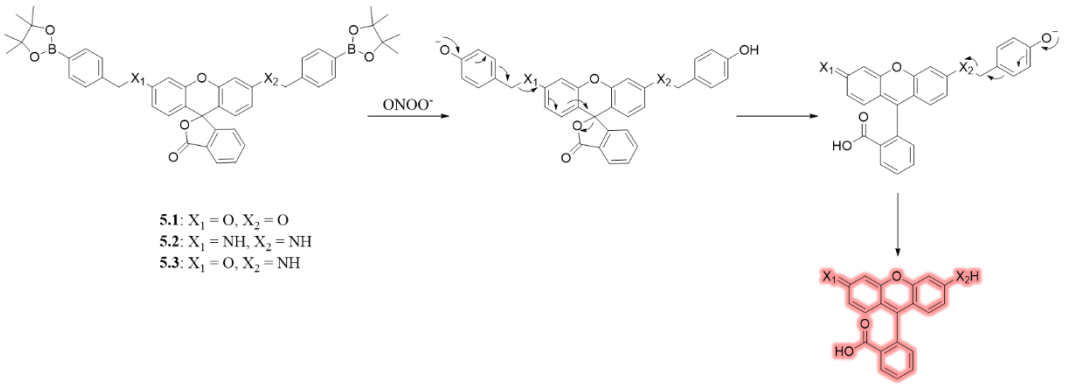

Scheme 9: Probe **5.1**, **5.2** and **5.3** reacting with $ONOO^-$ to generate fluorescent fluorescein, rhodamine and rhodol respectively.

2.2. Fluorescence Studies

Prior to fluorescence studies, initial UV spectra were recorded to observe changes in absorbance of the masked fluorescein **5.1**, rhodamine **5.2** and rhodol **5.3** alone and upon addition of $ONOO^-$ (Figure 6). Maximum absorption peaks at λ = 493, 510, 495 nm for **5.1**, **5.2** and **5.3** with $ONOO^-$ respectively were observed which mostly correlate with known absorption maxima of these fluorophores. Additionally, the maximum absorption correlates with the ideal excitation wavelength.

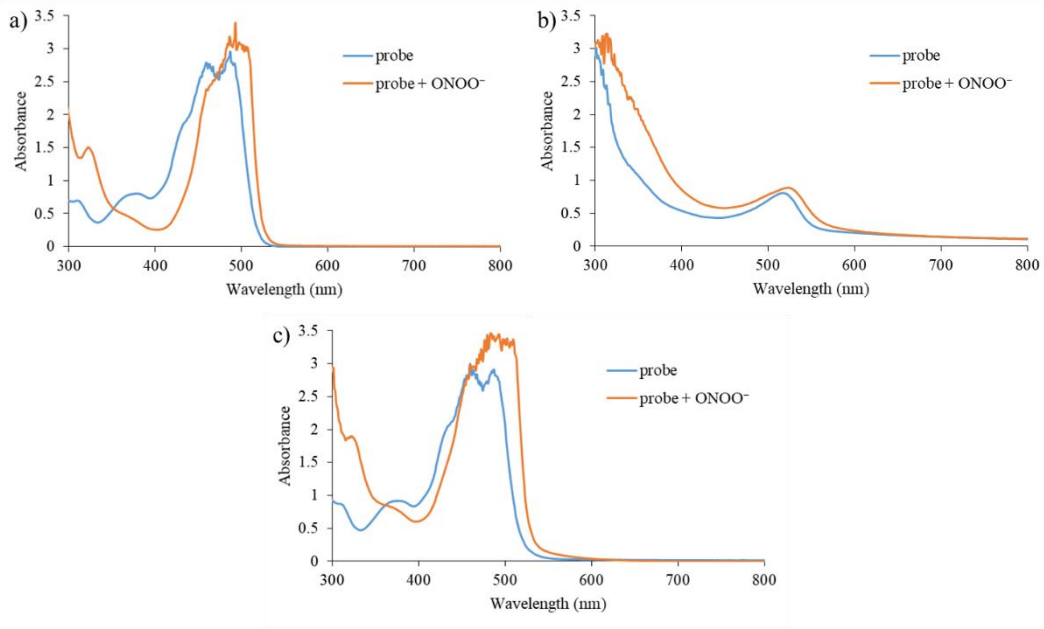

Figure 6: UV spectra of probes a) **5.1**, b) **5.2** and c) **5.3** without and with $ONOO^-$ (excess) in PBS buffer 52 % MeOH : H_2O, pH = 7.4 at 25 °C measured on a BMG Labtech CLARIOstar® plate reader.

First, a ROS selectivity study was carried out for each probe to validate its selectivity towards $ONOO^-$ over other ROS (Figure 7). Probes **5.1**, **5.2** and **5.3** preferentially detected $ONOO^-$ over a range of other ROS which were used at maximum biological concentrations to avoid any selectivity issues in future *in vitro* studies.

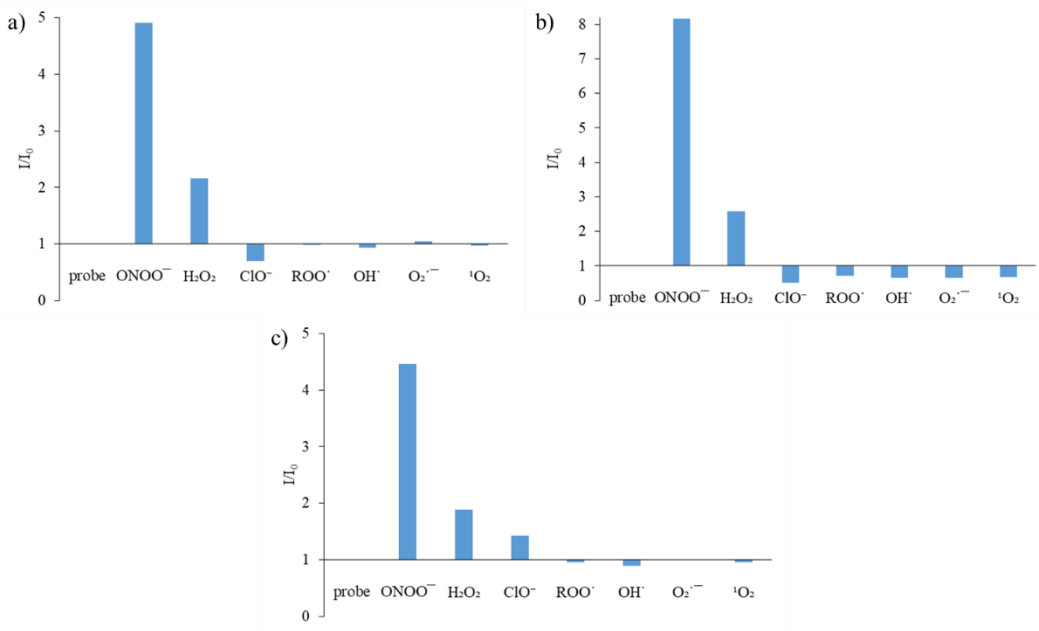

Figure 7: Selectivity data for probes a) **5.1** (500 nM), b) **5.2** (1 µM), and c) **5.3** (500 nM) in the presence of $ONOO^-$ (50 µM), $OH\cdot$ (500 µM), $O_2^{\cdot-}$ (500 µM), $^1O_2$ (500 µM) after 5 min. H_2O_2 (1 mM), $ROO\cdot$ (500 µM) and ClO^- (500 µM) were measured after 30 min. The data was obtained in PBS buffer 52 % MeOH : H_2O, pH = 7.4 at 25 °C at λ_{ex} = 475 (bandwith: 10) nm and max λ_{em} = 515 nm on a BMG Labtech CLARIOstar® plate reader.

5.1, **5.2** and **5.3** were initially evaluated with H_2O_2 by evaluating the change of fluorescence intensity over time (Figure 8). Hereby, it was noticed that all three probes **5.1**, **5.2**, and **5.3** are slightly fluorescent by themselves.

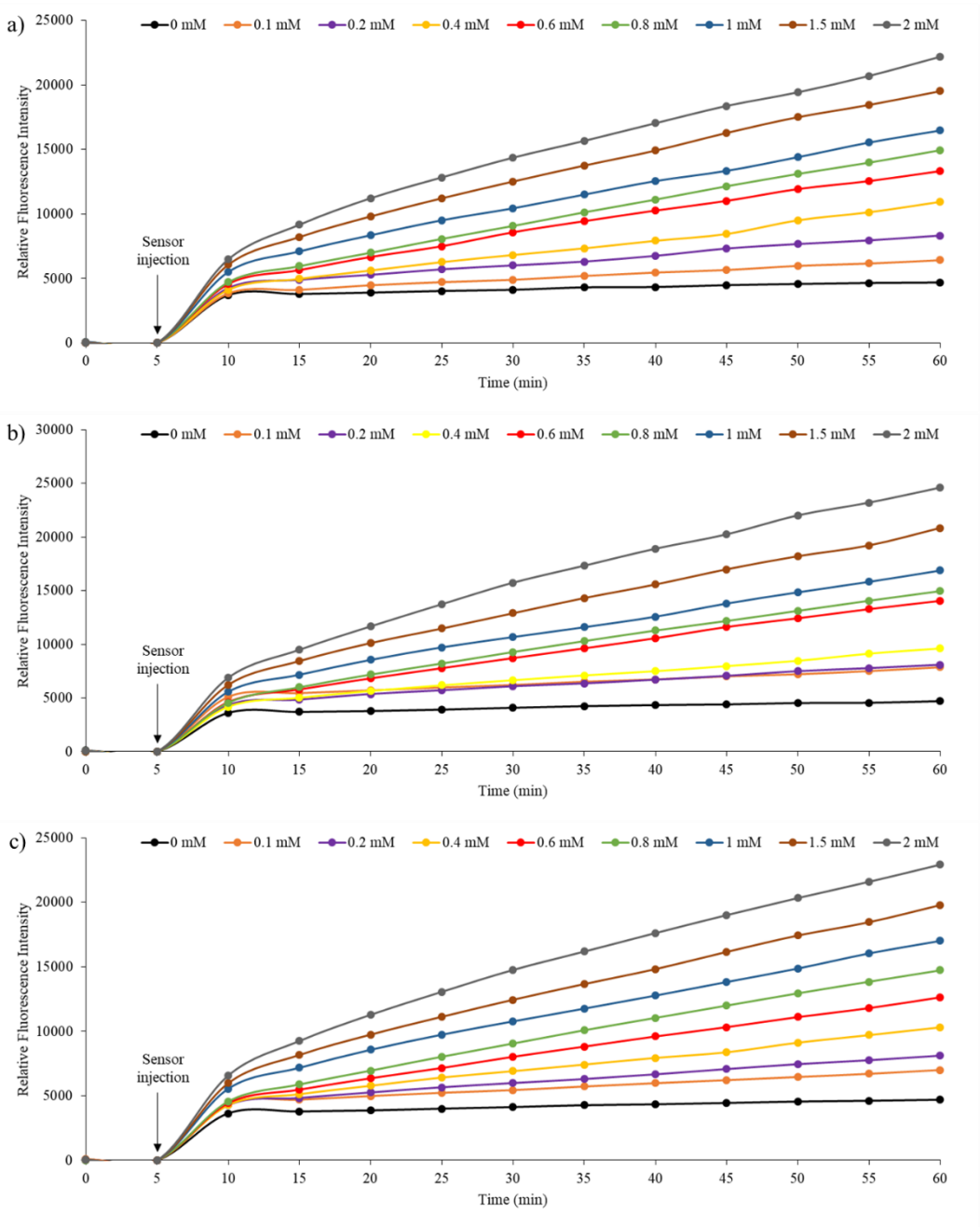

Figure 8: Fluorescence intensity changes over time for probes a) **5.1** (500 nM), b) **5.2** (500 nM) and c) **5.3** (500 nM) in the presence of H_2O_2 (0.1, 0.2, 0.4, 0.6, 0.8, 1, 1.5, 2 mM) in PBS buffer 52 % MeOH : H_2O, pH = 7.4 at 25 °C. Fluorescence intensities were measured with λ_{ex} = 475 (bandwith: 10) nm and max λ_{em} = 515 nm on a BMG Labtech CLARIOstar® plate reader.

Fluorescence titrations with H_2O_2 were carried out for **5.1**, **5.2** and **5.3** (Figure 9) with LoDs identified to be 6.5 µM, 103.7 µM, 126.3 µM respectively. Both **5.2** and **5.3**

seem to be slightly fluorescent by itself but still show good turn-on responses with H_2O_2.

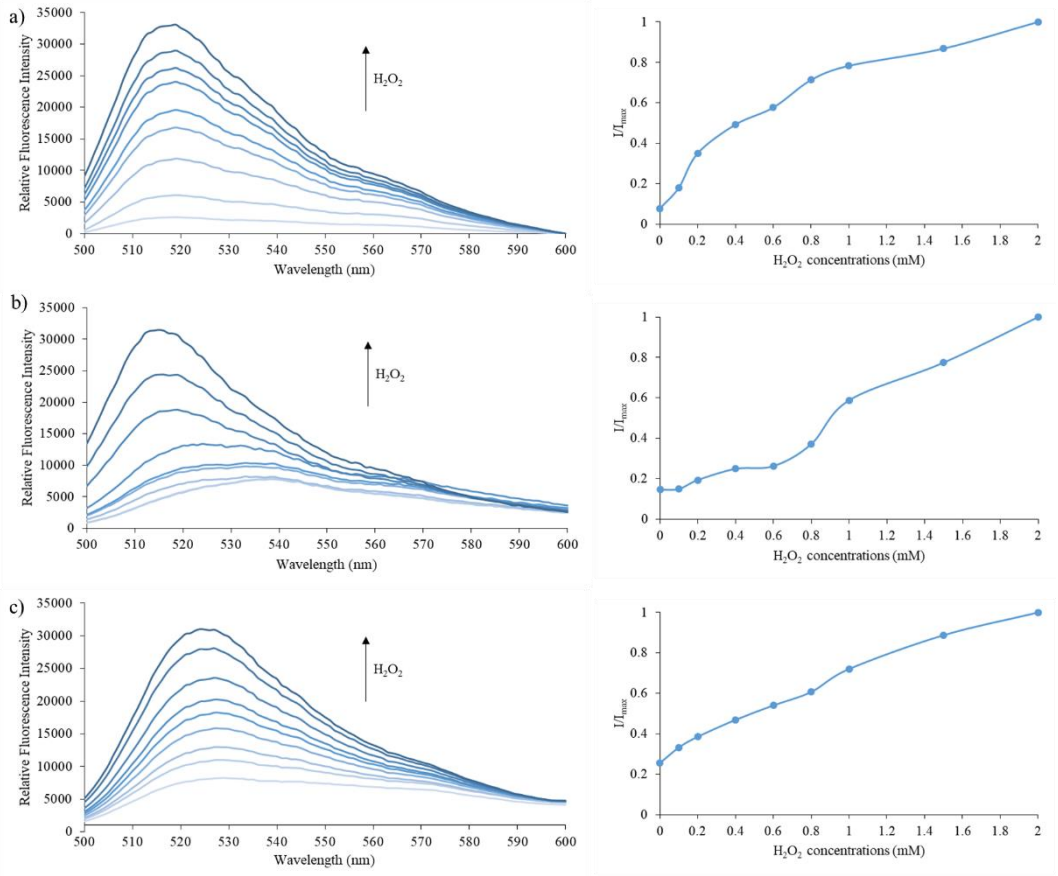

Figure 9: Emission spectra and dose dependence curve (I/I_{max}) a) **5.1** (500 nM), b) **5.2** (1 µM) and c) **5.3** (500 nM) in the presence of H_2O_2 (0.1, 0.2, 0.4, 0.6, 0.8, 1, 1.5, 2 mM) in PBS buffer 52 % MeOH : H_2O, pH = 7.4 at 25 °C. Fluorescence intensities were measured with λ_{ex} = 475 (bandwith: 10) nm and max λ_{em} = 515 nm on a BMG Labtech CLARIOstar® plate reader.

Following on from these results, $ONOO^-$ titrations confirmed better sensitivity towards $ONOO^-$ over H_2O_2 for all probes (Figure 10). Lower concentrations compared to H_2O_2 were used to achieve good turn-on responses for **5.1** and **5.3**. **5.2** required similar concentrations to H_2O_2 which might limit its ability to detect $ONOO^-$ *in vitro*. LoDs were determined: 0.89 µM, 27 µM and 0.49 µM for **5.1**, **5.2** and **5.3** respectively.

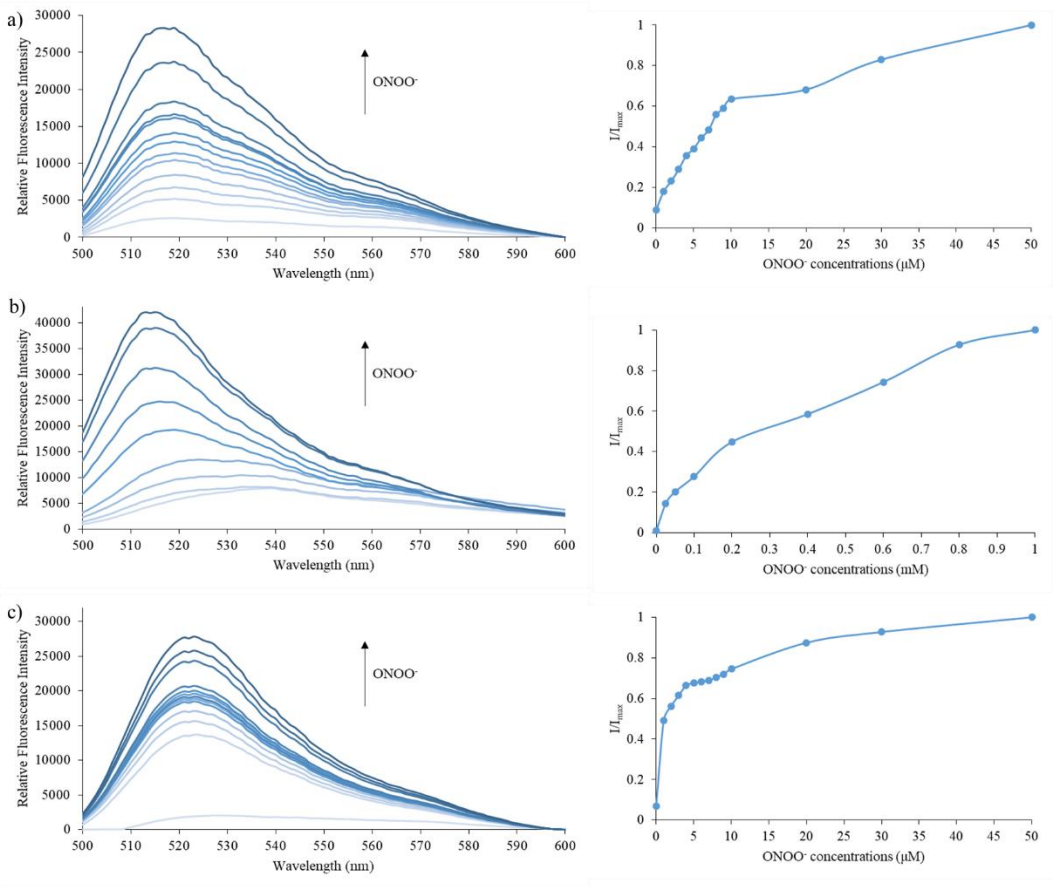

Figure 10: Emission spectra and dose dependence curve (I/I_{max}) for a) **5.1** (500 nM), and c) **5.3** (500 nM) in the presence of $ONOO^-$ (1, 2, 3, 4, 5, 6, 7, 8, 9, 10, 20, 30, 50 μM) and b) **5.2** (1 μM) in the presence of $ONOO^-$ (0.025, 0.05, 0.1, 0.2, 0.4, 0.6, 0.8, 1 mM) in PBS buffer 52 % MeOH : H_2O, pH = 7.4 at 25 °C. Fluorescence intensities were measured with λ_{ex} = 475 (bandwith: 10) nm and max λ_{em} = 515 nm on a BMG Labtech CLARIOstar® plate reader.

2.3. Cell Studies

All three probes **5.1**, **5.2** and **5.3** were evaluated in collaboration with the research group of Juyoung Yoon at Ewha Woman's University in Seoul, Korea. As an initial starting point, probes **5.1**, **5.2**, and **5.3** were tested in HeLa cells for their ability to detect exogenously generated $ONOO^-$ inside cells. HeLa cells were stimulated with exogenous $ONOO^-$ for 20 min followed by incubation of the probe for 20 min. Confocal imaging revealed that **5.1**, **5.2** and **5.3** are all cell permeable (Figure 11).

However, in the absence of $ONOO^-$, all three probes show significant background fluorescence. Upon addition of $ONOO^-$ (50 or 100 μM), the intensity of the fluorescence signal seems to stay the same when the probes **5.1**, **5.2** and **5.3** are incubated alone. This suggests that probes **5.1**, **5.2** and **5.3** might quickly decompose to fluorescein, rhodamine and rhodol respectively with the benzyl Bpin groups being labile enough *in vitro* prior to the presence of $ONOO^-$. Hence, no further cell studies were undertaken. Looking back to the cell studies carried out by Cohen *et al.* on **5.1**[141], a similar behaviour was observed when the probe was incubated alone compared to the presence of H_2O_2. The group looked into the mean fluorescence and was able to show a statistical significant difference in the fluorescence output. While this is not ideal, this could be looked into with all three probes **5.1**, **5.2** and **5.3** when exposed to $ONOO^-$. Nevertheless, further synthetic modifications are required to allow **5.1**, **5.2** and **5.3** to become effective fluorescent tools for *in vitro* and *in vivo* studies.

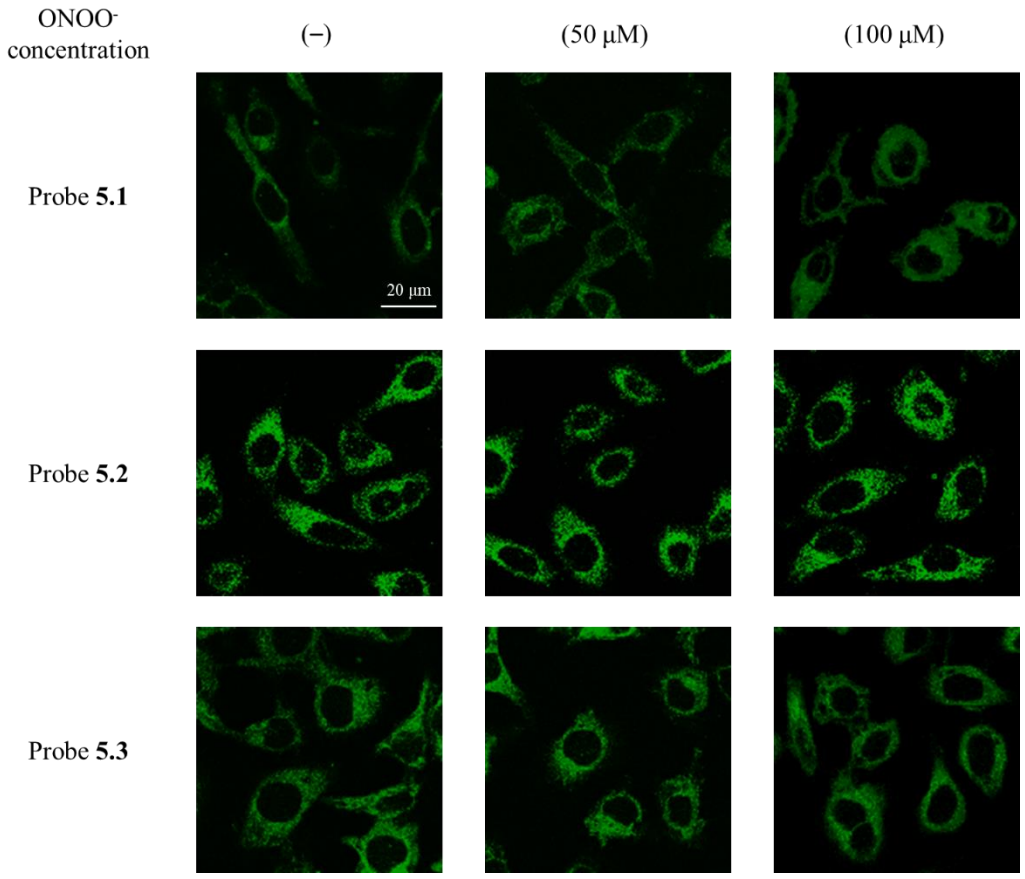

Figure 11: HeLa cells were stimulated with $ONOO^-$ (50 or 100 μM) for 20 min. Probe **5.1** (200 nM), **5.2** (500 nM) or **5.3** (500 nM) was incubated for 20 min. Green channel: λ_{ex} = 473 nm, λ_{em} = 490 – 590 nm. Scale bar: 20 μm. Magnification x60. N = 3. Cell imaging experiments were kindly carried out by Juyoung Yoon's research group.

3. Conclusions

We have successfully synthesised three $ONOO^-$ sensitive and selective probes based on different fluorophores: fluorescein for **5.1**, rhodamine for **5.2** and rhodol for **5.3**. While ROS selectivity studies revealed preferential detection of $ONOO^-$ for **5.1**, **5.2**, and **5.3**, it also showed that all three probes **5.1**, **5.2**, **5.3** exhibit some inherent fluorescence by themselves. Nevertheless, good turn-on responses were observed with both H_2O_2 and $ONOO^-$ titration studies, confirming the applicability of these probes. Cell studies with HeLa cells revealed that **5.1**, **5.2** and **5.3** showed inherent

fluorescence and no change in fluorescence signal upon the addition of $ONOO^-$ was observed.

4. Future Work

Despite probes **5.1**, **5.2** and **5.3** being inherently fluorescent in cells, further synthetic modifications could overcome this issue. To support the targeting aspect of **5.1**, **5.2** and **5.3**, additional relevant organelle targeting groups could be introduced into the scaffold (Figure 12).

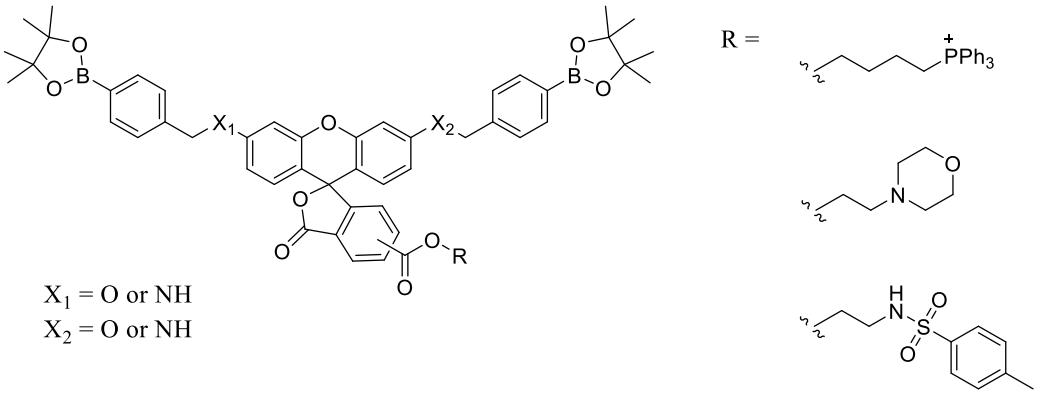

Figure 12: Enhanced targeting motifs incorporated into fluorescein, rhodamine and rhodol scaffolds.

The development of dual analyte sensing probes ($ONOO^-$ and esterase or other enzymatic triggers) or theranostic probes (Figure 13) could also offer further insights in cellular processes as well as combine diagnosis with therapy in an effort to move towards more clinically relevant tools.

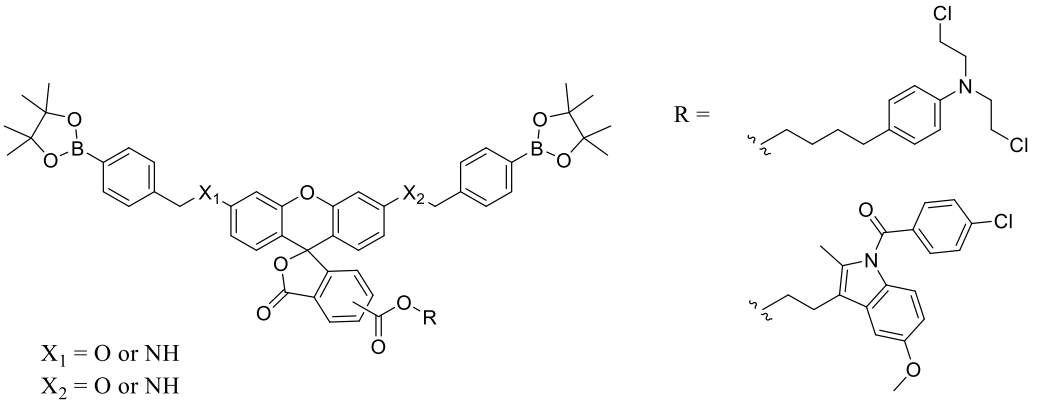

Figure 13: Suggested probes for theranostics applications.

If the benzyl Bpin structural motif and the additional synthetic modification will not suppress the fluorescence, another strategy could be to use already developed dual analyte probes in the James group[142, 143] and integrate the organelle targeting motifs (Figure 14). The tunability of the fluorophore scaffolds should allow to identify new organelle targeting probes for dual analyte detection.

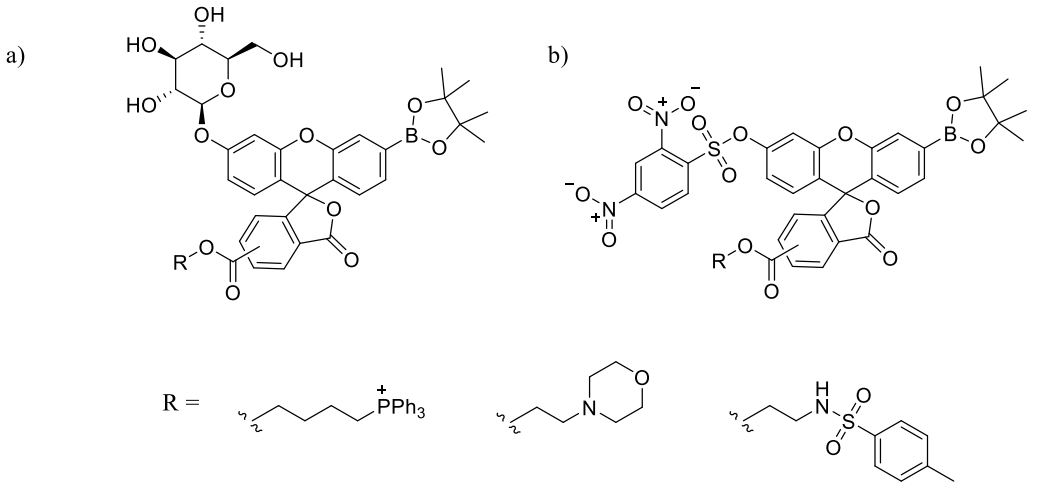

Figure 14: Dual analyte probes for a) H_2O_2 and β-glucosidase[143] and b) $ONOO^-$ and GSH[142] developed in the James group.

Chapter 5 – A Rhodamine Based Probe for the Selective and Sensitive Detection of GSH

1. Introduction

Glutathione (GSH) serves as an antioxidant, hence, playing a key role in oxidative stress. As the most abundant thiol based compound in cells, it is key to a variety of cellular functions. The interconversion of GSH to its oxidised form GSSG is the basis for some key metabolic processes (Scheme 1): GSSG is involved in protein modification and consequently, signal transduction.[144]

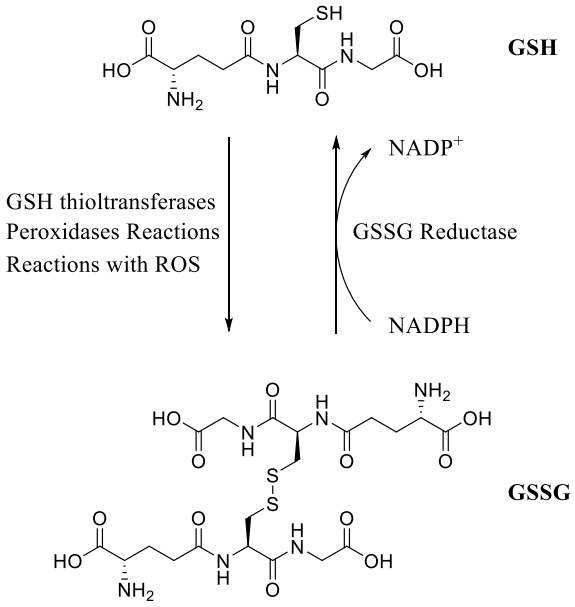

Scheme 1: Simplified diagram of the interconversion of GSH and GSSG.

Abnormal levels of GSH have been linked to cancer, liver and lung damage as well as Parkinson's disease.[145] Hence, the development of fluorescent probes would benefit understanding GSH's involvement in disease progression.[146] Yoon and co-workers have reviewed the main strategies for reaction based fluorescent probes for GSH[147], which include but are not limited to (Scheme 2):

a. Cleavage of sulphonamide, sulfonate ester, and related functional groups
b. Se–N bond cleavage
c. Aryl substitution reactions
d. Disulfide bond cleavage and cyclization
e. Michael addition

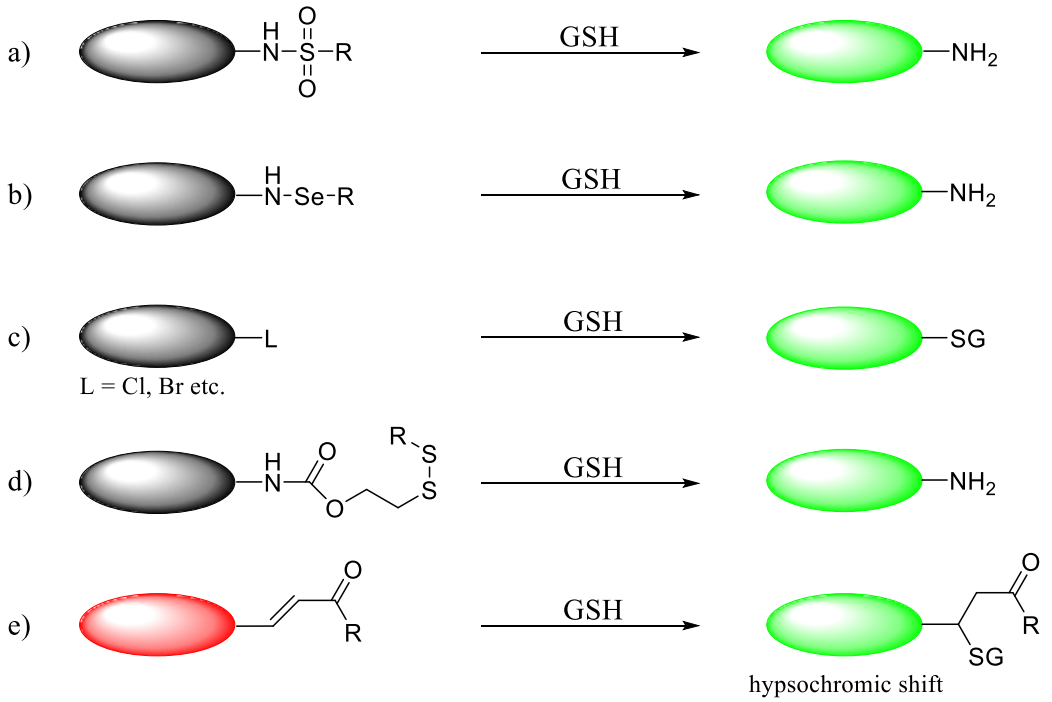

Scheme 2: Reaction based strategies for probes detecting GSH: black – non fluorescent, red or green: fluorescent.

Herein, an overview of the current literature for GSH probes will be discussed, which include some the above mentioned strategies.

Huang *et al*. developed a rhodamine based probe for GSH detection with a fast detection response that accumulated selectively in the lysosome, allowing it to be used over a wide range of pH values (Scheme 3).[148] Their sensing strategy is based on Michael addition of the nucleophilic thiol unit of GSH to the α,β-unsaturated alkene fragment of the probe. After Michael addition, formation of an H-bond between the rhodamine carbonyl and the N-H group of GSH promotes hydrolysis and ring opening of the spirocyclic amide bond to give rhodamine B, which is a well-known and studied

fluorophore. Fluorescence studies were performed on a range of amino acids, which showed preferential selectivity for detection of GSH. However, the authors failed to also perform a RSS and ROS selectivity test to show that no reactivity would occur with H_2S or other strong oxidants. The probe accumulated selectively in the lysosomes of HeLa cells.[149, 150]

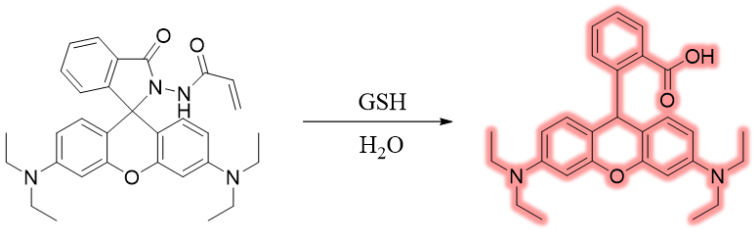

3.1 **Rhodamine B**

Scheme 3: A rhodamine based probe **3.1** for GSH detection in lysosomes.

Wu and co-workers also developed a rhodamine B based system for GSH detection based on Michael addition of the thiol unit of GSH to a maleimide moiety, which results in ring opening to afford a fluorescent rhodamine B structure **4.2** (Scheme 4).[151-153] Fluorescence studies against other amino acids confirmed its selectivity and sensitivity for GSH, although RSS and ROS selectivity tests were not carried out. Cell studies in HepG2 and HUVEC cells demonstrated that probe **4.1** could be used for *in vitro* detection of GSH.

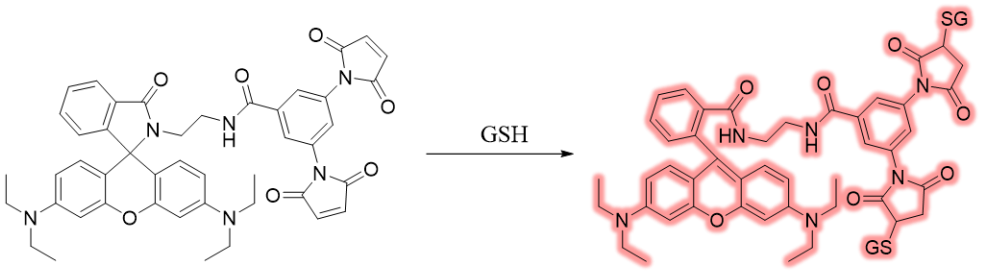

4.1 **4.2**

Scheme 4: Rhodamine B based scaffold with maleimide moieties **4.1** for GSH sensing.

Although selective detection of GSH is important, probes for the simultaneous detection of multiple biological thiol species (cysteine, homocysteine or H_2S) have also been developed. Many of these probes employ a dual or tri-channel sensing system, whereby reaction with a thiol analyte results in the fluorophore emitting at a different emission wavelength. Chen *et al.* developed a coumarin fluorescent probe **5.1** that emits at different wavelengths, depending on whether it reacts with GSH or H_2S_n (Scheme 5).[154] The phenylselenide moiety of the probe is substituted by the thiol group of GSH through a S_NAr substitution reaction to afford product **5.2** that emits green fluorescence. Reaction with H_2S_n also results in a S_NAr substitution followed by intramolecular cyclisation of the second thiol unit to afford an ester group, which results in the formation of non-fluorescent **5.4** and the blue fluorescent **5.3**. Therefore, access to two distinct emission channels enables probe **5.1** to be used for the selective discrimination between these two thiols in cellular systems such as RAW264.7 macrophages.

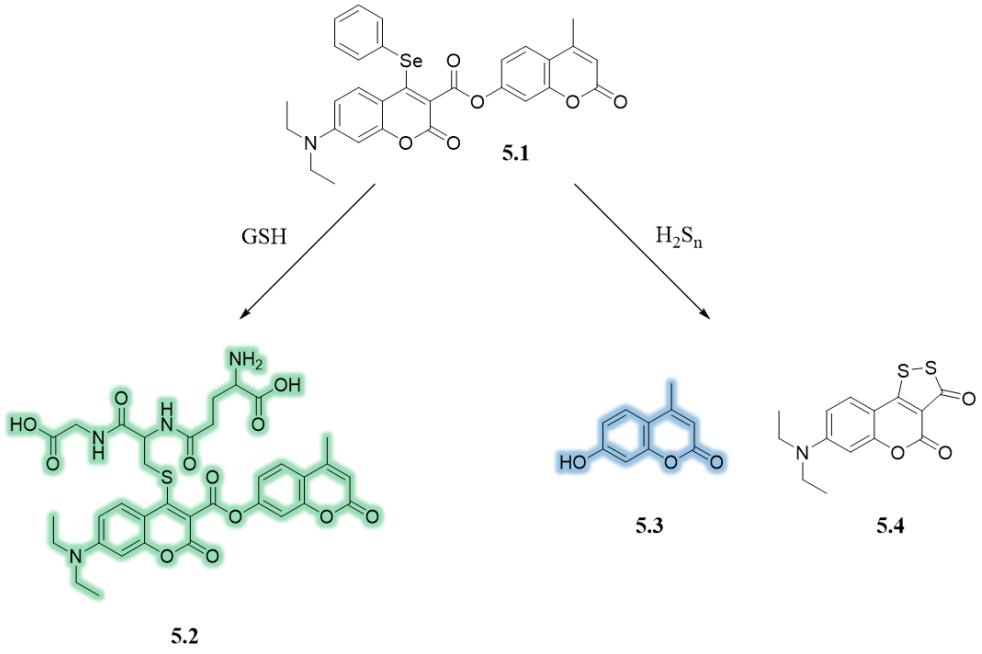

Scheme 5: A coumarin based probe **5.1** which can discriminate between GSH and H_2S_n through different mechanisms that generate either green or blue fluorescent outputs.

In the same manner, Churchill and co-workers have developed two doubly activated dual emission fluorescent probes for GSH and cysteine/homocysteine (Scheme 6).[155] The phenylselenium group quenches the fluorescence of the probe due to photoinduced electron transfer with the ethyl butanoate group, introduced to improve water solubility. The amino group of the GSH undergoes intramolecular reaction with the aldehyde group of probes **6.1**/**6.2** to afford a cyclic iminium species, with the thiol unit of the GSH fragment undergoing S_NAr displacement of the phenylselenium group to give a functionalised probe that exhibits red fluorescence.[156] Alternatively, the amino and thiol groups of cysteine/homocysteine react with the aldehyde group of the probe to afford a 5-membered oxazoline ring, with the amino group of a second molecule of cysteine/homocysteine then undergoing an S_NAr reaction of the SePh group to give a green fluorescent probe. The tandem reaction of S,N substitution-rearrangement in the case of cysteine/homocysteine in contrast to GSH allows for the selective discrimination of the two species. This strategy allows to evaluate different thiols with the same probe within different flourescence channels, an effective tool used throughout literature.[157-160] Both probes **6.1** and **6.2** showed good turn on response for GSH and cysteine in solution based studies, affording selective emission at two different wavelengths. However, cell studies with A549 cells revealed that **6.2** showed better turn-on response for GSH when compared to **6.1**, whose red fluorescence signal output was weak. Hence, only **6.2** was taken forward for further *in vivo* studies, with **6.2** shown to be capable of detecting high levels of GSH in A549 tumour bearing nude mice. The fluorescence signal of **6.2** in tumour mice was higher than in healthy mice, which still exhibited some weak fluorescence.

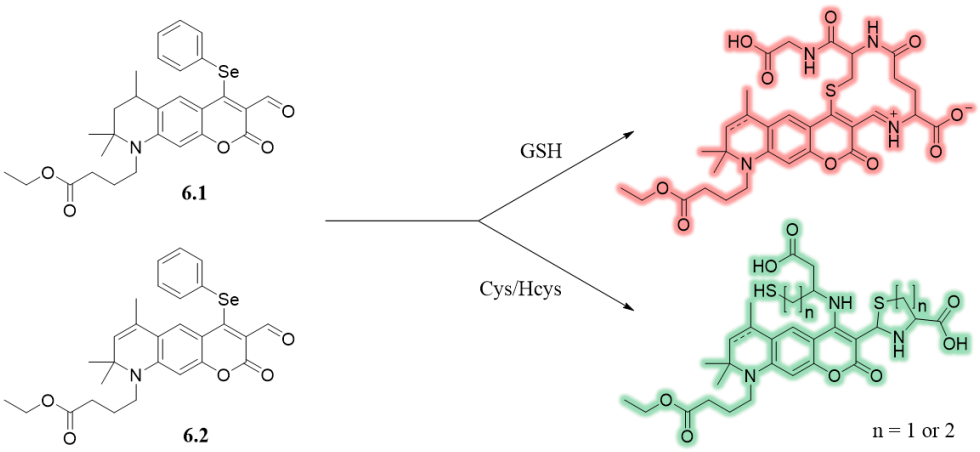

Scheme 6: Coumarin-based fluorescent probes **6.1** and **6.2** for the simultaneous detection of GSH and cysteine/homocysteine exhibit two distinct emission signals: red and green fluorescence.

Zhang *et al*. have designed a lysosome targeted fluorescent probe **7.1**, which can simultaneously detect H_2S, cysteine/homocysteine and GSH.[161] This probe incorporates two fluorophores (resorufin and coumarin) and a morpholine unit for lysosome targeting. The main site of reaction for all three species is the phenolic ether linkage connecting the two fluorophores. Scheme 7 shows the different fluorophore species postulated to form, when the probe reacts with H_2S, cysteine/homocysteine or GSH. Upon reaction with H_2S, resorufin is released which emits a red signal, whereas the displaced thio-coumarin derivative is non fluorescent. When **7.1** reacts with cysteine/homocysteine, resorufin is generated along with a new aza-coumarin (via rearrangement of the thio-coumarin intermediate) derivative. This results in the generation of red and blue fluorescent signals. Finally, the use of GSH results in a red and green fluorescence signal being produced, which are attributed to the formation of resorufin and a GSH-coumarin adduct, respectively. Probe **7.1** was shown to exhibit distinct signal patterns in HeLa cells: red for H_2S, blue-red for cysteine/homocysteine and green-red for GSH. This enabled discrimination of lysosomal H_2S, cysteine/homocysteine and GSH within the cells, with *N*-ethylmaleimide used as a thiol scavenger to establish negative controls.

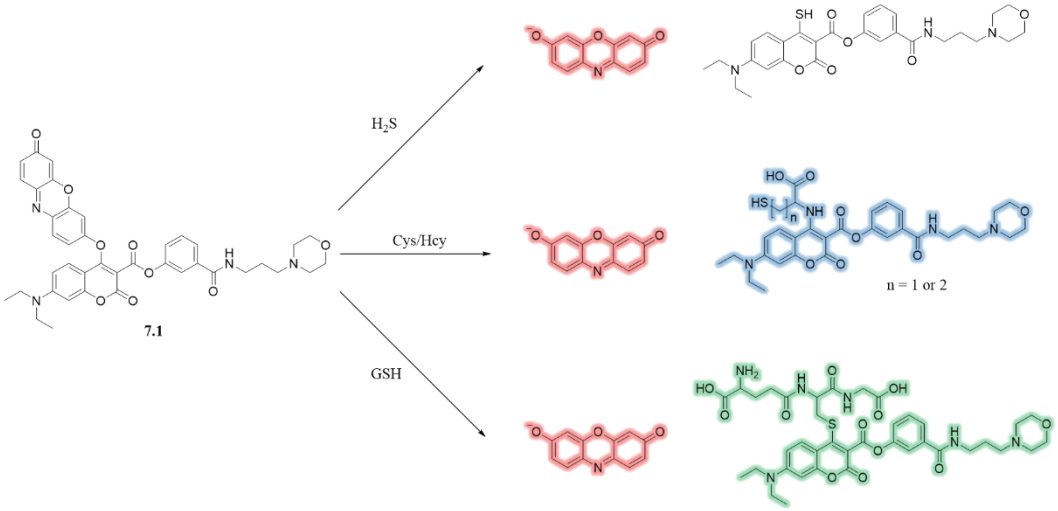

Scheme 7: Proposed mechanisms for the reaction of probe **7.1** with H_2S, cysteine/homocysteine and GSH.

1.1. Project Aim

The focused literature review reveals the development of selective and sensitive fluorescent probes for GSH, with more recent attention directed towards sensing two biothiols that are present at the same time. These probes have the potential to discriminate between multiple biothiols in the same biological environment and can be used as tools to probe their role in biological pathways. Hence, the development of a dual fluorescent probe that can discriminate between GSH and other biothiols (H_2S, cysteine etc.) at the same time was the broader aim of this project. This led in the first instance towards the validation of sensing a single biothiol: GSH.

2. Results & Discussion

First, azidorhodamine **8.4** was evaluated as a probe for H_2S, since it is known to act as both a good reducing agent and nucleophile in a variety of physiological processes required to maintain cellular health. Due to its inherent reactivity, H_2S can react with oxidised thiols[162] as well as interacting with a variety of metal centres.[163] Developing a probe to determine the involvement of H_2S as a reactive sulphur species in oxidative

stress processes would be beneficial. Azides have previously been reported as excellent sensing groups for H_2S,[164] which are reduced by H_2S to their corresponding amines (Scheme 8). A disubstituted azidorhodamine probe (and other mono azidorhodamine derivatives) has previously been synthesised by Chang and co-workers as a H_2S probe (Scheme 8).[165] Hence, I was confident that probe **8.4** would be a good probe for H_2S, whose free amine group could then be functionalised further with other sensing groups to allow for the development of a dual analyte probe.

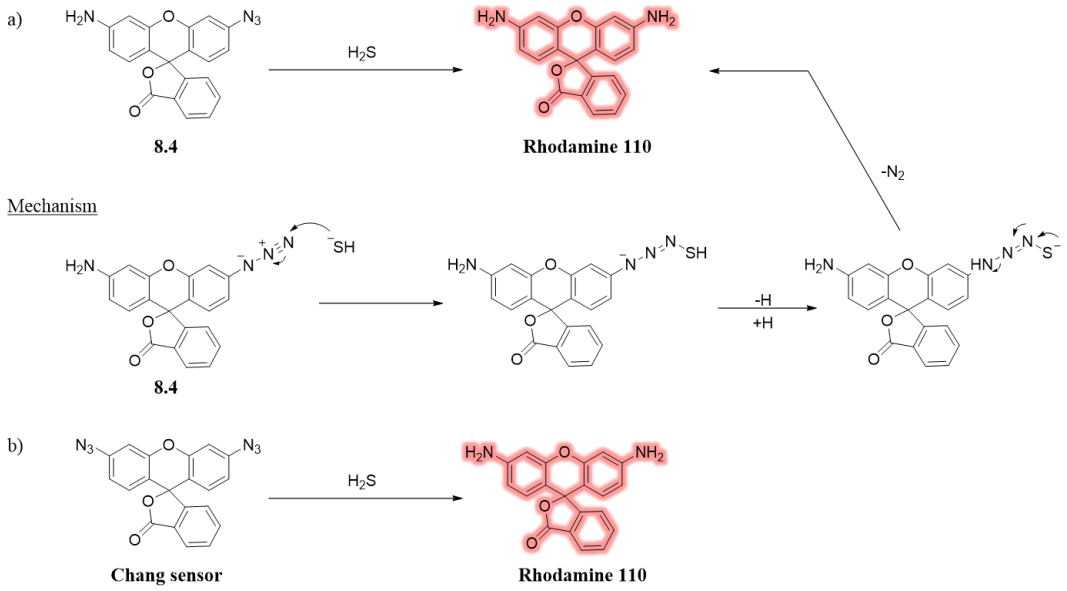

Scheme 8: a) Postulated conversion of **8.4** into rhodamine 110 upon reaction with H_2S, b) Diazidorhodamine made by Chang *et al.*[165] is reduced into rhodamine 110 upon reaction with H_2S.

Azidorhodamine probe **8.4** has previously been synthesised as an intermediate for imaging mRNA.[166, 167] Therefore, azidorhodamine **8.4** was easily prepared by refluxing 3-aminophenol **9.1** and 3-iodophenol **9.2** at 140 °C in the presence of methanesulfonic acid to afford iodorhodamine **9.3** in 48 % yield, which was double the 24 % yield previously reported in the literature.[167] Subsequently, the iodine group of **9.3** was substituted with azide via treatment with NaN_3, sodium ascorbate, CuI and DMEDA in DMSO/H_2O to afford azidorhodamine **8.4** in 60 % yield (Scheme 9).

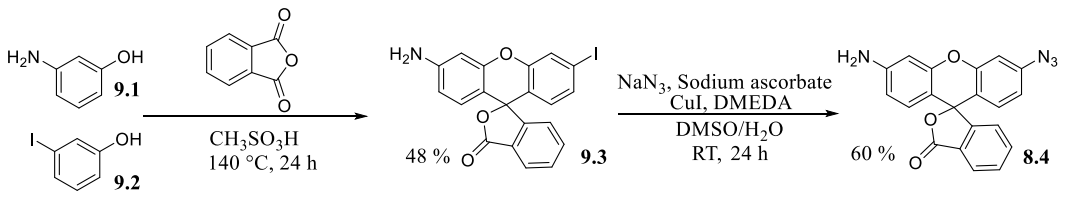

Scheme 9: Synthesis of azidorhodamine **8.4**.

Fluorescence analysis commenced with titration of various concentrations of H_2S with probe **8.4**, whose fluorescence profile was consistent with the formation of rhodamine 110. Hence, this allowed us to confirm the postulated conversion of azidorhodamine into rhodamine 110, with data analysis revealing a LoD of 0.33 µM (Figure 1).

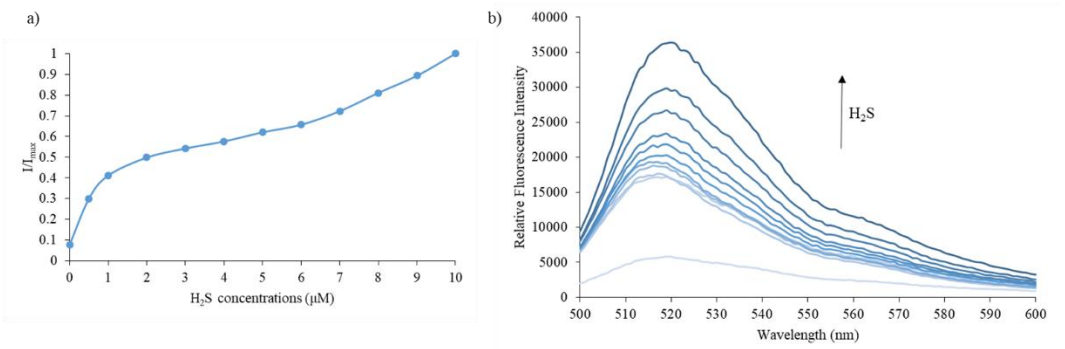

Figure 1: a) Dose dependence curve (I/I_{max}) and b) emission spectrum for probe **8.4** (500 nM) in the presence of H_2S (0.5, 1, 2, 3, 4, 5, 6, 7, 8, 9, 10 µM) in PBS buffer 52 % MeOH : H_2O, pH = 7.4 at 25 °C. Fluorescence intensities were measured with λ_{ex} = 472 (bandwith: 20) nm and max λ_{em} = 520 nm on a BMG Labtech CLARIOstar® plate reader after 30 min.

These positive results led us to perform a RSS and ROS selectivity test to confirm **8.4**'s ability to selectively detect H_2S, with relevant (maximum) biological levels for all RSS and ROS species used in these selectivity tests (Figure 2).

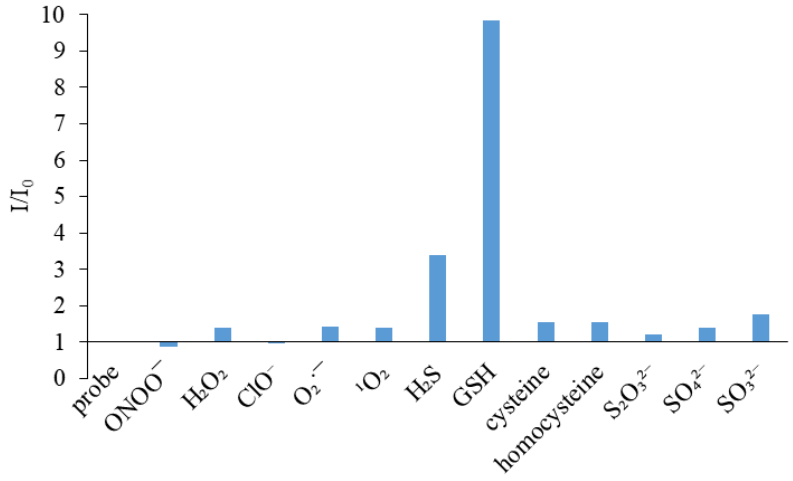

Figure 2: Selectivity data for probe **8.4** (500 nM) in the presence of $ONOO^-$ (50 µM), $O_2^{\cdot-}$ (500 µM), $^1O_2$ (500 µM) after 5 min. H_2O_2 (500 µM), ClO^- (500 µM), H_2S (10 µM), GSH (500 µM), cysteine (500 µM), homocysteine (500 µM), $S_2O_3^{2-}$ (500 µM), SO_4^{2-} (500 µM), and SO_3^{2-} (500 µM) were measured after 30 min. All data was obtained in PBS buffer 52 % MeOH : H_2O, pH = 7.4 at 25 °C at max λ_{em} = 520 nm on a BMG Labtech CLARIOstar® platereader.

Surprisingly, probe **8.4** showed a significantly higher preference for reaction with GSH than H_2S, which was unexpected, since the diazido version of **8.4** selectively reacts with H_2S over GSH.[165] There is one example in the literature where a probe containing an azide group had been shown to be capable of selectively detecting GSH and cysteine over H_2S.[168] This selectivity was achieved through the inherent reactivity of the ESIPT probe towards the different types of thiol analytes (Scheme 10), with GSH reported to react with an azide group to afford a fluorescent species containing a stable N-SH bond accompanied by release of N_2 (Scheme 11).

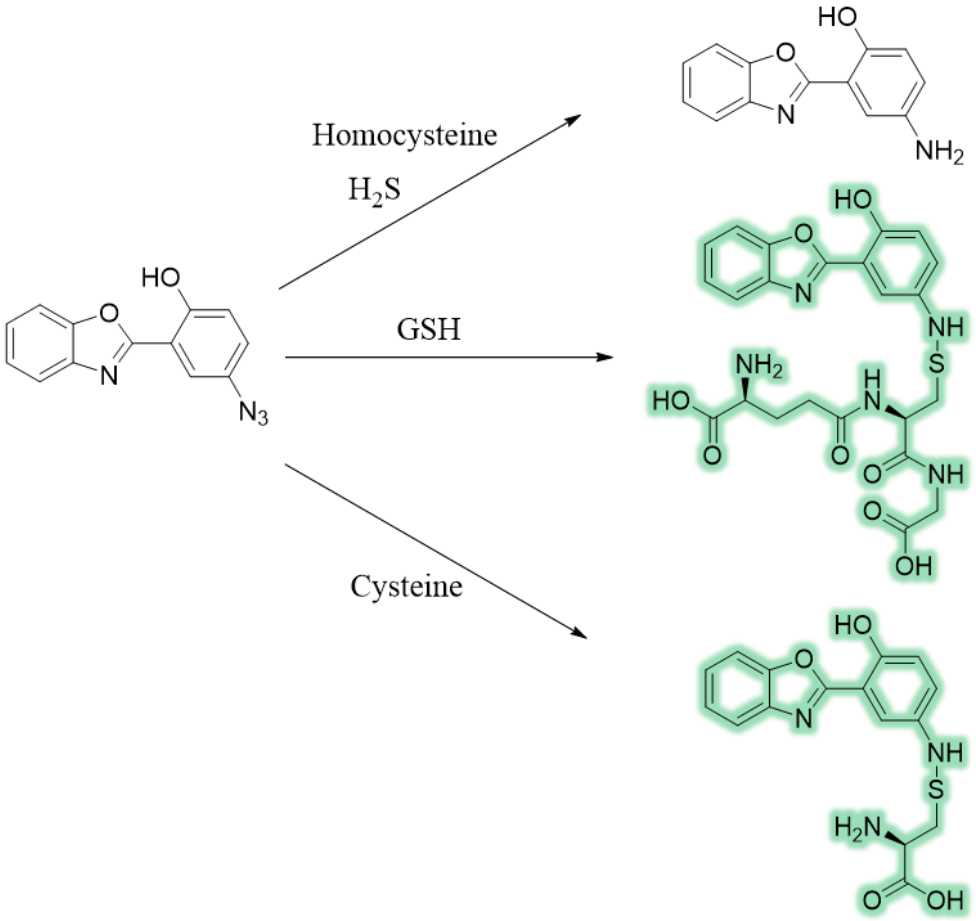

Scheme 10: ESIPT probe developed by Xu *et al.*[168] where the azide group acts as a sensing group for GSH and cysteine.

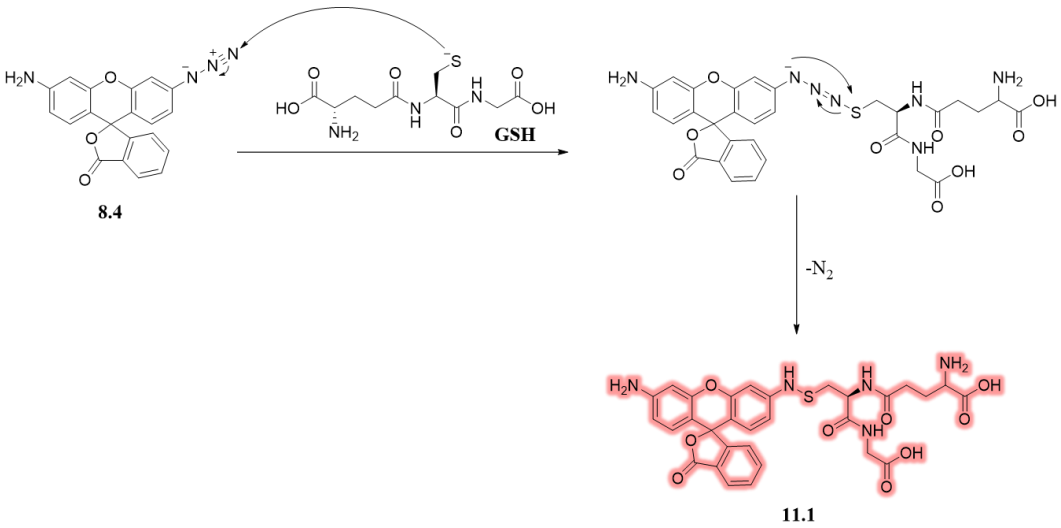

Scheme 11: GSH binding to azidorhodamine **8.4** generating fluorescent **11.1**.

Mass spectrometric analysis revealed that probe **8.4** also reacts with GSH to afford fluorescent species **11.1** via the mechanism shown in Scheme 11. The UV spectrum of azidorhodamine **8.4** was collected together with and without the presence of GSH (Figure 3). The presence of the azide group resulted in no significant absorption peaks being observed for **8.4**. However, addition of GSH resulted in a new peak appearing at 500 nm, which is close to the known maximum absorbance peak for rhodamine 110 of 492 nm.

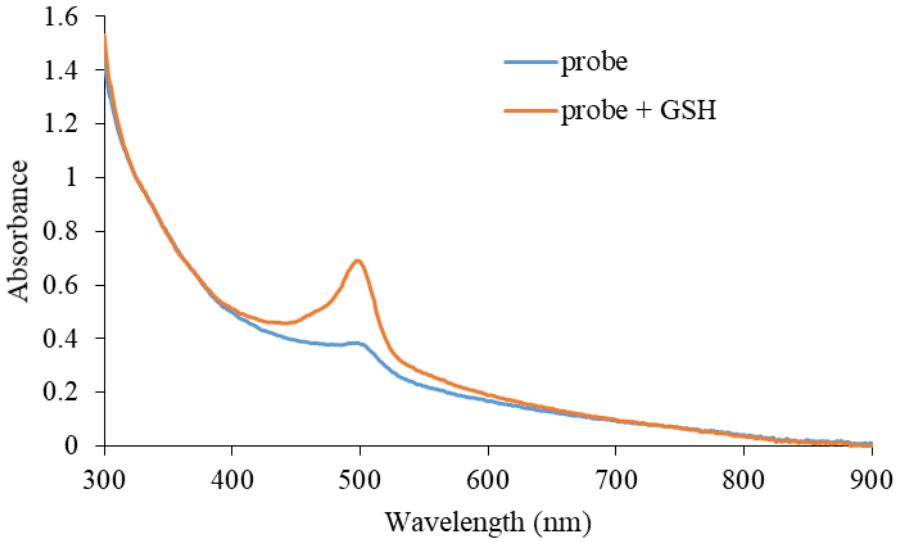

Figure 3: UV spectrum of azidorhodamine **8.4** in the absence and presence GSH (excess) in PBS buffer 52 % MeOH : H_2O, pH = 7.4 at 25 °C measured on a BMG Labtech CLARIOstar® plate reader.

Subsequently, a titration with GSH was carried out with concentrations ranging from 0.05 mM to 3 mM of GSH (Figure 4) consistent with the biologically relevant levels of GSH in cells that range from 0.2 to 10 mM.[169] It was noticed that after 3 mM, the fluorescence intensity of the azidorhodamine probe **8.4** started to decrease (not shown), with this dose dependence curve allowing us to calculate a LoD value of 0.29 mM.

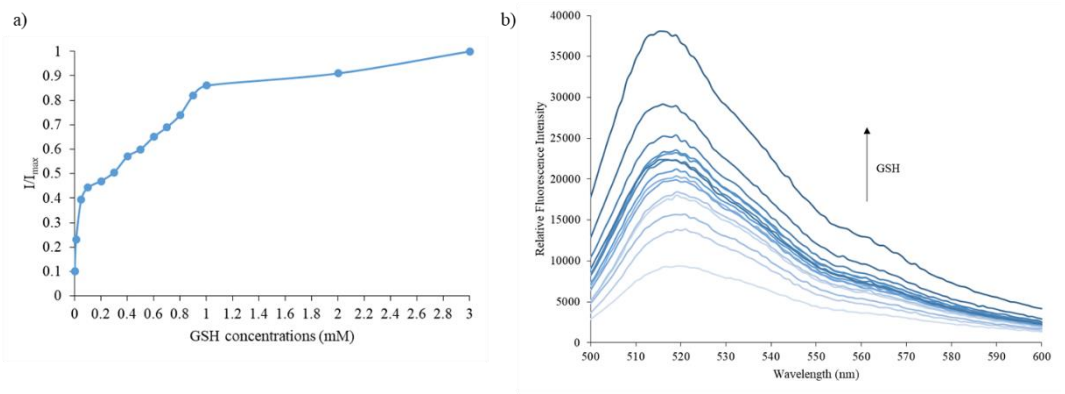

Figure 4: a) Dose dependence curve (I/I_{max}) and b) emission spectrum for probe **8.4** (500 nM) in the presence of GSH (0.01, 0.05, 0.1, 0.2, 0.3, 0.4, 0.5, 0.6, 0.7, 0.8, 0.9, 1, 2, 3 mM) in PBS buffer 52 % MeOH : H_2O, pH = 7.4 at 25 °C. Fluorescence intensities were measured for λ_{ex} = 472 (bandwith: 20) nm and max λ_{em} = 520 nm on a BMG Labtech CLARIOstar® plate reader.

Given the unusual selectivity of the azide group of this probe **8.4** for GSH, titrations were carried out with other relevant sulphur species to ensure no other unusual reactivity would occur. Figure 5 illustrates that probe **8.4** shows minimal fluorescence upon exposure to other sulphur containing analytes, such as homocysteine, cysteine, Na_2SO_4, $Na_2S_2O_3$ and Na_2SO_3, thus, confirming its selectivity for GSH.

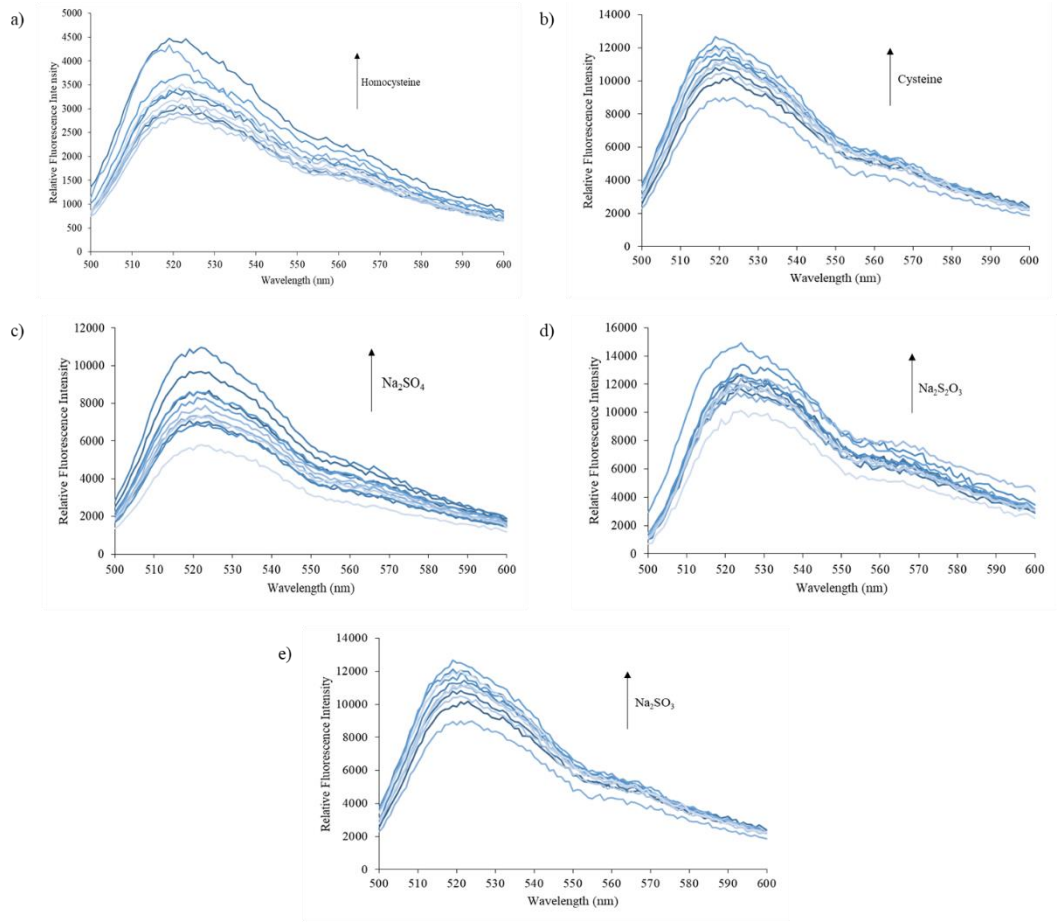

Figure 5: Titration studies of probe **8.4** with various sulphur species a) homocysteine, b) cysteine, c) Na_2SO_4, d) $Na_2S_2O_3$ and e) Na_2SO_3 at concentrations ranging from 1 – 500 μM in PBS buffer 52 % MeOH : H_2O, pH = 7.4 at 25 °C. Fluorescence intensities were measured for λ_{ex} = 472 (bandwith: 20) nm on a BMG Labtech CLARIOstar® plate reader.

Additionally, a selectivity study for the reaction of azidorhodamine **8.4** with various amino acids was also carried out, with negligible fluorescence being observed towards all of the 12 amino acids screened (Figure 6).

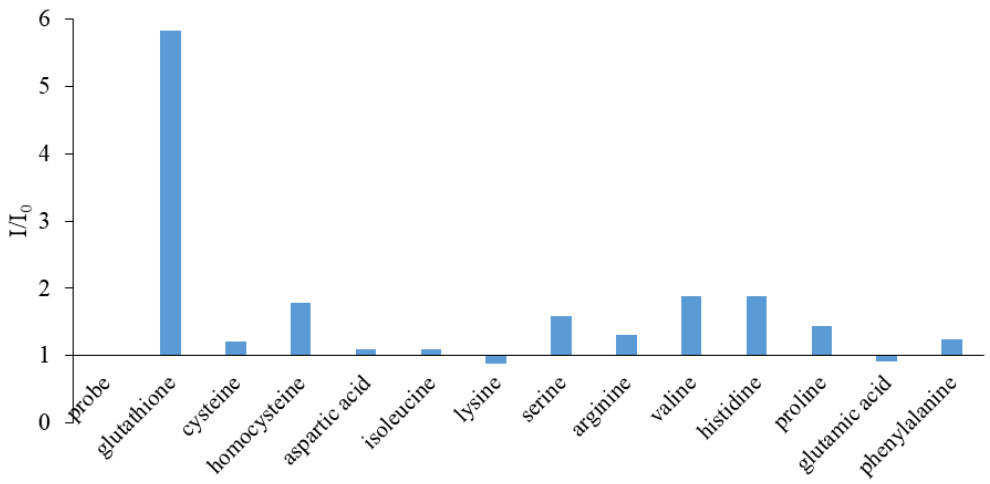

Figure 6: Selectivity data for probe **8.4** (500 nM) in the presence of GSH (500 µM), cysteine (500 µM), homocysteine (500 µM), aspartic acid (500 µM), isoleucine (500 µM), lysine (500 µM), serine (500 µM), arginine (500 µM), valine (500 µM), histidine (500 µM), proline (500 µM), glutamic acid (500 µM), and phenylalanine (500 µM) were measured after 30 min. Data was obtained in PBS buffer 52 % MeOH : H_2O, pH = 7.4 at 25 °C. Fluorescence intensities were measured for λ_{ex} = 472 (bandwith: 20) nm and max λ_{em} = 520 nm on a BMG Labtech CLARIOstar® plate reader.

Due the unusal reactivity profile of azidorhodamine **8.4** towards GSH, it was decided to evaluate the fluorescent properties of iodorhodamine **9.3** and rhodamine 110 in the presence of GSH. Rhodamine 110 is widely used as a fluorescent tool, so the addition of ROS and RSS was not expected to result in any change in fluorescence. However, exposure of rhodamine 110 to $ONOO^-$ and ClO^- resulted in its fluorescence being quenched (Scheme 12). It is most likely a result of these strong oxidants destroying the fluorophore. The amino acid screen test also revealed that all of the amino acids tested had no impact on the fluorescent profile of rhodamine 110 (Figure 7).

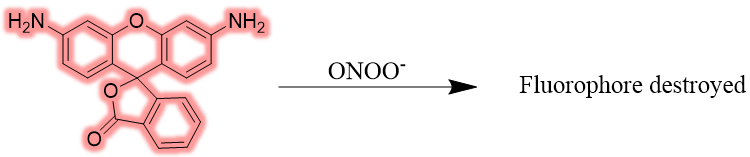

Scheme 12: The fluorescence of rhodamine 110 is quenched upon reaction with $ONOO^-$.

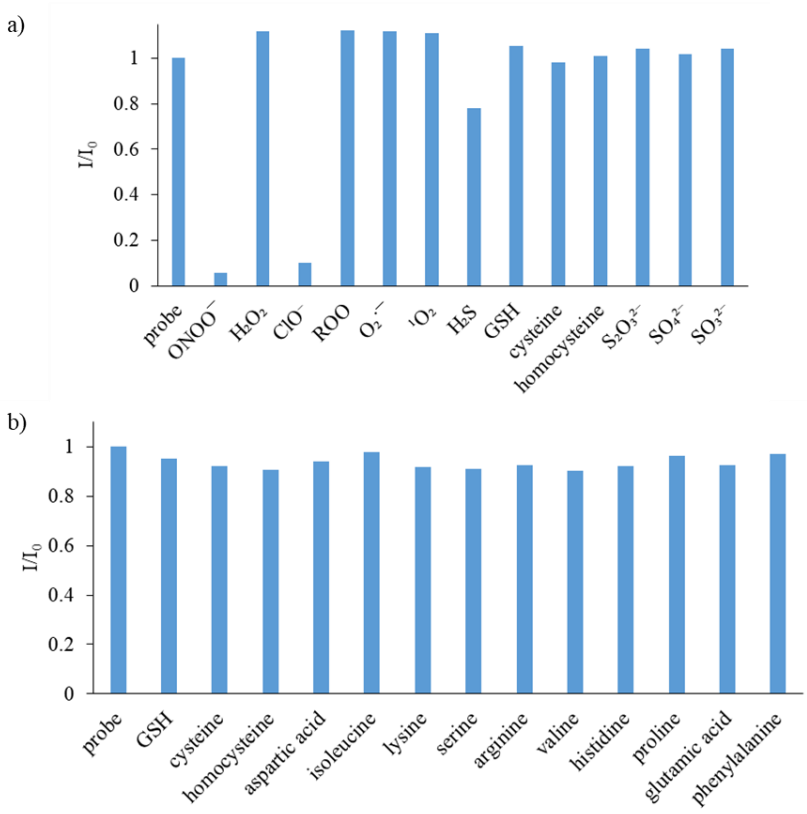

Figure 7: a) Selectivity data for rhodamine 110 (500 nM) in the presence of $ONOO^-$ (50 µM), $O_2^{\cdot-}$ (500 µM), $^1O_2$ (500 µM) after 5 min. H_2O_2 (500 µM), ClO^- (500 µM), H_2S (10 µM), GSH (500 µM), cysteine (500 µM), homocysteine (500 µM), $S_2O_3^{2-}$ (500 µM), SO_4^{2-} (500 µM), and SO_3^{2-} (500 µM) were measured after 30 min. b) Selectivity data for rhodamine 110 (500 nM) in the presence of GSH (500 µM), cysteine (500 µM), homocysteine (500 µM), aspartic acid (500 µM), isoleucine (500 µM), lysine (500 µM), serine (500 µM), arginine (500 µM), valine (500 µM), histidine (500 µM), proline (500 µM), glutamic acid (500 µM), and phenylalanine (500 µM) were measured after 30 min. Data was obtained in PBS buffer 52 % MeOH : H_2O, pH = 7.4 at 25 °C. Fluorescence intensities were measured for λ_{ex} = 472 (bandwith: 20) nm and max λ_{em} = 515 nm on a BMG Labtech CLARIOstar® plate reader.

Iodorhodamine **9.3** exhibited significant fluorescence and was shown to react with a variety of species, including H_2O_2, H_2S, and GSH (Figure 8). However, none of these analytes had a large effect on the fluorescence profile of **9.3**. An amino acid screen revealed that iodorhodamine **9.3** reacts with GSH and isoleucine preferentially (Figure

8). Nevertheless, the changes in fluorescence seen for rhodamine 110 and iodorhodamine **9.3** were not as signifcant as observed for azidorhodamine **8.4**.

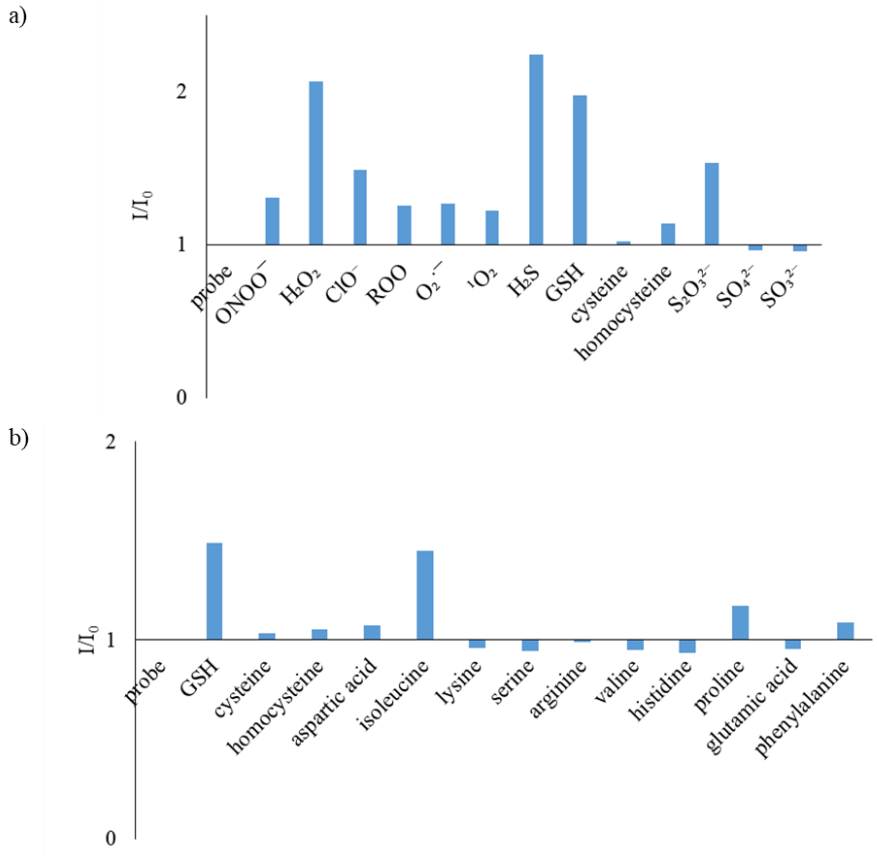

Figure 8: a) Selectivity data for iodorhodamine **9.3** (500 nM) in the presence of $ONOO^-$ (50 µM), $O_2^{\cdot-}$ (500 µM), $^1O_2$ (500 µM) after 5 min. H_2O_2 (500 µM), ClO^- (500 µM), H_2S (10 µM), GSH (500 µM), cysteine (500 µM), homocysteine (500 µM), $S_2O_3^{2-}$ (500 µM), SO_4^{2-} (500 µM), and SO_3^{2-} (500 µM) were measured after 30 min. b) Selectivity data for iodorhodamine **9.3** (500 nM) in the presence of GSH (500 µM), cysteine (500 µM), homocysteine (500 µM), aspartic acid (500 µM), isoleucine (500 µM), lysine (500 µM), serine (500 µM), arginine (500 µM), valine (500 µM), histidine (500 µM), proline (500 µM), glutamic acid (500 µM), and phenylalanine (500 µM) were measured after 30 min. Data was obtained in PBS buffer 52 % H_2O : MeOH, pH = 7.4 at 25 °C. Fluorescence intensities were measured for λ_{ex} = 472 (bandwith: 20) nm and max λ_{em} = 520 nm on a BMG Labtech CLARIOstar® plate reader.

3. Cell Studies

In collaboration with Prof. Juyoon Young and his research group at Ewha Woman's University in Seoul, Korea, probe **8.4** was evaluated in HeLa cells (Figure 9). First HeLa cells were treated with N-ethylmaleimide (NEM) which allows to reduce celullar thiol levels. Maleimides are commonly used as alkylating agents for thiols.[170] Using NEM allows for proof of concept experiments to study specific detection of thiols with probes *in vitro*. Different conditions with HeLa cells were examined: a) probe **8.4** alone, b) NEM + probe **8.4**, (c) NEM + Cys + probe **8.4**, (d) NEM + Hcy + probe **8.4** and (e) NEM + GSH-MEE + probe **8.4**. Unfortunately, probe **8.4** showed no ability to detect GSH *in vitro*. Probe **8.4** exhibited inherent fluorescence when the cells were untreated as well as when only treated with NEM. No or minimal fluorescence should have been observed for these conditions. Upon addition of GSH, the fluorescence signal seems to stay the same. An increase of the fluorescence response would have been expected, despite inherent fluorescence of the probe **8.4**. Gluthatione monoethyl ester (GSH-MEE) was used for exogenous addition of GSH since GSH-MEE is more readily cell permeable than pure GSH. Additionally, exogenous cysteine and homocysteine were evaluated in HeLa cells. This should have allowed validation of preferential detection of GSH with probe **8.4** over cysteine and homocysteine. However, probe **8.4** showed as in all previous conditions no change in fluorescence signal. Due to the azide group in probe **8.4**, it could potentiall be unstable in a cellular environment and readily generate fluorescent rhodamine 110 prior to GSH detection.

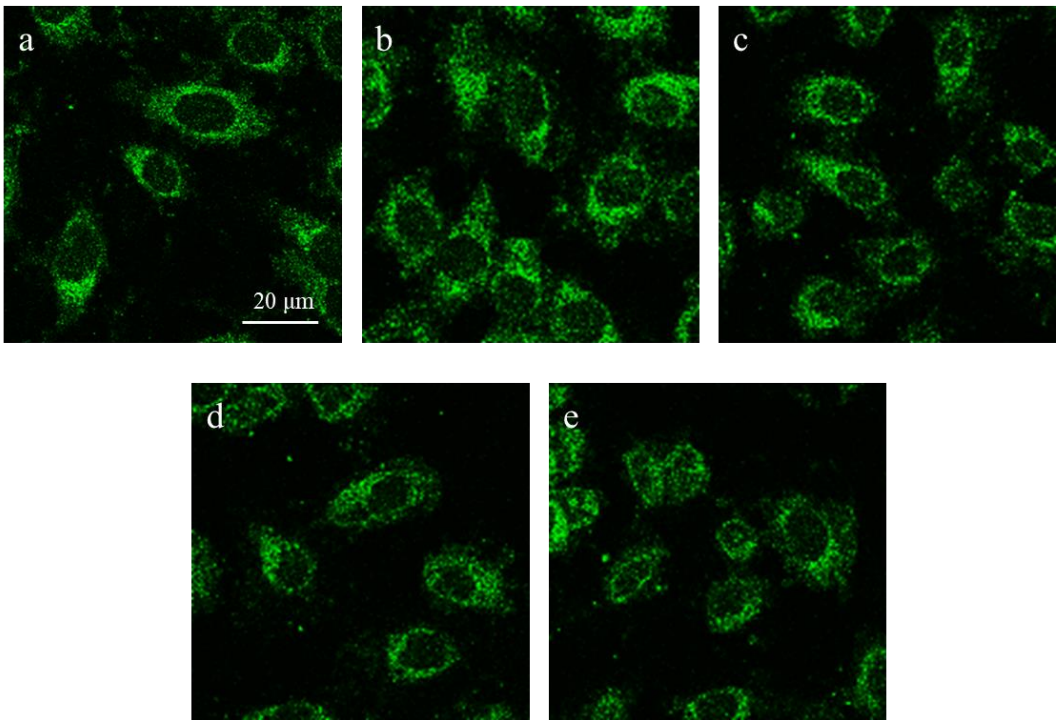

Figure 9: HeLa cells were treated with NEM (0.5 mM, 20 min), followed by treatment of cysteine (500 µM, 20 min), homocysteine (500 µM, 20 min) or GSH-MEE (500 µM, 20 min). The probe **8.4** (20 µM) was incubated for 20 min and fluorescence images were acquired by confocal microscopy. Legend: (a) probe **8.4**, (b) NEM + probe **8.4**, (c) NEM + Cys + probe **8.4**, (d) NEM + Hcy + probe **8.4** and (e) NEM + GSH-MEE + probe **8.4**. λ_{ex} = 473 nm, λ_{em} = 490 – 590 nm. Scale bar: 20 µm. Magnification: x60. N = 3. Cell imaging experiments were kindly carried out by Juyoung Yoon's research group.

4. Conclusions

To conclude, easily prepared azidorhodamine probe **8.4** has been shown to function as a selective and sensitive probe for GSH over a range of other amino acids, RSS and ROS. GSH reacts with the azide group of azidorhodamine **8.4** to afford a -S-NH- adduct whose fluorescence can be used to determine the concentration of GSH in solution. Unfortunately, HeLa cell studies with **8.4** showed that **8.4** cannot be used as a GSH sensing tool *in vitro*. It was postulated that the labile nature of the azide group could generate fluorescent rhodamine 110 readily. Hence, **8.4** cannot be used to gain

an understanding of GSH levels *in vitro* and remains only as an interesting solution model. Nevertheless, probe **8.4** has shown that azide groups are not selectively sensing H_2S when incorporated into an aromatic system. This unique feature opens up new possibilities in the design of dual analyte probes and thus, could overcome the inherent fluorescent properties *in vitro*.

5. Future Work

Derivatisation at the free amine position of probe **8.4** could potentially allow for further functionalisation to introduce other relevant sensing groups for biothiols or ROS, with simultaneous detection of different analytes beneficial to understand their essential metabolic roles. Therefore, it is anticipated that synthesis of multicomponent probes such as **12.1**, **12.2** and **12.3** might allow for cellular studies, as well as drug delivery and theranostic applications (Figure 10).

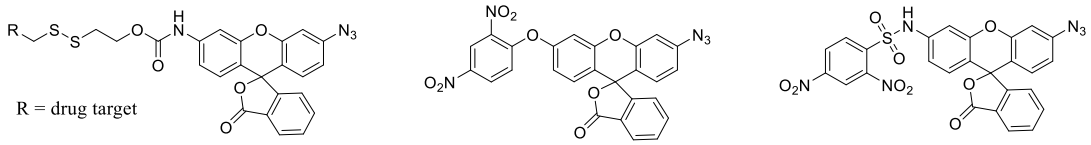

12.1 **12.2** **12.3**

Figure 10: Suggested probes **12.1**, **12.2**, and **12.3** for the simultaneous detection of GSH and other biothiols such as H_2S, cysteine and homocysteine.

Another possibility would be the inclusion of a boronic ester moiety, illustrated in structures **13.1**, **13.2** and **13.3** to allow for the detection of $ONOO^-$ and GSH at the same time (Figure 11). The simultaneous detection of these two analytes could offer the opportunity of understanding the interplay between $ONOO^-$ and GSH. $ONOO^-$ can interfere in the GSH/GSSG ratio[171], specifically in the mitochondria and hence, understanding redox homeostasis pathways would be beneficial. A rhodamine based structure such as **13.1** could allow for localisation in the mitochondria whereas the rhodol based structures such as in **13.2** and **13.3** might offer better localisation in the

endoplasmic reticulum.[172] This could offer insight and comparison of the interplay of $ONOO^-$ and GSH in different organelles.[173]

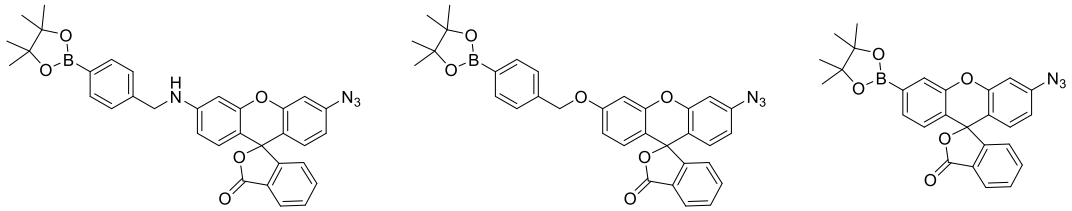

13.1 **13.2** **13.3**

Figure 11: Suggested probes **13.1**, **13.2**, and **13.3** for the simultaneous detection of H_2S/GSH and $ONOO^-$.

Chapter 6 – Experimental

General Materials and Methods

Chemistry

Unless stated otherwise, reagents and solvents were sourced from commercial suppliers, specifically: Acros Organics, Fisher Scientific, Fluka Chemie GmbH, Fluorochem, Sigma Aldrich and TCI and were used directly as received. Reactions requiring inert conditions were performed using dry solvents and under an atmosphere of nitrogen. Solvents were dried using an Innovative Technology Inc. PS-400-7 Solvent Purification System.

TLC was carried out on commercially available pre-coated aluminium-backed silica plates and compounds were visualised under UV light at 254 nm. Column chromatography was performed using 60 micron silica purchased from Sigma Aldrich.

^{1}H NMR and ^{13}C NMR spectra were recorded either in deuterated chloroform, acetone, methanol or DMSO at ambient temperature on either a Bruker Avance 250 (250 MHz), Bruker Avance 300 (300 MHz) or Bruker Avance 500 (500 MHz), with proton decoupling for all ^{13}C NMR spectra. Chemical shifts (δ / ppm) are referenced against tetramethylsilane as an internal standard and the abbreviations: s, d, t, q, quin, sext, m, and br, were used to denote singlet, doublet, triplet, quartet, quintet, sextet, multiplet, and broad respectively. Coupling constants (*J* / Hz) are reported where known.

Initially, analysis by mass spectrometry was conducted either by the EPSRC UK national mass spectrometry facility at Swansea University medical school on a electrospray ionisation LTQ Orbitrap XL 1 (Thermo Fisher Scientific) or on a microTOF electrospray time of flight (ESI-TOF) mass spectrometer (Bruker Dlatonik GmbH, Germany) at the University of Bath. More recently, LC-MS analyses were performed using an Agilent QTOF 6545 with Jetstream ESI spray source coupled to an Agilent 1260 Infinity II Quat pump HPLC with 1260 autosampler, column oven compartment and variable wavelength detector (VWD). The MS was operated in

either positive or negative ionisation mode with the gas temperature at 250 °C, the drying gas at 12 L/min and the nebuliser gas at 45 psi (3.10 bar). The sheath gas temperature and flow were set to 350 °C and 12 L/min, respectively. The MS was calibrated using reference calibrant introduced from the independent ESI reference sprayer. The VCap, Fragmentor and Skimmer was set to 3500, 125 and 45 respectively.

Fourier Transform Infrared (FTIR) spectra were recorded on an ATR Perkin−Elmer FTIR Spectrum 100 spectrometer. The spectra were measured between 4000 − 600 cm^{-1}. Selected absorption bands are reported in wavenumbers (cm^{-1}), and their relative intensities described as *s* (strong), *m* (medium), or *w* (weak). When applicable, peak shape was characterised by *br.* (broad) or *sh.* (shoulder).

Fluorescence

Fluorescence measurements were performed on a BMG Labtech CLARIOstar® plate reader using Greiner bio-one microplates, 96-well, PS, flat-bottom (chimney well), black. Data were collected via the BMG Labtech Clariostar data analysis software package MARS. All solvents used in fluorescence measurements were HPLC or fluorescence grade and the water was de-ionised.

UV-Vis measurements were performed on a Perkin-Elmer Lambda20 Spectrophotometer, utilising Starna Silica (quartz) cuvette with 10 mm path lengths, two faces polished. Data was collected *via* the Perkin-Elmer UVWinlab software package.

All pH measurements taken for buffer pH adjustments were recorded on a Hanna Instrument HI 9321 microprocessor pH meter which was routinely calibrated using Fishers standard buffer solutions (pH 4.0 – phthalate, 7.0 – phosphate, and 10.0 – borate).

Phosphate buffered saline (PBS) was freshly prepared from 52 % methanol in water with KCl (10 mM), KH_2PO_4 (2.75 mM) and Na_2HPO_4 (2.76 mM). The PBS buffer was adjusted to pH 7.4/8.2 with 1 M HCl (aq.) as indicated.

Stock solutions for a variety of ROS were freshly prepared prior to each experiment:

Hydrogen peroxide (H_2O_2)

Hydrogen peroxide (H_2O_2) is commercially available whereby the concentration of H_2O_2 was determined through spectrophotometrical analysis with $\varepsilon = 43.6\ cm^{-1}\ M^{-1}$ at 240 nm.

Peroxynitrite ($ONOO^-$)

Peroxynitrite ($ONOO^-$) stock solutions were freshly prepared each time prior to usage. A solution of 3 M NaOH was cooled to 0 °C to which simultaneously 0.7 M H_2O_2, 0.6 M $NaNO_2$ and 0.6 M HCl were added. The $ONOO^-$ solution was analyzed spectrophotometrically whereby the concentration of $ONOO^-$ was estimated through $\varepsilon = 1670\ cm^{-1}\ M^{-1}$ at 302 nm in 0.1 M NaOH (aq.).

Hypochlorite (ClO^-)

Commercially available NaOCl was analysed spectrophotometrically to determine its concentration using $\varepsilon = 350\ cm^{-1}\ M^{-1}$ at 292 nm.

Superoxide ($O_2^{\cdot-}$)

KO_2 (0.0335 g) and 18-crown-6 ether (0.1235 g) were dissolved in DMSO (5 mL) and stirred for 5 min to produce a 0.1 M solution of $O_2^{\cdot-}$.

Hydroxyl radical ($^{\cdot}OH$)

Iron(II) perchlorate hydrate (0.1274 g) and H_2O_2 (3.9 µL) were dissolved in H_2O (5 mL) to produce a 0.1 M solution of $^{\cdot}OH$.

Peroxyl radical ($ROO^{\cdot}$)

2,2′-Azobis(2-methylpropionamidine) dihydrochloride (0.136 g) was dissolved in H_2O (5 mL) and heated at 37 °C for 30 min to give a 0.1 M solution of $ROO^{\cdot}$.

Singlet oxygen ($^1O_2$)

H_2O_2 (1.3 µL) was added to 4 mL of 0.1 M NaOCl to give a 0.1M solution of $^1O_2$.

Fluorescence titrations of ROS/RNS were carried out at 25 °C in PBS buffer pH 7.4/8.2. Different concentrations of ROS/RNS were prepared accordingly and investigated with the probe at a concentration ranging from 500 nM to 5 µM.

1. Chapter 1

1.1. Synthesis

3,7-dibromo-*10H*-phenoxazine (1.2)

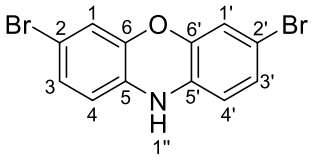

Phenoxazine (2.00 g, 7.38 mmol) was dissolved in chloroform (150 mL). NBS (2.63 g, 14.76 mmol) was slowly added to the mixture, which was left to stir at RT for 2 h. The mixture was quenched with water. After separation of the phases, the organic layer was washed with water (3 x 100 mL) and brine (1 x 100 mL), dried over $MgSO_4$, filtered and evaporated *in vacuo*. FC (SiO_2; petroleum ether/EtOAc 80:20) gave 3,7-dibromo-10*H*-phenoxazine (2.00 g, 80 %) as a blue solid.

^{1}H NMR (500 MHz, (C*D*$_3$)$_2$SO): δ = 6.96 – 6.85 (m, 2 H; Ar*H*), 6.71 – 6.63 (m, 3 H; Ar*H*), 6.06 – 5.91 ppm (m, 2 H; Ar*H*); ^{13}C NMR (75.5 MHz, (C*D*$_3$)$_2$SO): δ = 146.3, 132.9, 126.4, 122.1, 121.4, 111.3 ppm; m.p. 125 – 128 °C; IR (ATR): υ = 3393 cm^{-1} (*w*, N–H); HR-ESI-MS: m/z (%): 363.1144 ([*M*+Na]$^+$, calcd for $C_{12}H_7{}^{79}Br^{81}BrNONa^+$: 363.1104).

3,7-bis(4,4,5,5-tetramethyl-1,3,2-dioxaborolan-2-yl)-10*H*-phenoxazine (PR1)

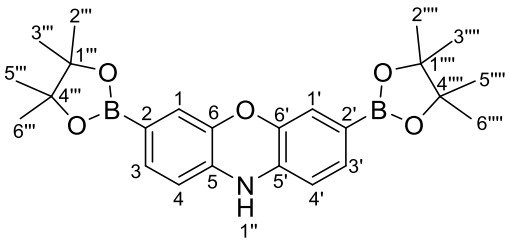

3,7-dibromo-*10H*-phenoxazine (2.70 g, 7.92 mmol), bis(pinacolato)diboron (6.04 g, 23.76 mmol) and KOAc (4.66g, 47.52 mmol) were dissolved in DMF (60 mL), degased under argon and treated with $PdCl_2$(dppf) (579 mg, 0.79 mmol). The mixture was refluxed at 90 °C for 3 h, and cooled to RT after completion. The solution was filtered through celite, diluted with EtOAc, washed with water (3 x 60 mL) and brine (3 x 60 mL), dried over $MgSO_4$, filtered and evaporated *in vacuo*. FC (SiO_2; petroleum ether/EtOAc 80:20) gave 3,7-bis(4,4,5,5-tetramethyl-1,3,2-dioxaborolan-2-yl)-10*H*-phenoxazine (2.42 g, 70 %) as a dark red solid.

^{1}H NMR (500 MHz, (C*D*$_3$)$_2$SO): δ = 8.70 (s, 1 H; H–N(1’’)), 7.04 (dd, *J* = 7.7 Hz, 1.3 Hz, 2 H; Ar*H*), 6.75 (d, *J* = 7.7 Hz, 2 H; Ar*H*), 6.43 (d, *J* = 1.3 Hz, 2 H; Ar*H*), 1.25 ppm (s, 24 H; H–C(2’’’), H–C(3’’’), H–C(5’’’), H–C(6’’’), H–C(2’’’’), H–C(3’’’’), H–C(5’’’’), H–C(6’’’’)); ^{13}C NMR (125.75 MHz, (C*D*$_3$)$_2$CO): δ = 143.1, 134.8, 131.0, 120.7, 112.9, 83.3, 24.3 ppm; m.p. 214 – 217 °C**;** IR (ATR): υ = 3404 cm^{-1} (*w*, N–H); FTMS + p APCI corona MS: m/z (%): 436.2462 ([*M*+H]$^+$, calcd for $C_{24}H_{32}B_2NO_5^+$: 436.2462).

1.2. *In vitro* Macrophage Assays

Materials

Unless stated otherwise, reagents and solvents were sourced from commercial suppliers, specifically: Biotium, Cayman Chemicals, Fisher Scientific, and Sigma Aldrich and were used directly as received. Phosphate buffered saline (PBS) was freshly prepared from milli-q water with NaCl (0.14 M), KCl (2.68 mM), Na_2HPO_4 (10.14 mM), KH_2PO_4 (1.76 mM), $CaCl_2{\cdot}2H_2O$ (0.90 mM) and $MgCl_2{\cdot}6H_2O$ (0.49 mM). The PBS buffer was adjusted to pH 7.4 with 1 M HCl (aq.).

Cell culture

J774.2 macrophages (ECACC 85011428) were purchased from the European collection of authenticated cell cultures. Cells are stored at -196 °C under liquid nitrogen until required. Cells are warmed up in a water bath (37 °C) for 2 min. The cell liquid was transferred into a falcon tube, to which media (5 mL) was added. The solution was centrifuged at 300 RCM for 5 min at 22 °C. After removal of the supernatant, fresh media (1 mL) was added and the cells were thrown quickly and incubated at 37 °C, 5 % CO_2. J774.2 macrophages were grown in culture media consisting of Dulbecco's Modified Eagle's Medium (DMEM) supplemented with heat inactivated fetal bovine serum (FBS) (10 % v/v), and penicillin/streptomycin (1 % v/v). During cell passage (every two days), media was removed, new media added and cells were detached with a cell scraper and transferred to a new flask according to the protocol provided by the European collection of authenticated cell cultures.

Confocal microscopy of J774.2 macrophages

Fluorescence microscopy images were captured on a Zeiss LSM880 using 8-well chambered cover glass with #1.5 high performance cover glass (Cellvis). Images were captured at different magnifications with the following parameters: MitoView Green λ_{ex} = 490 nm, λ_{em} = 523 nm and PR1 λ_{ex} = 572 nm, λ_{em} = 583 nm. Lasers 488 nm and 543 nm with intensities of 3 % and 50 % respectively were used. Processing and analy-

sis of confocal microscopy images were performed with Image J.

Fluorescence measurements

Fluorescence measurements were performed on a BMG Labtech CLARIOstar® plate reader with regulated O_2 and CO_2 gas control using Greiner bio-one microplates, 96-well, PS, flat-bottom (chimney well), black. Excitation and emission wavelength were set for resorufin presettings (λ_{ex} = 545 nm, λ_{em} = 600 nm). All solvents used in fluorescence measurements were HPLC or fluorescence grade and the water was of milli-q standard. Data collected via the BMG Labtech Clariostar plate reader was initially analysed with the data analysis software package MARS from BMG Labtech, followed by the GraphPad software Prism. Statistical analysis was performed using Prism. All fluorescence experiments were performed in triplicates three times.

Hypoxic cabinet

An asymmetric Sci-tive Dual (Baker Ruskin) was used for induction of a hypoxia environment. The hypoxic cabinet allows for regulation of O_2 %, CO_2 %, temperature and humidity. The hypoxic cabinet was switched on 2 h prior to usage to allow for calibration of the system. N_2, CO_2 and 25 % O_2/N_2 gases were used to induce the desired hypoxic cell culture environment.

Confocal microscopy study

Cells were plated in a 8-well chambered coverglass at a cell density of 5 x 10^4 cells/well in culture media (300 µL/well) and incubated for 16 h. Then, LPS (1 µg/ml) and IFN-γ (50 ng/ml) were incubated for 4 h at 37 °C, 5 % CO_2. The culture media was removed, cells were washed three times with PBS, the probe (15 µM) and MitoView Green (200 nM) in a probenecid (1 mM) and Opti-MEM solution were added respectively to the cells and incubated for 30 min at 37 °C, 5 % CO_2. The media solution was removed, cells were washed three times with PBS and subsequently dispensed in a solution of probenecid (1 mM) in PBS for confocal microscopy. Where specified, SIN-1 (15 µM) was added prior to imaging.

Investigation of different cell numbers

Cells were plated in a clear 96-well plate at a cell density of 1 x 10^4, 5 x 10^4, 1 x 10^5 cells/well in culture media (200 µL/well) and incubated for 24 h at 37 °C, 5 % CO_2. The culture media was removed, cells were washed three times with PBS. Images were captured using an EVOS FL microscope with an x20 objective.

Cells were plated in a black 96-well plate, the probe (15 µM) in Opti-MEM was added to the cells and incubated for 30 min at 37 °C, 5 % CO_2. The media solution was removed, cells were washed three times with PBS and subsequently dispensed in PBS for fluorescence measurements. SIN-1 (15 µM) was added via a computer controlled injector after 5 min. Fluorescence intensity recordings were performed for 30 min at 37 °C.

Investigation of different SIN-1 concentrations

Cells were plated in a black 96-well plate at a cell density of 5 x 10^4 cells/ well in culture media (200 µL/well) and incubated for 24 h at 37 °C, 5 % CO_2. The culture media was removed, cells were washed three times with PBS, the probe (15 µM) in Opti-MEM was added to the cells and incubated for 30 min at 37 °C, 5 % CO_2. The media solution was removed, cells were washed three times with PBS and subsequently dispensed in PBS for fluorescence measurements. SIN-1 (2, 5, 10, 15, 20, 40 µM) was added via a computer controlled injector after 5 min. Fluorescence intensity recordings were performed for 30 min at 37 °C.

Investigation of different LPS concentrations

Cells were plated in a black 96-well plate at a cell density of 5 x 10^4 cells/well in culture media (200 µL/well) and incubated with LPS (0.1, 1, 100, 1000 ng/ml) for 4 or 24 h at 37 °C, 5 % CO_2. The culture media was removed, cells were washed three times with PBS, the probe (15 µM) in Opti-MEM was added to the cells and incubated for 30 min at 37 °C, 5 % CO_2. The media solution was removed, cells were washed

three times with PBS and subsequently dispensed in PBS for fluorescence measurements. Fluorescence intensity recordings were performed for 30 min at 37 °C.

Investigation of different PMA concentrations

Cells were plated in a black 96-well plate at a cell density of 5 x 10^4 cells/well in culture media (200 µL/well) and incubated for 24 h, followed by LPS (100 ng/ml) for 4 h at 37 °C, 5 % CO_2. The culture media was removed, cells were washed three times with PBS, the probe (15 µM) in a solution of probenecid (1 mM) in Opti-MEM was added to the cells and incubated for 30 min at 37 °C, 5 % CO_2. The media solution was removed, cells were washed three times with PBS and subsequently dispensed in a solution of probenicid (1 mM) in PBS for fluorescence measurements. PMA (5, 10, 50, 100 nM) was added via a computer controlled injector after 5 min. Fluorescence intensity recordings were performed for 30 min at 37 °C.

Investigation of IFN-γ

Cells were plated in a black 96-well plate at a cell density of 5 x 10^4 cells/well in culture media (200 µL/well) and incubated for 24 h, followed by incubation with LPS (100 ng/ml) and IFN-γ (50 ng/ml) for 4 h at 37 °C, 5 % CO_2. The culture media was removed, cells were washed three times with PBS. The probe (15 µM) in Opti-MEM was added to the cells and incubated for 30 min at 37 °C, 5 % CO_2. The solutions were removed, cells were washed three times with PBS and subsequently dispensed in a solution of PBS for fluorescence measurements. Fluorescence intensity recordings were performed for 30 min at 37 °C.

Investigation of different $O_2^{\cdot-}$ scavengers

Cells were plated in a black 96-well plate at a cell density of 5 x 10^4 cells/well in culture media (200 µL/well) and incubated for 24 h, followed by LPS (100 ng/ml) for 4 h at 37 °C, 5 % CO_2. The culture media was removed, cells were washed three times with PBS. The scavenger (ebselen (1 mM), uric acid (1 mM), *N*-acetyl-L-cysteine (1 mM) and Mn-cpx3 (1 mM)) in Opti-MEM was incubated for 1 h at 37 °C, 5 % CO_2.

After 30 min of incubation with the scavenger, the probe (15 µM) in Opti-MEM was added to the cells and incubated for the remaining 30 min at 37 °C, 5 % CO_2. The solutions were removed, cells were washed three times with PBS and subsequently dispensed in a solution of PBS for fluorescence measurements. Fluorescence intensity recordings were performed for 30 min at 37 °C.

Investigation of different ebselen concentrations

Cells were plated in a black 96-well plate at a cell density of 5 x 10^4 cells/well in culture media (200 µL/well) and incubated for 24 h, followed by LPS (100 ng/ml) for 4 h at 37 °C, 5 % CO_2. The culture media was removed, cells were washed three times with PBS. Ebselen (0.1, 0.25, 0.5, 0.75, 1 mM) in Opti-MEM was incubated for 1 h at 37 °C, 5 % CO_2. After 30 min of incubation with ebselen, the probe (15 µM) in Opti-MEM was added to the cells and incubated for the remaining 30 min at 37 °C, 5 % CO_2. The solutions were removed, cells were washed three times with PBS and subsequently dispensed in a solution of PBS for fluorescence measurements. Fluorescence intensity recordings were performed for 30 min at 37 °C.

Investigation of different NO scavengers

Cells were plated in a black 96-well plate at a cell density of 5 x 10^4 cells/well in culture media (200 µL/well) and incubated for 24 h, followed respectively by LPS (100 ng/ml) and NO scavengers (N^G-methyl-L-arginine acetate and N_w-nitro-L-arginine: 0.1, 0.25, 0.5, 0.75, 1, 2 mM) for 4 h at 37 °C, 5 % CO_2. The culture media was removed, cells were washed three times with PBS. The probe (15 µM) in Opti-MEM was added to the cells and incubated for 30 min at 37 °C, 5 % CO_2. The solutions were removed, cells were washed three times with PBS and subsequently dispensed in a solution of PBS for fluorescence measurements. Fluorescence intensity recordings were performed for 30 min at 37 °C.

Investigation of IFN-γ with NOS inhibitors and $O_2^{\cdot-}$ and $ONOO^-$ scavengers

Cells were plated in a black 96-well plate at a cell density of 5 x 10^4 cells/well in culture media (200 µL/well) and incubated for 24 h, followed respectively by LPS (100 ng/ml), IFN-γ (50 ng/ml) and NO scavengers (N^G-methyl-L-arginine acetate (0.5 mM) and N_w-nitro-L-arginine (0.5 mM)) incubation for 4 h at 37 °C, 5 % CO_2 where appropriate. The culture media was removed, cells were washed three times with PBS. The scavenger (ebselen (1 mM) and uric acid (1 mM)) in Opti-MEM was incubated for 1 h at 37 °C, 5 % CO_2 where appropriate. After 30 min of incubation with the scavenger, the probe (15 µM) in a solution of probenicid (1 mM) in Opti-MEM was added to the cells and incubated for the remaining 30 min at 37 °C, 5 % CO_2. The solutions were removed, cells were washed three times with PBS and subsequently dispensed in a solution of probenecid (1 mM) in PBS for fluorescence measurements. Where appropriate, ATP (5 mM) and SIN-1 (15 µM) were added via a computer controlled injector after 5 min. Fluorescence intensity recordings were performed for 30 min at 37 °C.

Investigation of different ATP concentrations

Cells were plated in a black 96-well plate at a cell density of 5 x 10^4 cells/well in culture media (200 µL/well) and incubated for 24 h, followed by LPS (100 ng/ml) incubation for 4 h at 37 °C, 5 % CO_2. The culture media was removed, cells were washed three times with PBS, the probe (15 µM) in a solution of probenecid (1mM) in Opti-MEM was added to the cells and incubated for 30 min at 37 °C, 5 % CO_2. The media solution was removed, cells were washed three times with PBS and subsequently dispensed in a solution of probenecid (1 mM) in PBS for fluorescence measurements. ATP (0.1, 0.5, 1, 5 mM) was added via a computer controlled injector after 5 min. Fluorescence intensity recordings were performed for 30 min at 37 °C.

Investigation of different P2X7 antagonists

Cells were plated in a black 96-well plate at a cell density of 5 x 10^4 cells/well in culture media (200 µL/well) and incubated for 24 h, followed by LPS (100 ng/ml) for 4 h at 37 °C, 5 % CO_2. The culture media was removed, cells were washed three times

with PBS. P2X7 antagonists (A-438079 (0.1 mM) and CGS15943 (0.1 mM)) and the probe (15 μM) in Opti-MEM were added accordingly and incubated for 30 min at 37 °C, 5 % CO_2. ATP (1, 2, 3, 4, 5 mM) was added via a computer controlled injector after 5 min. Fluorescence intensity recordings were performed for 30 min at 37 °C.

Investigation of hypoxic vs normoxic environments

Cells were plated in a black 96-well plate at a cell density of 5 x 10^4 cells/well in culture media (200 μL/well) and incubated for 24 h under normoxic (5 % CO_2, 95 % air, 37 °C) and hypoxic (hypoxic cabinet settings: 1 % O_2, 5% CO_2, 37 °C) conditions separately. This was followed by incubation of LPS (100 ng/ml) for 4 h under hypoxic and normoxic conditions. The culture media was removed, cells were washed three times with PBS. The probe (15 μM) in Opti-MEM was added to the cells and incubated for 30 min under hypoxic and normic conditions. The solutions were removed, cells were washed three times with PBS and subsequently dispensed in a solution of PBS for fluorescence measurements. Under hypoxic conditions, the plate reader was calibrated to a 1 % O_2 environment using N_2 gas. SIN-1 (15 μM) was added via a computer controlled injector after 10 min. Fluorescence intensity recordings were performed for 30 min at 37 °C.

Statistical analysis

One-way analysis of variance was used for statistical analysis. The Newman-Keuls post-test was used for multiple comparisons. The results are expressed as the mean ± SEM. The differences were considered statistically significant when p values were less than 0.05.

2. Chapter 2

2.1. General Methods

Flow infusion analysis was conducted using a Maxis HD quadrupole electrospray time-of-flight (ESI-QTOF) mass spectrometer (Bruker Daltonik GmbH, Bremen, Germany) in negative-ion mode. The capillary voltage was set to 4500 V, nebulising gas at 1 bar, drying gas at 4 L/min. The drying gas temperature was increased from 200 – 280 °C during the first infusion. For the second infusion the freshly prepared sample was run at 280 °C, then increased to 320 °C. Extracted MS spectra represents drying gas conditions of 280 °C. The TOF scan range was from 50 – 1000 mass-to-charge ratio (*m/z*). Infusion injections were performed by the infusion pump using a flow rate of 3 µL/min. The MS instrument was calibrated using a sodium formate calibrant solution. The calibrant solution consisted of 3 parts of 1 M NaOH to 97 parts of 50 : 50 water : isopropanol with 2 % formic acid. Data processing was performed using the Compass Data Analysis software version 4.3 (Bruker Daltonik GmbH, Bremen, Germany).

2.2. Synthesis

4-(hydroxymethyl)phenyl pivalate (5.2)

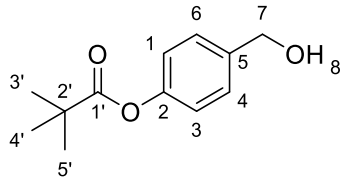

NaH–60 % mineral oil (1.70 g, 44.30 mmol) was dissolved in dry THF (200 ml) under a N_2 atmosphere. The mixture was cooled to 0 °C. 4-(hydroxymethyl)phenol (5.00 g, 40.30 mmol) was added and stirred at 0 °C until bubbling ceased. The mixture was allowed to warm up to RT and stirred at RT for 30 min. Subsequently, the mixture was cooled to 0 °C to which pivaloyl chloride (5.43 mL, 44.30 mmol) was added. The mixture was stirred for 30 min at 0 °C, warmed up to RT and stirred for a further 2 h. Sat. aq. $NaHCO_3$ (50 ml), followed by water (100 ml) were added to the mixture which was extracted with EtOAc (3 x 50 mL). The combined organic layers were washed with brine (2 x 50 ml), dried over $MgSO_4$, filtered and evaporated *in vacuo*. This gave 4-(hydroxymethyl)phenyl pivalate (8.25 g, 98 %) as a colourless oil.

^{1}H NMR (500 MHz, C*D*Cl$_3$): δ = 7.37 (d, *J* = 8.1 Hz, 2 H; Ar*H*), 7.04 (d, *J* = 8.5 Hz, 2 H; Ar*H*), 4.68 (s, 2 H; H–C(7)), 1.36 ppm (s, 9 H; H–C(3'), H–C(4'), H–C(5')); ^{13}C NMR (126 MHz, C*D*Cl$_3$): δ = 177.31, 150.67, 138.38, 128.14, 121.73, 64.92, 39.21, 27.28 ppm; IR (ATR): υ = 3346 (*w*, O–H), 1749 cm^{-1} (*m*, C=O); FTMS + p NSI MS: m/z (%): 226.1438 ([*M*+NH_4]$^+$, calcd for $C_{12}H_{20}NO_3^+$: 226.1438).

In accordance with literature.[174]

4-(bromomethyl)phenyl pivalate (5.3)

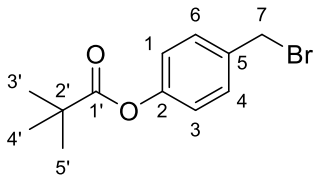

Lithium bromide (24.32 g, 0.28 mol) was dissolved in THF (60 mL) and triethylamine (10 mL, 0.73 mol) to which 4-(hydroxymethyl)phenyl pivalate (4.38 g, 0.02 mol) dissolved in THF (100 mL) was added. The mixture was cooled to 0 °C and methanesulfonyl chloride (18.21 g, 0.13 mol) was added dropwise. The solution was stirred for 2 h at 0 °C, quenched with water, and allowed to warm up to RT. The organic layer was extracted with DCM (3 x 50 mL), washed with sat. aq. $NaHCO_3$ (2 x 50 mL), dried over $MgSO_4$, filtered and evaporated *in vacuo*. FC (SiO_2; petroleum ether/EtOAc 90:10) gave 4-(bromomethyl)phenyl pivalate (4.14 g, 76 %) as a light yellow oil.

^{1}H NMR (300 MHz, C*D*Cl$_3$): δ = 7.42 – 7.37 (m, 2 H; Ar*H*), 7.06 – 7.01 (m, 2 H; Ar*H*), 4.49 (s, 2 H; H–C(7)), 1.35 ppm (s, 9 H; H–C(3'), H–C(4'), H–C(5')); ^{13}C NMR (75.5 MHz, C*D*Cl$_3$): δ = 177.07, 151.12, 135.22, 130.29, 122.01, 39.24, 32.95, 27.24 ppm; IR (ATR): υ = 1736 cm^{-1} (*m*, C=O); HR-ESI-MS: m/z (%): 271.0332 ([*M*+H]$^+$, calcd for $C_{12}H_{16}{}^{79}BrO_2^+$: 271.0334), 273.0311 ([*M*+H]$^+$, calcd for $C_{12}H_{16}{}^{81}BrO_2^+$: 273.0314).

In accordance with literature.[174]

4-((10*H*-phenoxazin-10-yl)methyl)phenyl pivalate (5.5)

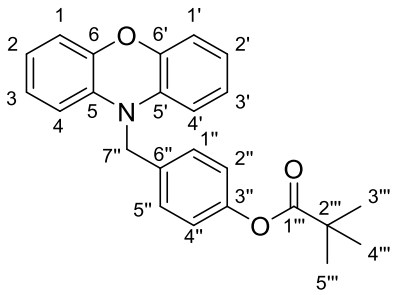

Phenoxazine (1.00 g, 5.46 mmol) was dissolved in THF (30 mL). The mixture was cooled down to 0 °C and left to stir for 10 min. NaH–60 % mineral oil (0.32 g, 8.19 mmol) was slowly added. After 10 min, 4-(bromomethyl)phenyl pivalate (2.96 g, 10.92 mmol) was added slowly. The solution was left to stir at RT for 4 h. The mixture was quenched with water (50 mL). After separation of the phases, the aqueous layer was extracted with EtOAc (2 x 40 mL). The combined organic layers were washed with water (3 x 50 mL), and brine (1 x 50 mL), dried over $MgSO_4$, filtered and evaporated *in vacuo*. FC (SiO_2; petroleum ether/EtOAc 90:10) gave 4-((10*H*-phenoxazin-10-yl)methyl)phenyl pivalate (1.28 g, 63 %) as a purple oil.

^{1}H NMR (300 MHz, C*D*Cl$_3$): δ = 7.45 – 7.35 (m, 2 H; Ar*H*), 7.34 – 7.28 (m, 2 H; Ar*H*), 7.10 – 6.98 (m, 4 H; Ar*H*), 6.74 – 6.64 (m, 2 H; Ar*H*), 6.38 – 6.27 (m, 2 H; Ar*H*), 4.49 (s, 2 H; H–C(7’’)), 1.35 ppm (s, 9 H; H–C(3’’’), H–C(4’’’), H–C(5’’’)); ^{13}C NMR (75.5 MHz, C*D*Cl$_3$): δ = 151.13, 150.29, 145.27, 135.22, 133.65, 130.29, 127.12, 123.87, 121.45, 115.42, 112.35, 58.75, 39.24, 27.25 ppm; IR (ATR): υ = 1747 (*m*, C=O), 1112 cm^{-1} (*s*, C–O); HR-ESI-MS: m/z (%): 374.1750 ([*M*+H]$^+$, calcd for $C_{24}H_{24}NO_3^+$: 374.1756).

4-((3,7-dibromo-10*H*-phenoxazin-10-yl)methyl)phenyl pivalate (5.6)

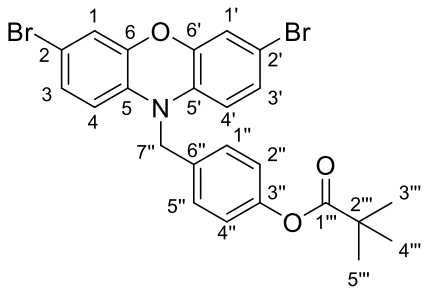

4-((10*H*-phenoxazin-10-yl)methyl)phenyl pivalate (900 mg, 2.41 mmol) was dissolved in chloroform (40 mL). NBS (858 mg, 4.82 mmol) was slowly added to the mixture, which was left to stir at RT for 1 h. The solution was quenched with water. After separation of the phases, the organic layer was washed with water (3 x 50 mL) and brine (1 x 50 mL), dried over $MgSO_4$, filtered and evaporated *in vacuo*. This gave 4-((3,7-dibromo-10*H*-phenoxazin-10-yl)methyl)phenyl pivalate (1.21 g, 95 %) as a green oil.

^{1}H NMR (300 MHz, C*D*Cl$_3$): δ = 7.38 – 7.31 (m, 2 H; Ar*H*), 7.10 – 6.98 (m, 4 H; Ar*H*), 6.87 – 6.75 (m, 2 H; Ar*H*), 6.16 (d, *J* = 9.0 Hz, 2 H; Ar*H*), 4.70 (s, 2 H; H–C(7'')), 1.35 ppm (s, 9 H; H–C(3'''), H–C(4'''), H–C(5''')); ^{13}C NMR (75.5 MHz, C*D*Cl$_3$): δ = 150.42, 145.35, 128.98, 126.85, 126.74, 122.36, 122.26, 121.59, 118.65, 113.36, 112.95, 65.49, 39.11, 27.14 ppm; IR (ATR): υ = 1747 (*m*, C=O), 1109 cm^{-1} (*s*, C–O); FTMS + p NSI MS: m/z (%): 530.9991 ([*M*+H]$^+$, calcd for $C_{24}H_{22}{}^{79}Br_2NO_3^+$: 530.9994), 531.9934 ([*M*+H]$^+$, calcd for $C_{24}H_{22}{}^{79}Br^{81}BrNO_3^+$: 531.9942), 532.9968 ([*M*+H]$^+$, calcd for $C_{24}H_{22}{}^{81}Br_2NO_3^+$: 532.9974).

4-((3,7-dibromo-10*H*-phenoxazin-10-yl)methyl)phenol (5.7)

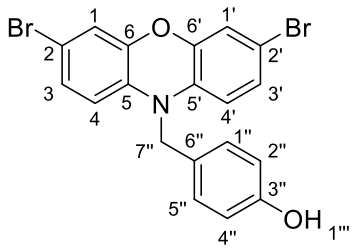

4-((3,7-dibromo-10*H*-phenoxazin-10-yl)methyl)phenyl pivalate (2.20 g, 4.14 mmol) was dissolved in toluene (60 mL) and cooled to 0 °C. DIBAL-H 1M in toluene (12 mL, 12.42 mmol) was slowly added. The mixture was stirred for 1 h at 0 °C and allowed to warm back to RT for 30 min. The mixture was quenched with sat. aq. $NH_4^+Cl^-$ (20 mL), diluted with EtOAc (30 mL), washed with water (3 x 60 mL), dried over $MgSO_4$, filtered and evaporated *in vacuo*. FC (SiO_2; petroleum ether/EtOAc 90:10) gave 4-((3,7-dibromo-10*H*-phenoxazin-10-yl)methyl)phenol (937 mg, 54 %) as a blue solid.

^{1}H NMR (300 MHz, C*D*Cl$_3$): δ = 7.18 – 7.05 (m, 2 H; Ar*H*), 6.90 – 6.73 (m, 6 H; Ar*H*), 6.28 – 6.11 (m, 2 H; Ar*H*)), 4.64 ppm (s, 2 H; H–C(7'')); ^{13}C NMR (75.5 MHz, C*D*Cl$_3$): δ = 154.60, 145.03, 132.36, 126.94, 126.67, 126.39, 118.27, 115.67, 113.01, 112.52, 48.34 ppm; m.p.: 162 – 165 °C; IR (ATR): υ = 3381 (*w*, O–H), 1107 cm^{-1} (*s*, C–O); TOF MS ASAP: m/z (%): 446.9298 ([*M*+H]$^+$, calcd for $C_{19}H_{14}{}^{79}Br_2NO_2^+$: 446.9294), 447.9353 ([*M*+H]$^+$, calcd for $C_{19}H_{14}{}^{79}Br^{81}BrNO_2^+$: 447.9372), 448.9302 ([*M*+H]$^+$, calcd for $C_{19}H_{19}{}^{81}Br_2NO_2^+$: 448.9404).

4-((3,7-bis(4,4,5,5-tetramethyl-1,3,2-dioxaborolan-2-yl)-10*H*-phenoxazin-10-yl)methyl)phenol (5.8)

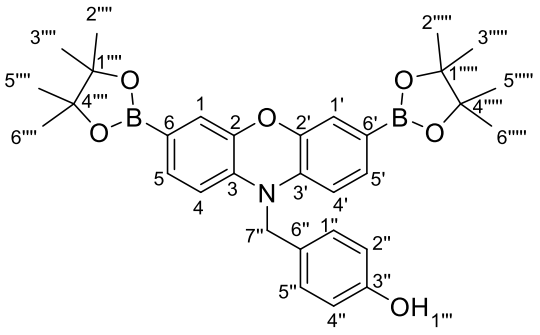

4-((3,7-dibromo-10*H*-phenoxazin-10-yl)methyl)phenol (300 mg, 0.67 mmol), bis(pinacolato)diboron (511 mg, 2.01 mmol) and KOAc (395 mg, 4.03 mmol) were dissolved in DMF (50 mL), degased under argon and treated with $PdCl_2$(dppf) (49 mg, 0.07 mmol). The mixture was heated at 90 °C for 6 h, and cooled to RT after completion. The solution was filtered through celite, diluted with EtOAc, washed with water (3 x 50 mL) and brine (3 x 50 mL), dried over $MgSO_4$, filtered and evaporated *in vacuo*. FC (SiO_2; petroleum ether/EtOAc 90:10 – 50:50) gave 4-((3,7-bis(4,4,5,5-tetramethyl-1,3,2-dioxaborolan-2-yl)-10*H*-phenoxazin-10-yl)methyl)phenol (193 mg, 53 %) as a light yellow solid.

^{1}H NMR (300 MHz, (C*D*$_3$)$_2$CO): δ = 8.34 (s, 1 H; H–O(1’’’)), 7.16 (m, 2 H, Ar*H*), 6.97 (s, 2 H, Ar*H*), 6.82 (d, *J* = 8.5 Hz, 2 H, Ar*H*), 6.54 (d, *J* = 7.9 Hz, 2 H, Ar*H*), 4.85 (s, 2 H; H–C(7’’)), 1.30 ppm (s, 24 H; H–C(2’’’’), H–C(3’’’’), H–C(5’’’’), H–C(6’’’’), H–C(2’’’’’), H–C(3’’’’’), H–C(5’’’’’), H–C(6’’’’’)); ^{13}C NMR (75 MHz, (C*D*$_3$)$_2$CO): δ = 157.9, 145.6, 137.3, 132.4, 128.6, 127.5, 121.7, 116.9, 116.8, 113.5, 84.7, 48.4, 25.5 ppm; m.p.: 230 – 233 °C; IR (ATR): υ = 3329 cm^{-1} (*w*, O–H); FTMS + p APCI corona MS: m/z (%): 538.2780 ([*M*–*H*]$^+$, calcd for $C_{31}H_{36}B_2NO_6^+$: 538.2796).

(5-chloro-5-oxopentyl)triphenylphosphonium (7.2)

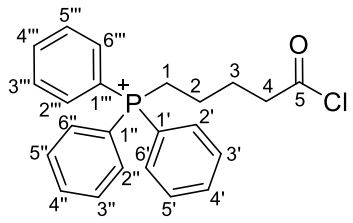

(4-carboxybutyl)triphenylphosphonium bromide (670 mg, 1.85 mmol) was dissolved in DCM/DMF (10 ml/10 µL). Thionyl chloride (0.7 mL, 9.62 mmol) was added slowly to the mixture. The solution was refluxed at 40 °C for 5 h. Solvent was evaporated *in vacuo* giving (5-chloro-5-oxopentyl)triphenylphosphonium (648 mg, 92 %) as an orange oil.

^{1}H NMR (300 MHz, C*D*Cl$_3$): δ = 7.88 – 7.58 (m, 15 H; Ar*H*), 3.65 – 3.47 (m, 2 H; H–C(4)), 3.06 – 3.00 (m, 2 H; H–C(1)), 2.11 – 2.00 (m, 2 H; H–C(3)), 1.88 – 1.64 ppm (m, 2 H; H–C(2)); ^{13}C NMR (126.5 MHz, C*D*Cl$_3$): δ = 207.19, 135.38, 133.80, 130.83, 118.44, 116.99, 25.86, 25.72, 21.48, 21.45 ppm; IR (ATR): υ = 1727 cm^{-1} (*s*, O=C); HR-ESI-MS: m/z (%): 381.1433 ([*M*]$^+$, calcd for $C_{23}H_{23}{}^{35}ClOP^+$: 381.1170).

(5-(4-((3,7-bis(4,4,5,5-tetramethyl-1,3,2-dioxaborolan-2-yl)-10*H*-phenoxazin-10-yl)methyl)phenoxy)-5-oxopentyl)triphenylphosphonium (6.1)

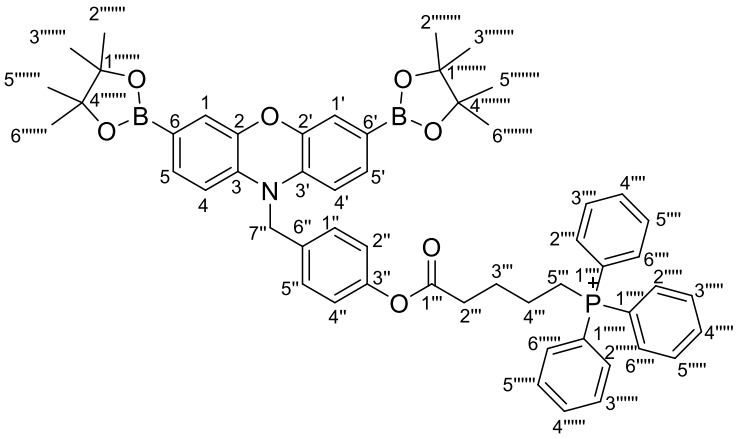

4-((3,7-bis(4,4,5,5-tetramethyl-1,3,2-dioxaborolan-2-yl)-10*H*-phenoxazin-10-yl)methyl)phenol (50 mg, 0.09 mmol) was dissolved in DCM (10 mL), cooled to 0 °C, to which triethylamine (0.02 mL, 0.18 mmol) and (5-chloro-5-oxopentyl) triphenylphosphonium (69 mg, 0.18 mmol) were added. The mixture was allowed to warm up to RT and stirred for 24 h. The reaction was quenched with water (30 mL). After separation of the phases, the organic layer was washed with water (3 x 20 mL), dried over $MgSO_4$, filtered and evaporated *in vacuo*. FC (SiO_2; petroleum ether/EtOAc 80:20) gave (5-(4-((3,7-bis(4,4,5,5-tetramethyl-1,3,2-dioxaborolan-2-yl)-10*H*-phenoxazin-10-yl)methyl)phenoxy)-5-oxopentyl)triphenylphosphonium (32 mg, 41 %) as a dark orange oil.

^{1}H NMR (500 MHz, $(CD_3)_2CO$): δ = 8.08 – 7.96 (m, 6 H; Ar*H*), 7.94 – 7.86 (m, 3 H; Ar*H*), 7.83 – 7.71 (m, 6 H; Ar*H*), 7.57 – 7.51 (m, 2 H; Ar*H*), 7.38 – 7.30 (m, 2 H; Ar*H*), 7.09 – 6.80 (m, 4 H; Ar*H*), 6.47 (d, *J* = 8.7 Hz, 2 H; Ar*H*), 4.90 (s, 2 H; H–C(7’’)), 4.05 – 3.92 (m, 2 H; H–C(2’’’)), 2.77 – 2.68 (m, 2 H; H–C(5’’’)), 1.96 – 1.84 (m, 2 H; H–C(3’’’)), 1.36 – 1.30 (m, 2 H; H–C(4’’’)), 1.21 ppm (s, 24 H; H–C(2’’’’’’’), H–C(3’’’’’’’), H–C(5’’’’’’’), H–C(6’’’’’’’), H–C(2’’’’’’’’), H–C(3’’’’’’’’), H–C(5’’’’’’’’), H–C(6’’’’’’’’)); ^{13}C NMR (126 MHz, $CDCl_3$): δ = 201.09, 145.40, 140.78, 136.18, 132.81, 131.09, 127.28, 127.23, 127.16, 126.77, 118.57, 117.39, 116.21, 113.47, 113.02, 112.78, 83.79, 83.67, 83.31, 45.91, 25.12, 24.90, 24.64, 24.51 ppm; IR (ATR): υ = 1752 cm^{-1} (*m*, C=O); FTMS + p NSI MS: m/z (%): 886.4222 ($[M]^+$, calcd for $C_{54}H_{59}B_2NO_7P^+$: 886.4227).

4-((3,7-bis(4,4,5,5-tetramethyl-1,3,2-dioxaborolan-2-yl)-10*H*-phenoxazin-10-yl) methyl)phenyl carbonochloridate (6.3)

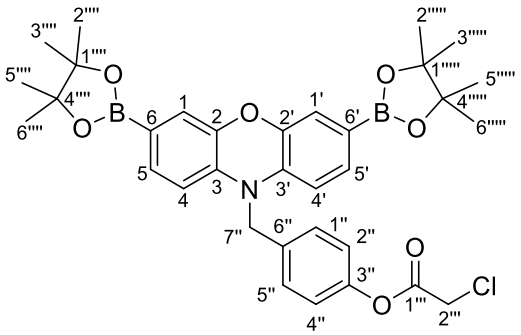

4-((3,7-bis(4,4,5,5-tetramethyl-1,3,2-dioxaborolan-2-yl)-10*H*-phenoxazin-10-yl)methyl)phenol (300 mg, 0.56 mmol) was dissolved in DCM (30 mL) and the solution cooled to 0 °C. Triethylamine (0.15 mL, 1.11 mmol) was then added, followed by 2-chloroacetyl chloride (0.09 mL, 1.11 mmol). The mixture was allowed to warm to RT and stirred for 24 h. The reaction was quenched with water (20 mL) and the phases were separated. The organic layer was washed with water (3 x 50 mL), dried over $MgSO_4$, filtered and evaporated *in vacuo*. FC (SiO_2; petroleum ether/ EtOAc 80:20) gave 4-((3,7-bis(4,4,5,5-tetramethyl-1,3,2-dioxaborolan-2-yl)-10*H*-phenoxazin-10-yl) methyl)phenyl carbonochloridate (41 mg, 12 %) as a dark green solid.

^{1}H NMR (300 MHz, C*D*Cl$_3$): δ = 7.24 (d, *J* = 8.6 Hz, 2 H; Ar*H*), 7.10 – 7.07 (m, 2 H; Ar*H*), 7.04 – 7.00 (m, 4 H; Ar*H*), 6.23 (d, *J* = 7.9 Hz, 2 H; Ar*H*), 4.72 (s, 2 H; H–C(2’’’), 4.62 (s, 2 H; H–C(7’’)), 1.23 ppm (s, 24 H; H–C(2’’’’’’’), H–C(3’’’’’’’), H–C(5’’’’’’’), H–C(6’’’’’’’), H–C(2’’’’’’’’), H–C(3’’’’’’’’), H–C(5’’’’’’’’), H–C(6’’’’’’’’)); ^{13}C NMR (126 MHz, C*D*Cl$_3$): δ = 183.21, 158.19, 145.36, 136.93, 131.94, 128.66, 127.75, 120.11, 117.33, 116.48, 113.55, 84.07, 62.16, 47.94, 25.25 ppm; m.p.: 171 – 174 °C; IR (ATR): υ = 1736 cm^{-1} (*w*, C=O); FTMS + p NSI MS: m/z (%): 618.2610 ([*M*+H]$^+$, calcd for $C_{33}H_{39}{}^{11}B_2{}^{35}ClNO_7{}^+$: 618.2607).

1-(2-(4-((3,7-bis(4,4,5,5-tetramethyl-1,3,2-dioxaborolan-2-yl)-10*H*-phenoxazin-10-yl)methyl)phenoxy)-2-oxoethyl)pyridin-1-ium (6.2)

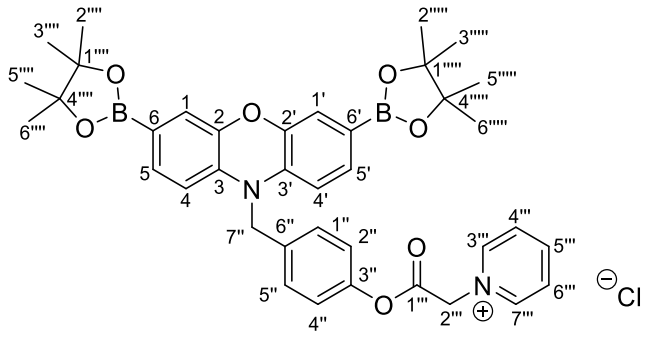

4-((3,7-bis(4,4,5,5-tetramethyl-1,3,2-dioxaborolan-2-yl)-10*H*-phenoxazin-10-yl)methyl)phenyl carbonochloridate (40 mg, 0.07 mmol) was dissolved in acetonitrile (10 mL). Pyridine (64 µL, 0.80 mmol) and potassium iodide (22 mg, 0.13 mmol) were then added. The mixture was refluxed at 80 °C for 24 h. The solvent was evaporated *in vacuo*. FC (SiO_2; petroleum ether/EtOAc 80:20) gave 1-(2-(4-((3,7-bis(4,4,5,5-tetramethyl-1,3,2-dioxaborolan-2-yl)-10*H*-phenoxazin-10-yl)methyl)phenoxy)-2-oxoethyl)pyridin-1-ium (27 mg, 59 %) as a yellow oil.

^{1}H NMR (300 MHz, C*D*Cl$_3$): δ = 8.69 – 8.68 (m, 2 H; Ar*H*), 7.53 – 7.48 (m, 1 H; Ar*H*), 7.17 – 7.12 (m, 4 H; Ar*H*), 7.07 – 7.05 (m, 2 H; Ar*H*), 6.81 – 6.78 (m, 2 H; Ar*H*), 6.34 – 6.32 (d, *J* = 7.9 Hz, 2 H; Ar*H*), 6.30 – 6.27 (d, *J* = 8.0 Hz, 2 H; Ar*H*), 5.77 (s, 2 H; H–C(2’’’)), 4.72 (s, 2 H; H–C(7’’)), 1.30 ppm (s, 24 H; H–C(2’’’’’’’), H–C(3’’’’’’’), H–C(5’’’’’’’), H–C(6’’’’’’’), H–C(2’’’’’’’’), H–C(3’’’’’’’’), H–C(5’’’’’’’’), H–C(6’’’’’’’’)); ^{13}C NMR (126 MHz, C*D*Cl$_3$): δ = 154.95, 146.56, 144.89, 136.18, 131.13, 130.67, 130.17, 129.88, 128.35, 127.67, 127.52, 121.11, 115.98, 111.84, 83.75, 63.76, 48.27, 24.96 ppm; IR (ATR): υ = 1702 cm^{-1} (*m*, C=O); FTMS + p NSI MS: m/z (%): 661.3266 ([*M*]$^+$, calcd for $C_{38}H_{43}B_2N_2O_7^+$: 661.3264).

pent-4-ynoyl chloride (11.2)

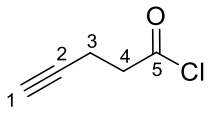

4-Pentynoic acid (300 mg, 3.06 mmol) was dissolved in DCM/DMF (10 ml/10 µL). Thionyl chloride (1.16 mL, 15.9 mmol) was added slowly to the mixture. The solution was refluxed at 40 °C for 6 h. Solvent was evaporated *in vacuo* giving pent-4-ynoyl chloride (270 mg, 76 %) as a light brown oil.

^{1}H NMR (500 MHz, C*D*Cl$_3$): δ = 3.13 (t, *J* = 7.1 Hz, 2 H; H–C(4)), 2.57 (td, *J* = 7.1, 2.7 Hz, 2 H; H–C(3)), 2.04 ppm (t, *J* = 2.7 Hz, 1 H; H–C(1)); ^{13}C NMR (126 MHz, C*D*Cl$_3$): δ = 172.12, 80.38, 70.26, 45.63, 14.69 ppm; IR (ATR): υ = 2119 (*w*, C≡C), 1693 cm^{-1} (*s*, C=O); HR-ESI-MS: m/z (%): 116.0097 ([*M*]$^+$, calcd for $C_5H_5ClO^+$: 116.0029).

4-((3,7-bis(4,4,5,5-tetramethyl-1,3,2-dioxaborolan-2-yl)-10*H*-phenoxazin-10-yl)methyl)phenyl pent-4-ynoate (10.1)

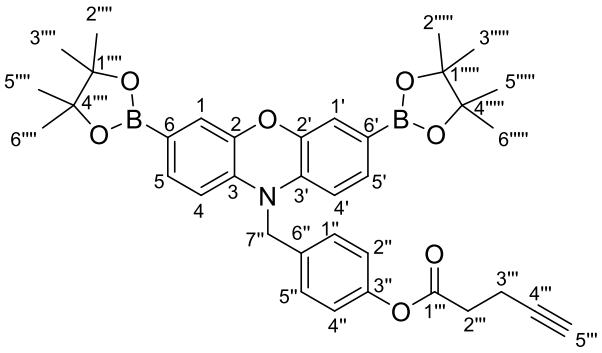

4-((3,7-bis(4,4,5,5-tetramethyl-1,3,2-dioxaborolan-2-yl)-10*H*-phenoxazin-10-yl)methyl)phenol (200 mg, 0.37 mmol) was dissolved in DCM (40 mL). The solution was cooled to 0 °C, followed by the addition of triethylamine (0.1 mL, 0.74 mmol), and pent-4-ynoyl chloride (86 mg, 0.74 mmol). The mixture was allowed to warm up to RT and stirred for 3 h. The reaction was quenched with water. After separation of the phases, the organic layer was washed with water (3 x 30 mL), dried over $MgSO_4$, filtered and evaporated *in vacuo*. FC (SiO_2; petroleum ether/EtOAc 80:20) gave 4-((3,7-bis(4,4,5,5-tetramethyl-1,3,2-dioxaborolan-2-yl)-10*H*-phenoxazin-10-yl)methyl)phenyl pent-4-ynoate (107 mg, 47 %) as a dark orange oil.

^{1}H NMR (300 MHz, C*D*Cl$_3$): δ = 7.33 – 7.23 (m, 2 H; Ar*H*), 7.20 – 7.10 (m, 2 H; Ar*H*), 7.10 – 7.01 (m, 4 H; Ar*H*), 6.30 (d, *J* = 7.9 Hz, 2 H; Ar*H*), 4.78 (s, 2 H; H–C(7’’)), 2.83 – 2.67 (m, 1 H; H–C(5’’’)), 2.63 – 2.48 (m, 2 H; H–C(2’’’)), 2.07 – 1.97 (m, 2 H; H–C(3’’’)), 1.26 ppm (s, 24 H; H–C(2’’’’), H–C(3’’’’), H–C(5’’’’), H–C(6’’’’), H–C(2’’’’’), H–C(3’’’’’), H–C(5’’’’’), H–C(6’’’’’)); ^{13}C NMR (126 MHz, C*D*Cl$_3$): δ = 170.40, 149.86, 144.84, 135.97, 134.87, 133.47, 131.37, 127.83, 127.21, 122.18, 121.19, 111.80, 83.77, 83.31, 75.26, 69.59, 33.62, 24.67 ppm; IR (ATR): υ = 2161 (*w*, C≡C), 1280 (*m*, C–N) 1121 cm^{-1} (*s*, C–O); FTMS + p APCI corona MS: m/z (%): 622.3123 ([*M*+H]$^+$, calcd for $C_{36}H_{42}{}^{11}B_2NO_7^+$: 622.3154).

4-((3,7-bis(4,4,5,5-tetramethyl-1,3,2-dioxaborolan-2-yl)-10*H*-phenoxazin-10-yl)methyl)phenyl pentanoate (10.2)

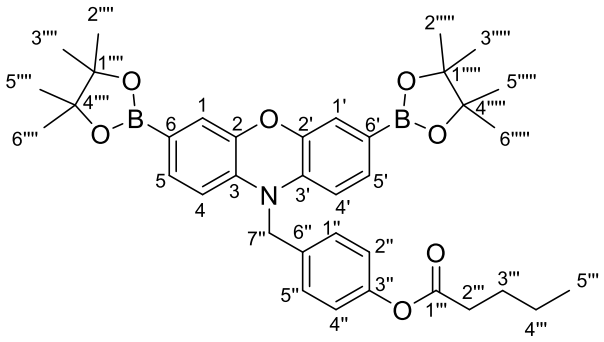

4-((3,7-bis(4,4,5,5-tetramethyl-1,3,2-dioxaborolan-2-yl)-10*H*-phenoxazin-10-yl)methyl)phenol (200 mg, 0.37 mmol) was dissolved in DCM (30 mL). The solution was cooled to 0 °C. First triethylamine (0.10 ml, 0.74 mmol) was added, followed by dropwise addition of valeroyl chloride (0.1 ml, 0.74 mmol). The mixture was stirred for 4 h at RT. The reaction was quenched with water, and the phases were separated. The organic phase was washed with water (3 x 20 ml), dried over $MgSO_4$, filtered and evaporated *in vacuo*. FC (SiO_2; petroleum ether/EtOAc 80:20) gave 4-((3,7-bis(4,4,5,5-tetramethyl-1,3,2-dioxaborolan-2-yl)-10*H*-phenoxazin-10-yl)methyl) phenyl pentanoate (72 mg, 31%) as a yellow/orange solid.

^{1}H NMR (500 MHz, C*D*Cl$_3$): δ = 7.28 (d, *J* = 8.4 Hz, 2 H; Ar*H*), 7.16 (dd, *J* = 7.9, 1.4 Hz, 2 H; Ar*H*), 7.07 (d, *J* = 1.4 Hz, 2 H; Ar*H*), 7.04 (d, *J* = 8.5 Hz, 2 H; Ar*H*), 6.31 (d, *J* = 8.0 Hz, 2 H; Ar*H*), 4.78 (s, 2 H; H–C(7’’)), 2.54 (t, *J* = 7.5 Hz, 2 H; H–C(2’’’)), 1.78 – 1.68 (m, 2 H; H–C(3’’’)), 1.48 – 1.38 (m, 2 H; H–C(4’’’’)), 1.31 (s, 24 H; H–C(2’’’’), H–C(3’’’’), H–C(5’’’’), H–C(6’’’’), H–C(2’’’’’), H–C(3’’’’’), H–C(5’’’’’), H–C(6’’’’’)), 1.01 – 0.94 ppm (m, 3 H; H–C(5’’’)); ^{13}C NMR (126 MHz, C*D*Cl$_3$): δ = 179.34, 172.42, 150.06, 144.86, 136.00, 133.19, 131.16, 127.16, 122.26, 121.17, 111.83, 83.76, 48.57, 33.76, 26.89, 24.95, 22.32, 13.82 ppm; m.p. 183 – 186 °C; IR (ATR): υ = 1706 cm^{-1} (*s*, C=O); HR-ESI-MS: m/z (%): 623.3457 ([*M*]$^-$, calcd for $C_{36}H_{45}O_7N^{10}B_2^-$: 623.3455).

10-(4-(prop-2-yn-1-yloxy)benzyl)-3,7-bis(4,4,5,5-tetramethyl-1,3,2-dioxaborolan-2-yl)-10*H*-phenoxazine (10.3)

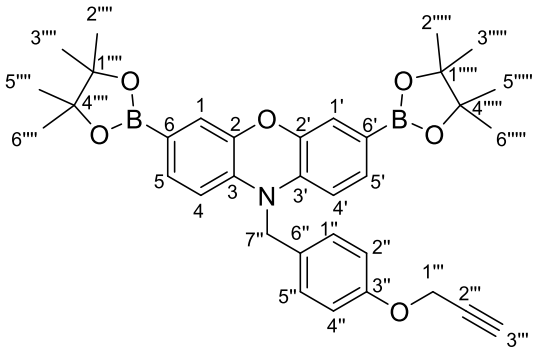

4-((3,7-bis(4,4,5,5-tetramethyl-1,3,2-dioxaborolan-2-yl)-10*H*-phenoxazin-10-yl)methyl)phenol (200 mg, 0.37 mmol) was dissolved in THF (30 mL). NaH – 60 % mineral oil (22 mg, 0.56 mmol) was added, followed by dropwise addition of propargyl bromide – 80 wt% in toluene (0.09 mL, 0.56 mmol). The mixture was stirred at RT for 20 h. The reaction was quenched with MeOH (20 mL), diluted with EtOAc (30 mL), washed with water (3 x 60 mL), dried over $MgSO_4$, filtered and evaporated *in vacuo*. FC (SiO_2; petroleum ether/EtOAc 80:20) gave 3,7-dibromo-10-(4-(prop-2-yn-1-yloxy)benzyl)-10*H*-phenoxazine (110 mg, 51 %) as a dark yellow oil.

^{1}H NMR (300 MHz, C*D*Cl$_3$): δ = 7.20 (d, *J* = 8.4 Hz, 2 H; Ar*H*), 7.15 (dd, *J* = 7.9, 1.4 Hz, 2 H; Ar*H*), 7.06 (d, *J* = 1.4 Hz, 2 H; Ar*H*), 6.93 (d, *J* = 8.7 Hz, 2 H; Ar*H*), 6.33 (d, *J* = 8.0 Hz, 2 H; Ar*H*), 4.74 (s, 2 H; H–C(7’’)), 4.66 (d, *J* = 2.4 Hz, 2 H; H–C(1’’’)), 2.51 (t, *J* = 2.3 Hz, 1 H; H–C(3’’’)), 1.26 ppm (s, 24 H; H–C(2’’’’), H–C(3’’’’), H–C(5’’’’), H–C(6’’’’), H–C(2’’’’’), H–C(3’’’’’), H–C(5’’’’’), H–C(6’’’’’)); ^{13}C NMR (126 MHz, (C*D*$_3$)$_2$CO): δ = 158.03, 145.41, 137.01, 132.17, 129.51, 128.42, 128.38, 121.56, 121.51, 116.26, 116.23, 113.19, 84.49, 79.92, 48.07, 25.32 ppm; IR (ATR): *υ* = 2160 (*w*, C≡C), 1346 cm^{-1} (*s*, C–O); FTMS + p APCI corona MS: m/z (%): 579.2958 ([*M*]$^+$, calcd for $C_{34}H_{39}{}^{11}B_2NO_6^+$: 579.2970).

10-(4-propoxybenzyl)-3,7-bis(4,4,5,5-tetramethyl-1,3,2-dioxaborolan-2-yl)-10*H*-phenoxazine (10.4)

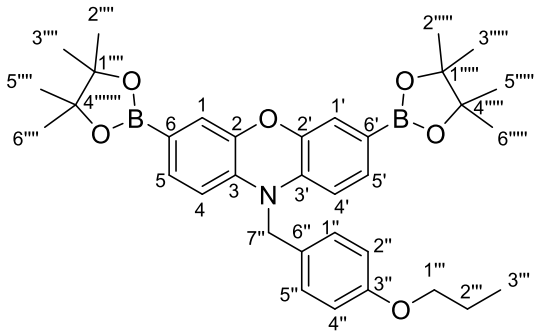

4-((3,7-bis(4,4,5,5-tetramethyl-1,3,2-dioxaborolan-2-yl)-10*H*-phenoxazin-10-yl)methyl)phenol (300 mg, 0.55 mmol) was dissolved in THF (30 mL). NaH–60 % mineral oil (32 mg, 0.83 mmol) was added, followed by dropwise addition of propargyl bromide – 80 wt% in toluene (0.15 mL, 0.83 mmol). The mixture was stirred at RT for 20 h. The reaction was quenched with MeOH (20 mL), diluted with EtOAc (30 mL), washed with water (3 x 60 mL), dried over $MgSO_4$, filtered and evaporated *in vacuo*. FC (SiO_2; petroleum ether/EtOAc 80:20) gave 10-(4-propoxybenzyl)-3,7-bis(4,4,5,5-tetramethyl-1,3,2-dioxaborolan-2-yl)-10*H*-phenoxazine (130 mg, 41 %) as a yellow solid.

^{1}H NMR (500 MHz, C*D*Cl$_3$): δ = 7.20 – 7.11 (m, 4 H; Ar*H*), 7.10 – 7.03 (m, 2 H; Ar*H*), 6.79 (dd, *J* = 8.5, 6.1 Hz, 1 H; Ar*H*), 6.70 – 6.64 (m, 1 H; Ar*H*), 6.34 (dd, *J* = 7.9, 3.8 Hz, 2 H; Ar*H*), 4.72 (s, 2 H; H–C(7’’)), 4.12 (q, *J* = 7.2 Hz, 2 H; H–C(1’’’)), 1.30 (s, 24 H; H–C(2’’’’), H–C(3’’’’), H–C(5’’’’), H–C(6’’’’), H–C(2’’’’’), H–C(3’’’’’), H–C(5’’’’’), H–C(6’’’’’)), 1.28 – 1.23 (m, 2 H; H–C(2’’’)) 0.89 – 0.83 ppm (m, 3 H; H–C(3’’’)); ^{13}C NMR (126 MHz, C*D*Cl$_3$): δ = 176.69, 171.50, 155.17, 155.05, 145.57, 144.88, 144.61, 136.82, 136.21, 133.42, 131.27, 131.12, 129.79, 127.75, 127.49, 127.47, 127.44, 127.25, 123.65, 121.75, 121.11, 115.96, 115.47, 115.39, 112.51, 111.89, 111.70, 83.85, 83.82, 70.68, 63.23, 24.93, 21.21, 14.33 ppm; m.p. 217 – 220 °C; IR (ATR): υ = 1138 cm^{-1} (*m*, C–O–C); HR-ESI-MS: m/z (%): 581.3365 ([*M*]$^+$, calcd for $C_{34}H_{43}O_6N^{10}B_2^+$: 581.3349).

4-((3,7-bis(4,4,5,5-tetramethyl-1,3,2-dioxaborolan-2-yl)-10*H*-phenoxazin-10-yl)methyl)phenyl 4-(4-(bis(2-chloroethyl)amino)phenyl)butanoate (26.1)

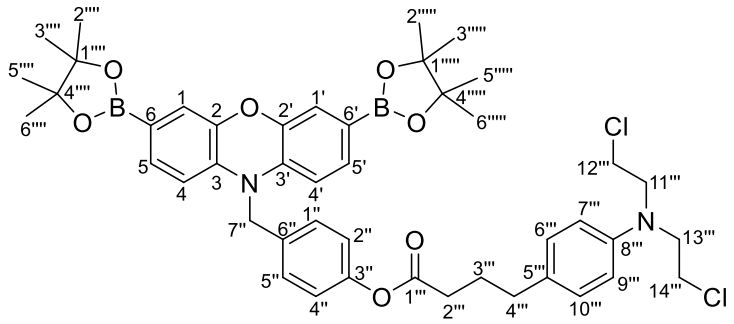

Chlorambucil (37 mg, 0.12 mmol) and HATU (49 mg, 0.13 mmol) were dissolved in DMF (5 ml) to which 4-((3,7-bis(4,4,5,5-tetramethyl-1,3,2-dioxaborolan-2-yl)-10*H*-phenoxazin-10-yl)methyl)phenol (100 mg, 0.18 mmol) and DIPEA (0.06 ml, 0.36 mmol) in DMF (5 ml) was added. The solution was left to stir at RT for 24 h. After completion, the mixture was diluted with EtOAc (15 ml), washed with water (1 x 20 ml) and brine (3 x 20 ml), dried with $MgSO_4$, filtered and evaporated *in vacuo*. FC (SiO_2; petroleum ether/EtOAc 80:20) gave 4-((3,7-bis(4,4,5,5-tetramethyl-1,3,2-dioxaborolan-2-yl)-10-phenoxazin-10-yl)methyl)phenyl 4-(4-(bis(2-chloroethyl) amino) phenyl)butanoate (30 mg, 20 %) as an orange solid.

^{1}H NMR (500 MHz, C*D*Cl$_3$): δ = 7.48 – 7.43 (m, 4 H; Ar*H*), 7.34 (dd, *J* = 7.9, 1.3 Hz, 2 H; Ar*H*), 7.29 (d, *J* = 8.2 Hz, 2 H; Ar*H*), 7.20 (d, *J* = 8.2 Hz, 2 H; Ar*H*), 6.82 (d, *J* = 8.3 Hz, 2 H; Ar*H*), 6.50 (d, *J* = 7.9 Hz, 2 H; Ar*H*), 4.96 (s, 2 H; H–C(7‘‘)), 3.89 (t, *J* = 7.0 Hz, 4 H; H–C(12‘‘‘),H–C(14‘‘‘)), 3.80 (t, *J* = 7.0 Hz, 4 H; H–C(11‘‘‘), H–C(13‘‘‘)), 2.83 (t, *J* = 7.5 Hz, 2 H; H–C(2‘‘‘)), 2.74 (t, *J* = 7.3 Hz, 2 H; H–C(4‘‘‘)), 2.21 (p, *J* = 7.4 Hz, 2 H; H–C(3‘‘‘)), 1.49 ppm (s, 24 H; H–C(2‘‘‘‘), H–C(3‘‘‘‘), H–C(5‘‘‘‘), H–C(6‘‘‘‘), H–C(2‘‘‘‘‘), H–C(3‘‘‘‘‘), H–C(5‘‘‘‘‘), H–C(6‘‘‘‘‘)); ^{13}C NMR (126 MHz, C*D*Cl$_3$): δ = 172.14, 149.99, 144.84, 144.57, 135.97, 133.24, 131.15, 130.48, 129.90, 127.17, 122.22, 121.18, 112.37, 111.81, 83.74, 53.76, 48.50, 40.66, 34.07, 33.78, 26.83, 24.95 ppm; m.p.: 105 – 108 °C; IR (ATR): *υ* = 1755 (*m*, C=O), 1113 cm^{-1} (*s*, C–O–C); HR-ESI-MS: m/z (%): 824.3514 ([*M*]$^+$, calcd for $C_{45}H_{54}O_7N_2{}^{35}Cl_2{}^{10}B_2{}^+$: 824.3567).

4 4-((3,7-bis(4,4,5,5-tetramethyl-1,3,2-dioxaborolan-2-yl)-10*H*-phenoxazin-10-yl)methyl)phenyl 2-(1-(4-chlorobenzoyl)-5-methoxy-2-methyl-1*H*-indol-3-yl)acetate (26.2)

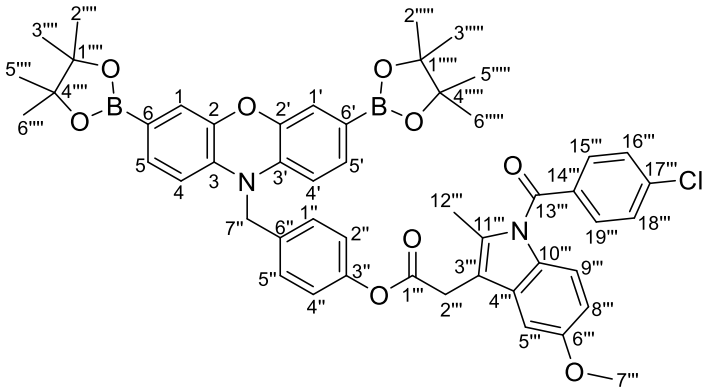

Indomethacin (43 mg, 0.12 mmol) and HATU (49 mg, 0.13 mmol) were dissolved in DMF (5 ml) to which 4-((3,7-bis(4,4,5,5-tetramethyl-1,3,2-dioxaborolan-2-yl)-10*H*-phenoxazin-10-yl)methyl)phenol (100 mg, 0.18 mmol) and DIPEA (0.06 ml, 0.36 mmol) in DMF (5 ml) was added.The solution was left to stir at RT for 24 h. After completion, the mixture was diluted with EtOAc (15 ml), washed with water (1 x 20 ml) and brine (3 x 20 ml), dried with $MgSO_4$, filtered and evaporated *in vacuo*. FC (SiO_2; petroleum ether/EtOAc 80:20) gave 4-((3,7-bis(4,4,5,5-tetramethyl-1,3,2-dioxaborolan-2-yl)-10*H*-phenoxazin-10-yl)methyl)phenyl 2-(1-(4-chlorobenzoyl)-5-methoxy-2-methyl-1*H*-indol-3-yl)acetate (45 mg, 28 %) as a dark orange solid.

^{1}H NMR (500 MHz, C*D*Cl$_3$): δ = 7.67 (dd, *J* = 8.4, 1.4 Hz, 2 H; Ar*H*), 7.49 – 7.45 (m, 2 H; Ar*H*), 7.16 – 7.10 (m, 4 H; Ar*H*), 7.08 – 7.03 (m, 4 H; Ar*H*), 6.89 (d, *J* = 9.1 Hz, 1 H; Ar*H*), 6.79 – 6.76 (m, 1 H; Ar*H*), 6.71 – 6.67 (m, 1 H; Ar*H*), 6.29 (d, J = 7.9 Hz, 2 H; Ar*H*), 4.76 (s, 2 H; H–C(7‘‘)), 3.89 (s, 2 H; H–C(2‘‘‘)), 3.83 (s, 3 H; H–C(7‘‘‘)), 2.44 (s, 3 H; H–C(12‘‘‘)), 1.31 ppm (s, 24 H; H–C(2‘‘‘‘), H–C(3‘‘‘‘), H–C(5‘‘‘‘), H–C(6‘‘‘‘), H–C(2‘‘‘‘‘), H–C(3‘‘‘‘‘), H–C(5‘‘‘‘‘), H–C(6‘‘‘‘‘)); ^{13}C NMR (126 MHz, C*D*Cl$_3$): δ = 169.42, 168.44, 156.28, 149.98, 144.87, 144.83, 139.48, 136.33, 136.19, 135.93, 131.33, 131.13, 129.28, 127.44, 127.21, 122.07, 121.19, 115.95, 115.16, 111.86, 111.77, 101.32, 83.78, 83.76, 55.89, 48.44, 30.70, 24.94, 13.56 ppm; m.p.: 162 – 165 °C; IR (ATR): υ = 1591 (*m*, C=O), 1346 cm^{-1} (*s*, C–O–C); HR-ESI-MS: m/z (%): 878.3460 ([*M*]$^+$, calcd for $C_{50}H_{51}O_9N_2{}^{35}Cl^{10}B_2{}^+$: 878.3542).

2.3. *In vitro* Studies

HeLa cells and RAW264.7 macrophages were obtained from ATCC (the American Type Culture Collection). RAW264.7 macrophages and HeLa cells were maintained in a Dulbecco's Modified Eagle's Medium supplemented with 10 % FBS in a humidified atmosphere of 5 % CO_2 and 95 % air at 37 ℃ and split when the cells reached 90 % confluency.

Cell viability assay

Cells were plated on 96-well plates in growth medium. After 24 h, cells were treated with probes at different concentrations (2.5, 5, 10, 20, and 40 μM) for 24 h. Then, cell viability was determined through a standard MTS cell proliferation assay.

Confocal laser scanning microscopy

Cells cultured in growth medium supplemented with 10 % FBS were plated onto 24-well microplates. Cells were maintained in a humidified atmosphere of 5 % CO_2 and 95 % air at 37 °C overnight. To detect $ONOO^-$ exogenously in HeLa cells and RAW264.7 macrophages, the cells were first incubated with the probe (20 μM, 1% DMSO in PBS, pH 7.4) for 30 min, followed by incubation with SIN-1 (500 μM) for 30 min. To quench the exogenously produced $ONOO^-$, the cells were pre-incubated with uric acid (100 μM) for 2 h, then SIN-1 (500 μM) for 30 min, and finally the probe (20 μM) for 30 min. To simulate endogenous $ONOO^-$, LPS (1 μg/mL) was first incubated for 24 h in RAW264.7 macrophages. After washing with PBS, the cells were incubated with the probe (20 μM) for 30 min. The cells were washed with PBS three times and fixed by 4 % paraformaldehyde for 20 min at RT. After rinsing twice with PBS, the cells were stained with Hoechst33342 (5 μg/mL) at 37 °C in a humidified atmosphere of 5 % CO_2 in air for 5 min. After three rinses with PBS, the samples were evaluated on a confocal laser scanning microscopy (Olympus, Japan) with λ_{ex} = 559 nm and λ_{em} = 580 – 650 nm for probes and λ_{ex} = 405 nm and λ_{em} = 470 – 520 nm for Hoechst33342.

2.4. *In vivo* Studies

All animal experiments were approved by the Animal Care and Use Committee of the Shanghai Institute of Materia Medica (SIMM), where the experiments were conducted. In addition, approval by the Animal Research Ethics Committee of the University of Bath was given

***In vivo* imaging**

Animals were housed in a SPF temperature-controlled room (22 ± 2°C) under a 12 h light/dark cycle in the Shanghai Institute of Materia Medica (SIMM) of the Chinese Academy of Science. Animals were anesthetized with pentobarbital sodium (50 mg/kg). At the end of the study, the mice were euthanized with CO_2 asphyxiation without recovery from the anaesthesia, according to the rules of Animal Care and Use Committee of the Shanghai Institute of Materia Medica. Mice were divided into four groups and three mice were used in each group from three independent experiments. In addition, four mice were used for preliminary experiments to explore conditions.

C57BL/6J mice were divided into two groups; the first group was given an intraperitoneal (i.p.) injection of saline (200 μL) as a control group, and the second group was injected i.p. with LPS (200 μL, 2 mg/ml in saline, Sigma Aldrich). After 4 h, animals were anesthetized and abdominal fur was removed using a razor. Then, mice were injected i.p. with the probe (100 μL, 200 μM in saline) or saline (100 μL). Whole body images were acquired in 30 min by using the IVIS spectrum imaging system (PerkinElmer, USA). The imaging mode was set as: λ_{ex} = 535 nm, λ_{em} = 600 nm.

3. Chapter 3

3.1. Synthesis

2-hydroxy-4-((4-(4,4,5,5-tetramethyl-1,3,2-dioxaborolan-2-yl)benzyl)oxy)benzaldehyde (5.3)

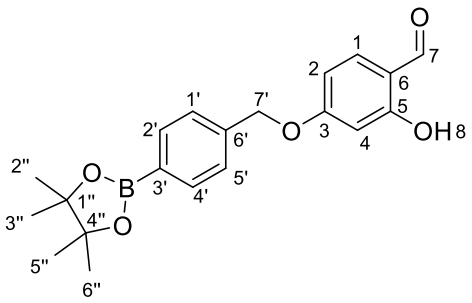

2,4-dihydroxybenzaldehyde (1.00 g, 7.24 mmol) and 4-(bromomethyl)benzene-boronic acid pinacol ester (2.20 g, 7.24 mmol) were dissolved in acetonitrile (15 ml) to which K_2CO_3 (1.00 g, 7.24 mmol) and KI (96 mg, 0.58 mmol) were added. The solution was refluxed at 80 °C for 2 h. After completion, the mixture was allowed to cool to RT, diluted with 1M HCl, extracted with DCM (3 x 10 ml), washed with brine (2 x 20 ml), dried over $MgSO_4$, filtered and evaporated *in vacuo*. Recrystallization in ethanol gave 2-hydroxy-4-((4-(4,4,5,5-tetramethyl-1,3,2-dioxaborolan-2-yl)benzyl)oxy) benzaldehyde (1.25 g, 49 %) gave a pale orange solid.

^{1}H NMR (500 MHz, C*D*Cl$_3$): δ = 11.44 (s, 1 H; O–H(8)), 9.71 (s, 1 H; H–C(7)), 7.86 – 7.81 (m, 2 H; Ar*H*), 7.42 (dd, *J* = 9.7, 8.2 Hz, 3 H; Ar*H*), 6.60 (dd, *J* = 8.7, 2.4 Hz, 1 H; Ar*H*), 6.49 (d, *J* = 2.3 Hz, 1 H; Ar*H*), 5.13 (s, 2 H; H–C(7‘)), 1.35 ppm (s, 9 H; H–C(2‘‘), H–C(3‘‘), H–C(5‘‘), H–C(6‘‘)); ^{13}C NMR (126 MHz, C*D*Cl$_3$): δ = 194.54, 165.97, 164.57, 138.84, 135.44, 135.31, 126.70, 126.55, 115.51, 109.06, 101.89, 84.06, 70.42, 25.02 ppm; m.p.: 80 – 83 °C; IR (ATR): *υ* = 2978 (*br*. *m*, H–C=O), 1649 (*s*, C=O), 1119 cm^{-1} (s, C–O–C); HR-ESI-MS: m/z (%): 355.1742 ([*M*+H]$^+$, calcd for $C_{20}H_{24}O_5{}^{11}B^+$: 355.1715).

Adapted from literature.[175]

2-oxo-7-((4-(4,4,5,5-tetramethyl-1,3,2-dioxaborolan-2-yl)benzyl)oxy)-2*H*-chromene-3-carboxylic acid (5.5)

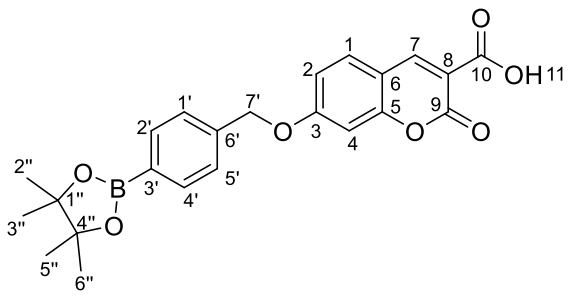

2-hydroxy-4-((4-(4,4,5,5-tetramethyl-1,3,2-dioxaborolan-2-yl)benzyl)oxy)benzaldehyde (1.00 g, 2.82 mmol) and 2,2-dimethyl-1,3-dioxan-4,6-dione (426 mg, 2.96 mmol) were dissolved in ethanol (15 ml) to which piperidine (6 µl, 0.06 mmol) and acetic acid (3.5 µl, 0.06 mmol) were added. The mixture was left to stir first at RT for 30 min and then refluxed at 78 °C for 3 h. After completion, the solution was cooled to RT, the precipitate filtered off and dried *in vacuo*. This gave 2-oxo-7-((4-(4,4,5,5-tetramethyl-1,3,2-dioxaborolan-2-yl)benzyl)oxy)-2*H*-chromene-3-carboxylic acid (657 mg, 55 %) as a pale yellow solid.

^{1}H NMR (500 MHz, (C*D*$_3$)$_2$SO): δ = 8.65 (s, 1 H; H–C(7)), 7.82 (d, *J* = 8.7 Hz, 1 H; Ar*H*), 7.71 (d, *J* = 7.7 Hz, 2 H; Ar*H*), 7.48 (d, *J* = 7.8 Hz, 2 H; Ar*H*), 7.16 – 7.03 (m, 2 H; Ar*H*), 5.30 (s, 2 H; H–C(7‘)), 1.29 ppm (s, 12 H; H–C(2‘‘), H–C(3‘‘), H–C(5‘‘), H–C(6‘‘)); ^{13}C NMR (126 MHz, (C*D*$_3$)$_2$SO): δ = 164.22, 163.17, 157.24, 156.55, 139.37, 134.62, 131.38, 129.02, 127.04, 113.71, 111.93, 105.47, 104.56, 101.18, 83.70, 69.85, 24.66 ppm; m.p.: 162 – 165 °C; IR (ATR): υ = 1746 (*m*, C=O), 1355 cm^{-1} (*s*, C–O–C); HR-ESI-MS: m/z (%): 445.1447 ([*M*+Na]$^+$, calcd for $C_{23}H_{23}O_7{}^{11}BNa^+$: 445.1433).

In accordance with literature.[175]

(4-aminobutyl)triphenylphosphonium bromide (6.2)

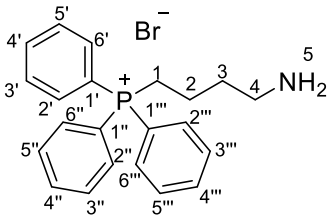

(4-bromobutyl)triphenylphosphonium bromide (250 mg, 0.63 mmol) was dissolved in an ammonia solution (7M in methanol, 25 ml). The solution was stirred at RT for 72 h and evaporated *in vacuo*. This gave (4-aminobutyl)triphenylphosphonium bromide as a white solid (158 mg, 76 %).

^{1}H NMR (500 MHz, C*D*Cl$_3$): δ = 8.01 – 7.57 (m, 15 H; Ar*H*), 3.66 (s, 2 H; H–C(4)), 3.15 (s, 2 H; H–C(1)), 2.27 (s, 2 H; H–C(3)), 1.95 ppm (s, 2 H; H–C(2)); ^{13}C NMR (126 MHz, C*D*Cl$_3$): δ = 135.38, 134.13, 134.05, 130.88, 118.45, 117.76, 39.33, 34.51, 23.17, 22.76 ppm; m.p.: 67 – 69 °C; IR (ATR): υ = 1587 cm^{-1} (*m*, N–H); HR-ESI-MS: m/z (%): 334.1775 ([*M*]$^+$, calcd for $C_{22}H_{25}NP^+$: 334.1719).

In accordance with literature.[176]

_N_-(2-aminoethyl)-4-methylbenzenesulfonamide (8.3)

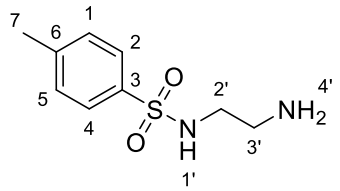

Ethylenediamine (0.85 ml, 10.0 mmol) was dissolved in DCM (10 ml) and cooled to 0 °C. Triethylamine (0.41 ml, 30 mmol) was slowly added, followed by 4-methylbenzenesulfonyl chloride (1.42 g, 7.5 mmol) dissolved previously in DCM (10 ml). The solution was allowed to warm up to RT and stirred for 24 h. The solution was further diluted with DCM (50 ml), washed with 15 % $NaHCO_3$ (3 x 20 mL) and water (3 x 30 mL), dried over $MgSO_4$, filtered and evaporated *in vacuo*. Recrystallization in ethanol gave *N*-(2-aminoethyl)-4-methylbenzenesulfonamide (1.00 g, 63 %) as a white solid.

^{1}H NMR (500 MHz, C*D*Cl_3): δ = 7.71 (d, *J* = 8.3 Hz, 2 H; H–C(2), H–C(4)), 7.31 (d, *J* = 7.9 Hz, 2 H; H–C(1), H–C(5)), 2.98 (s, 2 H; H–C(2')), 2.85 (s, 2 H; H–C(3')), 2.40 ppm (s, 3 H; H–C(7)); ^{13}C NMR (126 MHz, C*D*Cl_3): δ = 143.95, 136.60, 130.00, 129.85, 127.28, 43.14, 21.70 ppm; m.p.: 105 – 107 °C; IR (ATR): υ = 1596 cm^{-1} (*m*, N–H); HR-ESI-MS: m/z (%): 215.0934 ([*M*+H]$^+$, calcd for $C_9H_{15}N_2O_2S^+$: 215.0910).

In accordance with literature.[177]

(4-(2-oxo-7-((4-(4,4,5,5-tetramethyl-1,3,2-dioxaborolan-2-yl)benzyl)oxy)-2*H*-chromene-3-carboxamido)butyl)triphenylphosphonium (2.1)

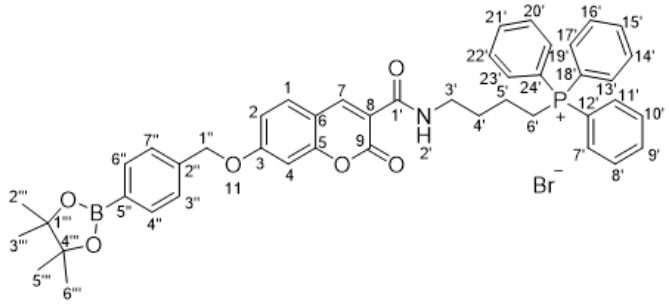

(4-aminobutyl)triphenylphosphonium bromide (80 mg, 0.24 mmol), HATU (95 mg, 0.25 mmol) and DMAP (15 mg, 0.12 mmol) were dissolved in DMF (5 ml) to which 2-oxo-7-((4-(4,4,5,5-tetramethyl-1,3,2-dioxaborolan-2-yl)benzyl)oxy)-2*H*-chromene-3-carboxylic acid (100 mg, 0.24 mmol) and DIPEA (60 µl, 0.36 mmol) in DMF (5 ml) was added. The solution was left to stir at RT for 16 h. After completion, the mixture was diluted with EtOAc (15 ml), washed with water (3 x 20 ml) and brine (3 x 20 ml), dried with $MgSO_4$, filtered and evaporated *in vacuo*. FC (SiO_2; petroleum ether/EtOAc 70:30) gave (4-(2-oxo-7-((4-(4,4,5,5-tetramethyl-1,3,2-dioxaborolan-2-yl)benzyl)oxy)-2*H*-chromene-3-carboxamido)butyl)triphenylphosphonium (31 mg, 18 %) as a yellow oil.

^{1}H NMR (500 MHz, C*D*Cl$_3$): δ = 8.48 (s, 1 H; H–C(7)), 8.23 – 8.15 (m, 4 H; Ar*H*), 7.87 – 7.75 (m, 4 H; Ar*H*), 7.75 – 7.62 (m, 4 H; Ar*H*), 7.41 (dd, *J* = 8.2, 3.3 Hz, 4 H; Ar*H*), 6.97 – 6.82 (m, 2 H; Ar*H*), 6.55 – 6.49 (m, 4 H; Ar*H*), 5.16 (d, *J* = 6.0 Hz, 2 H; H–C(1‘‘)), 3.38 – 3.29 (m, 2 H; H–C(3‘)), 3.00 – 2.82 (m, 2 H; H–C(6‘)), 1.65 (m, 2 H; H–C(4‘)), 1.44 – 1.35 (m, 2 H; H–C(5‘)), 1.33 ppm (s, 12 H; H–C(2‘‘‘), H–C(3‘‘‘), H–C(5‘‘‘), H–C(6‘‘‘)); ^{13}C NMR (126 MHz, C*D*Cl$_3$): δ = 164.21, 162.61, 157.53, 154.81, 149.02, 148.30, 142.82, 135.32, 135.29, 133.63, 133.60, 133.55, 133.52, 130.87, 130.80, 130.72, 130.70, 130.62, 129.62, 126.72, 126.69, 114.34, 113.94, 111.95, 106.76, 101.91, 101.62, 84.02, 70.65, 48.55, 43.20, 39.27, 24.99 ppm; IR (ATR): υ = 1717 (*m*, C=O), 1358 cm^{-1} (*s*, C–O–C); HR-ESI-MS: m/z (%): 738.3135 ([*M*]$^+$, calcd for $C_{45}H_{46}O_6{}^{11}BNP^+$: 737.3192).

_N_-(2-morpholinoethyl)-2-oxo-7-((4-(4,4,5,5-tetramethyl-1,3,2-dioxaborolan-2-yl)benzyl)oxy)-2_H_-chromene-3-carboxamide (2.2)

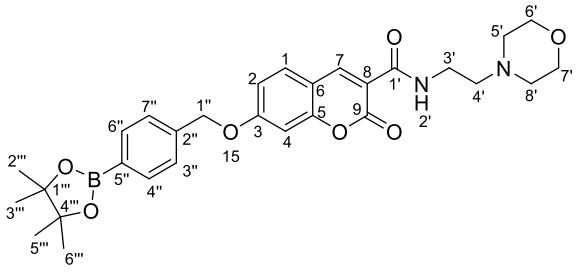

2-Morpholinoethylamine (31 mg, 0.24 mmol), HATU (95 mg, 0.25 mmol) and DMAP (15 mg, 0.12 mmol) were dissolved in DMF (5 ml) to which 2-oxo-7-((4-(4,4,5,5-tetramethyl-1,3,2-dioxaborolan-2-yl)benzyl)oxy)-2*H*-chromene-3-carboxylic acid (100 mg, 0.24 mmol) and DIPEA (60 µl, 0.36 mmol) in DMF (5 ml) were added. The solution was left to stir at RT for 16 h. After completion, the mixture was diluted with EtOAc (15 ml), washed with water (3 x 20 ml) and brine (3 x 20 ml), dried with $MgSO_4$, filtered and evaporated *in vacuo*. FC (SiO_2; petroleum ether/EtOAc 70:30) gave *N*-(2-morpholinoethyl)-2-oxo-7-((4-(4,4,5,5-tetramethyl-1,3,2-dioxaborolan-2-yl)benzyl)oxy)-2*H*-chromene-3-carboxamide (36 mg, 28 %) as a yellow solid.

^{1}H NMR (500 MHz, C*D*Cl$_3$): δ = 8.16 (s, 1 H; H–C(7)), 7.83 – 7.80 (m, 2 H; Ar*H*), 7.43 – 7.40 (m, 2 H; Ar*H*), 7.08 (d, *J* = 8.6 Hz, 1 H; Ar*H*), 6.47 – 6.42 (m, 2 H; Ar*H*), 5.08 (s, 2 H; H–C(1‘‘)), 3.73 – 3.70 (m, 4 H; H–C(6‘), H–C(7‘)), 3.68 – 3.64 (m, 2 H; H–C(3‘)), 2.66 (t, *J* = 6.7 Hz, 2 H; H–C(4‘)), 2.52 (dd, *J* = 5.7, 3.7 Hz, 4 H; H–C(5‘), H–C(8‘)), 1.34 ppm (s, 12 H; H–C(2‘‘‘), H–C(3‘‘‘), H–C(5‘‘‘), H–C(6‘‘‘)); ^{13}C NMR (126 MHz, C*D*Cl$_3$): δ = 166.26, 164.47, 162.96, 139.70, 135.25, 135.19, 135.14, 132.75, 126.76, 126.69, 112.57, 107.13, 102.56, 83.97, 69.98, 67.10, 59.18, 55.16, 53.99 ppm; m.p.: 125 – 128 °C; IR (ATR): υ = 1612 (*s*, C=O), 1114 cm^{-1} (*s*, C–O–C); HR-ESI-MS: m/z (%): 535.2614 ([*M*+H]$^+$, calcd for $C_{29}H_{36}O_7N_2{}^{11}B^+$: 535.2574).

_N_-(2-((4-methylphenyl)sulfonamido)ethyl)-2-oxo-7-((4-(4,4,5,5-tetramethyl-1,3,2-dioxaborolan-2-yl)benzyl)oxy)-2_H_-chromene-3-carboxamide (2.3)

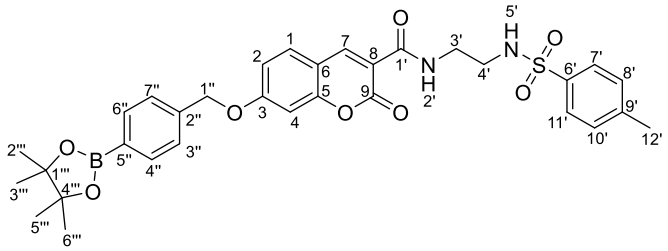

_N_-(2-aminoethyl)-4-methylbenzenesulfonamide (51 mg, 0.24 mmol), HATU (95 mg, 0.25 mmol) and DMAP (15 mg, 0.12 mmol) were dissolved in DMF (5 ml) to which 2-oxo-7-((4-(4,4,5,5-tetramethyl-1,3,2-dioxaborolan-2-yl)benzyl)oxy)-2_H_-chromene-3-carboxylic acid (100 mg, 0.24 mmol) and DIPEA (60 µl, 0.36 mmol) in DMF (5 ml) were added. The solution was left to stir at RT for 16 h. After completion, the mixture was diluted with EtOAc (15 ml), washed with water (3 x 20 ml) and brine (3 x 20 ml), dried with $MgSO_4$, filtered and evaporated _in vacuo_. FC (SiO_2; petroleum ether/EtOAc 70:30) gave _N_-(2-((4-methylphenyl)sulfonamido)ethyl)-2-oxo-7-((4-(4,4,5,5-tetramethyl-1,3,2-dioxaborolan-2-yl)benzyl)oxy)-2_H_-chromene-3-carboxamide (35 mg, 24 %) as a yellow oil.

^{1}H NMR (500 MHz, C_D_Cl_3): δ = 8.17 (s, 1 H; H–C(7)), 7.82 (dq, _J_ = 5.0, 3.1, 2.6 Hz, 2 H; Ar_H_), 7.71 – 7.64 (m, 3 H; Ar_H_), 7.45 – 7.37 (m, 2 H; Ar_H_), 7.31 – 7.17 (m, 2 H; Ar_H_), 6.52 – 6.47 (m, 2 H; Ar_H_), 5.18 – 5.13 (m, 2 H; H–C(1‘‘)), 3.02 (d, _J_ = 1.3 Hz, 2 H; H–C(3‘)), 2.41 (d, _J_ = 2.8 Hz, 2 H; H–C(4‘)), 2.39 (s, 3 H; H–C(12‘)), 1.33 ppm (s, 12 H; H–C(2‘‘‘), H–C(3‘‘‘), H–C(5‘‘‘), H–C(6‘‘‘)); ^{13}C NMR (126 MHz, C_D_Cl_3): δ = 154.65, 149.04, 148.76, 143.50, 136.90, 135.28, 130.88, 130.06, 129.82, 128.46, 127.14, 126.71, 126.68, 114.35, 114.28, 113.95, 106.74, 101.88, 101.60, 83.98, 70.78, 43.08, 39.21, 24.98, 21.61 ppm; IR (ATR): υ = 1720 (_m_, C=O), 1154 cm^{-1} (s, C–O–C); HR-ESI-MS: m/z (%): 619.2263 ([_M_+H]$^+$, calcd for $C_{32}H_{36}O_8N_2{}^{11}B^+$: 619.2243).

Tert-butyl (2-aminoethyl)carbamate (10.2)

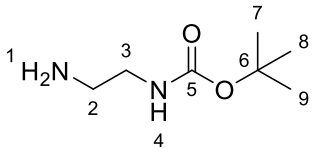

Ethylenediamine (30 ml, 0.45 mol) was dissolved in chloroform (70 ml) to which di-tert-butyl dicarbonate (10.00 g, 0.045 mol) in chloroform (50 ml) was very slowly added at 0 °C. The solution was left to stir at RT for 24 h. After completion, the mixture was poured into water (40 ml). The organic layer was separated and washed with brine (2 x 60 ml), dried over $MgSO_4$, and evaporated *in vacuo*. This gave *tert*-butyl (2-aminoethyl)carbamate (6.44 g, 89 %) as a colourless oil.

^{1}H NMR (500 MHz, C*D*Cl$_3$): δ = 4.88 (s, 1 H; H–C(4)), 3.16 (q, *J* = 6.1 Hz, 2 H; H–C(2)), 2.79 (td, *J* = 6.0, 1.3 Hz, 2 H; H–C(3)), 1.47 – 1.41 (m, 9 H; H–C(7), H–C(8), H–C(9)), 1.37 ppm (s, 2 H; H–C(1)); ^{13}C NMR (126 MHz, C*D*Cl$_3$): δ = 156.34, 79.37, 43.56, 31.38, 28.55 ppm; IR (ATR): υ = 1684 (*s*, C=O), 1506 cm^{-1} (*s*, N–H); HR-ESI-MS: m/z (%): 161.1309 ([*M*+H]$^+$, calcd for $C_7H_{17}O_2N_2^+$: 161.1285).

In accordance with literature.[178]

Tert-butyl (2-(6-bromo-1,3-dioxo-1_H_-benzo[de]isoquinolin-2(3_H_)-yl)ethyl)carbamate (10.4)

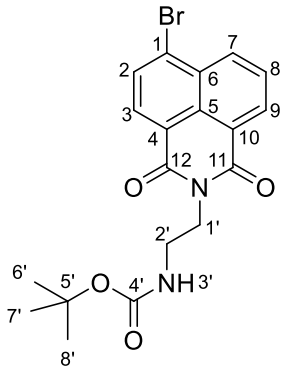

Tert-butyl (2-aminoethyl)carbamate (2.88 g, 18 mmol) was dissolved in ethanol (80 ml) to which 4-bromo-1,8-naphthalic anhydride (5.00 g, 18 mmol) was added. The mixture was refluxed at 75 °C for 2 h. After completion, the reaction was cooled to RT and the solid was filtered off. The precipitate was washed with cold ethanol and dried *in vacuo*. This gave *tert*-butyl (2-(6-bromo-1,3-dioxo-1*H*-benzo[de]isoquinolin-2(3*H*)-yl)ethyl)carbamate (6.41 g, 85 %) as a white solid.

^{1}H NMR (300 MHz, C*D*Cl$_3$): δ = 8.67 (dd, *J* = 7.3, 1.1 Hz, 1 H; Ar*H*), 8.58 (dd, *J* = 8.6, 1.1 Hz, 1 H; Ar*H*), 8.43 (d, *J* = 7.9 Hz, 1 H; Ar*H*), 8.05 (d, *J* = 7.9 Hz, 1 H; Ar*H*), 7.86 (dd, *J* = 8.5, 7.3 Hz, 1 H; Ar*H*), 4.92 (s, 1 H; N–H(3')), 4.36 (t, *J* = 5.7 Hz, 2 H; H–C(2')), 3.53 (d, *J* = 5.9 Hz, 2 H; H–C(1')), 1.27 ppm (s, 9 H; H–C(6'), H–C(7'), H–C(8')); ^{13}C NMR (126 MHz, C*D*Cl$_3$): δ = 164.16, 156.21, 137.48, 136.12, 134.40, 133.57, 133.03, 132.40, 131.57, 131.28, 130.81, 130.55, 129.28, 128.68, 128.24, 84.30, 40.19, 28.35 ppm; m.p. 178 – 181 °C; IR (ATR): υ = 3368 (*w*, O=C–N–H), 1701 cm^{-1} (*s*, C=O); HR-ESI-MS: m/z (%): 419.0617 ([*M*+H]$^+$, calcd for $C_{19}H_{20}O_4N_2{}^{79}Br^+$: 419.0601).

In accordance with literature.[178]

2-(2-aminoethyl)-6-bromo-1*H*-benzo[de]isoquinoline-1,3(2*H*)-dione (10.5)

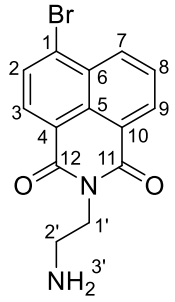

Tert-butyl(2-(6-bromo-1,3-dioxo-1*H*-benzo[de]isoquinolin-2(3*H*)-yl)ethyl) carbamate (250 mg, 0.6 mmol) was dissolved in DCM (5 ml) to which trifluroacteic acid (0.3 ml, 3.9 mmol) was added. The solution was left to stir at RT for 2 h. After completion, solvent and TFA were evaporated *in vacuo*. This gave 2-(2-aminoethyl)-6-bromo-1*H*-benzo[de]isoquinoline-1,3(2*H*)-dione (185 mg, 96 %) as a pale beige solid.

^{1}H NMR (500 MHz, C*D*Cl$_3$): δ = 8.54 (t, *J* = 8.5 Hz, 2 H; Ar*H*), 8.30 (d, *J* = 7.8 Hz, 1 H; Ar*H*), 7.97 (d, *J* = 7.6 Hz, 1 H; Ar*H*), 7.79 (t, *J* = 7.8 Hz, 1 H; Ar*H*), 6.90 (s, 2 H; *H*$_2$–N(3')), 4.59 – 4.47 (m, 2 H; H–C(1')), 3.56 – 3.49 ppm (m, 2 H; H–C(2')); ^{13}C NMR (126 MHz, (C*D*$_3$)$_2$SO): δ = 163.60, 163.56, 132.80, 131.61, 131.45, 130.99, 129.88, 129.21, 128.93, 128.56, 123.08, 122.30, 48.59, 37.58 ppm; m.p.: 193 – 196 °C; IR (ATR): υ = 3042 (*br. m*, N–H$_2$), 1653 cm^{-1} (s, C=O); HR-ESI-MS: m/z (%): 319.0079 ([*M*+H]$^+$, calcd for $C_{14}H_{11}O_2N_2{}^{79}Br^+$: 319.0037).

In accordance with literature.[178]

_N_-(2-(6-bromo-1,3-dioxo-1_H_-benzo[_de_]isoquinolin-2(3_H_)-yl)ethyl)-2-oxo-7-((4-(4,4,5,5-tetramethyl-1,3,2-dioxaborolan-2-yl)benzyl)oxy)-2_H_-chromene-3-carboxamide (10.6)

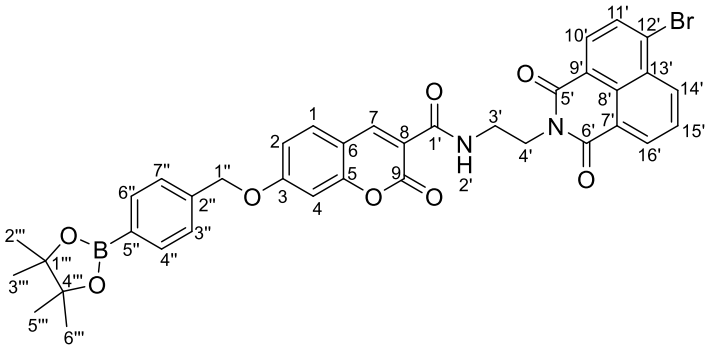

2-(2-aminoethyl)-6-bromo-1*H*-benzo[de]isoquinoline-1,3(2*H*)-dione (76 mg, 0.24 mmol), HATU (95 mg, 0.25 mmol) and DMAP (15 mg, 0.12 mmol) were dissolved in DMF (5 ml) to which 2-oxo-7-((4-(4,4,5,5-tetramethyl-1,3,2-dioxaborolan-2-yl)benzyl)oxy)-2*H*-chromene-3-carboxylic acid (100 mg, 0.24 mmol) and DIPEA (60 µl, 0.36 mmol) in DMF (5 ml) were added. The solution was left to stir at RT for 16 h. After completion, the mixture was diluted with EtOAc (15 ml), washed with water (3 x 20 ml) and brine (3 x 20 ml), dried with $MgSO_4$, filtered and evaporated *in vacuo*. FC (SiO_2; DCM/MeOH 90:10) gave *N*-(2-(6-bromo-1,3-dioxo-1*H*-benzo[*de*]isoquinolin-2(3*H*)-yl)ethyl)-2-oxo-7-((4-(4,4,5,5-tetramethyl-1,3,2-dioxaborolan-2-yl)benzyl)oxy)-2*H*-chromene-3-carboxamide (44 mg, 25 %) as a yellow solid.

^{1}H NMR (500 MHz, C*D*Cl$_3$): δ = 8.53 (s, 1 H; H–C(7)), 7.88 – 7.81 (m, 4 H; Ar*H*), 7.50 (d, *J* = 8.7 Hz, 1 H; Ar*H*), 7.44 – 7.40 (m, 4 H; Ar*H*), 6.95 (dd, *J* = 8.7, 2.4 Hz, 2 H; Ar*H*), 6.86 (d, *J* = 2.4 Hz, 1 H; Ar*H*), 5.18 (s, 2 H; H–C(1‘‘)), 2.99 (s, 2 H; H–C(3‘)), 1.66 (s, 2 H; H–C(4‘)), 1.34 ppm (s, 12 H; H–C(2‘‘‘), H–C(3‘‘‘), H–C(5‘‘‘), H–C(6‘‘‘)); ^{13}C NMR (126 MHz, C*D*Cl$_3$): δ = 164.36, 164.25, 157.64, 157.28, 149.58, 138.40, 135.39, 135.35, 132.78, 131.91, 131.46, 130.96, 129.62, 126.73, 126.71, 114.48, 113.99, 111.97, 101.64, 84.08, 60.54, 52.88, 25.01, 14.34 ppm; m.p.: 83 – 86 °C; IR (ATR): *ν* = 1743 (*m*, C=O), 1356 cm^{-1} (*s*, C-O-C); HR-ESI-MS: m/z (%): 725.1486 ([*M*+H]$^+$, calcd for $C_{37}H_{33}O_8N_2{}^{81}Br^{11}B^+$: 725.1448).

3.2. *In vitro* Studies

Confocal microscopy

Fluorescence microscopy images were captured on an Olympus, FLUOVIEW FV10i using 35 mm glass base dishes (Iwaki). Images were captured at a magnification of x60 with the following parameters: λ_{ex} = 405 nm, λ_{em} = 420 – 460 nm. Laser 405 nm with an intensity of 50 % was used. Processing and analysis of confocal microscopy images were performed with Image J.

Cell culture

RAW264.7 macrophages were kindly donated by Prof. Masaru Ishii from the Graduate School of Medicine, Osaka University. Cells are stored at -196 °C under liquid nitrogen until required. Cells are warmed up in a water bath (37 °C) for 2 min. The cell liquid was transferred into a falcon tube, to which media (5 mL) was added. The solution was centrifuged at 1000 x *g* for 5 min at 22 °C. After removal of the supernatant, fresh media (1 mL) was added and the cells were thrown quickly and incubated at 37 °C, 5 % CO_2. RAW 264.7 nacrophages were cultured in high-glucose Dulbecco's modified Eagle medium (DMEM) plus Gluta Max-I supplemented with 10 % FBS, penicillin (100 U/mL) and streptomycin (100 µg/mL) (P/S). The cells were incubated at 37 °C in a humidified atmosphere with 5 % CO_2. During cell passaging (every two days), media was removed, washed with PBS (2 x 4 ml), PET (4 ml) was added and incubated for 3 min at 37 °C, 5 % CO_2. The solution was mixed and 1 ml of cell solution transferred to a new culture dish containing 10 ml of DMEM (supplemented with FBS and P/S).

Investigating Cou-mito, Cou-lys and Cou-endo with SIN-1

Cells were plated in a glass bottom dish at a cell density of 5 x 10^5 cells in DMEM (with FBS, no P/S; 2 ml/dish) and incubated for 18 h. The culture media was removed, cells were washed with HBSS (2 x 2 ml), SIN-1 (100 µM) in DMEM (no phenol red, no FBS, no P/S) was added and incubated for 30 min / 1 h at 37 °C, 5 % CO_2. The

culture media was removed, cells were washed with HBSS (2 x 2 ml), the probe (20 μM) in DMEM (no phenol red, no FBS, no P/S) was added and incubated for 30 min at 37 °C, 5 % CO_2. This was then directly used for confocal imaging.

Investigate Cou-lys with LPS, IFN-γ and ebselen

Cells were plated in a glass bottom dish at a cell density of 5 x 10^5 cells in DMEM (with FBS, no P/S; 2 ml/dish) and incubated for 18 h at 37 °C, 5 % CO_2. LPS (1 μg/ml) and IFN-γ (50 ng/ml) were added and incubated for 4 h at 37 °C, 5 % CO_2. The culture media was removed, cells were washed with HBSS (2 x 2ml), (where indicated, ebselen (50 μM) was incubated for 1 h prior to addition of the probe), the probe (20 μM) in DMEM (no phenol red, no FBS, no P/S) was added and incubated for 30 min at 37 °C, 5 % CO_2. This was then directly used for confocal imaging.

Investigating Cou-lys with PMA

Cells were plated in a glass bottom dish at a cell density of 5 x 10^5 cells in DMEM (with FBS, no P/S; 2 ml/dish) and incubated for 18 h at 37 °C, 5 % CO_2. The culture media was removed, cells were washed with HBSS (2 x 2 ml), PMA (1 μg/ml) in DMEM (no phenol red, no FBS, no P/S) was added and incubated for 1 h respectively at 37 °C, 5 % CO_2. The culture media was removed, cells were washed with HBSS (2 x 2 ml), the probe (20 μM) in DMEM (no phenol red, no FBS, no P/S) was added and incubated for 30 min at 37 °C, 5 % CO_2. This was then directly used for confocal imaging.

4. Chapter 4

4.1. Synthesis

3',6'-bis((4-(4,4,5,5-tetramethyl-1,3,2-dioxaborolan-2-yl)benzyl)oxy)-3*H*-spiro[isobenzofuran-1,9'-xanthen]-3-one (5.1)

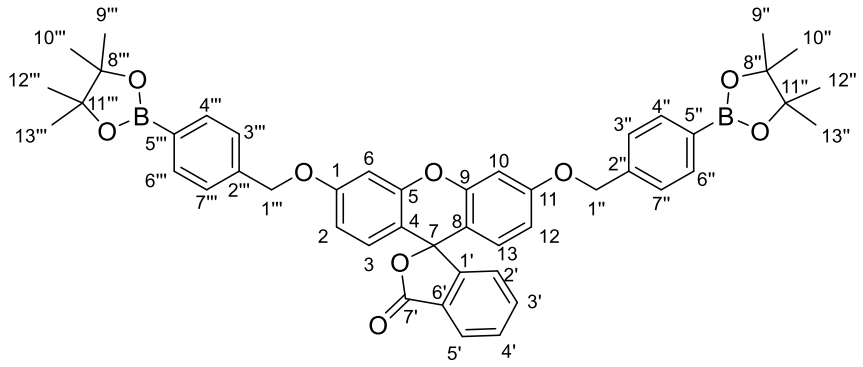

Fluorescein (400 mg, 1.20 mmol) was dissolved in acetonitrile (20 ml) to which 4-bromomethylphenylboronic acid pinacol ester (1.07 g, 3.6 mmol) and caesium carbonate (1.17 g, 3.6 mmol) were added. The solution was refluxed at 80 °C for 18 h under N_2, then cooled to RT, filtered and rinsed with DCM (50 ml). Solvent was evaporated *in vacuo*. FC (SiO_2; petroleum ether/EtOAc 80:20) gave 3',6'-bis((4-(4,4,5,5-tetramethyl-1,3,2-dioxaborolan-2-yl)benzyl)oxy)-3*H*-spiro[isobenzofuran-1,9'-xanthen]-3-one (275 mg, 30 %) as an orange solid.

^{1}H NMR (500 MHz, C*D*$_3$O*D*): δ = 8.33 – 8.27 (m, 1 H; Ar*H*), 7.84 – 7.67 (m, 4 H; Ar*H*), 7.55 – 7.44 (m, 3 H; Ar*H*), 7.37 – 7.30 (m, 1 H; Ar*H*), 6.98 – 6.89 (m, 3 H; Ar*H*), 6.79 – 6.71 (m, 2 H; Ar*H*), 6.57 – 6.49 (m, 2 H; Ar*H*), 6.30 (td, *J* = 4.5, 2.0 Hz, 2 H; Ar*H*), 5.34 – 5.20 (m, 4 H; H–C(1’’), H–C(1’’’)), 1.36 ppm (s, 24 H; H–C(9’’), H–C(10’’), H–C(12’’), H–C(13’’), H–C(9’’’), H–C(10’’’), H–C(12’’’), H–C(13’’’)); ^{13}C NMR (126 MHz, C*D*$_3$O*D*): δ = 166.67, 165.58, 136.08, 136.06, 135.95, 134.88, 134.07, 132.41, 131.65, 131.61, 131.26, 128.46, 128.32, 128.05, 127.93, 127.85, 85.26, 85.19, 68.49, 25.21 ppm; m.p. 252 – 254 °C; IR (ATR): υ = 1717 (*m*, C=O), 1282 cm^{-1} (*s*, C–O); HR-ESI-MS: m/z (%): 765.3450 ([*M*+H]$^+$, calcd for $C_{46}H_{48}{}^{11}B_2O_9^+$: 765.3415).

In accordance with literature values.[141]

Rhodamine 110 (7.3)

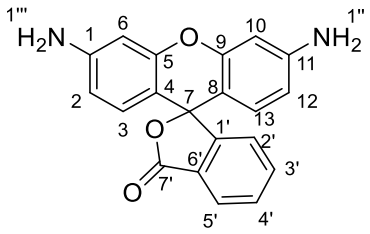

3-aminophenol (3.95 g, 36.62 mol) and phthalic anhydride (2.71 g, 18.31 mmol) were dissolved in methansulfonic acid (16 ml). The mixture was refluxed at 140 °C for 24 h. The solution was allowed to cool down and poured into ice water (60 ml). The pH was neutralized with dropwise addition of 10 M NaOH, followed by acidification with 1 M HCl. The solid was filtered off and dried *in vacuo*. The solid was resuspended in methanol and solvent was evaporated *in vacuo*. FC (SiO_2; petroleum ether/EtOAc 80:20) gave rhodamine 110 (2.12 g, 35 %) as a red solid.

^{1}H NMR (300 MHz, $(CD_3)_2CO$): δ = 7.68 – 7.45 (m, 2 H; Ar*H*), 7.16 – 7.03 (m, 3 H; Ar*H*), 6.83 (td, *J* = 7.9, 0.4 Hz, 1 H; Ar*H*), 6.49 (ddd, *J* = 8.1, 2.4, 1.0 Hz, 2 H; Ar*H*), 6.20 – 6.02 (m, 2 H; Ar*H*), 2.93 ppm (s, 4 H; H–N(1’’), H–N(1’’’)); ^{13}C NMR (75.5 MHz, CD_3OD): δ = 169.82, 134.86, 134.33, 132.62, 131.45, 130.60, 129.99, 129.98, 129.21, 128.39, 123.55, 123.09, 117.62, 116.41, 115.71, 114.76, 113.75, 113.04, 109.68, 96.96 ppm; m.p.: 250 – 252 °C; IR (ATR): υ = 1722 (*s*, C=O), 1596 cm^{-1} (*s*, N–H); HR-ESI-MS: m/z (%): 331.1057 ($[M+H]^+$, calcd for $C_{20}H_{15}N_2O_3^+$: 331.1077).

4-(4,4,5,5-tetramethyl-1,3,2-dioxaborolan-2-yl)benzaldehyde (7.5)

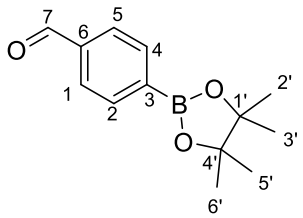

4-bromobenzaldehyde (300 mg, 1.63 mmol), bis(pinacolato)diboron (828 mg, 3.26 mmol), KOAc (958 mg, 9.78 mmol) were dissolved in DMF (15 mL), and degased under argon for 10 min. $PdCl_2$(dppf) (117 mg, 0.16 mmol) was added to the mixture which was refluxed at 90 °C for 24 h. The solution was cooled to RT, filtered through celite, diluted with EtOAc (30 ml), washed with water (3 x 30 ml) and brine (3 x 30 ml), dried over $MgSO_4$, filtered and evaporated *in vacuo*. FC (SiO_2; petroleum ether/EtOAc 80:20) gave 4-(4,4,5,5-tetramethyl-1,3,2-dioxaborolan-2-yl)benzaldehyde (258 mg, 68 %) as a dark yellow oil.

^{1}H NMR (500 MHz, C*D*Cl$_3$): δ = 10.05 (s, 1 H; H–C(7)), 7.96 (d, *J* = 8.0 Hz, 2 H; H–C(2), H–C(4)), 7.86 (d, *J* = 8.2 Hz, 2 H; H–C(1), H–C(5)), 1.36 ppm (s, 12 H; H–C(2'), H–C(3'), H–C(5'), H–C(6')); ^{13}C NMR (126 MHz, C*D*Cl$_3$): δ = 192.78, 138.27, 135.36, 128.84, 127.89, 84.48, 24.72 ppm; IR (ATR): υ = 1703 cm^{-1} (*m*, C=O); HR-ESI-MS: m/z (%): 233.1354 ([*M*+H]$^+$, calcd for $C_{13}H_{19}{}^{11}BO_3{}^+$: 233.1346).

In accordance with literature values.[179]

3',6'-bis((4-(4,4,5,5-tetramethyl-1,3,2-dioxaborolan-2-yl)benzyl)amino)-3*H*-spiro[isobenzofuran-1,9'-xanthen]-3-one (5.2)

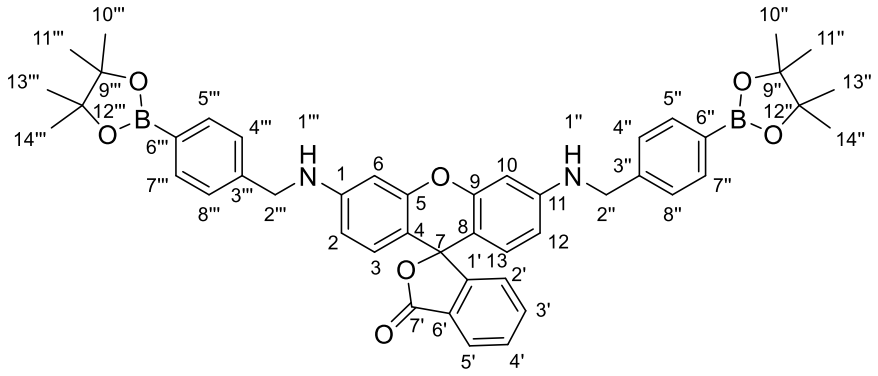

Rhodamine 110 (200 mg, 0.61 mmol) and 4-bromobenzaldehyde (283 mg, 1.22 mmol) were dissolved in ethanol/toluene (20 ml, 9:1). A Dean and Stark trap was fitted and the solution was refluxed at 77 °C for 24 h. Solvent was evaporated *in vacuo* and the solid was resuspended in methanol (15 ml) to which sodium borohydride (93 mg, 18.36 mmol) was slowly added. This was left to stir at RT for 2 h and subsequently poured into ice water (10 ml). The organic phase was extracted with DCM (3 x 15 ml), dried over $MgSO_4$, filtered and evaporated *in vacuo*. FC (SiO_2; petroleum ether/EtOAc 80:20) gave 3',6'-bis((4-(4,4,5,5-tetramethyl-1,3,2-dioxaborolan-2-yl)benzyl)amino)-3*H*-spiro[isoben-zo furan-1,9'-xanthen]-3-one (124 mg, 27 %) as a red solid.

^{1}H NMR (500 MHz, C*D*$_3$O*D*): δ = 7.69 (dd, *J* = 12.4, 7.7 Hz, 4 H; Ar*H*), 7.63 – 7.53 (m, 4 H; Ar*H*), 7.49 (d, *J* = 7.2 Hz, 2 H; Ar*H*), 7.42 (d, *J* = 7.5 Hz, 2 H; Ar*H*), 7.33 (d, *J* = 7.0 Hz, 4 H; Ar*H*), 6.49 (d, *J* = 5.3 Hz, 2 H; Ar*H*), 4.70 – 4.47 (m, 4 H; H–C(2’’), H–C(2’’’)), 1.32 ppm (s, 24 H; H–C(10’’), H–C(11’’), H–C(13’’), H–C(14’’), H–C(10’’’), H–C(11’’’), H–C(13’’’), H–C(14’’’)); ^{13}C NMR (126 MHz, C*D*$_3$O*D*): δ = 150.34, 134.48, 134.33, 133.80, 133.02, 132.97, 132.66, 132.09, 132.07, 130.92, 130.83, 129.73, 129.70, 129.70, 129.65, 129.53, 129.22, 128.40, 128.37, 128.31, 128.26, 127.40, 127.09, 126.44, 126.20, 125.68, 124.71, 123.30, 123.23, 122.96, 122.77, 120.73, 111.35, 110.67, 109.78, 108.93, 107.75, 105.39, 74.42, 74.06, 73.98, 73.23, 73.13, 35.73, 23.80, 23.61 ppm; m.p.: 100 – 102 °C; IR (ATR): υ = 1610 cm^{-1} (*s*, N–H); HR-ESI-MS: m/z (%): 763.3726 ([*M*+H]$^+$, calcd for $C_{46}H_{49}{}^{11}B_2N_2O_7^+$: 763.3735).

Rhodol (8.2)

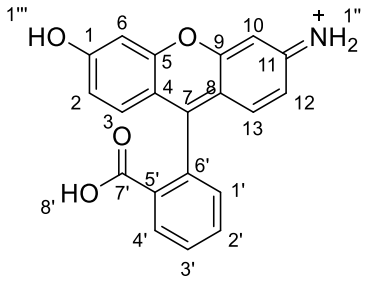

3-aminophenol (2.00 g, 18.30 mmol), resorcinol (2.01 g, 18.30 mmol) and phthalic anhydride (2.71 g, 18.30 mmol) were dissolved in methansulfonic acid (16 ml). The mixture was refluxed at 140 °C for 24 h. The solution was allowed to cool down and poured into ice water. The pH was neutralised with dropwise addition of 10M NaOH, followed by acidification with 1M HCl. The solid was filtered off and dried *in vacuo*. The solid was resuspended in methanol and solvent was evaporated *in vacuo*. FC (SiO_2; petroleum ether/EtOAc 80:20) gave rhodol (1.97 g, 33 %) as an orange/red solid.

^{1}H NMR (500 MHz, C*D*$_3$O*D*): δ = 8.00 (d, *J* = 7.6 Hz, 1 H; Ar*H*), 7.77 – 7.71 (m, 2 H; Ar*H*), 7.68 (t, *J* = 7.5 Hz, 1 H; Ar*H*), 7.56 (dd, *J* = 5.6, 3.3 Hz, 1 H; Ar*H*), 7.19 (d, *J* = 7.5 Hz, 1 H; Ar*H*), 6.71 (d, *J* = 2.2 Hz, 2 H; Ar*H*), 6.61 – 6.52 ppm (m, 2 H; Ar*H*); ^{13}C NMR (126 MHz, C*D*$_3$O*D*): δ = 171.38, 161.66, 154.30, 136.37, 135.68, 132.01, 131.98, 131.06, 130.23, 129.85, 128.28, 126.07, 125.55, 124.45, 113.84, 111.61, 103.50 ppm; m.p.: 190 – 192 °C; IR (ATR): υ = 2814 (*br*. *m*, O–H), 1702 (*m*, C=O), 1594 cm^{-1} (*s*, N–H); HR-ESI-MS: m/z (%): 333.0773 ([*M*+H]$^+$, calcd for $C_{20}H_{14}N_1O_4^+$: 333.1001).

2-(3-((4-(4,4,5,5-tetramethyl-1,3,2-dioxaborolan-2-yl)benzyl)amino)-6-((4-(4,4,5,5-tetramethyl-1,3,2-dioxaborolan-2-yl)benzyl)oxy)-9*H*-xanthen-9-yl)benzoic acid (5.3)

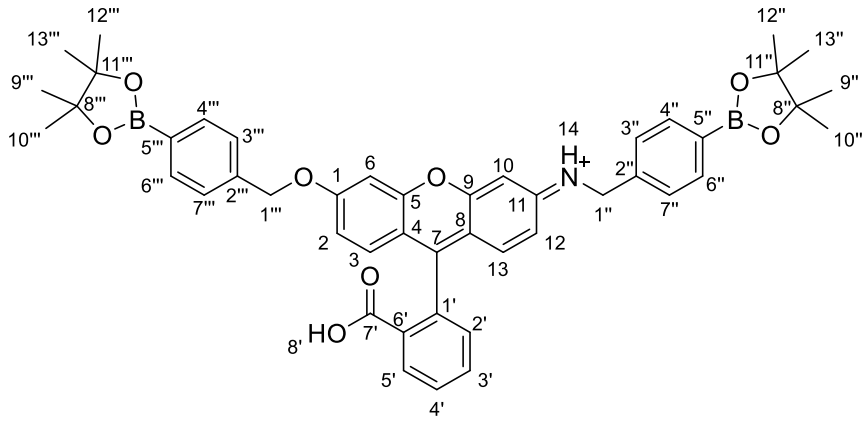

Rhodol (800 mg, 2.4 mmol) was dissolved in acetonitrile (40 ml) to which 4-bromomethylphenylboronic acid pinacol ester (1.43 g, 4.8 mmol) followed by caesium carbonate (1.56 g, 4.8 mmol) were added. The solution was refluxed at 80 °C for 18 h under N_2, then cooled to RT, filtered and rinsed with DCM (50 ml). Solvent was evaporated *in vacuo*. FC (SiO_2; petroleum ether/EtOAc 80:20) gave 3',6'-bis((4-(4,4,5,5-tetramethyl-1,3,2-dioxaborolan-2-yl)benzyl)oxy)-3*H*-spiro[isobenzofuran-1,9'-xanthen]-3-one (600 mg, 33 %) as an orange solid.

^{1}H NMR (500 MHz, C*D*Cl$_3$): δ = 8.28 (dd, *J* = 7.8, 1.4 Hz, 1 H; Ar*H*), 7.88 – 7.85 (m, 2 H; Ar*H*), 7.80 (dd, *J* = 7.9, 5.0 Hz, 2 H; Ar*H*), 7.71 (td, *J* = 7.5, 1.5 Hz, 2 H; Ar*H*), 7.65 (dd, *J* = 7.8, 1.5 Hz, 3 H; Ar*H*), 7.49 – 7.44 (m, 2 H; Ar*H*), 7.37 (dt, *J* = 8.2, 0.7 Hz, 1 H; Ar*H*), 6.95 – 6.91 (m, 2 H; Ar*H*), 6.82 (dd, *J* = 7.8, 2.5 Hz, 3 H; Ar*H*), 5.26 – 5.14 (m, 3 H; H–C(1’’’), H–C(7)), 4.72 (s, 2 H; H–C(1’’)), 1.34 ppm (s, 24 H; H–C(9’’), H–C(10’’), H–C(12’’), H–C(13’’), H–C(9’’’), H–C(10’’’), H–C(12’’’), H–C(13’’’); ^{13}C NMR (126 MHz, C*D*Cl$_3$): δ = 179.74, 165.13, 158.69, 155.65, 135.22, 135.04, 135.03, 132.69, 131.43, 130.44, 128.85, 127.33, 126.68, 126.04, 125.66, 121.04, 108.87, 107.51, 105.35, 101.37, 83.93, 67.46, 65.31, 60.38, 24.85 ppm; m.p. 102 – 104 °C; IR (ATR): υ = 1722 (*m*, C=O), 1596 cm^{-1} (*s*, N–H); HR-ESI-MS: m/z (%): 765.3501 ([*M*]$^+$, calcd for $C_{46}H_{49}{}^{11}B_2NO_8^+$: 765.3594).

4.2. *In vitro* Studies

HeLa cells were purchased from the Korean Cell Line Bank (Seoul, Korea). HeLa cells were cultured in MEM (Minimum Essential Media, Welgene, Korea) supplemented with 10 % FBS (Hyclone, USA), penicillin (100 U/ml) and streptomycin (100 U/ml) (Welgene). Cells were subcultured every 3 days and at 37 ℃, 5 % CO_2.

Cells were seeded in 35-mm glass bottomed dishes at a density of 3 x 10^5 cells/dish in culture media and incubated overnight at 37 ℃, 5 % CO_2. Cells were washed with PBS (Welgene), incubated with 0, 50, 100 μM of $ONOO^-$ (Cayman, USA) for 20 min, washed with PBS, treated with the probe (200 nM or 500 nM) for 20 min and washed with PBS. For fluorescence cell imaging, confocal laser microscopy (FV1200, Olympus, Japan) and FV10-ASW 4.0 software were used. Cells were excited by a 473 nm diode laser and detected with BA 490 – 590 nm emission filter with the following conditions: objective lens magnification: x60, laser transmissivity : 4%, PMT voltage: 720 V.

5. Chapter 5

5.1. Synthesis

3'-amino-6'-iodo-3*H*-spiro[isobenzofuran-1,9'-xanthen]-3-one (9.3)

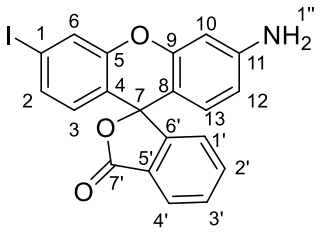

3-aminophenol (1.00 g, 9.17 mmol), 3-iodophenol (2.02 g, 9.17 mmol) and phthalic anhydride (1.36 g, 9.17 mmol) were dissolved in methansulfonic acid (8 ml). The mixture was refluxed at 140 °C for 24 h. The solution was allowed to cool down and poured into ice water. The pH was neutralised with dropwise addition of 10 M NaOH, followed by acidification with 1 M HCl. The solid was filtered off and dried *in vacuo*. The solid was resuspended in MeOH and solvent was evaporated *in vacuo*. FC (SiO_2; petroleum ether/EtOAc 80:20) gave 3'-amino-6'-iodo-3*H*-spiro[isobenzofuran-1,9'-xanthen]-3-one (1.92 g, 48 %) as a red solid.

^{1}H NMR (500 MHz, (C*D*$_3$)$_2$SO): δ= 8.04 (d, *J* = 7.60 Hz, 1 H; Ar*H*), 7.81 (d, *J* = 1.7 Hz, 2 H; Ar*H*), 7.75 (t, *J* = 7.5 Hz, 2 H; Ar*H*), 7.50 (dd, *J* = 8.3, 1.7 Hz, 2 H; Ar*H*), 7.35 (dt, *J* = 7.6, 1.0 Hz, 1 H; Ar*H*), 6.62 ppm (d, *J* = 8.3 Hz, 2 H; Ar*H*); ^{13}C NMR (126 MHz, (C*D*$_3$)$_2$SO): δ = 168.83, 161.11, 152.58, 150.77, 138.76, 136.53, 133.83, 131.09, 130.07, 127.85, 125.96, 125.52, 125.49, 124.46, 118.77, 116.16, 104.81, 97.40, 83.67, 81.08 ppm; m.p.: 267 – 269 °C; IR (ATR): *υ* = 1746 (*s*, C=O), 1588 cm^{-1} (*s*, N–H); HR-ESI-MS: m/z (%): 441.9935 ([*M*+H]$^+$, calcd for $C_{20}H_{13}INO_3^+$: 441.9935).

In accordance with literature.[180]

3'-amino-6'-azido-3*H*-spiro[isobenzofuran-1,9'-xanthen]-3-one (8.4)

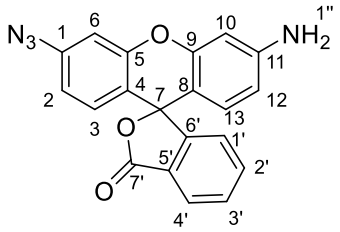

3'-amino-6'-iodo-3*H*-spiro[isobenzofuran-1,9'-xanthen]-3-one (500 mg, 1.13 mmol), sodium azide (147 mg, 2.26 mmol) and sodium ascorbate (11 mg, 0.06 mmol) were dissolved in DMSO/H_2O (6/1.2 ml). The solution was degased under N_2. Copper iodide (44 mg, 0.23 mmol) and *N'N*-dimethylethylenediamine (19 µl, 0.17 mmol) wered added. The mixture was left to stir at RT for 24 h. The solution was diluted with brine (20 ml), extracted with EtOAc (3 x 10 ml), washed with brine (3 x 15 ml), dried over $MgSO_4$, filtered and evaporeted *in vacuo*. FC (SiO_2; petroleum ether/EtOAc 60:40) gave 3'-amino-6'-azido-3*H*-spiro[isobenzofuran-1,9'-xanthen]-3-one (240 mg, 60 %) as a pink solid.

^{1}H NMR (500 MHz, C*D*Cl_3): δ = 8.04 (d, *J* = 7.60 Hz, 1 H; Ar*H*), 7.81 (d, *J* = 1.7 Hz, 2 H; Ar*H*), 7.75 (t, *J* = 7.5 Hz, 2 H; Ar*H*), 7.50 (dd, *J* = 8.3, 1.7 Hz, 2 H; Ar*H*), 7.35 (dt, *J* = 7.6, 1.0 Hz, 1 H; Ar*H*), 6.62 ppm (d, *J* = 8.3 Hz, 2 H; Ar*H*); ^{13}C NMR (126 MHz, C*D*Cl_3): δ = 150.98, 135.57, 133.44, 130.34, 129.30, 126.48, 125.88, 125.59, 123.79, 118.80, 95.71 ppm; m.p.: 285 – 288 °C; IR (ATR): υ = 1746 (*s*, C=O), 1588 cm^{-1} (*s*, N–H); HR-ESI-MS: m/z (%): 357.1027 ([*M*+H]$^+$, calcd for $C_{20}H_{13}N_4O_3^+$: 357.0982).

In accordance with literature.[180]

5.2. Fluorescence

For the RSS and amino acid selectivity studies, 5 mM stock solutions in water were prepared from commercially available reagents and salts: GSH, H_2S, NaS_2O_3, Na_2SO_4, Na_2SO_3, cysteine, homocysteine, aspartic acid, isoleucine, lysine, serine, arginine, valine, histidine, proline, glutamic acid, and phenylalanine.

5.3. *In vitro* Studies

HeLa cells were purchased from the Korean Cell Line Bank (Seoul, Korea). HeLa cells were cultured in MEM (Minimum Essential Media, Welgene, Korea) supplemented with 10 % FBS (Hyclone, USA), penicillin (100 U/ml) and streptomycin (100 U/ml) (Welgene). Cells were subcultured every 3 days and kept at 37 ℃, 5 % CO_2.

Cells were seeded in 35-mm glass bottomed dishes at a density of 3 x 10^5 cells/dish in culture media and incubated overnight at 37 ℃, 5 % CO_2. HeLa cells were washed with PBS (Welgene) treated with *N*-ethylmaleimide (0.5 mM) for 20 min, washed with PBS and then treated either with cysteine (500 μM), homocysteine (500 μM), or GSH-MEE (500 μM) for 20 min, washed with PBS, stained with the probe (20 μM) for 20 min, and washed with PBS. For fluorescence cell imaging, confocal laser microscopy (FV1200, Olympus, Japan) and FV10-ASW 4.0 software were used. Cells were excited by a 473 nm diode laser and detected with BA 490 – 590 nm emission filter with the following conditions: objective lens magnification: x60, laser transmissivity : 4%, PMT voltage : 720 V.

References

1. F. Randow, J. D. MacMicking and L. C. James, *Science*, 2013, **340**, 701-706.
2. B. Beutler, *Mol. Immunol.*, 2004, **40**, 845-859.
3. M. Kasahara, *Immune System: Evolutionary Pressure of Infectious Agents*, Encyclopedia of Life Sciences, 2011.
4. D. D. Chaplin, *J. Allergy Clin. Immunol.*, 2010, **125**, S3-S23.
5. P. Bhat, G. Leggatt, N. Waterhouse and I. H. Frazer, *Cell Death Dis.*, 2017, **8**, e2836-e2836.
6. M. L. Kapsenberg, *Nat. Rev. Immunol.*, 2003, **3**, 984-993.
7. J. Camps, *Oxidative Stress and Inflammation in Non-communicable Diseases: Molecular Mechanisms and Perspectives in Therapeutics*, Springer, 2014.
8. C. A. Thaiss, M. Levy, S. Itav and E. Elinav, *Trends Immunol.*, 2016, **37**, 84-101.
9. E. Latz, T. S. Xiao and A. Stutz, *Nat. Rev. Immunol.*, 2013, **13**, 397-411.
10. A. Sica and A. Mantovani, *J. Clin. Invest.* , 2012, **122**, 787-795.
11. A. Shapouri-Moghaddam, S. Mohammadian, H. Vazini, M. Taghadosi, S.-A. Esmaeili, F. Mardani, B. Seifi, A. Mohammadi, J. T. Afshari and A. Sahebkar, *J. Cell Physiol.*, 2018, **233**, 6425-6440.
12. M. Locati, A. Mantovani and A. Sica, *Advances in Immunology*, Academic Press, 2013, **120**, pp. 163-184.
13. C. Atri, F. Z. Guerfali and D. Laouini, *Int. J. Mol. Sci.*, 2018, **19**, 1801.
14. A. A. Starkov, *Ann. N. Y. Acad. Sci.*, 2008, **1147**, 37-52.
15. T. Finkel and N. J. Holbrook, *Nature*, 2000, **408**, 239-247.
16. B. Uttara, A. V. Singh, P. Zamboni and R. T. Mahajan, *Curr. Neuropharmacol.*, 2009, **7**, 65-74.
17. S. S. Sabharwal and P. T. Schumacker, *Nat. Rev. Cancer*, 2014, **14**, 709-721.
18. C. C. Winterbourn, *Nat. Chem. Biol.*, 2008, **4**, 278-286.
19. K. Krumova and G. Cosa, *Singlet Oxygen: Applications in Biosciences and Nanosciences*, The Royal Society of Chemistry, 2016, **1**, pp. 1-21.
20. B. Ghesquière, B. W. Wong, A. Kuchnio and P. Carmeliet, *Nature*, 2014, **511**, 167.

21. H.-Y. Tan, N. Wang, S. Li, M. Hong, X. Wang and Y. Feng, *Oxid. Med. Cell Longev.*, 2016, 16.
22. M. Lamkanfi and V. M. Dixit, *Cell*, 2014, **157**, 1013-1022.
23. F. Martinon, K. Burns and J. Tschopp, *Mol. Cell*, 2002, **10**, 417-426.
24. M. Dagenais, A. Skeldon and M. Saleh, *Cell Death Differ.*, 2012, **19**, 5-12.
25. T. Strowig, J. Henao-Mejia, E. Elinav and R. Flavell, *Nature*, 2012, **481**, 278.
26. S. M. Man and T.-D. Kanneganti, *Immunol. Rev.*, 2015, **265**, 6-21.
27. A. Chawla, K. D. Nguyen and Y. P. S. Goh, *Nat. Rev. Immunol.*, 2011, **11**, 738.
28. M. Lamkanfi, T.-D. Kanneganti, L. Franchi and G. Núñez, *J. Leukoc. Biol.*, 2007, **82**, 220-225.
29. S. Vanaja, V. K. Rathinam and K. A. Fitzgerald, *Trends Cell Biol.*, 2015, **25**, 308-315.
30. F. S. Sutterwala, S. Haasken and S. L. Cassel, *Ann. N. Y. Acad. Sci.*, 2014, **1319**, 82-95.
31. M. T. Lin and M. F. Beal, *Nature*, 2006, **443**, 787-795.
32. H.-M. Lee, J.-J. Kim, H. J. Kim, M. Shong, B. J. Ku and E.-K. Jo, *Diabetes*, 2013, **62**, 194-204.
33. Y.-H. Youm, T.-D. Kanneganti, B. Vandanmagsar, X. Zhu, A. Ravussin, A. Adijiang, J. S. Owen, M. J. Thomas, J. Francis, J. S. Parks and V. D. Dixit, *Cell Rep.*, 2012, **1**, 56-68.
34. B. Guo, S. Fu, J. Zhang, B. Liu and Z. Li, *Sci. Rep.*, 2016, **6**, 36107.
35. E. Ozaki, M. Campbell and S. L. Doyle, *J. Inflamm. Res.*, 2015, **8**, 15-27.
36. J.-W. Yu and M.-S. Lee, *Arch. Pharm. Res.*, 2016, **39**, 1503-1518.
37. H. Guo, J. B. Callaway and J. P. Y. Ting, *Nat. Med.*, 2015, **21**, 677-687.
38. H. J. Kim, J. Lim, Y. S. Jang, E. C. Shin, H. R. Kim, J. Y. Seoh, J. S. Lee, S. N. Lee, J. L. Kang and Y. H. Choi, *Cell. Physiol. Biochem.*, 2017, **42**, 2467-2480.
39. S. I. Dikalov and D. G. Harrison, *Antioxid. Redox Signal.*, 2014, **20**, 372-382.
40. Y. Zhang, M. Dai and Z. Yuan, *Anal. Methods*, 2018, **10**, 4625-4638.
41. S. Dikalov, K. K. Griendling and D. G. Harrison, *Hypertension*, 2007, **49**, 717-727.
42. S. I. Liochev and I. Fridovich, *Arch. Biochem. Biophys.*, 1997, **337**, 115-120.

43. B. Kalyanaraman, V. Darley-Usmar, K. J. A. Davies, P. A. Dennery, H. J. Forman, M. B. Grisham, G. E. Mann, K. Moore, L. J. Roberts and H. Ischiropoulos, *Free Radic. Biol. Med.*, 2012, **52**, 1-6.
44. X. Wang, H. Fang, Z. Huang, W. Shang, T. Hou, A. Cheng and H. Cheng, *J. Mol. Med.*, 2013, **91**, 917-927.
45. E. W. Miller, A. E. Albers, A. Pralle, E. Y. Isacoff and C. J. Chang, *J. Am. Chem. Soc*, 2005, **127**, 16652-16659.
46. J.-T. Hou, J. Yang, K. Li, Y.-X. Liao, K.-K. Yu, Y.-M. Xie and X.-Q. Yu, *Chem. Commun.*, 2014, **50**, 9947-9950.
47. Z.-J. Chen, W. Ren, Q. E. Wright and H.-W. Ai, *J. Am. Chem. Soc*, 2013, **135**, 14940-14943.
48. B. Brüne, N. Dehne, N. Grossmann, M. Jung, D. Namgaladze, T. Schmid, A. von Knethen and A. Weigert, *Antioxid. Redox Signal.*, 2013, **19**, 595-637.
49. H. Zhang, J. Liu, Y.-Q. Sun, Y. Huo, Y. Li, W. Liu, X. Wu, N. Zhu, Y. Shi and W. Guo, *Chem. Commun.*, 2015, **51**, 2721-2724.
50. F. Di Virgilio, T. H. Steinberg and S. C. Silverstein, *Cell Calcium*, 1990, **11**, 57-62.
51. R. J. Singh, N. Hogg, J. Joseph, E. Konorev and B. Kalyanaraman, *Arch. Biochem. Biophys.*, 1999, **361**, 331-339.
52. M. Feelisch and M. Kelm, *Biochem. Biophys. Res. Commun.*, 1991, **180**, 286-293.
53. K. Sree Kumar, V. K. Singh, W. Jackson and T. M. Seed, *Exp. Mol. Pathol.*, 2003, **74**, 68-73.
54. S. Wang, L. Chen, P. Jangili, A. Sharma, W. Li, J.-T. Hou, C. Qin, J. Yoon and J. S. Kim, *Coord. Chem. Rev.*, 2018, **374**, 36-54.
55. R. Radi, *J. Biol. Chem.*, 2013, **288**, 26464-26472.
56. E. J. Swindle, J. A. Hunt and J. W. Coleman, *J. Immunol.*, 2002, **169**, 5866-5873.
57. R. Rastogi, X. Geng, F. Li and Y. Ding, *Front. Cell Neurosci.*, 2016, **10**, 301.
58. T. H. Steinberg, A. S. Newman, J. A. Swanson and S. C. Silverstein, *J. Cell Biol.*, 1987, **105**, 2695-2702.
59. B. J. Lipman, S. C. Silverstein and T. H. Steinberg, *J. Biol. Chem.*, 1990, **265**, 2142-2147.

60. A. Bhaskaracharya, P. Dao-Ung, I. Jalilian, M. Spildrejorde, K. K. Skarratt, S. J. Fuller, R. Sluyter and L. Stokes, *PLOS ONE*, 2014, **9**, e93058.
61. T. K. Held, X. Weihua, L. Yuan, D. V. Kalvakolanu and A. S. Cross, *Infect. Immun.*, 1999, **67**, 206-212.
62. Z.-N. Sun, H.-L. Wang, F.-Q. Liu, Y. Chen, P. K. H. Tam and D. Yang, *Org. Lett.*, 2009, **11**, 1887-1890.
63. J. D. Lambeth, *Nat. Rev. Immunol.*, 2004, **4**, 181.
64. R. Leurs, H. Timmerman and A. Bast, *Biochem. Int.*, 1989, **18**, 295-299.
65. H. Sies, *Free Radic. Biol. Med.*, 1993, **14**, 313-323.
66. S. M. E. Smith, J. Min, T. Ganesh, B. Diebold, T. Kawahara, Y. Zhu, J. McCoy, A. Sun, J. Snyder, H. Fu, Y. Du, I. Lewis and J. D. Lambeth, *Chem. Biol.*, 2012, **19**, 752-763.
67. G. K. Azad and R. S. Tomar, *Mol. Biol. Rep.*, 2014, **41**, 4865-4879.
68. G. L. Squadrito, R. Cueto, A. E. Splenser, A. Valavanidis, H. Zhang, R. M. Uppu and W. A. Pryor, *Arch. Biochem. Biophys.*, 2000, **376**, 333-337.
69. T. Fukai and M. Ushio-Fukai, *Antioxid. Redox Signal.*, 2011, **15**, 1583-1606.
70. A. Orucevic and P. K. Lala, *Cancer Immunol. Immunother.*, 1996, **42**, 38-46.
71. N. M. Olken, K. M. Rusche, M. K. Richards and M. A. Marletta, *Biochem. Biophys. Res. Commun.*, 1991, **177**, 828-833.
72. D. A. Peterson, D. C. Peterson, S. Archer and E. K. Weir, *Biochem. Biophys. Res. Commun.*, 1992, **187**, 797-801.
73. S. Pfeiffer, E. Leopold, K. Schmidt, F. Brunner and B. Mayer, *Br. J. Pharmacol.*, 1996, **118**, 1433-1440.
74. S. Rotzinger, C. M. G. Aragon, F. Rogan, S. Amir and Z. Amit, *Life Sci.*, 1995, **56**, 1321-1324.
75. D. B. Kuhns, D. G. Wright, J. Nath, S. S. Kaplan and R. E. Basford, *Lab Invest*, 1988, **58**, 448-453.
76. P. A. Ward, T. W. Cunningham, K. K. McCulloch and K. J. Johnson, *Lab Invest.*, 1988, **58**, 438-447.
77. M. S. Alam, M. G. Costales, C. Cavanaugh and K. Williams, *Biomolecules*, 2015, **5**, 775-792.
78. N.-i.-H. Syed and C. Kennedy, *Wiley Interdiscip. Rev. Membr. Transp. Signal.*, 2012, **1**, 16-30.

79. G. Haskó, P. Pacher, E. A. Deitch and E. S. Vizi, *Pharmacol. Ther.*, 2007, **113**, 264-275.
80. J. Hewinson and A. B. MacKenzie, *Biochem. Soc. Trans.*, 2007, **35**, 1168-1170.
81. R. Bartlett, J. J. Yerbury and R. Sluyter, *Mediators Inflamm.*, 2013, **2013**, 271813.
82. Z. Nie, Y. Mei, M. Ford, L. Rybak, A. Marcuzzi, H. Ren, G. L. Stiles and V. Ramkumar, *Mol. Pharmacol.*, 1998, **53**, 663-669.
83. B. Muz, P. de la Puente, F. Azab and A. K. Azab, *Hypoxia*, 2015, **3**, 83-92.
84. V. Petrova, M. Annicchiarico-Petruzzelli, G. Melino and I. Amelio, *Oncogenesis*, 2018, **7**, 10.
85. M. Tafani, L. Sansone, F. Limana, T. Arcangeli, E. De Santis, M. Polese, M. Fini and M. A. Russo, *Oxid. Med. Cell Longev.*, 2016, 3907147.
86. A. Egners, M. Erdem and T. Cramer, *Mediators Inflamm.*, 2016, 10.
87. K. A. D. Sauter, L. J. Wood, J. Wong, M. Iordanov and B. E. Magun, *Cancer Biol. Ther.*, 2011, **11**, 1008-1016.
88. N. A. Thornberry, H. G. Bull, J. R. Calaycay, K. T. Chapman, A. D. Howard, M. J. Kostura, D. K. Miller, S. M. Molineaux, J. R. Weidner, J. Aunins, K. O. Elliston, J. M. Ayala, F. J. Casano, J. Chin, G. J. F. Ding, L. A. Egger, E. P. Gaffney, G. Limjuco, O. C. Palyha, S. M. Raju, A. M. Rolando, J. P. Salley, T.-T. Yamin, T. D. Lee, J. E. Shively, M. MacCross, R. A. Mumford, J. A. Schmidt and M. J. Tocci, *Nature*, 1992, **356**, 768.
89. V. Towne, M. Will, B. Oswald and Q. Zhao, *Anal. Biochem.*, 2004, **334**, 290-296.
90. M. G. Choi, J. Hwang, S. Eor and S.-K. Chang, *Org. Lett.*, 2010, **12**, 5624-5627.
91. T. Ma, H. Ding, H. Xu, Y. Lv, H. Liu, H. Wang and Z. Tian, *Analyst*, 2015, **140**, 322-329.
92. Y. Qian, J. Lin, L. Han, L. Lin and H. Zhu, *Biosens. Bioelectron.*, 2014, **58**, 282-286.
93. K. N. Bobba, Y. Zhou, L. E. Guo, T. N. Zang, J. F. Zhang and S. Bhuniya, *RSC Adv.*, 2015, **5**, 84543-84546.
94. S. Garrod, M. E. Bollard, A. W. Nicholls, S. C. Connor, J. Connelly, J. K. Nicholson and E. Holmes, *Chem. Res. Toxicol.*, 2005, **18**, 115-122.

95. H. Li, W. Liu, F. Zhang, X. Zhu, L. Huang and H. Zhang, *Anal. Chem.*, 2018, **90**, 855-858.
96. W. Chen, Z. Li, W. Shi and H. Ma, *Chem. Commun.*, 2012, **48**, 2809-2811.
97. M.-C. Frantz and P. Wipf, *Environ. Mol. Mutagen.*, 2010, **51**, 462-475.
98. J. Zielonka, J. Joseph, A. Sikora, M. Hardy, O. Ouari, J. Vasquez-Vivar, G. Cheng, M. Lopez and B. Kalyanaraman, *Chem. Rev.*, 2017.
99. S. Arai, S.-C. Lee, D. Zhai, M. Suzuki and Y. T. Chang, *Sci. Rep.*, 2014, **4**, 6701.
100. H. Zhang, J. Fan, H. Dong, S. Zhang, W. Xu, J. Wang, P. Gao and X. Peng, *J. Mater. Chem. B*, 2013, **1**, 5450-5455.
101. J.-T. Hou, M.-Y. Wu, K. Li, J. Yang, K.-K. Yu, Y.-M. Xie and X.-Q. Yu, *Chem. Commun.*, 2014, **50**, 8640-8643.
102. M. Schieber and N. S. Chandel, *Curr. Biol.*, 2014, **24**, R453-R462.
103. D. Lee, S. Khaja, J. C. Velasquez-Castano, M. Dasari, C. Sun, J. Petros, W. R. Taylor and N. Murthy, *Nat. Mater.*, 2007, **6**, 765.
104. E.-J. Kim, S. Bhuniya, H. Lee, H. M. Kim, C. Cheong, S. Maiti, K. S. Hong and J. S. Kim, *J. Am. Chem. Soc.*, 2014, **136**, 13888-13894.
105. S. Bhuniya, S. Maiti, E.-J. Kim, H. Lee, J. L. Sessler, K. S. Hong and J. S. Kim, *Angew. Chem.*, 2014, **53**, 4469-4474.
106. D. R. Webb, *Biochem. Pharmacol.*, 2014, **87**, 121-130.
107. X. Chen, F. Wang, J. Y. Hyun, T. Wei, J. Qiang, X. Ren, I. Shin and J. Yoon, *Chem. Soc. Rev.*, 2016, **45**, 2976-3016.
108. L.-C. Lo and C.-Y. Chu, *Chem. Commun.*, 2003, **0**, 2728-2729.
109. J. Kim, J. Park, H. Lee, Y. Choi and Y. Kim, *Chem. Commun.*, 2014, **50**, 9353-9356.
110. L. Yuan, W. Lin, J. Song and Y. Yang, *Chem. Commun.*, 2011, **47**, 12691-12693.
111. N. Soh, K. Makihara, T. Ariyoshi, D. Seto, T. Maki, H. Nakajima, K. Nakano and T. Imato, *Anal. Sci.*, 2008, **24**, 293-296.
112. X. Zhou, Y. Kwon, G. Kim, J.-H. Ryu and J. Yoon, *Biosens. Bioelectron.*, 2015, **64**, 285-291.
113. L. Long, D. Zhang, X. Li, J. Zhang, C. Zhang and L. Zhou, *Anal. Chim. Acta*, 2013, **775**, 100-105.
114. H. Zhu, J. Fan, J. Du and X. Peng, *Acc. Chem. Res.*, 2016, **49**, 2115-2126.

115. W. Li, X. Wang, Y.-M. Zhang and S. X.-A. Zhang, *Dyes Pigm.*, 2018, **148**, 348-352.
116. C. Szíjjártó, E. Pershagen, N. O. Ilchenko and K. E. Borbas, *Chem. Eur. J.*, 2013, **19**, 3099-3109.
117. C. Li, R. Pan, P. Li, Q. Guan, J. Ao, K. Wang, L. Xu, X. Liang, X. Jin, C. Zhang and X. Zhu, *Anal. Chem.*, 2017, **89**, 5966-5975.
118. X. Zhou, F. Su, H. Lu, P. Senechal-Willis, Y. Tian, R. H. Johnson and D. R. Meldrum, *Biomaterials*, 2012, **33**, 171-180.
119. B. Dong, X. Song, C. Wang, X. Kong, Y. Tang and W. Lin, *Anal. Chem.*, 2016, **88**, 4085-4091.
120. L. He, W. Lin, Q. Xu and H. Wei, *Chem. Commun.*, 2015, **51**, 1510-1513.
121. A. R. Lippert, G. C. Van de Bittner and C. J. Chang, *Acc. Chem. Res.*, 2011, **44**, 793-804.
122. M. C. Y. Chang, A. Pralle, E. Y. Isacoff and C. J. Chang, *J. Am. Chem. Soc.*, 2004, **126**, 15392-15393.
123. E. W. Miller, O. Tulyathan, E. Y. Isacoff and C. J. Chang, *Nat Chem Biol*, 2007, **3**, 263-267.
124. B. C. Dickinson and C. J. Chang, *J. Am. Chem. Soc*, 2008, **130**, 9638-9639.
125. D. Yang, H.-L. Wang, Z.-N. Sun, N.-W. Chung and J.-G. Shen, *J. Am. Chem. Soc.*, 2006, **128**, 6004-6005.
126. D. Yang, Y.-C. Tang, J. Chen, X.-C. Wang, M. D. Bartberger, K. N. Houk and L. Olson, *J. Am. Chem. Soc.*, 1999, **121**, 11976-11983.
127. T. Peng and D. Yang, *Org. Lett.*, 2010, **12**, 4932-4935.
128. T. Peng, N.-K. Wong, X. Chen, Y.-K. Chan, D. H.-H. Ho, Z. Sun, J. J. Hu, J. Shen, H. El-Nezami and D. Yang, *J. Am. Chem. Soc*, 2014, **136**, 11728-11734.
129. T. Peng, X. Chen, L. Gao, T. Zhang, W. Wang, J. Shen and D. Yang, *Chem. Sci.*, 2016, **7**, 5407-5413.
130. R. Weissleder, *Nat Biotech*, 2001, **19**, 316-317.
131. J.-T. Hou, K. Li, J. Yang, K.-K. Yu, Y.-X. Liao, Y.-Z. Ran, Y.-H. Liu, X.-D. Zhou and X.-Q. Yu, *Chem. Commun.*, 2015, **51**, 6781-6784.
132. K. Li, J.-T. Hou, J. Yang and X.-Q. Yu, *Chem. Commun.*, 2017.
133. L. F. Yousif, K. M. Stewart and S. O. Kelley, *ChemBioChem*, 2009, **10**, 1939-1950.
134. J. M. Meinig, L. Fu and B. R. Peterson, *Angew. Chem.*, 2015, **54**, 9696-9699.

135. D. Wu, J.-C. Ryu, Y. W. Chung, D. Lee, J.-H. Ryu, J.-H. Yoon and J. Yoon, *Anal. Chem.*, 2017, **89**, 10924-10931.
136. B. Zhu, M. Zhang, L. Wu, Z. Zhao, C. Liu, Z. Wang, Q. Duan, Y. Wang and P. Jia, *Sens. Actuators B Chem.*, 2018, **257**, 436-441.
137. K. E. Knewtson, D. Rane and B. R. Peterson, *Chem. Biol.*, 2018, **13**, 2595-2602.
138. D. K. B., A. Arpita, M. Marianne and C. S. M., *ChemBioChem*, 2013, **14**, 593-598.
139. K. K. Kim, J. O. Escobedo, N. N. St. Luce, O. Rusin, D. Wong and R. M. Strongin, *Org. Lett.*, 2003, **5**, 5007-5010.
140. S. Jiang, J. O. Escobedo, K. K. Kim, O. Alptürk, G. K. Samoei, S. O. Fakayode, I. M. Warner, O. Rusin and R. M. Strongin, *J. Am. Chem. Soc.*, 2006, **128**, 12221-12228.
141. K. B. Daniel, A. Agrawal, M. Manchester and S. M. Cohen, *ChemBioChem*, 2013, **14**, 593-598.
142. A. C. Sedgwick, H.-H. Han, J. E. Gardiner, S. D. Bull, X.-P. He and T. D. James, *Chem. Sci.*, 2018, **9**, 3672-3676.
143. M. L. Odyniec, J. E. Gardiner, A. C. Sedgwick, X.-P. He, S. D. Bull and T. D. James, *Front. Chem. Sci. Eng.*, 2019.
144. T. Ida, T. Sawa, H. Ihara, Y. Tsuchiya, Y. Watanabe, Y. Kumagai, M. Suematsu, H. Motohashi, S. Fujii, T. Matsunaga, M. Yamamoto, K. Ono, N. O. Devarie-Baez, M. Xian, J. M. Fukuto and T. Akaike, *Proc. Natl. Acad. Sci. U.S.A.*, 2014, **111**, 7606-7611.
145. N. Ballatori, S. M. Krance, S. Notenboom, S. Shi, K. Tieu and C. L. Hammond, *Biol. Chem.*, 2009, **390**, 191-214.
146. A. Ortega and E. Obrador, *Crit. Rev. Clin. Lab. Sci.*, 2006, **43**, 143-181.
147. S. Lee, J. Li, X. Zhou, J. Yin and J. Yoon, *Coord. Chem. Rev.*, 2018, **366**, 29-68.
148. R. Huang, B.-B. Wang, X.-M. Si-Tu, T. Gao, F.-F. Wang, H. He, X.-Y. Fan, F.-L. Jiang and Y. Liu, *Chem. Commun.*, 2016, **52**, 11579-11582.
149. K.-K. Yu, K. Li, J.-T. Hou, J. Yang, Y.-M. Xie and X.-Q. Yu, *Polym. Chem.*, 2014, **5**, 5804-5812.
150. H. Li, C. Wang, M. She, Y. Zhu, J. Zhang, Z. Yang, P. Liu, Y. Wang and J. Li, *Anal. Chim. Acta*, 2015, **900**, 97-102.

151. X. Wu, H. Shu, B. Zhou, Y. Geng, X. Bao and J. Zhu, *Sens. Actuators B-Chem.*, 2016, **237**, 431-442.
152. Y. Zhang, F. Huo, C. Yin, Y. Yue, J. Hao, J. Chao and D. Liu, *Sens. Actuators B Chem.*, 2015, **207**, 59-65.
153. L. Qu, C. Yin, F. Huo, J. Li, J. Chao and Y. Zhang, *Sens. Actuators B Chem.*, 2014, **195**, 246-251.
154. W. Chen, X. Yue, H. Zhang, W. Li, L. Zhang, Q. Xiao, C. Huang, J. Sheng and X. Song, *Anal. Chem.*, 2017, **89**, 12984-12991.
155. S. V. Mulay, Y. Kim, M. Choi, D. Y. Lee, J. Choi, Y. Lee, S. Jon and D. G. Churchill, *Anal. Chem.*, 2018, **90**, 2648-2654.
156. S. T. Manjare, Y. Kim and D. G. Churchill, *Acc. Chem. Res.*, 2014, **47**, 2985-2998.
157. J. Liu, Y.-Q. Sun, H. Zhang, Y. Huo, Y. Shi and W. Guo, *Chem. Sci.*, 2014, **5**, 3183-3188.
158. Y. Zhang, X. Shao, Y. Wang, F. Pan, R. Kang, F. Peng, Z. Huang, W. Zhang and W. Zhao, *Chem. Commun.*, 2015, **51**, 4245-4248.
159. L.-Y. Niu, Y.-S. Guan, Y.-Z. Chen, L.-Z. Wu, C.-H. Tung and Q.-Z. Yang, *Chem. Commun.*, 2013, **49**, 1294-1296.
160. L.-Y. Niu, Y.-S. Guan, Y.-Z. Chen, L.-Z. Wu, C.-H. Tung and Q.-Z. Yang, *J. Am. Chem. Soc.*, 2012, **134**, 18928-18931.
161. H. Zhang, L. Xu, W. Chen, J. Huang, C. Huang, J. Sheng and X. Song, *ACS Sens* 2018, **3**, 2513-2517.
162. N. E. Francoleon, S. J. Carrington and J. M. Fukuto, *Arch. Biochem. Biophys.*, 2011, **516**, 146-153.
163. M. D. Hartle, S. K. Sommer, S. R. Dietrich and M. D. Pluth, *Inorg. Chem.*, 2014, **53**, 7800-7802.
164. V. S. Lin, W. Chen, M. Xian and C. J. Chang, *Chem. Soc. Rev.*, 2015, **44**, 4596-4618.
165. V. S. Lin, A. R. Lippert and C. J. Chang, *Proc. Natl. Acad. Sci. U.S.A.*, 2013, **110**, 7131-7135.
166. Z. Pianowski, K. Gorska, L. Oswald, C. A. Merten and N. Winssinger, *J. Am. Chem. Soc.*, 2009, **131**, 6492-6497.
167. K. Gorska, A. Manicardi, S. Barluenga and N. Winssinger, *Chem. Commun.*, 2011, **47**, 4364-4366.

168. D. Zhang, Z. Yang, H. Li, Z. Pei, S. Sun and Y. Xu, *Chem. Commun.*, 2016, **52**, 749-752.
169. M. E. Anderson, *Chem. Biol. Interact.*, 1998, **111-112**, 1-14.
170. J. R. Winther and C. Thorpe, *Biochim. Biophys. Acta.*, 2014, **1840**, 838-846.
171. F. Yu, P. Li, B. Wang and K. Han, *J. Am. Chem. Soc.*, 2013, **135**, 7674-7680.
172. D. Pendin, E. Greotti, K. Lefkimmiatis and T. Pozzan, *J. Gen. Physiol.*, 2017, **149**, 1-36.
173. L. V. Johnson, M. L. Walsh and L. B. Chen, *Proc. Natl. Acad. Sci. U.S.A.*, 1980, **77**, 990-994.
174. M. B. Andrus, E. J. Hicken, J. C. Stephens and D. K. Bedke, *J. Org. Chem.*, 2006, **71**, 8651-8654.
175. W. Li, X. Wang, Y.-M. Zhang and S. X.-A. Zhang, *Dyes Pigm.*, 2018, **148**, 348-352.
176. J. Chen, X. Jiang, C. Zhang, K. R. MacKenzie, F. Stossi, T. Palzkill, M. C. Wang and J. Wang, *ACS Sens.*, 2017, **2**, 1257-1261.
177. T. Yonghe, M. Yanyan, X. An, X. Gaoping and L. Weiying, *Methods Appl. Fluoresc.*, 2017, **5**, 024005.
178. X. Zhou, F. Su, H. Lu, P. Senechal-Willis, Y. Tian, R. H. Johnson and D. R. Meldrum, *Biomaterials*, 2012, **33**, 171-180.
179. L. Jie, G. Zhong-Zhi, G. Jian-Wu and Z. Zhan-Hui, *Appl. Organomet. Chem.*, 2011, **25**, 537-541.
180. Z. Pianowski, K. Gorska, L. Oswald, C. A. Merten and N. Winssinger, *J. Am. Chem. Soc*, 2009, **131**, 6492-6497.

Appendix

PR1 functionalised sensors developed as part of the PhD but not discussed as part of this thesis.